University of Cincinnati

Date: 8/1/2023

I, Li Meng, hereby submit this original work as part of the requirements for the degree of Doctor of Philosophy in Mechanical Engineering.

It is entitled:

Discrete and Continuum Modeling of Brittle and Ductile Fracture within the Framework of Finite Element Method

Student's name: **Li Meng**

This work and its defense approved by:

Committee chair: Ala Tabiei, Ph.D.

Committee member: Michael Alexander-Ramos, Ph.D.

Committee member: Christopher Calhoun, Ph.D.

Committee member: Woo Kyun Kim, Ph.D.

Committee member: Gui-Rong Liu, Ph.D.

46704

Discrete and Continuum Modeling of Brittle and Ductile Fracture within the Framework of Finite Element Method

A dissertation submitted to the

Graduate School

of the University of Cincinnati

in partial fulfillment of the

requirements for the degree of

Doctor of Philosophy

in the Department of Mechanical and Materials Engineering

of the College of Engineering and Applied Science

August 2023

by

Li Meng

M.S. Chongqing University, Chongqing, China, June 2018

B.S. Jiangsu University, Jiangsu, China, June 2015

Committee chair: Dr. Ala Tabiei

Abstract

Accurate prediction of fracture propagation is of great importance in both academy and industry. In this dissertation, numerical modeling of brittle and ductile fracture using cohesive zone model (discrete description) and phase field model (continuum description) is investigated.

For cohesive zone model, two improvements on damage evolution and artificial compliance are presented. Before explaining these two improvements, background of cohesive zone model is presented first to help better understand this topic, including local coordinate system, stiffness matrix, internal nodal force, and constitutive law and damage criteria. For damage evolution, two commonly used damage evolution methods are compared and analyzed to investigate the discontinuous force in cohesive element, and it is found that monotonically increasing damage factor method can avoid discontinuous force that happens in monotonically increasing effective separation method. Unreasonable failure is also explained in detail that happens in monotonically increasing effective separation method when mixed mode ratio changes. For artificial compliance, it is found to be related to cohesive element modeling method and stiffness parameter selection. By using finite-thickness cohesive element and proper stiffness parameter, artificial compliance can be totally removed.

The effects of strain rate, plastic strain, and variable damping are considered together into one cohesive element. To extend the scope of application of cohesive zone model to more materials, strain rate and plastic strain are considered. Based on the damage factor in classical bilinear cohesive law, a generalized damage factor model is proposed to cover all materials from zero plastic strain to maximum plastic strain. By adding a variable damping into cohesive element, spurious oscillation and excessive cohesive element deletion in cohesive zone model are improved, and there is no discontinuous force like when using a constant damping. Several simulations are presented to verify these three effects.

For phase field model, the modeling of brittle fracture is investigated. Geometric function and degradation function are investigated separately to solve the nonlinearity and inelasticity in the stress-strain curve of classical phase field model. First, by using a generalized quadratic geometric function and applying

phase zeroing, nonlinearity and inelasticity can be completely removed, and a good thing is that this still leads to a linear FEM problem. Second, instead of using a second order degradation function, some higher order degradation functions with more constrains could give more options for stress-strain curve. However, higher order degradation function leads to a nonlinear FEM problem, and Newton-Raphson method is used to solve this nonlinear problem. Both methods proposed in this dissertation work well for brittle materials.

Apart from phase field modeling of brittle fracture, phase field model for ductile fracture is also investigated. Based on the ductile material with isotropic hardening, phase field model is coupled into this material. One difference here from the classical phase field model for brittle fracture is the calculation of strain energy, and strain energy is not limited in the linear elastic range. To model the degradation of material, parameters for ductile material with isotropic hardening are multiplied with degradation function, i.e., Young's modulus, yield stress, and hardening modulus. Depending on the degradation function, both linear and nonlinear FEM formulation can also be used like the modeling of brittle fracture in Section 4.

Keywords: Brittle Fracture, Ductile Fracture, Cohesive Zone Model, Damage Evolution, Artificial Compliance, Strain Rate, Plastic Strain, Variable Damping, Phase Field Model, Geometric Function, Degradation Function, Length Scale Insensitive, Γ convergence, Isotropic Hardening

Acknowledgment

I would like to express my deepest gratitude to my advisor, Dr. Ala Tabiei, for his constant support and encouragement throughout my graduate studies. He has always been a person that I look up to for his hardworking and passionate attitude. His patient way of teaching has deepened my interest in this field – computational solid mechanics. This dissertation would not have been possible without his amazing mentorship.

I would like to thank Dr. Christopher A. Calhoun, Dr. Gui-Rong Liu, Dr. Michael J. Alexander-Ramos, and Dr. Woo Kyun Kim for guiding me on my dissertation committee and helping me improve my work. Dr. Gui-Rong Liu's teaching style makes Advanced Finite Element Method class more interesting to me, even though I was struggling to understand the concepts in that class.

I would like to thank Dr. Manish Kumar, Dr. Milind Jog, Prof. Michael L. Mains, Dr. Christopher A. Calhoun, and Dr. Amir Salehpour for supporting me with teaching assistant job. I would also like to thank UC P&G Digital Accelerator for supporting me, and the wonderful people I worked with, Melissa Ryan, Ken Comer, Bryan Kadlubowski, Catherine Rojas, Amanda Schwartz, Rakesh Gummalla, Richard Hamm, and Shuoran Du. Special thanks to Wenlong Zhang, Abinash Patro, Pietro Pascale, and Varad Maitra for their valuable help during my graduate studies.

I would like to thank my parents, my older brother, and all my friends who stood beside me and encouraged me. In closing, I am reminded of the words that have fueled my journey thus far, inspiring me to reach this very point.

The path of learning is filled with hardships; perseverance is required!

求學之路多艱辛，需持之以恆!

Table of contents

List of figures

List of tables

1 Introduction

1.1 Motivation of this dissertation

Fracture has been a longstanding challenge accompanying the existence of man-made structures, but it is in the past several decades that the field of fracture mechanics has experienced significant advancements. This progress can be attributed to notable fracture accidents and substantial economic losses that prompted increased attention and research in this field. During World War II (1939-1945), the Liberty ships were mass-produced cargo ships built to aid in the transportation of supplies and materials, but these ships experienced numerous fractures and structural failures, particularly in the midship region, see Figure 1.1. In 1983, according to the "NBS Special Publication 604: Costs of Fracture to the United States" published by the National Bureau of Standards (now known as the National Institute of Standards and Technology), the estimated annual costs of failure due to fracture in the United States were approximately $119 billion in 1981. These costs encompassed a wide range of sectors, including transportation, manufacturing, construction, and infrastructure.

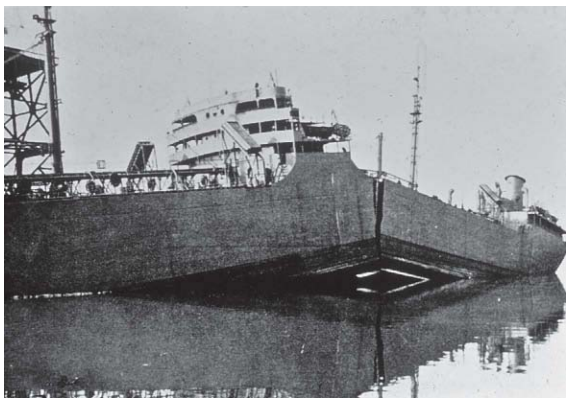

Figure 1.1 Fracture of Liberty ship

In 2007, the collapse of the I-35W Mississippi River Bridge was a significant infrastructure failure that occurred in Minneapolis, Minnesota, United States. The collapse resulted in tragic consequences, with 13 people losing their lives and many others injured, see Figure 1.2 (a). The American Society of Civil Engineers (ASCE) provides periodic reports on the state of infrastructure in the United States. According

to their 2021 Infrastructure Report Card, the estimated investment gap for only addressing bridge deficiencies alone is $125 billion. In 2011, there was an incident involving a Southwest Airlines Boeing 737-300 aircraft. During a flight from Phoenix, Arizona to Sacramento, California, the aircraft experienced a rapid decompression due to a fatigue crack in the fuselage. The crack had propagated and eventually led to a five-foot-long hole in the top portion of the fuselage, see Figure 1.2 (b).

(a) (b)

Figure 1.2 (a) the collapse of the I-35W Mississippi River Bridge, (b) the five-foot hole in the 15-year-old Southwest Airlines jet

More recently, on 18 June 2023, unfortunately, Titan, a submersible operated by American tourism and expeditions company OceanGate, imploded during its fifth expedition to view the wreck of the Titanic in the North Atlantic Ocean off the coast of Newfoundland, Canada, causing five people to lose their lives. The OceanGate's Titan submersible departed from the more traditional titanium-sphere design for deep-ocean submersibles, stitching a carbon-fiber cylinder between two titanium hemispheres to create a larger pressure hull that could accommodate more passengers. Searchers found the two titanium end caps on the ocean floor, separated from the cylinder. This failure is believed to have occurred due to the experimental design of the vessel's hull, which was primarily made of less-durable, less understood carbon fibers instead of traditional materials, see Figure 1.3 (b).

(a)

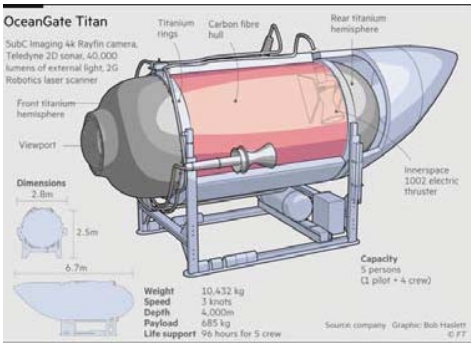

(b)

Figure 1.3 (a) Titan submersible, (b) the design of Titan submersible

From the examples shown above, fracture-induced failures not only contribute to repair expenses, replacement costs, traffic disruptions, and economic inefficiencies, but also could lead to hazardous situations to people's lives. What's more, now more and more different materials are used in structures that have complicated failure modes, and a good understanding of fracture mechanics is required to avert disasters which not only cause financial losses but may also cost human lives.

Finite element method, as a popular method for numerically solving differential equations arising in engineering and mathematical modeling, plays a key role in design decisions. In the field of structural analysis, the prevention of fracture-induced failure is one of the major concerns to analysts, and the numerical modeling of fracture process could be helpful in this situation. Depending on the orientation of fracture with respect to load, the type of fracture can be divided into three modes: Mode I (opening mode, normal direction), Mode II (sliding mode, tangential direction 1), and Mode III (tearing mode, tangential direction 2), see Figure 1.4.

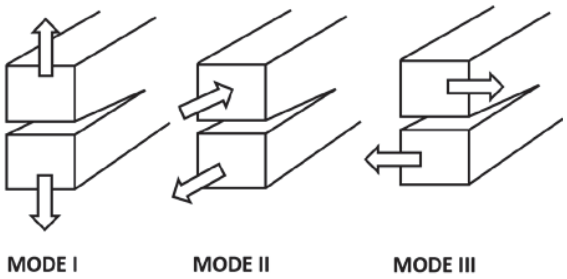

Figure 1.4 Modes of failure

A wide variety of fracture models has been proposed in publications, and a key feature of these models

is the fracture energy term that relates energy dissipation to the formulation of new crack surface [1]. Griffith's theory for brittle fracture stands as a particularly successful example, where the potential energy of a body depends on both the accumulated elastic strain energy and the surface energy associated with newly formed crack. A crack extends when a critical strain energy value is reached. Apart from brittle fracture, the modeling of ductile fracture is also a hot topic. In this dissertation, numerical modeling of brittle and ductile fracture within the framework of finite element method is investigated.

1.2 Review of the computational modeling of fracture

Over the past several decades, many efforts have been put into modeling fracture propagation, and there are two main categories: discrete modeling and continuum modeling. The discrete modeling of fracture incorporates a discontinuity into the displacement field, whereas the continuum modeling does not. Usually, continuum modeling, or smeared crack approach, incorporates a damage parameter into the model that controls the degradation of the strength of material [1].

1.2.1 Discrete modeling of fracture

Examples of discrete modeling of fracture include Element Deletion Method (EDM) [2], Extended Finite Element Method (XFEM) [3], Cohesive Segments Method (CSM) [4], Cohesive Zone Model (CZM) [5], and so on. Element deletion method represents the crack by a series of elements in which the stress is set to zero [2]. Extended finite element method allows for the crack to pass arbitrarily through elements by incorporating enrichment functions to handle the field discontinuities, no need of remeshing [3]. In cohesive segments method, the crack is represented by a set of overlapping cohesive segments, and these cohesive segments are inserted into finite elements as discontinuities in displacement field by exploiting the partition-of-unity property of shape functions [4]. In cohesive zone model, the crack is modeled by separation along element interfaces. In this method, the continuum is characterized by two constitutive relations: a volumetric constitutive law that relates stress and strain in the bulk elements, and a cohesive interface constitutive relation between traction and displacement jump across a specified set of cohesive elements [6]. These approaches have been studied in depth, and it has been shown that they can model crack

propagation behavior in 2D and 3D scenarios successfully.

1.2.2 Continuum modeling of fracture

Continuum modeling of fracture is based on constitutive equation coupled with damage at the material point level so that the material models are often referred to as Continuum Damage Mechanics (CDM). Examples of continuum modeling of fracture include Isotropic Damage Model (IDM) [7], Anisotropic Damage Model (ADM) [8], Microplane Damage Model (MDM) [9], Phase Field Model (PFM) [10], and so on. The assumption of isotropic damage model for which the stiffness degradation is isotropic and independent on the direction of loading can only be justified to a certain extent for materials that behave isotropically in the elastic domain [7]. For anisotropic damage model, a damage tensor instead of a scalar damage parameter like isotropic damage model is required to model anisotropic damage [8]. The microplane damage model allows for the description of damage induced anisotropy in a natural manner by introducing constitutive laws for quantities on individual microplane at each material point [9]. One drawback of these models is that the damage zone tends to widen in a direction normal to the crack direction as the simulation proceeds [1]. And this behavior limits the effectiveness of continuum damage models when modeling large dominant cracks.

In phase field model, a continuous scalar-valued phase field is introduced in the domain to indicate whether the material is in unfractured or fractured phase, which is similar to the damage variable in the three models mentioned above [7-9]. However, phase field model also uses a length scale parameter to control the width of the approximation of crack, which is not used in other continuum damage models mentioned above [6].

Among these different approaches, the focus of this dissertation will be on cohesive zone model (discrete modeling) and phase field model (continuum modeling) to simulate brittle and ductile fracture. More details about cohesive zone model and phase field model are shown as below.

1.3 Discrete modeling: Cohesive zone model

Cohesive zone model has been used extensively in studying fracture propagation, where cohesive

element is used to model cohesive interface between edges of shell elements, faces of shell elements, and faces of solid elements, typically for treating delamination. Cohesive zone model is based on the cohesive zone concept proposed by Barenblatt [11] and Dugdale [12]. It is assumed that at the ahead of crack tip, there is a thin layer separating two solids in which damage mechanisms leading to crack are localized, and the behavior of this crack process zone is characterized by traction separation law called cohesive law. There are two categories of cohesive law: (1) intrinsic cohesive law that has an initial elastic range, (2) extrinsic cohesive law that is initially rigid, see Figures 1.5 (b) and 1.5 (c). An example of a tensile test of a polymethyl methacrylate plate using cohesive zone model is shown in Figure 1.6, where damage factor is in [0,1].

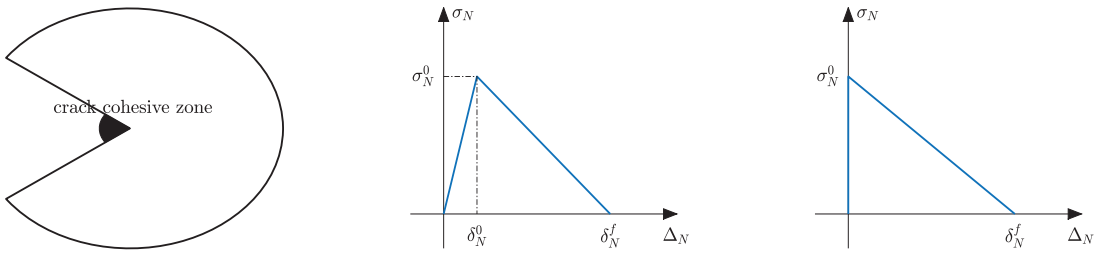

(a) (b) (c)

Figure 1.5 (a) cohesive zone at crack tip, (b) intrinsic cohesive law, (c) extrinsic cohesive law

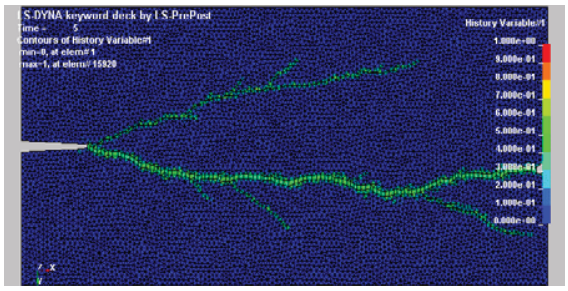

Figure 1.6 Tensile test of a polymethyl methacrylate plate, damage from 0 to 1

Another way to differentiate different cohesive law is the shape of its constitutive law, and the commonly used in publications includes bilinear shape [13], trapezoidal shape [14], polynomial shape [15], and exponential shape [16]. Fernández-Cañadas et al. [17] investigate the influence of this shape on the failure of adhesively-bonded single-lap joint. For all these different cohesive laws, bilinear cohesive law has become an important part of them. The major advantage of bilinear cohesive law is that a very simple traction separation law can provide results good enough to model with accuracy delamination and fracture

[18]. Computational implementation is straightforward and parameters needed can be easily identified from standard tests, like Double Cantilever Beam (DCB) test and End Notched Flexure (ENF) test. Cohesive zone model with bilinear cohesive law will be investigated in this dissertation.

When it comes to bilinear cohesive law, the important damage criteria are quadratic stress criterion, power law, and B-K law [19,20], and they are about how to define the initiation of damage and the failure of damage evolution. For the initiation of damage in many papers, the situation between positive and negative normal tractions is different. The common method is that normal and tangential tractions are coupled when normal traction is positive, but these two tractions are uncoupled when normal traction is negative. The assumption behind this is that negative normal traction does not contribute to the damage evolution. However, the fact is that no structure can hold infinite negative normal traction, and there are many coupled criteria that have been used in publications. Hou et al. [21,22] introduce two formulas to depict damage initiation when cohesive element undergoes tensile and compressive loads, and both tensile load and compressive load are coupled with tangential load. Naik et al. [23-25] consider the difference between positive and negative normal tractions in woven-fabric composites and use different fracture strength values for tensile and compressive loads. In 2015, Abrate et al. [18] write a comprehensive summary including many different failure models and different criteria predicting the initiation of damage.

After constitutive law and damage criterion have been defined, the next to be considered could be damage evolution, which is about how to define loading, unloading, and reloading. Two common methods for bilinear cohesive law are monotonically increasing effective separation method and monotonically increasing damage factor method. The change from loading to unloading and reloading depends on whether current effective separation or current damage factor is larger than its maximum history value. Kregting [26] uses monotonically increasing effective separation method to simulate composite delamination, but discontinuous force is found when mixed mode ratio changes. Gao et al. [27] also use this method to simulate impact fracture behavior of laminated glass. To remove discontinuous force in this method, Zhang and Tabiei [28] use linear interpolation based on the mixed mode ratio at each time step to obtain tractions. Another problem with this method is that unreasonable failure can happen when maximum separations in

Mode I and Mode II are different. If maximum history effective separation for a loading process is larger than the maximum allowable separation in some mixed mode ratios, cohesive element could fail just because of a change of mixed mode ratio, and power law or B-K law will not be strictly followed. Discontinuous force and unreasonable failure in cohesive zone model are still needed to investigate.

For intrinsic bilinear cohesive law, a common numerical problem is artificial compliance, and many methods have been proposed to try to solve it. Peng et al. [29] find that the implementation of zero-thickness cohesive element in tape introduces artificial compliance, which would affect the mechanical behavior of the tape. Song et al. [30] use a potential-based exponential cohesive law to simulate the fracture of asphalt concrete, and initial elastic part is replaced by an adjustable initial slope to reduce artificial compliance. Fan and Tadmor [31] analyze the relation between effective material properties and cohesive element properties, and rescaling of cohesive element thickness is proposed to reduce the effect of artificial compliance and obtain mesh-independent results. As an important and even critical factor in dynamic problem, the delay of stress wave caused by artificial compliance should be in an acceptable range. Figure 1.7 shows the delay of stress wave in a bar under impact load.

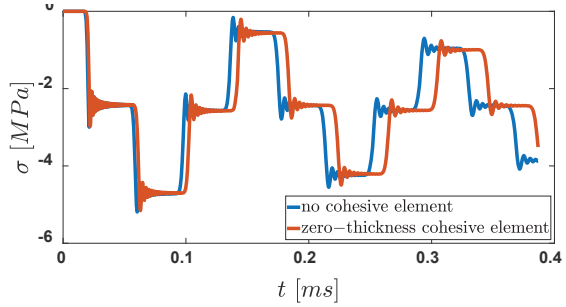

Figure 1.7 An example of artificial compliance

Another hot topic for cohesive zone model over the past few decades is the effects of strain rate and plastic strain on cohesive laws. Marzi et al. [32,33] investigate rate-dependent cohesive zone model and rate-dependent elasto-plastic cohesive zone model for a crash analysis of adhesively bonded joints. Carlberger et al. [34] investigate the influence of temperature and strain rate on cohesive properties of a structural epoxy adhesive. For the effect of plastic strain, the classical bilinear cohesive law does not consider this effect, so it can only be used for brittle materials. Based on experiment results, Cui [35]

investigates a failure criterion for ductile adhesive, but plastic strain is not considered. Marzi et al. [32] propose a new damage factor model to consider plastic strain for adhesively bonded joints, and later this damage factor model is used as a new material type in LS-DYNA [20]. Cazes et al. [36] extend an elastic-damageable model to an elastic-plastic damageable model, and this model can handle material's softening well. The common problem in these papers is that the negative quadrant of cohesive law is not mentioned and then the reciprocating load is not guaranteed. What's more, a single plastic strain model is not enough to cover all materials since different material usually means different plastic strain properties.

Apart from the effects of strain rate and plastic strain, one more effect investigated in this dissertation is damping in bilinear cohesive law. Spurious oscillation is a problem often found in explicit time integration codes using cohesive elements, and too much oscillation could lead to incorrect results and conclusions. Usually, a damper is a good component to damp oscillation for a mechanical system. To avoid undesirable oscillation in surface contact, a damper perpendicular to the two contact surfaces is added in [37]. In some researches [38-40], damping is used to consider rate-related effects for cohesive element, but most of them use a constant damping. One problem with this constant damping is that, it cannot describe fully debonding because traction does not decrease to zero at high strain rate when cohesive element fails [32], which would influence the original cohesive law. Giambanco and Fileccia Scimemi [41] have formulated an interface model in the framework of visco-plasticity for generalized standard materials, and a decrease of viscosity with the increase of damage is considered to enable fully debonding. Compared with constant damping, variable damping without extra huge traction discontinuity at the start and end of cohesive law is more suitable for the modeling of damping effect in cohesive elements.

Overall, even though cohesive zone model has been used widely in fracture propagation, there are still some problems overlooked and to be solved. First, damage evolution and artificial compliance are investigated in this dissertation. Second, strain rate, plastic strain, and variable damping are considered into one cohesive element for a wilder application. Variable damping is used to help improve spurious oscillation that could lead to excessive cohesive element deletion and then consequently underestimate fragment size.

1.4 Continuum modeling: Phase field model

Phase field model has been used widely in computational modeling for complex fracture propagation, especially in static and dynamic scenarios with brittle and ductile materials [42-45]. The major advantage of phase field model is that arbitrary nucleation, propagation, branching, and merging can be modeled in a single standard-alone framework, no need of any *ad hoc* criterion and extrinsic tracking algorithm [46]. The theory behind this model is the minimization of total energy proposed by Francfort and Marigo [47], where potential energy consists of strain energy and fracture energy. To provide a feasible numerical method for difficult free-discontinuity problem, Bourdin et al. [48] regularize the fracture energy as an elliptic functional of the displacement field and an auxiliary field called phase field. This regularized energy functional is characterized by a length scale which controls the width of crack band [49]. The main idea is the transform from line integral and surface integral to a volume integral for the fracture surface calculation, which then could be coupled with the volume integral of other energies, like kinetic energy, strain energy, and external work. In this way, the solid domain with crack can be described by displacement field and phase field together. Refer to Wu et al. [50] for a comprehensive review of phase field modeling of fracture. Figure 1.8 shows an example of tensile test using phase field model.

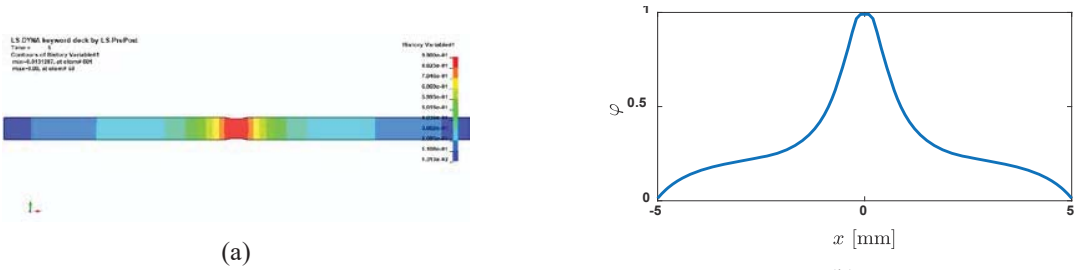

(a) (b)

Figure 1.8 (a) phase field model for a tensile test, (b) phase profile extracted from the tensile test left

Based on the variational formulation of Griffith's theory [47], phase field model of quasi-static brittle fracture is implemented for the first time by Bourdin et al. [48]. More recently, a quasi-static phase field formulation aligned with thermodynamic arguments is proposed by Miehe et al. [43]. Dynamic brittle fracture using phase field model is also a hot topic [44,51]. Liu et al. [52] investigate quasi-static and dynamic fracture, and solve the problem using monolithic and staggered schemes. In 2014, Miehe and

Schänzel [53] extend the phase field model to ductile materials to consider large strain. Different method to derive the governing equations has also been presented in papers. Based on the first and second laws of thermodynamics, Wu [54] derives the governing equations from the variation of energy dissipation. Based on the Hamilton's principle, Borden et al. [44] obtain the governing equations from the minimization of energy (including kinetic energy and potential energy) using Euler-Lagrange equation. More information about Hamilton's principle refers to [55].

Even though phase field model has been used widely, some aspects of it are still under investigation. The first is the split of strain energy to depict the degradation of material. A directional split method is introduced, analyzed, and compared with the two commonly used formulations (spectral split and volumetric-deviatoric split) in [56]. An orthogonal split of strain tensor into compressive and tensile parts is implemented to mimic unilateral contact condition in [57]. A methodology of splitting energy density function is proposed in [58] that can be applied to a large variety of polyconvex energies. Several existing approaches are reviewed to account for the tension-compression asymmetry of fracture behavior of materials in [59]. After the phase field problem is fully defined, the next is about how to solve it. Common ways to solve phase field model include staggered algorithm and monolithic algorithm [60,61]. An improved staggered iteration scheme is proposed in [62] where nonlinear subproblems are solved by a one-pass procedure. Broyden-Fletcher-Goldfarb-Shanno (BFGS) algorithm to solve in a monolithic manner the system of coupled governing equations is proposed in [63]. To make sure fracture surface and fracture energy results are correct, Γ convergence is still a hot topic in phase field model. Theoretical proofs about Γ convergence can be found in [64,65]. Miehe et al. [43] shows that as length scale approaches to 0 the regularized functional converges to the Griffith's theory in the sense of Γ convergence. However, it is also found that in practical setting, error has been reported in numerical solutions regarding the approximated fracture surface and dissipated energy [66]. The approximation of fracture energy in phase field model is studied in [67]. More researches are still needed in this direction.

Even though phase field model has been used widely in brittle materials, but some issues with the modeling of brittle fracture behavior are still to be solved. One of them is the stiffness reduction in the

initial part of stress-strain curve. From the homogeneous solution of governing equation in [44], even with small strain, there is a non-zero auxiliary phase, which causes stiffness reduction under the effect of degradation function. Figure 1.9 shows the stiffness reduction before fracture strength when using the classical phase field model.

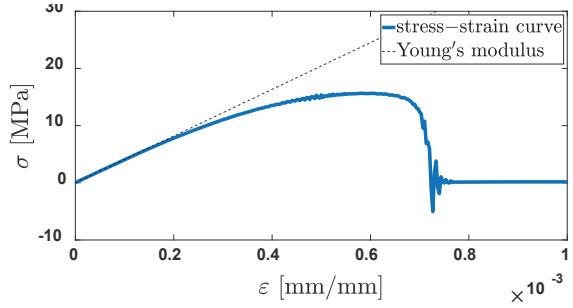

Figure 1.9 Stiffness reduction in stress-strain curve before fracture strength

To solve this problem, Miehe et al. [68] set a minimum strain energy threshold to keep the stiffness constant before reaching fracture strength. This strain energy threshold is also used in [69,70]. However, the stiffness determined from this strain energy threshold could be larger or lower than the material's Young's modulus, so it should be used with caution. Another way to solve this problem is from geometric function. From a numerical point of view, the choice of geometric function in the classical phase field model renders a linear FEM formulation of phase field model (within a staggered scheme) and thus computationally attractive, but the drawback is stiffness reduction. Pham et al. [71] propose a nonstandard phase field model using a linear geometric function, resulting in a diffuse localization band with a parabolic phase profile and global responses with an initial linear elastic stage. Wu et al. [54] propose a generalized geometric function with an extra parameter, and the parameter chosen leads to a geometric function same as [72], which gives a narrower crack band. Some other geometric functions [50,73,74] are also used for brittle materials. Different geometric functions have been investigated well, but a narrower crack band and linear elastic behavior are not easily realized in one geometric function.

Apart from geometric function, degradation function can also be used to solve these problems. Arriaga and Waisman [75] use a generalized degradation function to describe stress-strain curve for a wide range of materials, including brittle materials. Bourdin et al. [48] introduce cubic and quartic functions to obtain

more brittle behavior. To consider the different behaviors of materials, Wu [54] propose an algebraic fraction degradation function with several parameters to adjust degradation function, and make the phase field model a length scale insensitive model. Arriaga and Waisman [76] use cubic function with a parameter to adjust degradation function, which can give more options for the behavior of material. Steinke and Kaliske [56] consider an algebraic fraction degradation function with exponential function to try to cover more materials. Yin et al. [77] try a sinusoidal form of degradation function to investigate strain-rate-dependent fracture toughness. Even though the degradation function can be set more and more complex, it loses some good properties like phase in [0,1]. Zhang et al. [78] use the degradation function in [54], but the phase is not in [0,1], and an extra phase constraint function is needed for a successful simulation. What's worse, analytical homogeneous solution is not available for some special degradation functions, which makes it difficult to investigate some basic features of phase field model that is based on homogeneous solution.

Overall, phase field model has been used widely in brittle materials, but some issues with modeling brittle fracture behavior are still to be solved. One of them is the nonlinearity and inelasticity in the stress-strain curve of brittle material. This problem will be investigated from the point of view of geometric function and degradation function separately. Even though phase field modeling of brittle fracture has been well studied, more investigations are still needed for phase field modeling of ductile fracture. The application of phase field model to ductile fracture with isotropic hardening material will also be presented in this dissertation.

1.5 Contribution and organization of this dissertation

In Section 2, two improvements of cohesive zone model on damage evolution and artificial compliance are presented. Before explaining these two improvements, background of cohesive zone model is presented first to help better understand this topic, including local coordinate system, stiffness matrix, internal nodal force, and constitutive law and damage criteria. For damage evolution, two commonly used damage evolution methods are compared and analyzed to investigate the discontinuous force in cohesive element,

and it is found that monotonically increasing damage factor method can avoid discontinuous force that happens in monotonically increasing effective separation method. Unreasonable failure is also explained in detail that happens in monotonically increasing effective separation method when mixed mode ratio changes. For artificial compliance, it is found to be related to cohesive element modeling method and stiffness parameter selection. By using finite-thickness cohesive element and proper stiffness parameter, artificial compliance can be totally removed.

In Section 3, the effects of strain rate, plastic strain, and variable damping are considered together into one cohesive element. To extend the scope of application of cohesive zone model to more materials, strain rate and plastic strain are considered. Based on the damage factor in classical bilinear cohesive law, a generalized damage factor model is proposed to cover all materials from zero plastic strain to maximum plastic strain. By adding a variable damping into cohesive element, spurious oscillation and excessive cohesive element deletion in cohesive zone model are improved, and there is no discontinuous force like when using a constant damping. Several simulations are presented to verify these three effects.

In Section 4, phase field model for brittle fracture is investigated. Geometric function and degradation function are investigated separately to solve the nonlinearity and inelasticity in the stress-strain curve of classical phase field model. First, by using a generalized quadratic geometric function and applying phase zeroing, nonlinearity and inelasticity can be completely removed, and a good thing is that this still leads to a linear FEM problem. Second, instead of using a second order degradation function, some higher order degradation functions with more constrains could give more options for stress-strain curve. However, higher order degradation function leads to a nonlinear FEM problem, and Newton-Raphson method is used to solve this nonlinear problem. Both methods proposed in this dissertation work well for brittle materials.

In Section 5, phase field model for ductile fracture is investigated. Based on the ductile material with isotropic hardening, phase field model is coupled into this material. One difference here from the classical phase field model for brittle fracture is the calculation of strain energy, and strain energy is not limited in the linear elastic range. To model the degradation of material, parameters for ductile material with isotropic hardening are multiplied with degradation function, i.e., Young's modulus, yield stress, and hardening

modulus. Depending on the degradation function, both linear and nonlinear FEM formulation can also be used like the modeling of brittle fracture in Section 4.

In Section 6, conclusion and future work of this dissertation are given. By using the methods proposed in this dissertation, the modeling of brittle and ductile fracture using cohesive zone model (discrete description) and phase field model (continuum description) is improved. Considering the complexity of ductile fracture, more investigations are still needed.

In Section 7, appendix is put there. To save space and improve readability, four more examples using cohesive zone model are presented in this section. After that, five subroutines used in LS-DYNA for cohesive zone model and phase field model are provided.

2 Improvement of cohesive zone model on damage evolution and artificial compliance

In this section, two improvements of cohesive zone model on damage evolution and artificial compliance are presented. Before explaining these two improvements, background of cohesive zone model is presented first to help better understand this topic, including local coordinate system, stiffness matrix, internal nodal force, and constitutive law and damage criteria. For damage evolution, two commonly used damage evolution methods are compared and analyzed to investigate the discontinuous force in cohesive element, and it is found that monotonically increasing damage factor method can avoid discontinuous force that happens in monotonically increasing effective separation method. Unreasonable failure is also explained in detail that happens in monotonically increasing effective separation method when mixed mode ratio changes. For artificial compliance, it is found to be related to cohesive element modeling method and stiffness parameter selection. By using finite-thickness cohesive element and proper stiffness parameter, artificial compliance can be totally removed.

2.1 Background of cohesive zone model

2.1.1 Local coordinate system

Cohesive element between faces of eight-node solid elements is investigated here, see the blue element in Figure 2.1. Instead of dealing with stress-strain relation, cohesive law deals with traction-separation or stress-separation relation. To get the local stress in cohesive element, local separation $\boldsymbol{s}_l$ between top and bottom faces of cohesive element is obtained first from global displacement $\boldsymbol{u}_t$ and $\boldsymbol{u}_b$, see Equation (2.1), where $\boldsymbol{Q}$ is the coordinate system transformation matrix from global to local coordinate system, and $\boldsymbol{s}_l^0$ is the initial local separation or the initial thickness of cohesive element in case of finite-thickness cohesive element is used. $\boldsymbol{u}_t$ and $\boldsymbol{u}_b$ can be expressed as shape function N_i $(i = 1, 2, 3, 4)$ and node displacement $\boldsymbol{u}_{ti}$ and $\boldsymbol{u}_{bi}$ on top and bottom faces. Because local separation is only related to top and bottom faces, the shape function used here is only a function of two local iso-parametric element variables ξ and η. This can

be obtained by setting the third variable $\varsigma = \pm 1$ for the shape function of a common eight-node solid element, see Equations (2.2) and (2.3). It is convenient to adopt the convention in this dissertation that if a subscript appears twice in the same term, then summation over that subscript is implied, unless indicated otherwise.

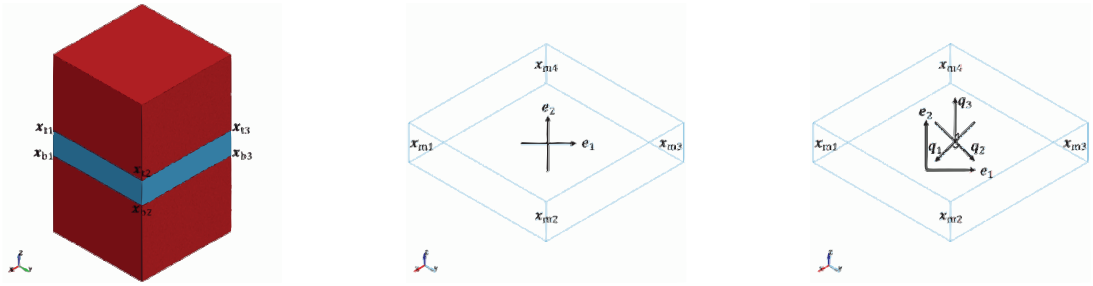

(a) (b) (c)

Figure 2.1 Schematic of cohesive element, (a) cohesive element between faces of eight-node solid elements, (b) unit vectors obtained from middle nodes, (c) local coordinate system $\{\boldsymbol{q}_1, \boldsymbol{q}_2, \boldsymbol{q}_3\}$

$$\boldsymbol{s}_l = \boldsymbol{Q}(\boldsymbol{u}_t - \boldsymbol{u}_b) - \boldsymbol{s}_l^0 \tag{2.1}$$

$$\begin{cases} \boldsymbol{u}_t = N_i(\xi, \eta)\boldsymbol{u}_{ti}, & i = 1,2,3,4 \\ \boldsymbol{u}_b = N_i(\xi, \eta)\boldsymbol{u}_{bi}, & i = 1,2,3,4 \end{cases} \tag{2.2}$$

$$\begin{cases} N_i(\xi, \eta) = \dfrac{1}{4}(1 + \boldsymbol{\xi}_i^*\xi)(1 + \boldsymbol{\eta}_i^*\eta), & i = 1,2,3,4 \\ \boldsymbol{\xi}^* = [1,1,-1,-1] \\ \boldsymbol{\eta}^* = [-1,1,1,-1] \end{cases} \tag{2.3}$$

To get the $\boldsymbol{Q}$ in Equation (2.1), middle nodes between top and bottom faces are calculated first, as shown in Equation (2.4). Equation (2.5) shows unit vectors ($\boldsymbol{e}_1$ and $\boldsymbol{e}_2$) obtained from middle nodes $\boldsymbol{x}_{m3}$, $\boldsymbol{x}_{m1}$ and $\boldsymbol{x}_{m4}$, $\boldsymbol{x}_{m2}$, respectively, see Figure 2.1 (b). The direction of x axis ($\boldsymbol{q}_1$) in local coordinate system is the opposite of the sum of $\boldsymbol{e}_1$ and $\boldsymbol{e}_2$; the direction of y axis ($\boldsymbol{q}_2$) in local coordinate system is same as the difference between $\boldsymbol{e}_1$ and $\boldsymbol{e}_2$; the direction of z axis ($\boldsymbol{q}_3$) in local coordinate system is the cross product of $\boldsymbol{q}_1$ and $\boldsymbol{q}_2$, see Equation (2.6) and Figure 2.1 (c). Since $\boldsymbol{e}_1$ and $\boldsymbol{e}_2$ are unit vectors, $\boldsymbol{q}_1$ and $\boldsymbol{q}_2$ are perpendicular to each other (diagonals of a rhombus are perpendicular to each other).

$$\boldsymbol{x}_{mi} = \frac{\boldsymbol{x}_{ti} + \boldsymbol{x}_{bi}}{2}, \qquad i = 1,2,3,4 \tag{2.4}$$

$$\begin{cases} \boldsymbol{e}_1 = \dfrac{\boldsymbol{x}_{m3} - \boldsymbol{x}_{m1}}{|\boldsymbol{x}_{m3} - \boldsymbol{x}_{m1}|} \\ \boldsymbol{e}_2 = \dfrac{\boldsymbol{x}_{m4} - \boldsymbol{x}_{m2}}{|\boldsymbol{x}_{m4} - \boldsymbol{x}_{m2}|} \end{cases} \tag{2.5}$$

$$\begin{cases} \boldsymbol{q}_1 = -\dfrac{\boldsymbol{e}_1 + \boldsymbol{e}_2}{|\boldsymbol{e}_1 + \boldsymbol{e}_2|} \\ \boldsymbol{q}_2 = \dfrac{\boldsymbol{e}_1 - \boldsymbol{e}_2}{|\boldsymbol{e}_1 - \boldsymbol{e}_2|} \\ \boldsymbol{q}_3 = \boldsymbol{q}_1 \times \boldsymbol{q}_2 \end{cases} \tag{2.6}$$

After the local coordinate system is defined (or the $\boldsymbol{Q}$), the separation in local coordinate system can be calculated from Equation (2.1). Different traction can be constructed with the increase of this local separation, like bilinear cohesive law [13], trapezoidal cohesive law [14], polynomial cohesive law [15], exponential cohesive law [16], and so on. Bilinear cohesive law will be investigated in this dissertation.

2.1.2 Stiffness matrix

Strain energy of cohesive element is expressed in local coordinate system first, as shown in Equations (2.7~1) and (2.7~2). And this strain energy is further expressed in global coordinate system to obtain the stiffness matrix, as shown in Equation (2.7~3). The relation between local traction and local separation is expressed in Equations (2.8) and (2.9), where n, $t1$, and $t2$ mean Mode I, Mode II, and Mode III, respectively. Before the initiation of damage, damage factor d is 0, and constitutive matrix $\boldsymbol{C}$ is a constant matrix.

$$U = \frac{1}{2}\iint_A (\boldsymbol{s}_l)^T \boldsymbol{\sigma}_l \mathrm{d}A = \frac{1}{2}\iint_A (\boldsymbol{s}_l)^T \boldsymbol{C}\boldsymbol{s}_l \mathrm{d}A = \frac{1}{2}\iint_A (\boldsymbol{u}_t - \boldsymbol{u}_b)^T \boldsymbol{Q}^T \boldsymbol{C}\boldsymbol{Q}(\boldsymbol{u}_t - \boldsymbol{u}_b)\mathrm{d}A \tag{2.7}$$

$$\boldsymbol{\sigma}_l = \boldsymbol{C}\boldsymbol{s}_l \tag{2.8}$$

$$\begin{bmatrix} \sigma_l^n \\ \tau_l^{t1} \\ \tau_l^{t2} \end{bmatrix} = \begin{bmatrix} (1-d)E_n^0 & 0 & 0 \\ 0 & (1-d)E_{t1}^0 & 0 \\ 0 & 0 & (1-d)E_{t2}^0 \end{bmatrix} \begin{bmatrix} s_l^n \\ s_l^{t1} \\ s_l^{t2} \end{bmatrix} \tag{2.9}$$

Follow the Equations (2.2) and (2.3), global displacement $\boldsymbol{u}_t$ and $\boldsymbol{u}_b$ can be expressed in terms of global displacement of nodes on top and bottom faces, as shown in Equation (2.10). The summation form of global separation can be expressed into matrix form, as shown in Equation (2.11). $\boldsymbol{N}$ is shape function

matrix, $\boldsymbol{H}$ is the matrix mapping node displacement to global separation between top and bottom nodes, $\boldsymbol{d}$ is a 24 × 1 column vector with node displacement in global coordinate system. $\boldsymbol{H}$ is a 12 × 24 matrix. Only the first row of $\boldsymbol{H}$ is shown in Equation (2.13) because of the size of $\boldsymbol{H}$, but the rest can be obtained in the same way by checking $(\boldsymbol{u}_t - \boldsymbol{u}_b)$ and $\boldsymbol{d}$.

$$U = \frac{1}{2}\iint_A (N_i\boldsymbol{u}_{ti} - N_i\boldsymbol{u}_{bi})^T\boldsymbol{Q}^T\boldsymbol{C}\boldsymbol{Q}(N_i\boldsymbol{u}_{ti} - N_i\boldsymbol{u}_{bi})\mathrm{d}A \tag{2.10}$$

$$N_i\boldsymbol{u}_{ti} - N_i\boldsymbol{u}_{bi} = \boldsymbol{N}\boldsymbol{H}\boldsymbol{d} \tag{2.11}$$

$$\boldsymbol{N} = \begin{bmatrix} N_1 & 0 & 0 & N_2 & 0 & 0 & N_3 & 0 & 0 & N_4 & 0 & 0 \\ 0 & N_1 & 0 & 0 & N_2 & 0 & 0 & N_3 & 0 & 0 & N_4 & 0 \\ 0 & 0 & N_1 & 0 & 0 & N_2 & 0 & 0 & N_3 & 0 & 0 & N_4 \end{bmatrix} \tag{2.12}$$

$$\boldsymbol{H}(1,:) = [1,0,0,0,0,0,0,0,0,0,0,0,-1,0,0,0,0,0,0,0,0,0,0,0] \tag{2.13}$$

$$\boldsymbol{d} = \begin{bmatrix} u_{t1}, v_{t1}, w_{t1}, u_{t2}, v_{t2}, w_{t2}, u_{t3}, v_{t3}, w_{t3}, u_{t4}, v_{t4}, w_{t4}, \dots \\ u_{b1}, v_{b1}, w_{b1}, u_{b2}, v_{b2}, w_{b2}, u_{b3}, v_{b3}, w_{b3}, u_{b4}, v_{b4}, w_{b4} \end{bmatrix} \tag{2.14}$$

Put Equation (2.11) into Equation (2.10), strain energy is expressed as matrix form in global coordinate system, as shown in Equation (2.15), and stiffness matrix is obtained as Equation (2.16~1). Note that if shape function matrix is expressed as $\overline{\boldsymbol{N}} = \boldsymbol{N}\boldsymbol{H}$, where $\overline{\boldsymbol{N}}$ is a 3 × 24 matrix, stiffness matrix can be shown in Equation (2.16~2). For the iso-parametric element used in FEM, dA is mapped into natural coordinate system as $|\boldsymbol{J}|\mathrm{d}\xi\mathrm{d}\eta$, where $|\boldsymbol{J}|$ is the determinant of Jacobean matrix, and a 2D numerical integration can be used to calculate stiffness matrix, see Equation (2.17).

$$\mathrm{U} = \frac{1}{2}\iint_A \boldsymbol{d}^T\boldsymbol{H}^T\boldsymbol{N}^T\boldsymbol{Q}^T\boldsymbol{C}\boldsymbol{Q}\boldsymbol{N}\boldsymbol{H}\boldsymbol{d}\mathrm{d}A = \frac{1}{2}\boldsymbol{d}^T\iint_A \boldsymbol{H}^T\boldsymbol{N}^T\boldsymbol{Q}^T\boldsymbol{C}\boldsymbol{Q}\boldsymbol{N}\boldsymbol{H}\mathrm{d}A\,\boldsymbol{d} \tag{2.15}$$

$$\boldsymbol{K} = \iint_A \boldsymbol{H}^T\boldsymbol{N}^T\boldsymbol{Q}^T\boldsymbol{C}\boldsymbol{Q}\boldsymbol{N}\boldsymbol{H}\mathrm{d}A = \iint_A \overline{\boldsymbol{N}}^T\boldsymbol{Q}^T\boldsymbol{C}\boldsymbol{Q}\overline{\boldsymbol{N}}\mathrm{d}A \tag{2.16}$$

$$\boldsymbol{K} = \iint_A \boldsymbol{H}^T\boldsymbol{N}^T\boldsymbol{Q}^T\boldsymbol{C}\boldsymbol{Q}\boldsymbol{N}\boldsymbol{H}|\boldsymbol{J}|\mathrm{d}\xi\mathrm{d}\eta = \iint_A \overline{\boldsymbol{N}}^T\boldsymbol{Q}^T\boldsymbol{C}\boldsymbol{Q}\overline{\boldsymbol{N}}|\boldsymbol{J}|\mathrm{d}\xi\mathrm{d}\eta \tag{2.17}$$

The stiffness matrix presented above can be applied into linear elastic range, but the problem becomes

nonlinear after the initiation of damage because then damage factor is larger than 0 and becomes a variable. A general nonlinear equation can be solved by using Newton-Raphson method through a sequence of linearization, and an incremental procedure with a tangent stiffness matrix is needed. The general stain energy is shown in Equation (2.18), where $\boldsymbol{u}$ is displacement, $\overline{\boldsymbol{u}}$ is virtual displacement, $\bar{\boldsymbol{\varepsilon}}$ is virtual strain. Linearization of this strain energy is shown in Equation (2.19). Considering that incremental stress can be expressed as tangent stiffness and incremental strain, the linearization of strain energy can be further expressed as tangent constitutive matrix, as shown in Equations (2.20) and (2.21). The first integrand in Equation (2.21) is similar to the stiffness term in linear system, and it is called tangent stiffness. The second integrand only happens in geometric nonlinear problem, and it is called initial stress stiffness, see [79] for more detailed information.

$$\mathrm{U}(\boldsymbol{u}, \overline{\boldsymbol{u}}) = \iiint_{\Omega_0} \boldsymbol{\sigma}(\boldsymbol{u}) : \bar{\boldsymbol{\varepsilon}}(\boldsymbol{u}, \overline{\boldsymbol{u}}) \, \mathrm{d}\Omega \tag{2.18}$$

$$L[\mathrm{U}(\boldsymbol{u}, \overline{\boldsymbol{u}})] = \iiint_{\Omega_0} (\delta\boldsymbol{\sigma} : \bar{\boldsymbol{\varepsilon}} + \boldsymbol{\sigma} : \delta\bar{\boldsymbol{\varepsilon}}) \, \mathrm{d}\Omega \tag{2.19}$$

$$\delta\boldsymbol{\sigma} = \frac{\partial \boldsymbol{\sigma}}{\partial \boldsymbol{\varepsilon}} : \delta\boldsymbol{\varepsilon} = \boldsymbol{C}^{\tan} : \delta\boldsymbol{\varepsilon} \tag{2.20}$$

$$L[\mathrm{U}(\boldsymbol{u}, \overline{\boldsymbol{u}})] = \iiint_{\Omega_0} (\bar{\boldsymbol{\varepsilon}} : \boldsymbol{C}^{\tan} : \delta\boldsymbol{\varepsilon} + \boldsymbol{\sigma} : \delta\bar{\boldsymbol{\varepsilon}}) \, \mathrm{d}\Omega \tag{2.21}$$

Geometric nonlinearity of cohesive element is not considered in this dissertation, and this is also taken by other papers [80-82]. Incremental traction is related to incremental separation through tangent constitutive matrix as $\mathrm{d}\boldsymbol{\sigma}^l = \boldsymbol{C}^{tan} \mathrm{d}\boldsymbol{s}^l$, as shown in Equation (2.22). To get the partial derivative of traction with respect to separation, damage factor for bilinear cohesive law should be defined. This damage factor d could be a really complicated function of local separation s_l^n, s_l^{t1}, and s_l^{t2}. What's more, different failure criterion can have different δ_m^0 and δ_m^f functions (separation at the initiation of damage and the failure of damage evolution, respectively) of s_l^n, s_l^{t1}, and s_l^{t2}, so the detailed expression of damage factor is not shown here. But the element at first row and first column in $\boldsymbol{C}^{tan}$ is shown in Equation (2.23) to get an idea

of it, and the others can be obtained in the same manner. After the tangent constitutive matrix is obtained, the tangent stiffness matrix can be obtained similarly, as shown in Equation (2.24).

$$\boldsymbol{C}^{tan} = \begin{bmatrix} \frac{\partial \sigma_l^n}{\partial s_l^n} & \frac{\partial \sigma_l^n}{\partial s_l^{t1}} & \frac{\partial \sigma_l^n}{\partial s_l^{t2}} \\ \frac{\partial \tau_l^{t1}}{\partial s_l^n} & \frac{\partial \tau_l^{t1}}{\partial s_l^{t1}} & \frac{\partial \tau_l^{t1}}{\partial s_l^{t2}} \\ \frac{\partial \tau_l^{t2}}{\partial s_l^n} & \frac{\partial \tau_l^{t2}}{\partial s_l^{t1}} & \frac{\partial \tau_l^{t2}}{\partial s_l^{t2}} \end{bmatrix} \tag{2.22}$$

$$\frac{\partial \sigma_l^n}{\partial s_l^n} = (1-d)E_n^0 + \left(1 - \frac{\partial d}{\partial s_l^n}\right) E_n^0 s_l^n \tag{2.23}$$

$$\boldsymbol{K}^{tan} = \iint_A \boldsymbol{H}^T \boldsymbol{N}^T \boldsymbol{Q}^T \boldsymbol{C}^{tan} \boldsymbol{Q} \boldsymbol{N} \boldsymbol{H} \mathrm{d}A = \iint_A \bar{\boldsymbol{N}}^T \boldsymbol{Q}^T \boldsymbol{C}^{tan} \boldsymbol{Q} \bar{\boldsymbol{N}} \mathrm{d}A \tag{2.24}$$

2.1.3 Internal nodal force

To get the interaction between cohesive element and bulk element, internal nodal forces should be calculated. The principle of virtual power states that the internal power equals the external power. External power can be from concentrated load, surface load, and body load, as shown in Equation (2.25). However, surface force and body force are not considered in this derivation because cohesive element used in this dissertation is surrounded by solid bulk elements and has no mass. The time derivative of local separation can be obtained directly from Equations (2.1) and (2.2), as shown in Equation (2.26).

$$\iint_A (\dot{\boldsymbol{s}}_l)^T \boldsymbol{\sigma}_l \mathrm{d}A = (\dot{\boldsymbol{x}}_{ti})^T \boldsymbol{f}_{ti} + (\dot{\boldsymbol{x}}_{bi})^T \boldsymbol{f}_{bi} + \iint_A (\dot{\boldsymbol{x}})^T \boldsymbol{f}_S \mathrm{d}A + \iiint_V (\dot{\boldsymbol{x}})^T \boldsymbol{f}_B \mathrm{d}V\,, \qquad i = 1,2,3,4 \tag{2.25}$$

$$(\dot{\boldsymbol{s}}_l)^T = [(\dot{\boldsymbol{x}}_{ti})^T N_i(\xi,\eta) - (\dot{\boldsymbol{x}}_{bi})^T N_i(\xi,\eta)]\boldsymbol{Q}^T, \qquad i = 1,2,3,4 \tag{2.26}$$

Substitute Equation (2.26) back into Equation (2.25) to get Equation (2.27), and by comparing the left-hand side and right-hand side, internal nodal forces on top and bottom faces can be obtained, as shown in Equation (2.28).

$$\iint_A (\dot{\boldsymbol{s}}_l)^T \boldsymbol{\sigma}_l \mathrm{d}A = (\dot{\boldsymbol{x}}_{ti})^T \iint_A N_i(\xi,\eta) \boldsymbol{Q}^T \boldsymbol{\sigma}_l \mathrm{d}A - (\dot{\boldsymbol{x}}_{bi})^T \iint_A N_i(\xi,\eta) \boldsymbol{Q}^T \boldsymbol{\sigma}_l \mathrm{d}A\,, \qquad i = 1,2,3,4 \tag{2.27}$$

$$\begin{cases} \boldsymbol{f}_{ti} = \iint_A N_i(\xi,\eta)\boldsymbol{Q}^T\boldsymbol{\sigma}_l \mathrm{d}A\,, \qquad i = 1,2,3,4 \\ \boldsymbol{f}_{bi} = -\iint_A N_i(\xi,\eta)\boldsymbol{Q}^T\boldsymbol{\sigma}_l \mathrm{d}A\,, \qquad i = 1,2,3,4 \end{cases} \tag{2.28}$$

2.1.4 Commonly used constitutive law and damage criteria

For the commonly used constitutive law in bilinear cohesive law proposed by Davila et al. [83] and Camanho et al. [84], three independent parameters can define it, i.e., separation at the end of strengthening part δ^0, separation at the end of softening part δ^f, and fracture strength σ^0. The area below this traction separation curve is critical energy release rate G_C. Considering the difference between tensile load and compressive load in Mode I, positive quadrant and negative quadrant of Mode I in this constitutive law are different, as shown in Figure 2.2 (a). Here, the negative normal traction can be infinite and no damage would happen in this negative normal direction. In this dissertation, according to the shape in negative quadrant of Mode I, this constitutive law is called as constant stiffness model (a straight line). However, tangential direction Mode II and Mode III do not have this difference, see Figure 2.2 (b). Without considering plastic strain, the orange dashed line is a possible load path up to failure for this model.

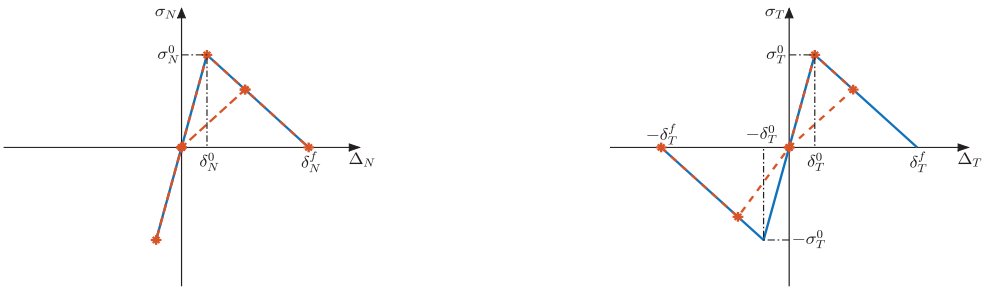

(a) (b)

Figure 2.2 (a) constant stiffness model in Mode I, (b) constant stiffness model in Mode II and Mode III

After constitutive law is presented, criteria in bilinear cohesive law is to be covered. Usually, quadratic stress criterion is used for the initiation of damage, as shown in Equation (2.29); power law and B-K law are used for the failure of damage evolution, as shown in Equations (2.30) and (2.31), respectively. Exponent 1 and 2 are commonly used in power law, but curve fitting based on experiment results is

suggested. B-K law is a good choice because curve fitting is needed for different materials. From Equations (2.29), (2.30), and (2.31), one thing to mention is the difference between tensile load and compressive load. Normal traction and tangential traction are coupled when it is tensile load, but normal traction is not shown in the criteria when it is compressive load. The reason to do so is that compressive strength is assumed to be infinite and it cannot cause any damage to cohesive element.

$$\begin{cases} \left(\frac{\sigma_N}{\sigma_N^0}\right)^2 + \left(\frac{\sigma_T}{\sigma_T^0}\right)^2 = 1, & \sigma_N \geq 0 \\ \left(\frac{\sigma_T}{\sigma_T^0}\right)^2 = 1, & \sigma_N < 0 \end{cases} \tag{2.29}$$

$$\begin{cases} (\frac{G_I}{G_{IC}^0})^n + (\frac{G_{II}}{G_{IIC}^0})^n = 1, & \sigma_N \geq 0 \\ (\frac{G_{II}}{G_{IIC}^0})^n = 1, & \sigma_N < 0 \end{cases} \tag{2.30}$$

$$\begin{cases} G_I + G_{II} = G_{IC}^0 + \left(G_{IIC}^0 - G_{IC}^0\right)\gamma^\eta, & \sigma_N \geq 0 \\ G_{II} = G_{IIC}^0, & \sigma_N < 0 \end{cases} \tag{2.31}$$

where, σ_N and σ_T are traction in normal direction and tangential direction, respectively; σ_N^0 and σ_T^0 are fracture strength in Mode I and Mode II, respectively; G_I and G_{II} are energy release rate in normal direction and tangential direction, respectively; G_{IC}^0 and G_{IIC}^0 are critical energy release rate in Mode I and Mode II, respectively; energy release rate ratio γ is $G_{II}/(G_I + G_{II})$; η is a parameter determined from curve fitting. Some other criteria about the failure of damage evolution can be refereed from [85].

2.1.5 Two more constitutive laws and damage criteria

Even though the bilinear cohesive law in previous section has been used widely, there are still some other different constitutive laws. According to the negative quadrant of Mode I, contact connection model (no negative quadrant) and double bilinear model (similar to positive quadrant) are also used in publications, as shown in Figures 2.3 (a) and 2.3 (b), respectively. Without considering plastic strain, contact connection model has same Mode II and Mode III as that constant stiffness model in Figure 2.2 (b). The negative quadrant of double bilinear model for Mode I is similar to its positive quadrant, but three different parameters are needed to consider the difference between tensile load and compressive load. The Mode II

and Mode III for double bilinear model are shown in Figure 2.3 (c). An advantage of this double bilinear model is that plastic strain and reciprocal load can be considered in this model. The orange dashed line in Figures 2.3 (b) and 2.3 (c) are a possible load path up to failure with considering plastic strain. Refer to [5] for detailed information about plastic strain in double bilinear model.

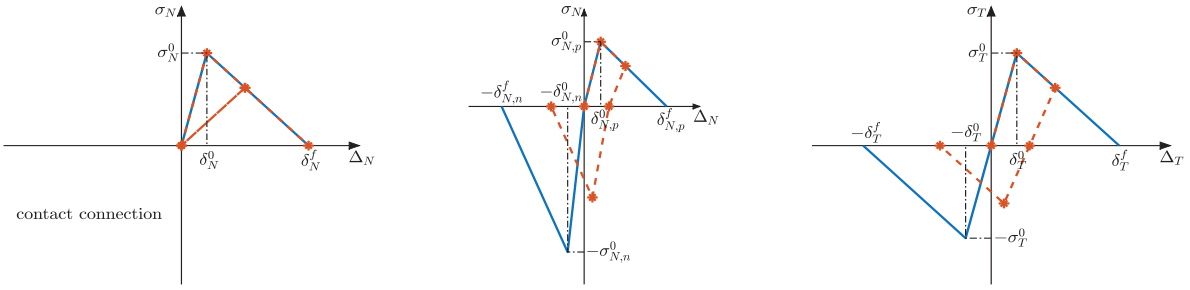

(a) (b) (c)

Figure 2.3 (a) contact connection model in Mode I, (b) double bilinear model in Mode I, (c) double bilinear model in Mode II and Mode III

For the contact connection model, since negative quadrant of Mode I is not available and not coupled with tangential traction under compressive load, the criteria used are same as that for constant stiffness model in Equations (2.29), (2.30), and (2.31). However, for double bilinear model, because its negative quadrant of Mode I is like positive quadrant, negative traction can also be used in the normal-tangential coupled criteria. Quadratic stress criterion, power law, and B-K law for the double bilinear model are shown in Equations (2.32), (2.33), and (2.34), respectively. The advantage of this normal-tangential coupled property on stress wave propagation will be shown in Section 3.4.4 Kalthoff block under impact load.

$$\begin{cases} \left(\frac{\sigma_{N,p}}{\sigma_{N,p}^0}\right)^2 + \left(\frac{\sigma_T}{\sigma_T^0}\right)^2 = 1, & \sigma_N \geq 0 \\ \left(\frac{\sigma_{N,n}}{\sigma_{N,n}^0}\right)^2 + \left(\frac{\sigma_T}{\sigma_T^0}\right)^2 = 1, & \sigma_N < 0 \end{cases} \tag{2.32}$$

$$\begin{cases} \left(\frac{G_{I,p}}{G_{IC,p}^0}\right)^n + \left(\frac{G_{II}}{G_{IIC}^0}\right)^n = 1, & \sigma_N \geq 0 \\ \left(\frac{G_{I,n}}{G_{IC,n}^0}\right)^n + \left(\frac{G_{II}}{G_{IIC}^0}\right)^n = 1, & \sigma_N < 0 \end{cases} \tag{2.33}$$

$$\begin{cases} G_{I,p} + G_{II} = G_{IC,p}^0 + \left(G_{IIC}^0 - G_{IC,p}^0\right)\gamma^{\eta p}, & \sigma_N \geq 0 \\ G_{I,n} + G_{II} = G_{IC,n}^0 + \left(G_{IIC}^0 - G_{IC,n}^0\right)\gamma^{\eta n}, & \sigma_N < 0 \end{cases} \tag{2.34}$$

where, p and n mean positive and negative normal directions, respectively, and the meaning of these letters is similar to that in Equations (2.29), (2.30), and (2.31). One thing worth mentioning for double bilinear model is critical energy release rate. Theoretically, the critical energy release rate for constant stiffness model in negative Mode I is infinite, and no contribution to damage evolution from compressive load. Experiments also show that for some materials compressive strength could be much larger than tensile strength. To make sure that Mode II is dominant for damage evolution when cohesive element undergoes compressive load, the critical energy release rate relation between negative Mode I and Mode II is adjustable, like 1, 2, and 3 times of the critical energy release rate in Mode II, or even higher. Figure 2.4 shows this relation for B-K law. When critical energy release rate in negative Mode I is much larger than that in Mode II, Mode II should be dominant for the damage propagation since negative Mode I is much harder to fail.

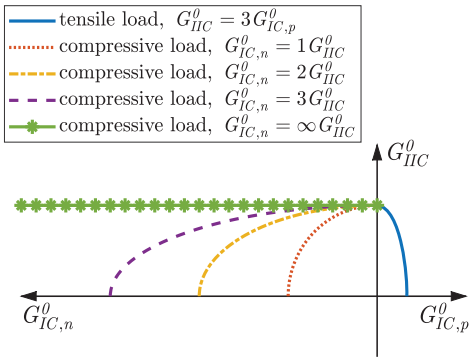

Figure 2.4 Critical energy release rate relation between Mode I and Mode II

The criteria shown above are all based on stress and energy release rate, which are not primary unknows in simulation. The fact is that primary unknow (displacement) is calculated first in simulation, and then get stress and energy release rate based on displacement. So, it is necessary to transfer stress and energy release rate to displacement and stiffness. Before this transformation, a new parameter is defined as mixed mode ratio $\beta = \sqrt{(\Delta_{m,T}/\Delta_{m,N})^2}$. Equations (2.35), (2.36), and (2.37) are used to get the separation at the initiation of damage and at the failure of damage evolution.

$$\begin{cases} \sigma_{N,p} = E_N^0 \delta_{N,p,m}^0 \\ \sigma_T = E_T^0 \delta_{T,m}^0 \\ \sigma_{N,p}^0 = E_N^0 \delta_{N,p}^0 \\ \sigma_T^0 = E_T^0 \delta_T^0 \end{cases} \tag{2.35}$$

$$\begin{cases} G_{I,p} = \dfrac{E_N^0 \delta_{N,p,m}^0 \delta_{N,p,m}^f}{2} \\ G_{II} = \dfrac{E_T^0 \delta_{T,m}^0 \delta_{T,m}^f}{2} \end{cases} \tag{2.36}$$

$$\begin{cases} \sqrt{\left(\delta_{N,p,m}^0\right)^2 + \left(\delta_{T,m}^0\right)^2} = \sqrt{1+\beta^2}\delta_{N,p,m}^0 = \dfrac{\sqrt{1+\beta^2}}{\beta}\delta_{T,m}^0 = \delta_{m,p}^0 \\ \sqrt{\left(\delta_{N,p,m}^f\right)^2 + \left(\delta_{T,m}^f\right)^2} = \sqrt{1+\beta^2}\delta_{N,p,m}^f = \dfrac{\sqrt{1+\beta^2}}{\beta}\delta_{T,m}^f = \delta_{m,p}^f \end{cases} \tag{2.37}$$

where, m means mixed mode case; E_N^0 and E_T^0 are the stiffness in Mode I and Mode II, respectively. For quadratic stress criterion, $\delta_{m,p}^0$ is obtained from Equations (2.32), (2.35), and (2.37); for B-K law, $\delta_{m,p}^f$ is obtained from Equations (2.34), (2.36), and (2.37), as shown in Equation (2.38). Even though this equation is used in positive quadrant, double bilinear model can still use this equation in its negative quadrant because negative Mode I has similar traction separation relation. $\delta_{m,p}^f$ for power law can be obtained similarly, but it is not shown here to save space, interested readers please refer to MAT 138 in [20].

$$\begin{cases} \delta_{m,p}^0 = \delta_{N,p}^0 \delta_T^0 \sqrt{\dfrac{1+\beta^2}{\left(\beta\delta_{N,p}^0\right)^2 + (\delta_T^0)^2}} \\ \delta_{m,p}^f = \dfrac{2(1+\beta^2)}{\delta_{m,p}^0 (E_N^0 + \beta^2 E_T^0)} \left[G_{IC,p}^0 + \left(G_{IIC}^0 - G_{IC,p}^0\right) \left(\dfrac{\beta^2 E_T^0}{E_N^0 + \beta^2 E_T^0} \right)^\eta \right] \end{cases} \tag{2.38}$$

2.1.6 Comparison and analysis of the three constitutive laws

(1) Deficiency of plastic strain

To introduce plastic strain into bilinear cohesive law, a generalized damage factor model is proposed in [5], where five typical damage factor models (maximum, convex, linear, concave, and minimum damage factor) can handle material from zero to maximum plastic strain in sequence, will see in Section 3.2. However, this plastic strain can only be achieved in positive quadrant for constant stiffness model and

contact connection model. For constant stiffness model, the loading and unloading track is same in negative Mode I, so no compressive plastic strain can be obtained. For contact connection model, negative Mode I is not available, let alone the plastic strain in negative normal direction. What's more, when cohesive element undergoes reciprocating load, a loop of traction cannot be obtained for these two models, but double bilinear model does not have these issues.

(2) Inherent discontinuity of constitutive law

The damage factor without plastic strain is shown in Equation (2.39), and damage factor curve for the three models mentioned above are shown in Figure 2.5. For all the three models, it is normal-tangential coupled in positive quadrant ($\delta_{m,\bullet}$ means effective separation obtained from normal and tangential separations together). However, the situation is different when normal traction is negative. For constant stiffness model, normal traction and tangential traction are uncoupled in negative quadrant, and the initiation of damage and the failure of damage evolution are only controlled by tangential traction. For contact connection model, the connection changes from cohesive law to contact connection when it is in negative quadrant. From a coupled model to an uncoupled model, or from a coupled cohesive law to a contact algorithm, both constant stiffness model and contact connection model have a kind of inherent discontinuity of constitutive law.

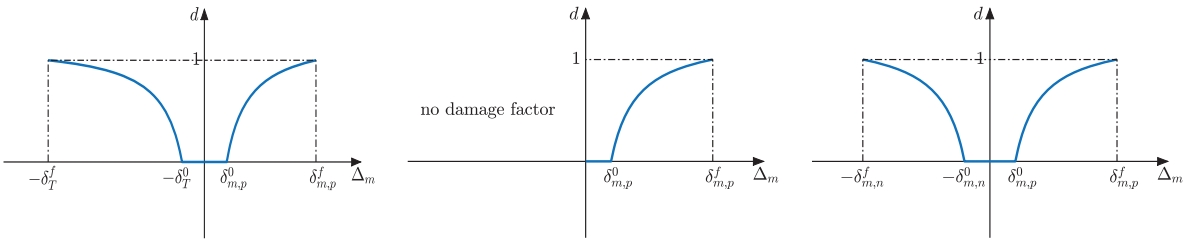

(a) (b) (c)

Figure 2.5 Damage factor, (a) constant stiffness model, (b) contact connection model, (c) double bilinear model

(3) Inherent discontinuity of force

For the constant stiffness model, because negative normal traction has no limit, it can reach to an extremely high value, but a sudden drop to zero can happen when cohesive element fails, which could be one source of spurious oscillation and one reason for incorrect damage evolution. This discontinuous force

has been found in my previous 3D simulation in [5]. For the contact connection model, when load changes from tensile load to compressive load, the traction between two adjacent bulk elements switches from cohesive element tractions to contact force, and oscillation between every two bulk elements and increased time of computation could be its limitations.

2.2 Improvement on damage evolution

For the commonly used constitutive law in bilinear cohesive law, the unloading track is the line that connects the point on bilinear cohesive law and the origin, as shown in Figure 2.2 (a) before. In this case, the damage factor of this line can be calculated, as shown in Equation (2.39). Equation (2.40) shows the relation between damage factor and stiffness.

$$d = \begin{cases} 0, & 0 \le \Delta_m < \delta_m^0 \\ \dfrac{\delta_m^f}{\Delta_m}\left(\dfrac{\Delta_m - \delta_m^0}{\delta_m^f - \delta_m^0}\right), & \delta_m^0 \le \Delta_m < \delta_m^f \\ 1, & \delta_m^f \le \Delta_m \end{cases} \tag{2.39}$$

$$\begin{cases} E_N = (1-d)E_N^0 \\ E_T = (1-d)E_T^0 \end{cases} \tag{2.40}$$

where, d is damage factor; Δ_m is mixed effective separation; E_N and E_T are the current stiffness in normal and tangential directions, respectively. Although the damage factor is well defined, damage evolution method is another thing, which is about how to define the progress of damage. Two damage evolution methods, monotonically increasing effective separation method [26,28] and monotonically increasing damage factor method [20], are widely used. The difference between these two methods can be seen from their names and from the formula shown in Equations (2.41) and (2.42).

$$\begin{cases} \Delta_{m,i}^{true} = \max\left(\Delta_{m,[1,i-1]}^{max}, \Delta_{m,i}\right) \\ d_{m,i}^{true} = \dfrac{\delta_m^f}{\Delta_{m,i}^{true}}\left(\dfrac{\Delta_{m,i}^{true} - \delta_m^0}{\delta_m^f - \delta_m^0}\right) \end{cases} \tag{2.41}$$

$$\begin{cases} d_{m,i} = \dfrac{\delta_m^f}{\Delta_{m,i}}\left(\dfrac{\Delta_{m,i} - \delta_m^0}{\delta_m^f - \delta_m^0}\right) \\ d_{m,i}^{true} = \max\left(d_{m,[1,i-1]}^{max}, d_{m,i}\right) \end{cases} \tag{2.42}$$

where, $\Delta_{m,[1,i-1]}^{max}$ is the maximum history effective separation from 1th step to (i-1)th step; $\Delta_{m,i}$ is the current effective separation at ith step; $\Delta_{m,i}^{true}$ is the true effective separation at ith step; same thing for the damage factor d. It is straightforward that cohesive element is in loading when current effective separation or current damage factor is larger than its maximum history value, otherwise it is in unloading or reloading. Equations (2.43) and (2.44) show the condition of unloading and reloading for the two damage evolution methods.

$$\Delta_{m,i} \leq \Delta_{m,[1,i-1]}^{max} \tag{2.43}$$

$$d_{m,i} \leq d_{m,[1,i-1]}^{max} \tag{2.44}$$

2.2.1 Discontinuous force in damage evolution method

Even though both damage evolution methods mentioned above have been used widely, the details about traction evolution are overlooked, and problems related to discontinuous force can happen in the monotonically increasing effective separation method.

2.2.1.1 Monotonically increasing effective separation method, with discontinuous force

Constant unloading and reloading are an easy and straightforward method to deal with unloading and reloading, which means stiffness is a constant during unloading and reloading process. Here, this stiffness is same as the stiffness that happens at the maximum history effective separation or maximum history damage factor, depending on the damage evolution method used. For monotonically increasing effective separation method, constant unloading and reloading works well for a single mixed mode ratio case. However, for a case with changing mixed mode ratio, discontinuous force can happen at the end of reloading, which could cause artificial oscillation and even meaningless results. A single cohesive element is used to explain this. The material parameters used for this cohesive element are shown in Table 2.1, and power law with $n = 1$ is used here for the sake of simplicity. In simulation, the total number of time steps is 800.

Table 2.1 Bilinear cohesive law parameters for discontinuous force analysis

Mode	Stiffness [MPa/mm]	Fracture strength [MPa]	Critical energy release rate [N/mm]
Mode I	100000	30	0.25
Mode II	100000	60	1.00

First, two load cycles with same mixed mode ratio are investigated. Displacement load data and mixed mode ratio range are shown in Figure 2.6, where the mixed mode ratio is a constant. For monotonically increasing effective separation method, the maximum history effective separation is shown in Figure 2.7 (a), and this value is kept increasing. The damage factor is shown in Figure 2.7 (b). Figures 2.7 (c) and 2.7 (d) show the tangential traction response in 2D and 3D plots, respectively. As shown in these figures, discontinuous force is not found in these two cycles, and the stiffness in the unloading and reloading is same. So, constant unloading and reloading works well for monotonically increasing effective separation method when mixed mode ratio does not change.

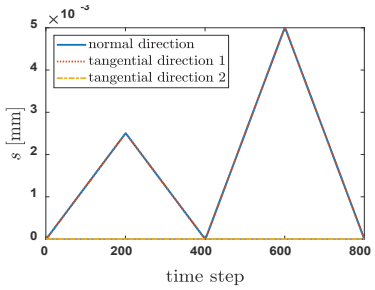

(a)

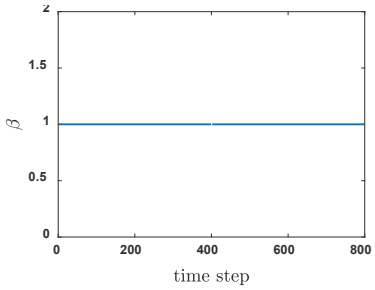

(b)

Figure 2.6 (a) displacement load data, (b) mixed mode ratio range

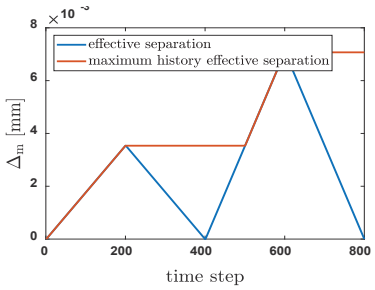

(a)

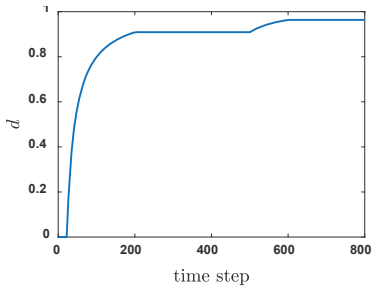

(b)

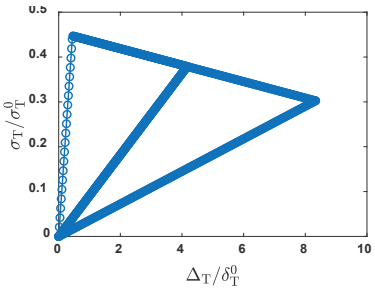

(c)

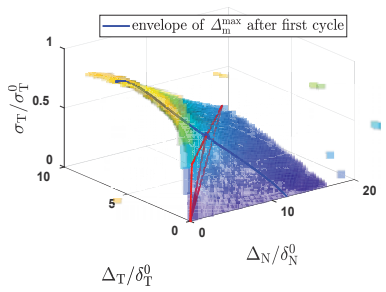

(d)

Figure 2.7 (a) effective separation and maximum history effective separation, (b) damage factor, (c) tangential traction in 2D plot, (d) tangential traction in 3D plot

Second, two load cycles with different mixed mode ratio are investigated. Displacement load data and mixed mode ratio range are shown in Figure 2.8, where mixed mode ratio changes. For monotonically increasing effective separation method, the maximum history effective separation is shown in Figure 2.9 (a), and its value is still kept increasing. The damage factor is shown in Figure 2.9 (b). Figures 2.9 (c) and 2.9 (d) show the tangential traction response in 2D and 3D plots, respectively. Discontinuous force is found in the second cycle at the end of reloading if constant unloading and reloading is used. This discontinuous force can also be seen from damage factor in Figure 2.9 (b). The displacement load is continuous, but the damage factor at the end of reloading is not continuous. The correct stiffness of reloading in the second cycle is shown in Figures 2.9 (c) and 2.9 (d) with dashed line.

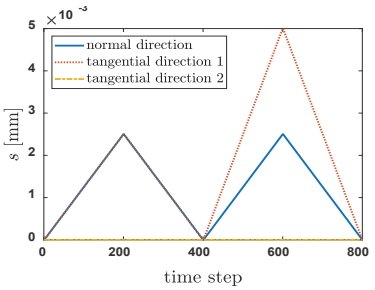

(a)

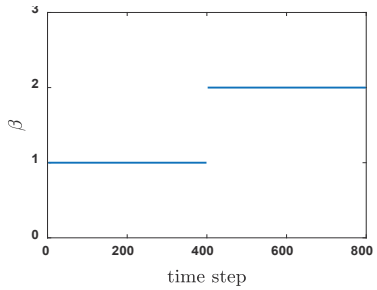

(b)

Figure 2.8 (a) displacement load data, (b) mixed mode ratio range

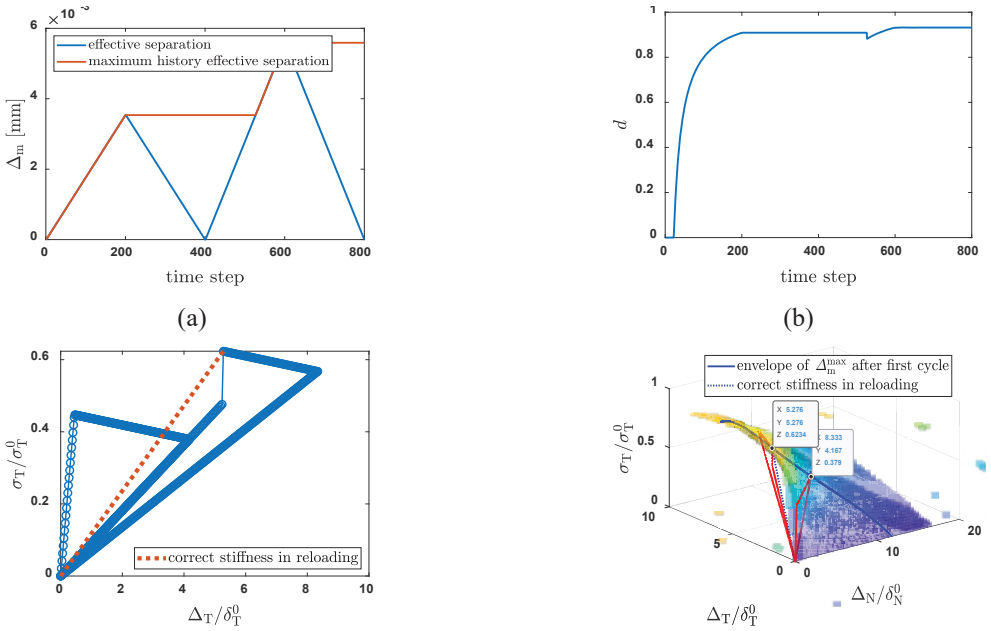

Figure 2.9 (a) effective separation and maximum history effective separation, (b) damage factor, (c) tangential traction in 2D plot, (d) tangential traction in 3D plot

A general loading process is shown in Figure 2.10 (a), and it has a wider range of mixed mode ratio, which changes in the whole loading process in Figure 2.10 (b). Effective separation and damage factor are shown in Figures 2.11 (a) and 2.11 (b), respectively. Figures 2.11 (c) and 2.11 (d) show the tangential traction response in 2D and 3D plots, respectively. As shown in these figures, discontinuous force is found in each cycle at the end of reloading, which agrees with what found in previous simulations. The traction during loading should be exactly on the 3D cohesive law surface, but some tractions are above the 3D cohesive law in Figure 2.11 (d) during reloading.

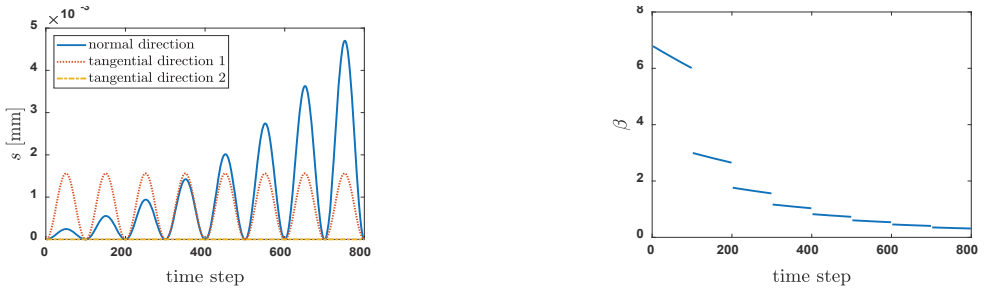

Figure 2.10 (a) displacement load data, (b) mixed mode ratio range

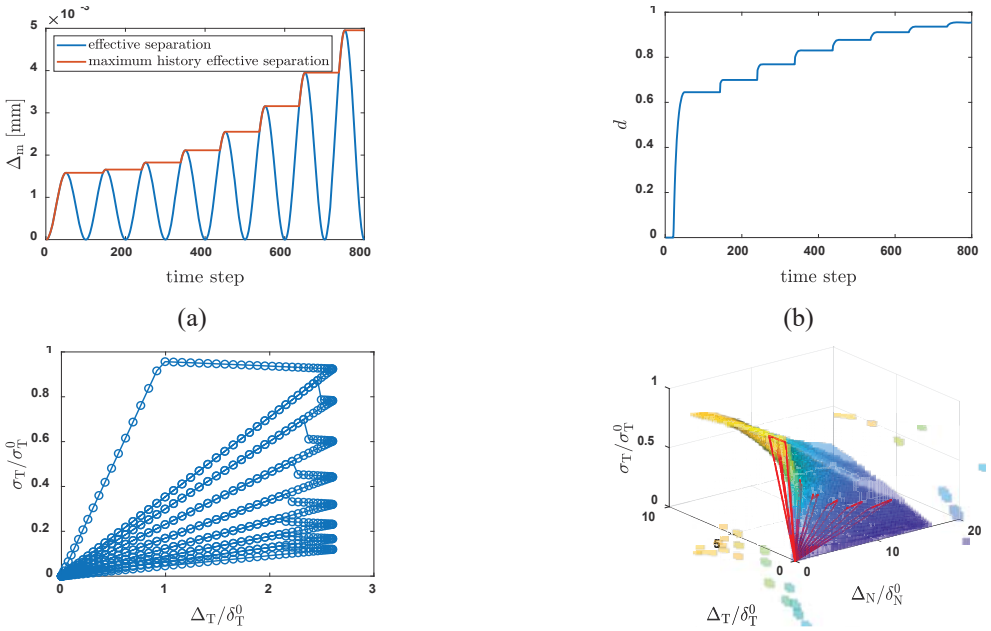

Figure 2.11 (a) effective separation and maximum history effective separation, (b) damage factor, (c) tangential traction in 2D plot, (d) tangential traction in 3D plot

2.2.1.2 Monotonically increasing effective separation method, without discontinuous force

For monotonically increasing effective separation method, different mixed mode ratio at same maximum history effective separation means different stiffness, and it is better to get this stiffness based on current mixed mode ratio, not a fixed stiffness that happens at last maximum history effective separation. Without considering plastic strain, the unloading and reloading should be on the line that connects the point on bilinear cohesive law and the origin, and then the slope (or stiffness) of this line can be calculated. Under the current mixed mode ratio, assume the point with maximum history effective separation Δ_m^{max} is $(X, Y, Z, T_n, T_{t1}, T_{t2})$ and the point in unloading and reloading is $(x, y, z, t_n, t_{t1}, t_{t2})$, where (X, Y, Z, x, y, z) are separations and $(T_n, T_{t1}, T_{t2}, t_n, t_{t1}, t_{t2})$ are tractions in three directions. (t_n, t_{t1}, t_{t2}) is to be determined. Then linear interpolation can be used to get tractions at each time step based on the current mixed mode ratio, as shown in Equation (2.45). Effective separation and damage factor are shown in Figures 2.12 (a) and 2.12 (b), respectively.

$$\begin{cases} \sqrt{X^2+Y^2+Z^2} = \Delta_m^{max} \\ \dfrac{\sqrt{y^2+z^2}}{|x|} = \dfrac{\sqrt{Y^2+Z^2}}{|X|} \\ \dfrac{x}{X} = \dfrac{t_n}{T_n}, \dfrac{y}{Y} = \dfrac{t_{t1}}{T_{t1}}, \dfrac{z}{Z} = \dfrac{t_{t2}}{T_{t2}} \end{cases} \tag{2.45}$$

Figures 2.12 (c) and 2.12 (d) show the tangential traction response in 2D and 3D plots, respectively. As shown in these figures, discontinuous force is not found in each cycle at the end of reloading, and the stiffness of the unloading and reloading are not same and not constant in Figure 2.12 (c). It is easy to see that constant unloading and reloading does not work for the monotonically increasing effective separation method. The envelope of Δ_m^{max} after first cycle is shown in Figure 2.12 (d), and the point with maximum history effective separation after first cycle is shown in the figure. Looking downward from the top, this envelope curve is just a quarter circle with maximum history effective separation.

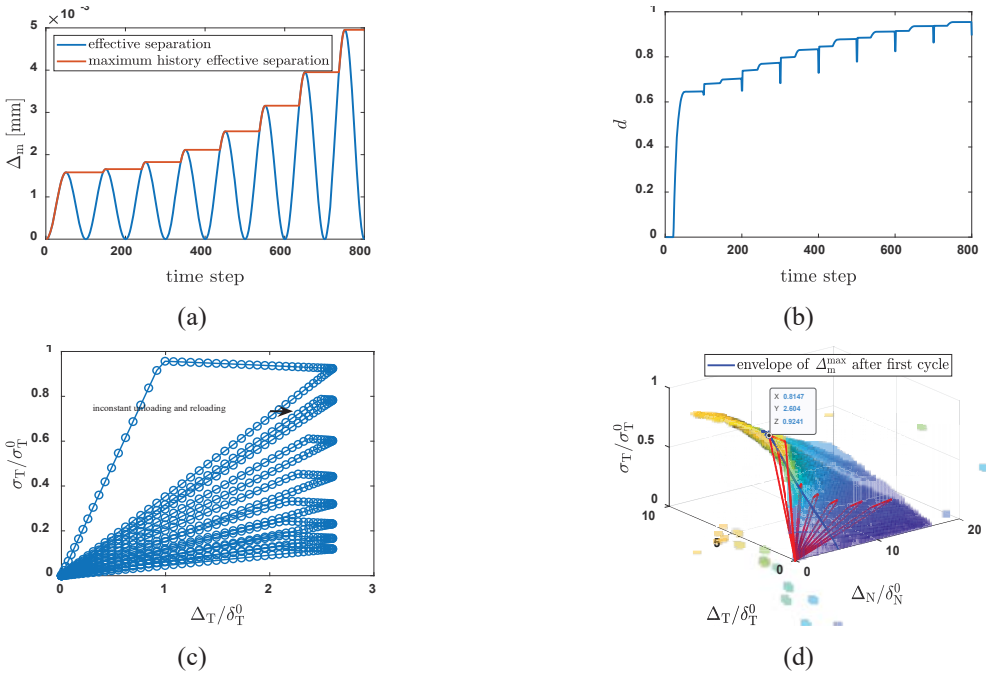

Figure 2.12 (a) effective separation and maximum history effective separation, (b) damage factor, (c) tangential traction in 2D plot, (d) tangential traction in 3D plot

2.2.1.3 Monotonically increasing damage factor method, without discontinuous force

Monotonically increasing damage factor method is applied to the same displacement load. Effective separation and damage factor are shown in Figures 2.13 (a) and 2.13 (b), respectively. Instead of the

monotonically increasing effective separation, the maximum history damage factor is kept increasing, and effective separation can increase and decrease. Similarly, the point with maximum history damage factor is $(X, Y, Z, T_n, T_{t1}, T_{t2}, D)$ and the point in unloading and reloading is $(x, y, z, t_n, t_{t1}, t_{t2}, d)$, where (t_n, t_{t1}, t_{t2}) is to be determined, as shown in Equation (2.46). Here, effective separation at $(X, Y, Z, T_n, T_{t1}, T_{t2}, D)$ is not required to be the maximum history effective separation. This damage evolution method is also used in MAT 240 in [33].

$$\begin{cases} d = D = d_m^{max} \\ \dfrac{\sqrt{y^2 + z^2}}{|x|} = \dfrac{\sqrt{Y^2 + Z^2}}{|X|} \\ \dfrac{x}{X} = \dfrac{t_n}{T_n}, \dfrac{y}{Y} = \dfrac{t_{t1}}{T_{t1}}, \dfrac{z}{Z} = \dfrac{t_{t2}}{T_{t2}} \end{cases} \tag{2.46}$$

Figures 2.13 (c) and 2.13 (d) show the tangential traction response in 2D and 3D plots, respectively. As shown in these figures, discontinuous force is not found in each cycle at the end of reloading. The big difference with monotonically increasing effective separation method is that, the stiffness of the unloading and reloading in Figure 2.13 (c) are same and constant, which is because this damage evolution process is controlled by damage factor. Before damage factor increases, it is kept same. In this case, constant unloading and reloading works well for monotonically increasing damage factor method. The envelope of d_m^{max} after first cycle is shown in Figure 2.13 (d), and the point with maximum history damage factor after first cycle is shown in the figure. Looking downward from the top, this envelope curve is similar to power law boundary with maximum history damage factor.

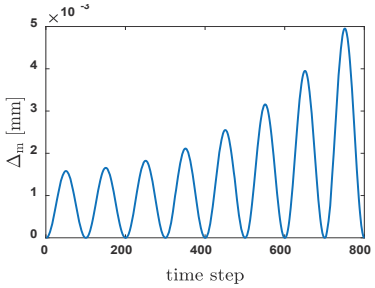

(a)

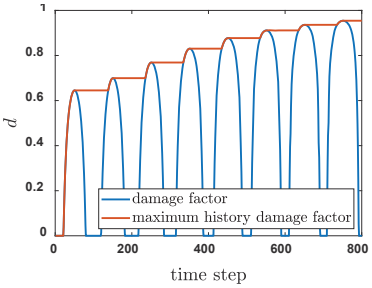

(b)

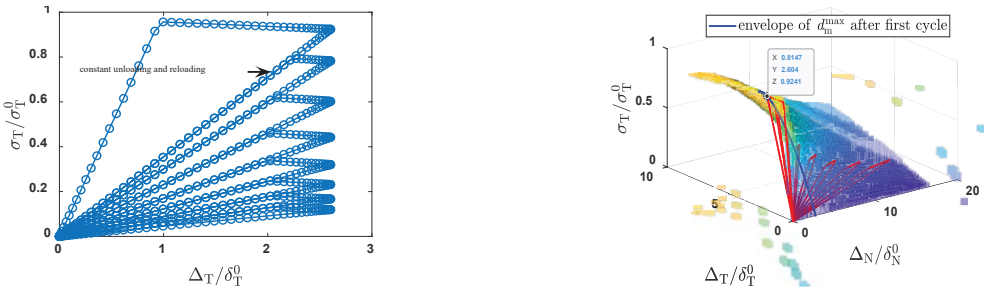

(c) (d)

Figure 2.13 (a) effective separation, (b) damage factor and maximum history damage factor, (c) tangential traction in 2D plot, (d) tangential traction in 3D plot

2.2.2 Unreasonable failure in damage evolution method

Even though the discontinuous force in monotonically increasing effective separation method can be solved, there are still some problems with monotonically increasing effective separation method. First, if effective separation is kept monotonically increasing, then damage factor is not guaranteed to be monotonically increasing, which means healing effect can happen in this method. Second, if maximum normal separation and maximum tangential separation in bilinear cohesive law are different, cohesive element could fail if a sudden change of mixed mode ratio happens, but no more energy is needed to cause this element to fail; and cohesive element could also fail in its unloading when mixed mode ratio changes gradually, which is not reasonable. A single cohesive element analysis is used to show the difference and verify the statements above.

The four nodes at the back of a hexahedral element are fixed, and prescribed displacement is applied on the front four nodes of this element. Finite element model and deformation during simulation are shown in Figure 2.14. The detailed prescribed displacement load is show in Figure 2.15. Two cases are considered, case 1 with sudden change of mixed mode ratio from infinity (pure tangential load) to 1, and case 2 with gradual change of mixed mode ratio from infinity (pure tangential load) to 0 (pure normal load), as shown in Figure 2.16. Material parameters used are shown in Table 2.2, and power law with $n = 1$ is used here for the sake of simplicity.

(a) (b)

Figure 2.14 (a) finite element model of single cohesive element, (b) deformation on the front surface

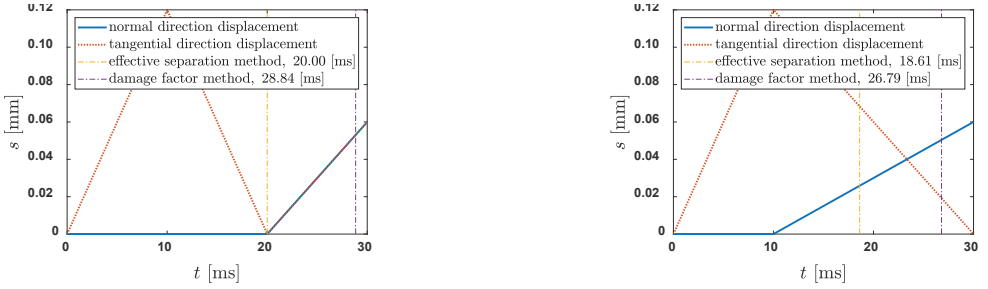

(a) (b)

Figure 2.15 Prescribed displacement load, (a) case 1 with sudden change of mixed mode ratio, (b) case 2 with gradual change of mixed mode ratio

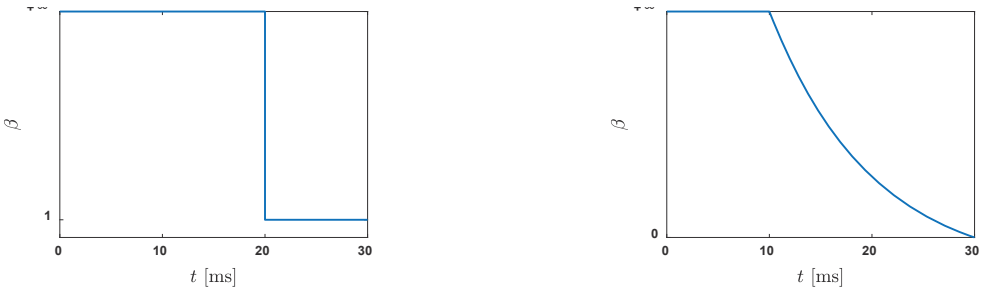

(a) (b)

Figure 2.16 Mixed mode ratio, (a) case 1 with sudden change of mixed mode ratio, (b) case 2 with gradual change of mixed mode ratio

Table 2.2 Bilinear cohesive law parameters for unreasonable failure analysis

Parameter	Positive Mode I	Negative Mode I	Mode II
Stiffness [MPa/mm]	10000	10000	10000
Fracture strength [MPa]	60	60	60
Critical energy release rate [N/mm]	1.5	4.5	9.0

The maximum normal separation δ_N^f for this material is 0.05 mm, while the maximum tangential separation δ_T^f is 0.15 mm. The loading path for case 1 is *OAOC*, as shown in Figure 2.17 (a), whereas the loading path for case 2 is *OAEC*, as shown in Figure 2.17 (b). For monotonically increasing damage factor

method, cohesive element would fail at point *C* for both cases, which is on the boundary defined by power law. However, for monotonically increasing effective separation method, cohesive element would fail at point *O* and *E*, respectively. Both failed in the unloading and reloading process, and both are not on the boundary defined by power law. The reason is that for monotonically increasing effective separation method, maximum history effective separation in this loading process is at point *A*, 0.12 mm, and when the loading path goes into the mixed mode ratio range where maximum allowable effective separation is less than 0.12 mm (i.e., the area surrounded by curve *OBCDO*), the cohesive element would just fail. This is why we see cohesive element fails at point *O* and *E*. The internal energy consumed is shown in Figure 2.18. When the energy changes to 0, it means that cohesive element fails. The time of the failure is also marked in the prescribed displacement load in Figure 2.15, and it agrees with the analysis of loading path in Figure 2.17 here. From this example, it is seen that damage evolution method can influence the time of failure and the internal energy consumed.

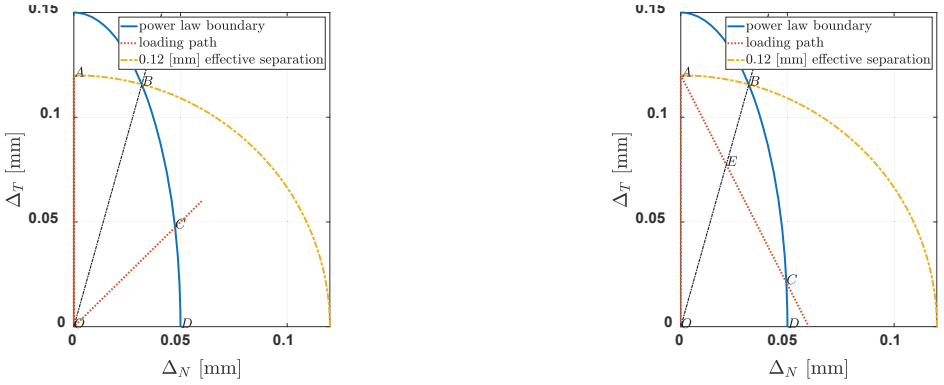

Figure 2.17 Loading path, (a) case 1 with sudden change of mixed mode ratio, (b) case 2 with gradual change of mixed mode ratio

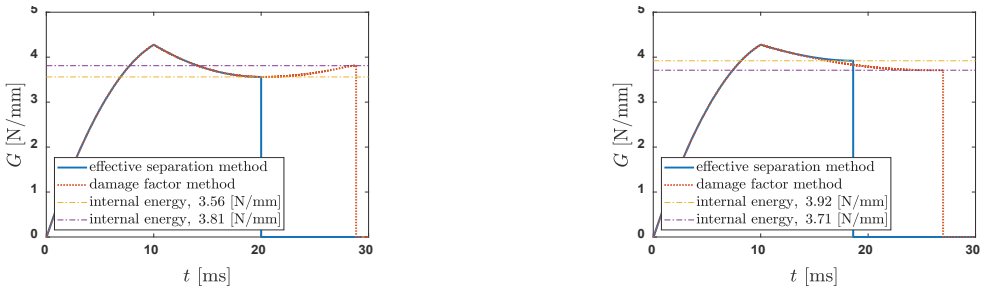

(a) (b)

Figure 2.18 Internal energy, (a) case 1 with sudden change of mixed mode ratio, (b) case 2 with gradual change of mixed mode ratio

2.3 Improvement on artificial compliance

2.3.1 Reason for artificial compliance

For intrinsic bilinear cohesive law, a common numerical problem is artificial compliance. Stress wave speeds in 1D, 2D, and 3D solid are shown in Equation (2.47). As shown in the equations, Young's modulus E, Poisson's ratio v, and density ρ are the three parameters that can alter the speed. Zero-thickness cohesive element can handle FEM modeling well, but the overall effective stiffness is implicitly decreased. To show the change caused by cohesive element, three different types of FEM modeling are shown in Figure 2.19, where blue lines and strips mean zero-thickness cohesive element and finite-thickness cohesive element, respectively.

$$\begin{cases} V_{1D} = \sqrt{\dfrac{E}{\rho}} \\ V_{2D} = \sqrt{\dfrac{E}{[(1-v^2)\rho]}} \\ V_{3D} = \sqrt{\dfrac{E(1-v)}{[(1+v)(1-2v)\rho]}} \end{cases} \tag{2.47}$$

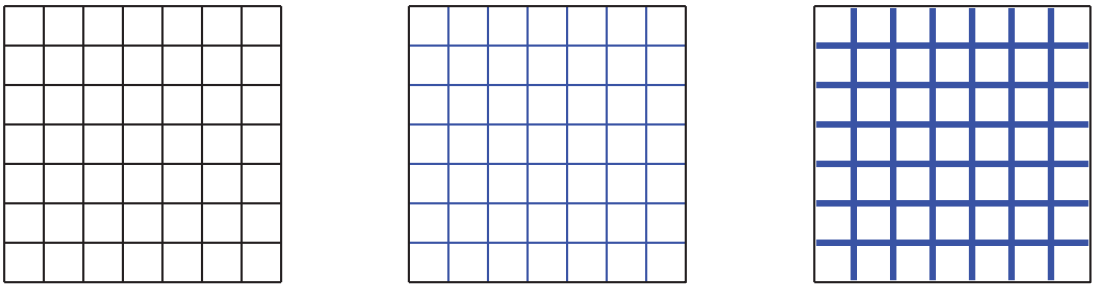

(a) (b) (c)

Figure 2.19 Different FEM modeling methods, (a) bulk elements only, (b) bulk elements with zero-thickness cohesive elements, (c) bulk elements with finite-thickness cohesive elements

A 1D model of springs in series corresponding to Figure 2.19 is used to explain the reason for artificial compliance, as shown in Figure 2.20. l_b and l_c are the length of bulk element and cohesive element, respectively; k_b and k_c are the stiffness of bulk element and cohesive element, respectively. The difference of finite-thickness cohesive element is that a thin layer of solid is replaced by cohesive element, and then deformation of cohesive element is based on this initial material, not like zero-thickness cohesive element where its deformation is not based on any material, which does not happen in reality. Parameter selection is investigated in [86,87] on stress wave speed, but cannot totally solve this problem because zero-thickness cohesive element means extra stiffness and extra deformation. However, by adjusting k_c in Figure 2.20 (c), the effective stiffness can be equal to that in Figure 2.20 (a), and then the increase of artificial compliance and the decrease of stress wave speed can be solved.

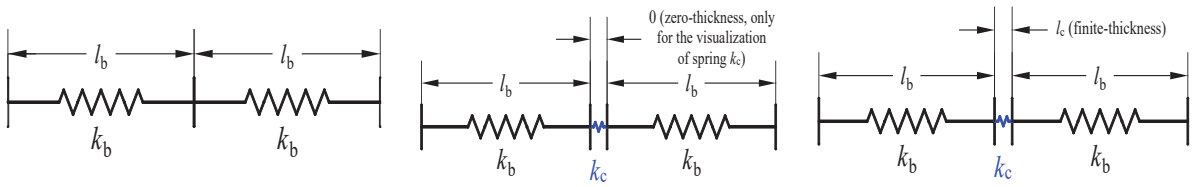

(a) (b) (c)

Figure 2.20 Different spring models, (a) bulk elements only, (b) bulk elements with zero-thickness cohesive elements, (c) bulk elements with finite-thickness cohesive elements

Theoretically, the time needed for stress wave to pass through zero-thickness cohesive elements is 0 since its length is 0, but cohesive elements would have small deformation when it is loaded, and some time is needed to pass through these deformed cohesive elements. This is the deep reason why zero-thickness

cohesive element can decrease the stress wave speed. Klein et al. [88] use a 1D example to illustrate the relation between effective stiffness and stiffness of zero-thickness cohesive element. Here, the deformation and effective stiffness corresponding to the three cases in Figure 2.20 are shown in Figure 2.21. For a general case with n bulk elements, the effective stiffness is shown in Equation (2.48).

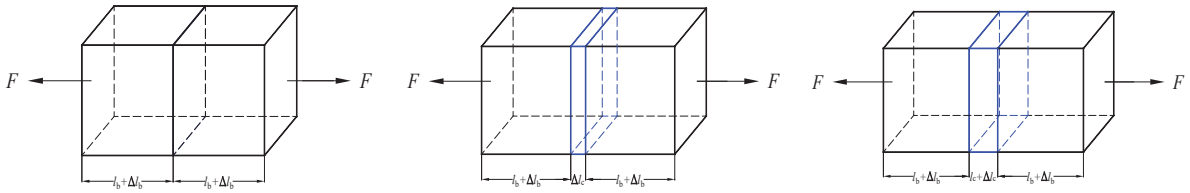

(a) (b) (c)

Figure 2.21 Deformation after load applied and illustration of artificial compliance in 1D case, (a) bulk elements only, (b) bulk elements with zero-thickness cohesive elements, (c) bulk elements with finite-thickness cohesive elements

$$\begin{cases} E_{eff} = E, & \text{bulk elements only} \\ E_{eff}^{zero} = E\left[1 - \dfrac{1}{1 + \dfrac{(n+1)l_b k_c}{nE}}\right], & \text{zero} - \text{thickness} \\ E_{eff}^{finite} = E\left[1 + \dfrac{n\dfrac{l_c}{l_b} - n\dfrac{E}{k_c l_b}}{(n+1) + \dfrac{nE}{k_c l_b}}\right], & \text{finite} - \text{thickness} \end{cases} \tag{2.48}$$

For zero-thickness cohesive element, since the coefficient after Young's modulus E in Equation (2.48) is always less than 1, its effective stiffness is always less than the stiffness of bulk element. And this artificial compliance would be worse if smaller bulk element (l_b) is used in FEM model. However, smaller element is usually required in simulations to get spatial (or grid) convergence. For finite-thickness cohesive element, if the cohesive element stiffness k_c equals E/l_c, its effective stiffness should be equal to the stiffness of bulk element, which means no artificial compliance. It is worth mentioning that, from Equation (2.48), the expression of stiffness for these two kinds of cohesive elements are different. For zero-thickness cohesive element, its stiffness is Young's modulus E over bulk element size l_b, while it is Young's modulus E over cohesive element size l_c (not bulk element size l_b) for finite-thickness cohesive element. After the reason of artificial compliance is explained, finite-thickness cohesive element is proposed as an easy and effective way to solve this artificial compliance problem.

Artificial compliance is not only shown on stress wave speed, but also on static deformation. Next, 1D and 3D simulations about static deformation, dynamic normal stress, and dynamic shear stress are used to explain and verify artificial compliance, and this problem is completely solved if finite-thickness cohesive element is used with a proper stiffness.

2.3.2 Numerical verification of artificial compliance

2.3.2.1 Deformation in quasi-static simulation

The deformation of a bar in quasi-static condition is investigated through MATLAB code. The bar has a square cross section, and the length of side is 20 mm, and the total length in axial direction is 200 mm. The left end of the bar is fixed, and load is applied at the right end. The geometry, boundary condition, and load are shown in Figure 2.22. The material parameters used are Young's modulus E 210 GPa, density ρ 0.00785 g/mm^3. The total number of bulk elements is 100, so the length of the bulk element l_b is 2 mm. However, for the finite-thickness cohesive elements case, the length of bulk element l_b *is* 1.9 mm, and the length of cohesive element l_c is 0.1 mm. The dynamic equation of motion is shown in Equation (2.49), and mass matrix $\boldsymbol{M}_\mathrm{b}$, $\boldsymbol{M}_\mathrm{c}$ and stiffness matrix $\boldsymbol{K}_\mathrm{b}$, $\boldsymbol{K}_\mathrm{c}$ for the three cases in Figure 2.21 are shown in Equations (2.50), (2.51), and (2.52), respectively. Note that mass matrix for zero-thickness cohesive element is set as 0 here. r in Equations (2.51) and (2.52) is used to adjust the stiffness of cohesive element.

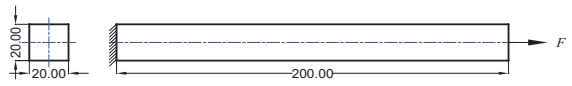

(a)

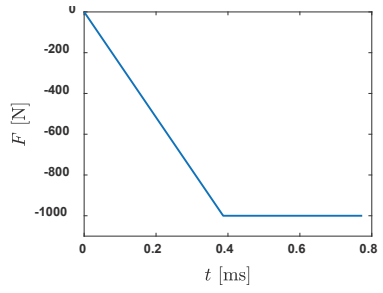

(b)

Figure 2.22 (a) geometry, boundary condition, and load of the 1D bar, unit [mm], (b) detailed load at right end for the quasi-static condition

$$[\boldsymbol{M}]\{\ddot{\boldsymbol{U}}\} + [\boldsymbol{C}]\{\dot{\boldsymbol{U}}\} + [\boldsymbol{K}]\{\boldsymbol{U}\} = \{\boldsymbol{F}^{ext}\} \tag{2.49}$$

$$\boldsymbol{M}_b = \frac{\rho A l_b}{6}\begin{bmatrix}2 & 1\\ 1 & 2\end{bmatrix}, \boldsymbol{K}_b = \frac{EA}{l_b}\begin{bmatrix}1 & -1\\ -1 & 1\end{bmatrix} \tag{2.50}$$

$$\boldsymbol{M}_c^{zero} = \begin{bmatrix} 0 & 0 \\ 0 & 0 \end{bmatrix}, \boldsymbol{K}_c^{zero} = r\frac{EA}{l_b}\begin{bmatrix} 1 & -1 \\ -1 & 1 \end{bmatrix} \tag{2.51}$$

$$\boldsymbol{M}_c^{finite} = \frac{\rho A l_c}{6}\begin{bmatrix} 2 & 1 \\ 1 & 2 \end{bmatrix}, \boldsymbol{K}_c^{finite} = r\frac{EA}{l_c}\begin{bmatrix} 1 & -1 \\ -1 & 1 \end{bmatrix} \tag{2.52}$$

Rayleigh damping is used to construct damping matrix to reduce oscillation and reach steady state more quickly, as shown in Equation (2.53). $\alpha 1$ and $\alpha 2$ are two coefficients to be determined from frequency range of interest and mode damping ratio. In this dissertation, the interested frequency range is the frequency component that has period equal to the time that stress wave passes through the whole bar ω_1 and one bulk element ω_2. The two mode damping ratios are same and are chosen as 0.1 in this dissertation, i.e., $\xi_1 = \xi_2 = 0.1$ in Equation (2.54). Central difference method is used to solve the equation.

$$[\boldsymbol{C}] = \alpha 1[\boldsymbol{M}] + \alpha 2[\boldsymbol{K}] \tag{2.53}$$

$$0.5\begin{bmatrix} \frac{1}{\omega_1} & \omega_1 \\ \frac{1}{\omega_2} & \omega_2 \end{bmatrix}\begin{bmatrix} \alpha 1 \\ \alpha 2 \end{bmatrix} = \begin{bmatrix} \xi_1 \\ \xi_2 \end{bmatrix} \tag{2.54}$$

Figure 2.23 (a) shows the displacement at right end of the bar obtained for different FEM models. With the increase of r for zero-thickness cohesive element, displacement gets closer and closer to the bulk elements only case, but there is still a discrepancy between $100E/l_{\mathrm{b}}$ case and bulk elements only case. However, finite-thickness cohesive element can have displacement totally same as the bulk elements only case. Figure 2.23 (b) shows time step size scale factor needed for a successful simulation, and this scale factor decreases fast with the increase of cohesive element stiffness. Even though finite-thickness case has almost same scale factor as zero-thickness $100E/l_{\mathrm{b}}$ case, finite-thickness case can remove artificial compliance completely.

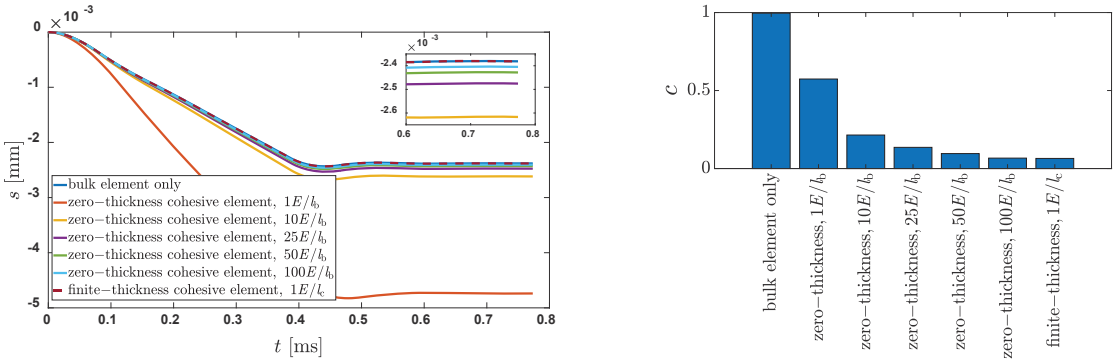

(a) (b)

Figure 2.23 (a) displacement at the right end of the bar, (b) time step size scale factor needed for a successful simulation

2.3.2.2 Normal stress in dynamic simulation

Normal stress in dynamic simulation is also investigated, and 1D case in MATLAB and 3D case in LS-DYNA are presented. For the 1D case, it is almost same as previous section except that load is an impact load, as shown in Figure 2.24 (a). Stress wave at the right end of the bar is plotted in Figure 2.25. For zero-thickness cohesive element, stress wave is delayed even in $100E/l_b$ case, but this delay is not found for the finite-thickness cohesive element.

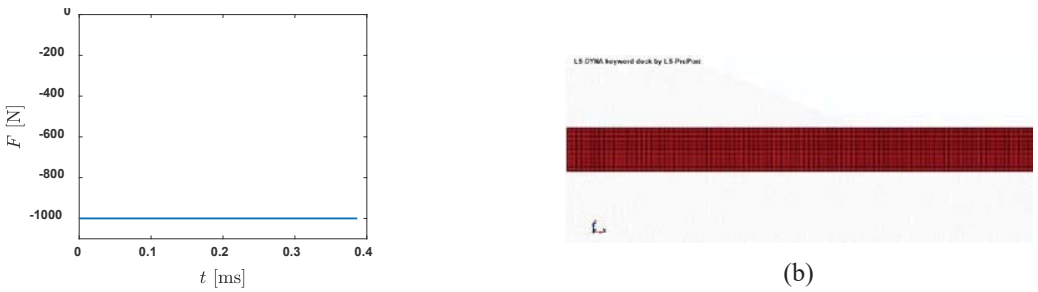

(a) (b)

Figure 2.24 (a) detailed load at right end for the dynamic condition in 1D case, (b) the bar in LS-DYNA in 3D case

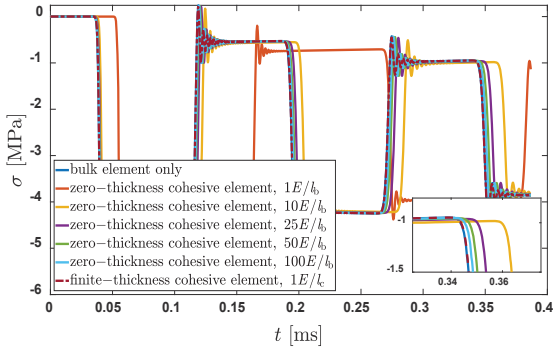

Figure 2.25 Stress wave at the right end of the bar in 1D case

In the 1D case, from Equations (2.50), (2.51), and (2.52), zero-thickness cohesive element has similar stiffness as bulk element, and finite-thickness cohesive element has totally same stiffness as bulk element. However, in 3D case, their stiffnesses are different. In general, bulk element has 6 stress components, but cohesive element only deals with 3 stress components, so it is still necessary to investigate this artificial compliance in 3D case. To make a better comparison between these two types of cohesive elements, the stiffnesses are both used as E/l_c in 3D case. The length of bulk element l_b is 1 mm, and the length of cohesive element l_c is 0.01 mm in the simulation, a very thin layer. For 3D case, one more parameter needed is Poisson's ratio v 0.3. The FEM model is shown in Figure 2.24 (b), and load is same as Figure 2.24 (a). As shown in Figure 2.26 (a), zero-thickness cohesive element cannot avoid stress wave delay even with high stiffness, but stress wave delay is removed in Figure 2.26 (b) with a lower stiffness. The reason why stiffness in 3D case should be a little larger than the stiffness E/l_c is that Poisson's ratio v 0.3 for bulk element, and speed wave is faster than $\sqrt{E/\rho}$ if v 0.3 is considered, see Equation (2.47). Stress wave speed can even be faster when a larger stiffness is used in finite-thickness cohesive element, as shown in Figure 2.26 (b).

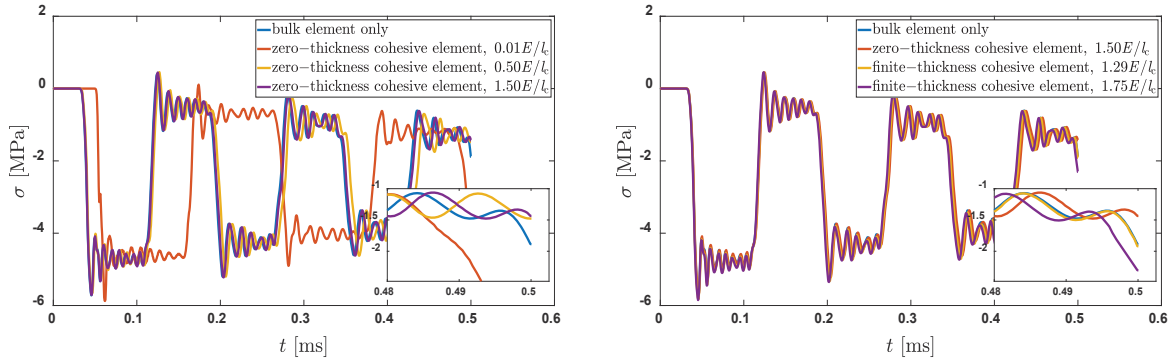

(a) (b)

Figure 2.26 Stress wave at the right end of the bar for 3D case, (a) zero-thickness cohesive element, (b) finite-thickness cohesive element

2.3.2.3 Shear stress in dynamic simulation

Shear stress in dynamic simulation in 3D case is also investigated. The top and bottom sides of a plate with 1 mm thickness is fixed. One layer of element is used to mesh the plate, and cube element size is 1 mm. Concentrated load is applied to the 10 nodes at the center of the left side of the plate, and the load on each node is shown in Figure 2.27 (b). This load is small enough that maximum stress in the simulation is still in elastic range. The shear stress at the point 24.5 mm × 24.5 mm from the left bottom corner is extracted.

(a) (b)

Figure 2.27 (a) schematic of the plate, unit [mm], (b) concentrated load on the left side of the plate

Stress wave of the point is shown in Figure 2.28, and similar results as normal stress case in previous section can be found. Zero-thickness cohesive element cannot avoid stress wave delay even with high stiffness, but stress wave delay is removed in Figure 2.28 (b) finite-thickness cohesive element with a lower stiffness. And stress wave speed can be even higher than bulk elements only case when a larger stiffness $1.75E/l_c$ is used. It is also found that stress wave is not correct for the zero-thickness cohesive element case when a really low stiffness $0.01E/l_c$ is used in Figure 2.28 (a), so great caution should be taken on

stiffness selection.

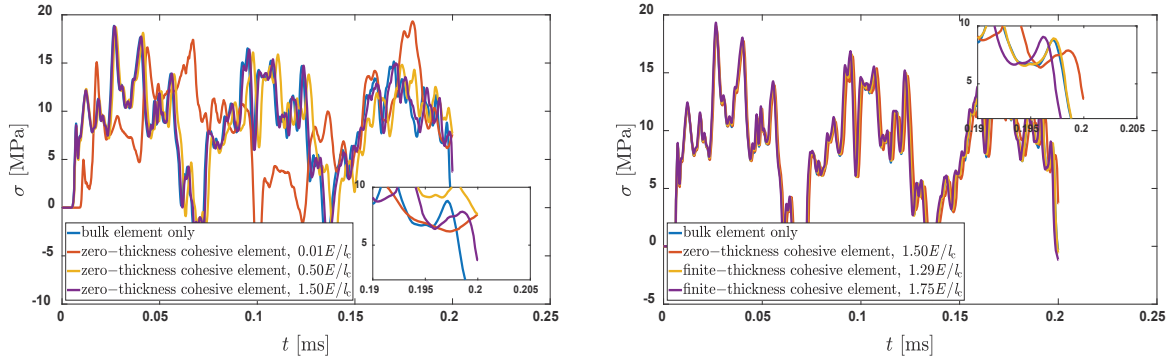

(a) (b)

Figure 2.28 Stress wave of the point, (a) zero-thickness cohesive element, (b) finite-thickness cohesive element

3 Cohesive zone model considering strain rate, plastic strain, and variable damping

In this section, the effects of strain rate, plastic strain, and variable damping are considered together into one cohesive element. To extend the scope of application of cohesive zone model to more materials, strain rate and plastic strain are considered. Based on the damage factor in classical bilinear cohesive law, a generalized damage factor model is proposed to cover all materials from zero plastic strain to maximum plastic strain. By adding a variable damping into cohesive element, spurious oscillation and excessive cohesive element deletion in cohesive zone model are improved, and there is no discontinuous force like when using a constant damping. Several simulations are presented to verify these three effects.

3.1 Bilinear cohesive law considering strain rate

When the effect of strain rate is considered in publications, usually, stiffness, fracture strength, and critical energy release rate are functions of strain rate or opening speed of cohesive element. Because the range of magnitude of strain rate or opening speed could be really large, most of the time a logarithmic function is used. Generalized functions of the influence of opening speed on cohesive law parameters are shown in Equations (3.1) - (3.6). The detailed information about those parameters can be found in [89]. However, for different material and different experiment data, the form of these equations can be different. The main idea here is obtaining the relation that shows the influence of strain rate or opening speed on material parameters.

$$E_N^0\left(\dot{\Delta}_N\right) = E_N^{ref} \tag{3.1}$$

$$E_T^0\left(\dot{\Delta}_T\right) = E_T^{ref} \tag{3.2}$$

$$\sigma_N^0\left(\dot{\Delta}_N\right) = \begin{cases} \sigma_N^{ref}, & \left|\dot{\Delta}_N\right| < \dot{\Delta}_N^{ref} \\ \sigma_N^{ref}\left[1 + c_N ln\left(\dfrac{\left|\dot{\Delta}_N\right|}{\dot{\Delta}_N^{ref}}\right)\right], & \dot{\Delta}_N^{ref} \le \left|\dot{\Delta}_N\right| \end{cases} \tag{3.3}$$

$$\sigma_T^0(\dot{\Delta}_T) = \begin{cases} \sigma_T^{ref}, & |\dot{\Delta}_T| < \dot{\Delta}_T^{ref} \\ \sigma_T^{ref}\left[1 + c_T ln\left(\frac{|\dot{\Delta}_T|}{\dot{\Delta}_T^{ref}}\right)\right], & \dot{\Delta}_T^{ref} \le |\dot{\Delta}_T| \end{cases} \tag{3.4}$$

$$G_{IC}^0(\dot{\Delta}_N) = \begin{cases} G_{IC}^{ref}, & |\dot{\Delta}_N| < \dot{\Delta}_N^{ref} \\ G_{IC}^{ref}\left[1 + m_N ln\left(\frac{|\dot{\Delta}_N|}{\dot{\Delta}_N^{ref}}\right)\right], & \dot{\Delta}_N^{ref} \le |\dot{\Delta}_N| < \dot{\Delta}_N^{inf} \\ G_{IC}^{inf}, & \dot{\Delta}_N^{inf} \le |\dot{\Delta}_N| \end{cases} \tag{3.5}$$

$$G_{IIC}^0(\dot{\Delta}_T) = \begin{cases} G_{IIC}^{ref}, & |\dot{\Delta}_T| < \dot{\Delta}_T^{ref} \\ G_{IIC}^{ref}\left[1 + m_T ln\left(\frac{|\dot{\Delta}_T|}{\dot{\Delta}_T^{ref}}\right)\right], & \dot{\Delta}_T^{ref} \le |\dot{\Delta}_T| < \dot{\Delta}_T^{inf} \\ G_{IIC}^{inf}, & \dot{\Delta}_T^{inf} \le |\dot{\Delta}_T| \end{cases} \tag{3.6}$$

where, $|\dot{\Delta}_N|$ and $|\dot{\Delta}_T|$ are the absolute opening speed in normal and tangential directions, respectively; $\dot{\Delta}_N^{ref}$ and $\dot{\Delta}_T^{ref}$ are the quasi-static opening speed in Mode I and Mode II, respectively; $\dot{\Delta}_N^{inf}$ and $\dot{\Delta}_T^{inf}$ are the upper limit of opening speed in Mode I and Mode II, respectively; E_N^{ref} and E_T^{ref} are the quasi-static stiffness in Mode I and Mode II, respectively; σ_N^{ref} and σ_T^{ref} are the quasi-static fracture strength in Mode I and Mode II, respectively; G_{IC}^{ref} and G_{IIC}^{ref} are the quasi-static critical energy release rate in Mode I and Mode II, respectively; G_{IC}^{inf} and G_{IIC}^{inf} are the upper limit of critical energy release rate in Mode I and Mode II, respectively.

3.2 Bilinear cohesive law considering plastic strain

The relation between damage factor and plastic strain is explained in this section. The most common damage factor for bilinear cohesive law is the one without considering plastic strain, and the unloading and reloading curve is the line that connects the point on bilinear cohesive law and the origin. In this case, the damage factor and the stiffness of the line can be calculated, which has been shown in Equation (2.39) before. This damage factor does not consider the effect of plastic strain. To introduce plastic strain into the bilinear cohesive law, the damage factor should be changed. In this dissertation, a generalized damage factor model is proposed. It is very simple and only a little change on the original damage factor is needed,

as shown in Equation (3.7).

$$d = \begin{cases} 0, & 0 \le \Delta_m < \delta_m^0 \\ \dfrac{\delta_m^f}{\phi}\left(\dfrac{\Delta_m - \delta_m^0}{\delta_m^f - \delta_m^0}\right), & \delta_m^0 \le \Delta_m < \delta_m^f \\ 1, & \delta_m^f \le \Delta_m \end{cases} \tag{3.7}$$

where, ϕ is a new parameter in the generalized damage factor model. By changing the variable ϕ, the bilinear cohesive law can change from zero plastic strain model to maximum plastic strain model. It is worth mentioning that three typical damage factor models can be obtained from Equation (3.7) when

$\phi = \Delta_m$, zero plastic strain model, corresponding to maximum damage factor;

$\phi = \delta_m^f$, linear damage factor model, corresponding to LS-DYNA material type MAT 240 [20];

$\phi = \infty$, maximum plastic strain model or no damage model (stiffness is a constant), corresponding to minimum damage factor.

What's more, if the third power of zero plastic strain model and linear damage factor model shown above are used as damage factor model, another two typical damage factor models (convex and concave) and their parameter ϕ can be obtained as

$\phi = \dfrac{\Delta_m}{\left[\frac{\delta_m^f}{\Delta_m}\left(\frac{\Delta_m - \delta_m^0}{\delta_m^f - \delta_m^0}\right)\right]^2}$, convex damage factor model, $d = \left[\dfrac{\delta_m^f}{\Delta_m}\left(\dfrac{\Delta_m - \delta_m^0}{\delta_m^f - \delta_m^0}\right)\right]^3$;

$\phi = \dfrac{\delta_m^f}{\left[\frac{\delta_m^f}{\delta_m^f}\left(\frac{\Delta_m - \delta_m^0}{\delta_m^f - \delta_m^0}\right)\right]^2}$, concave damage factor model, $d = \left[\dfrac{\delta_m^f}{\delta_m^f}\left(\dfrac{\Delta_m - \delta_m^0}{\delta_m^f - \delta_m^0}\right)\right]^3$.

The difference of these five damage factor models is shown in Figure 3.1 (a), and different damage factor model means different unloading and reloading track and plastic strain, as shown in Figure 3.1 (b). In this example, δ_m^0 is 0.001 mm, δ_m^f is 0.01 mm, and σ_m^0 is 60 MPa. Different materials could lead to different damage factor shapes, and the suggestion is that get this damage factor from experiments. A cohesive law considering plastic strain can expand its application range since zero plastic strain damage factor only applies for brittle material failure. In this dissertation, because of the lack of experiment data, linear damage factor model is used as a reference to consider plastic strain, which is also used in LS-DYNA

MAT 240 [20].

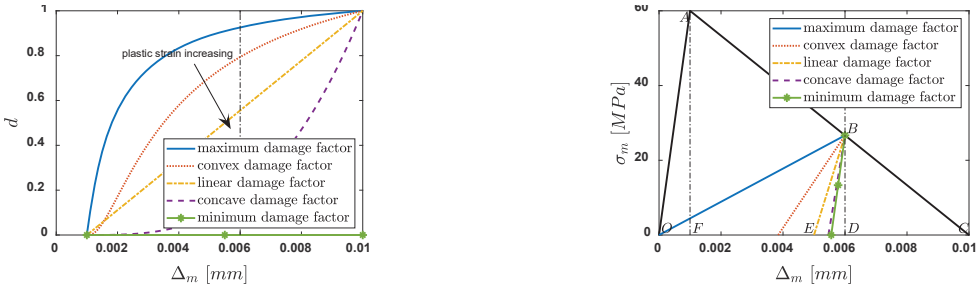

(a) (b)

Figure 3.1 (a) different types of damage factor, (b) different tractions because of different types of damage factor

There is a feature for the linear damage factor model during the unloading and reloading process. The length of DE for any point B on AC part is always equal to δ_m^0, i.e., the length of OF. The proof of this conclusion is straightforward. The horizontal coordinate of point B is Δ_m, and the vertical coordinate of point B is σ_m, and the damage factor at point B is d.

$$d = \frac{\delta_m^f}{\delta_m^f}\left(\frac{\Delta_m - \delta_m^0}{\delta_m^f - \delta_m^0}\right) = \frac{\Delta_m - \delta_m^0}{\delta_m^f - \delta_m^0}$$

$$\text{so, } \Delta_m = d\left(\delta_m^f - \delta_m^0\right) + \delta_m^0$$

$$\frac{CD}{CF} = \frac{BD}{AF}$$

$$\frac{CD}{CF} = \frac{\delta_m^f - \Delta_m}{\delta_m^f - \delta_m^0} = \frac{\left(\delta_m^f - \delta_m^0\right) - d\left(\delta_m^f - \delta_m^0\right)}{\delta_m^f - \delta_m^0} = 1 - d, \frac{BD}{AF} = \frac{\sigma_m}{\sigma_m^0}$$

$$\text{so, } \sigma_m = (1-d)\sigma_m^0$$

The traction at point B is $(1-d)\sigma_m^0$, and the stiffness of BE is $(1-d)E_m^0$, so the ratio between these two values is still δ_m^0, which means the length of DE is always δ_m^0.

One finding obtained from this feature is that if δ_m^0 is much smaller than δ_m^f, the plastic strain difference between linear damage factor model and minimum damage factor model could be very small, and in some situation, a linear damage factor model could be almost a minimum damage factor model which has maximum plastic strain. In this case, many different plastic strain models would happen between maximum damage factor model and linear damage factor model, i.e., convex damage factor model. This

finding will be verified in Section 3.4.1 and Section 3.4.2. The damage factor can be transferred into a 3D situation, as shown in Figure 3.2, and the difference between different damage factor models can be seen much clearer. In Figure 3.2, the separations in normal and tangential directions are normalized with their maximum separations.

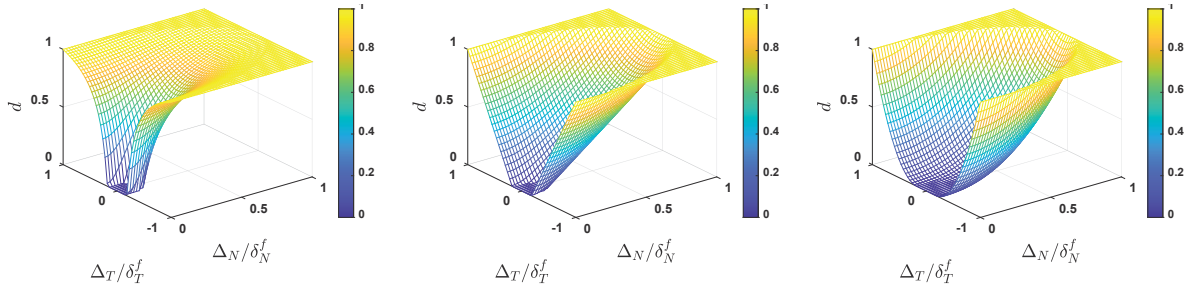

(a) (b) (c)

Figure 3.2 Damage factor model, (a) convex damage factor, (b) linear damage factor, (c) concave damage factor

By defining correct damage factor model, plastic strain can be considered into cohesive elements, but the part shown above only talks about the traction in positive quadrant, not negative quadrant, and many papers dealing with plastic strain stop here. However, the load path can have many different situations in simulation, and when cohesive elements undergo reciprocating load (both positive traction and negative traction), it would be totally different. Inspired from [90], the difference between zero plastic strain and with plastic strain in Mode II is shown in Figure 3.3, same thing in Mode I. For zero plastic strain model, the load path is $O_{T1}ABO_{T1}EF$; for with plastic strain model, the load path is $O_{T1}ABO_{T2}DE$. One thing needed to mention is that because the critical energy release rate is same, the consumed energy is same when cohesive element fails in both cases, but the traction response is totally different. Another thing needed to mention is that for zero plastic strain model, after unloading the separation goes back to the origin, and there is no need to update local coordinate system when separation becomes negative. However, for with plastic strain model, after unloading the local coordinate system becomes $O_{T2}\Delta_{T2}\sigma_{T2}$, not the original $O_{T1}\Delta_{T1}\sigma_{T1}$, so the update of local coordinate system is needed.

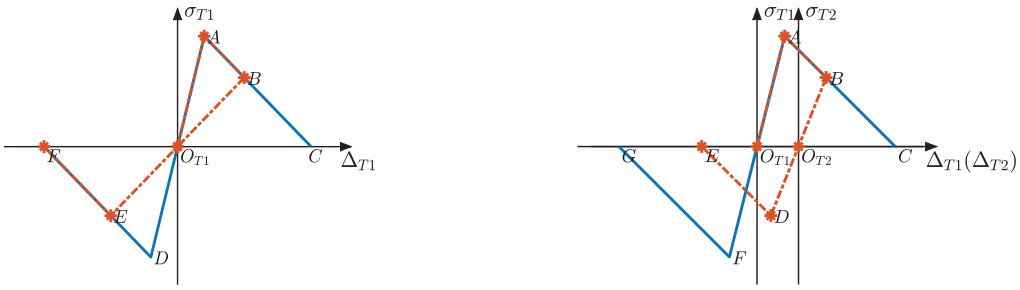

(a) (b)

Figure 3.3 Traction in cohesive element undergoing reciprocating load up to failure, (a) zero plastic strain, (b) with plastic strain

Separation and traction can be obtained correctly without the update of coordinate system if traction is always positive or negative, but every time when the sign of traction changes, the coordinate system and bilinear cohesive law parameters are needed to update. In this dissertation, whether or not update is based on the damage factor, as shown in Equation (3.8). The coordinate system update process is shown in Equation (3.9). For example, for the load path $O_{T1}ABO_{T2}DE$ shown in Figure 3.3 (b), the load point is going through point O_{T2} and the coordinate system will be updated at ith step.

$$\begin{cases} d_i < d_{min}(or\ d_{OT2}), & \text{update} \\ d_{min}(or\ d_{OT2}) \le d_i, & \text{no update} \end{cases} \tag{3.8}$$

$$\begin{cases} \widehat{CS_x} = CS_x - \text{sign}\{x_{i-1}\} d_{max}\left(\delta^f_{m,x,i-1} - \delta^0_{m,x,i-1}\right) \\ \widehat{CS_y} = CS_y - \text{sign}\{y_{i-1}\} d_{max}\left(\delta^f_{m,y,i-1} - \delta^0_{m,y,i-1}\right) \\ \widehat{CS_z} = CS_z - \text{sign}\{z_{i-1}\} d_{max}\left(\delta^f_{m,z,i-1} - \delta^0_{m,z,i-1}\right) \end{cases} \tag{3.9}$$

where, d_i is the damage factor at ith step; d_{OT2} is the damage factor at point O_{T2}, which is the minimum damage factor for this step; CS_x, CS_y, and CS_z are the coordinate system location in x, y, and z directions at $(i-1)$th step, respectively; $\widehat{CS_x}$, $\widehat{CS_y}$, and $\widehat{CS_z}$ are the new coordinate system location in x, y, and z directions at ith step, respectively; $\text{sign}\{x_{i-1}\}$, $\text{sign}\{y_{i-1}\}$, and $\text{sign}\{z_{i-1}\}$ are the sign of x, y, and z separations at $(i-1)$ th step, respectively; $\delta^0_{m,x,i-1}$, $\delta^0_{m,y,i-1}$, and $\delta^0_{m,z,i-1}$ are the separation at the initiation of damage in x, y, and z directions under $(i-1)$th step's mixed mode ratio, respectively; $\delta^f_{m,x,i-1}$, $\delta^f_{m,y,i-1}$, and $\delta^f_{m,z,i-1}$ are the separation at the failure of damage evolution in x, y, and z directions under $(i-1)$th step's mixed mode ratio, respectively; d_{max} is the maximum damage factor up to $(i-1)$th step,

which is the damage factor at point B in this example, as shown in Figure 3.3 (b). Different damage factor models have different plastic strains, and this plastic strain should be calculated first and then used in the update of coordinate system. Equation (3.9) here is only the example for linear damage factor model. The update of bilinear cohesive law parameters for linear damage factor model is shown in Equation (3.10). Other damage factor model can be obtained similarly.

With the update of coordinate system, the bilinear cohesive law parameters are also needed to update, otherwise the cohesive element may not fail forever in some situations. The cohesive law parameters are updated based on maximum damage factor, and under this maximum damage factor, the remaining critical energy release rate, fracture strength, stiffness, separation at the failure of damage evolution, and separation at the initiation of damage are set as new bilinear cohesive law parameters. After the update of all bilinear cohesive law parameters, the maximum damage factor is reset to 0, as shown in Equation (3.10).

$$
\begin{cases}
\widehat{G_{IC,p}^{ref}} = (1-d_{max})E_{N,p}^0\delta_{N,p}^0\left[\delta_{N,p}^f - d_{max}\left(\delta_{N,p}^f - \delta_{N,p}^0\right)\right]/2 \\
\widehat{G_{IC,n}^{ref}} = (1-d_{max})E_{N,n}^0\delta_{N,n}^0\left[\delta_{N,n}^f - d_{max}\left(\delta_{N,n}^f - \delta_{N,n}^0\right)\right]/2 \\
\widehat{G_{IIC}^{ref}} = (1-d_{max})E_{T}^0\delta_{T}^0\left[\delta_{T}^f - d_{max}\left(\delta_{T}^f - \delta_{T}^0\right)\right]/2 \\
\widehat{\sigma_{N,p}^{ref}} = (1-d_{max})E_{N,p}^0\delta_{N,p}^0 \\
\widehat{\sigma_{N,n}^{ref}} = (1-d_{max})E_{N,n}^0\delta_{N,n}^0 \\
\widehat{\sigma_{T}^{ref}} = (1-d_{max})E_{T}^0\delta_{T}^0 \\
\widehat{E_{N,p}^{ref}} = (1-d_{max})E_{N,p}^0 \\
\widehat{E_{N,n}^{ref}} = (1-d_{max})E_{N,n}^0 \\
\widehat{E_{T}^{ref}} = (1-d_{max})E_{T}^0 \\
\widehat{\delta_{N,p}^f} = \delta_{N,p}^f - d_{max}\left(\delta_{N,p}^f - \delta_{N,p}^0\right) \\
\widehat{\delta_{N,n}^f} = \delta_{N,n}^f - d_{max}\left(\delta_{N,n}^f - \delta_{N,n}^0\right) \\
\widehat{\delta_{T}^f} = \delta_{T}^f - d_{max}\left(\delta_{T}^f - \delta_{T}^0\right) \\
\widehat{\delta_{N,p}^0} = \delta_{N,p}^0 \\
\widehat{\delta_{N,n}^0} = \delta_{N,n}^0 \\
\widehat{\delta_{T}^0} = \delta_{T}^0 \\
\widehat{d_{max}} = 0
\end{cases}
\tag{3.10}
$$

where, $\widehat{\cdot\cdot}$ means new bilinear cohesive law parameters; same meaning of these letters can be found in

Section 2.

3.3 Bilinear cohesive law considering variable damping

To decrease spurious oscillation in simulations using cohesive elements, a damper is added into the double bilinear model based on the idea of "viscous damping" to deal with oscillation between contact surfaces in [37]. Usually, a constant damper is used in mechanical system to damp oscillation. However, in bilinear cohesive law, this common constant damper cannot depict a fully debonding under high strain rate situation [33,41], and it can cause high discontinuous force at the start and end of bilinear cohesive law. To solve this problem, a variable damping is used in this dissertation, and the damping coefficient is multiplied by two independent variables, which are used in the strengthening part and softening part separately, as shown in Equation (3.11). The range of α_1 is [0,1], and the range of α_2 is [1,0], so these two variables are continuous at the turning point between strengthening part and softening part. In this way, discontinuous force at the start and end of bilinear cohesive law would not come from damper. Under a constant opening speed, the comparison among original bilinear cohesive law, bilinear cohesive law with constant damper, and bilinear cohesive law with variable damper is shown in Figure 3.4. Equation (3.12) shows a common way to estimate damping coefficient c.

$$\begin{cases} \alpha_1 = \dfrac{\Delta_m}{\delta_m^0}, & 0 \le \Delta_m < \delta_m^0 \\ \alpha_2 = \dfrac{\delta_m^f - \Delta_m}{\delta_m^f - \delta_m^0}, & \delta_m^0 \le \Delta_m < \delta_m^f \end{cases} \tag{3.11}$$

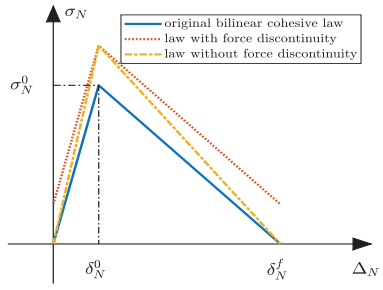

Figure 3.4 Comparison between with discontinuous force and without discontinuous force

$$\begin{cases} m = min(m_1, m_2) \\ \omega = \sqrt{k\dfrac{m_1 + m_2}{m_1 m_2}} \\ c = 2m\omega \; or \; c = 2em\omega \end{cases} \tag{3.12}$$

where, m_1 and m_2 are the mass connected through cohesive element; k is the stiffness of cohesive element; ω is the natural frequency of the two lumped mass system. Stiffness matrix for cohesive element has been shown in Equation (2.17). Usually, the damping coefficient is not a constant, and it depends on the oscillation frequency under the specific loading condition. The scale factor e in Equation (3.12) is used for this. Then, the extra traction in normal direction from the variable damper can be written as Equation (3.13). The extra traction in tangential direction from this damper can be obtained similarly.

$$\begin{cases} \sigma_{N,damp} = \alpha_1 c\dot{\Delta}_N, & 0 \le \Delta_m < \delta_m^0 \\ \sigma_{N,damp} = \alpha_2 c\dot{\Delta}_N, & \delta_m^0 \le \Delta_m < \delta_m^f \end{cases} \tag{3.13}$$

3.4 Numerical verification of strain rate, plastic strain, and variable damping

In this section, a single cohesive element analysis is presented first to show the change of constitutive law by the generalized damage factor model. After that, one fixed delamination propagation (Tapered Double Cantilever Beam test), one free fracture propagation in 2D (PMMA test), and one free fracture propagation in 3D (Kalthoff test) are used to verify the methodology proposed in this Section 2 and Section 3. LS-DYNA user-defined material is used for these simulations.

3.4.1 Single cohesive element analysis of constitutive law

Three kinds of comparisons are presented in this section. The first case is about the effect of plastic strain; the second case is about the effect of strain rate; the third case is about the difference among different damage factor models. The bilinear cohesive law parameters are referred from [89], and detailed information is shown in Table 3.1. To investigate the situation that critical energy release rate increases with the increase of opening speed, the critical energy release rate coefficients are positive. In those simulations, the stiffness and fracture strength in negative Mode I are 3 times of the parameters in Mode II,

and the quasi-static critical energy release rate and upper limit of critical energy release rate in negative Mode I are 5 times of the parameters in Mode II. Note that the main purpose here is on the different types of traction response, not the specific values.

Table 3.1 Bilinear cohesive law parameters for the analysis of single cohesive element

Parameters	**Positive Mode I**	**Negative Mode I**	**Mode II**
Stiffness [MPa/mm]	100000	300000	100000
Quasi-static fracture strength [MPa]	60	180	60
Quasi-static critical energy release rate [N/mm]	1.5	7.5	1.5
Quasi-static opening speed [mm/s]	20	20	20
Upper limit opening speed [mm/s]	100000	100000	100000
Fracture strength coefficient c_N, c_T	0.22	0.22	0.22
Critical energy release rate coefficient m_N, m_T	0.0783	0.0783	0.0783
Upper limit critical energy release rate [N/mm]	2.5	12.5	2.5

The finite element model is a single cohesive element, and all the nodes on the back side are fixed, and a prescribed motion is applied at the nodes on the front side. The finite element model and prescribed motion are shown in the Figure 3.5. To have a better comparison, the prescribed motion is same for all the three cases. And to avoid velocity discontinuity, the displacement is made from Hanning window function because it has a smooth first order derivative, see Figure 3.6. The number of time step is 600, and the step size is 1×10^{-4} ms.

(a) (b)

Figure 3.5 (a) finite element model, (b) prescribed motion on front side

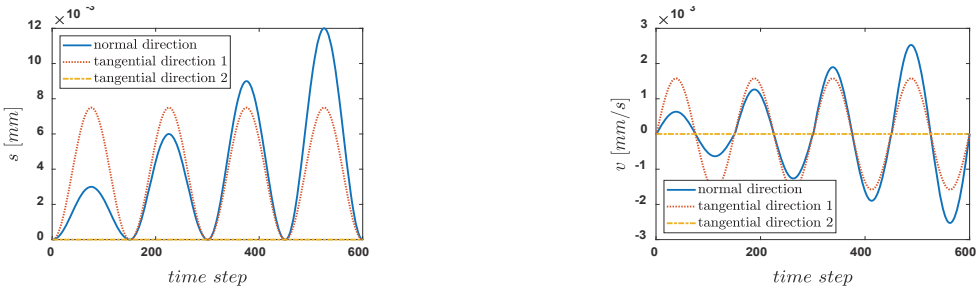

(a) (b)

Figure 3.6 (a) prescribed displacement load data, (b) velocity data

(1) Zero plastic strain model versus with plastic strain model

Zero plastic strain model is based on the maximum damage factor model, whereas with plastic strain model is based on the linear damage factor. Damage factor evolution is shown in Figure 3.7. Zero plastic strain model has monotonically increasing damage factor, and it is the maximum value of the current damage factor. However, with plastic strain model has maximum and minimum damage factors, and every time when the sign of traction changes, the damage factor becomes zero. From the first load cycle, damage factor in zero plastic strain model increases very fast and then is close to 1, but in with plastic strain model it increases much slower. This agrees with the damage factor shapes shown in Figure 3.1 (a). For zero plastic strain model, the cohesive element does not fail till to time step 600, but for with plastic strain model, the cohesive element fails at time step 474.

According to traction shown in Figure 3.8, the big difference between these two models are the sign and shape of traction. For the zero plastic strain model, because the separation of displacement load is always positive, the traction is always positive. However, for the with plastic strain model, because of the influence of plastic strain, there are negative traction even with positive separation. Another thing we can find is that for with plastic strain model, the cyclic displacement load would produce traction loop response, which agrees with experiment of plastic material under cyclic loading condition.

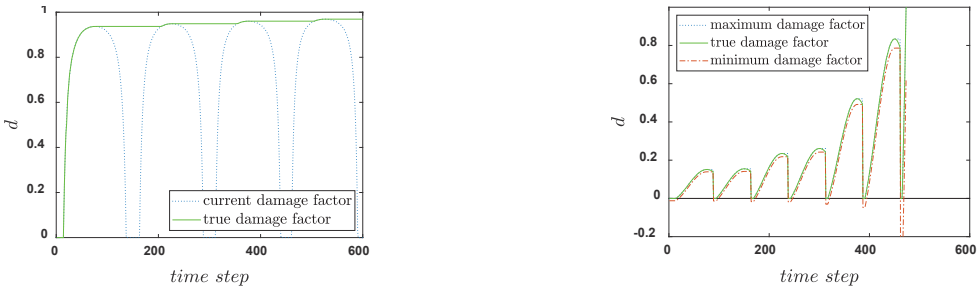

(a) (b)

Figure 3.7 Damage factor comparison, (a) zero plastic strain model, (b) with plastic strain model

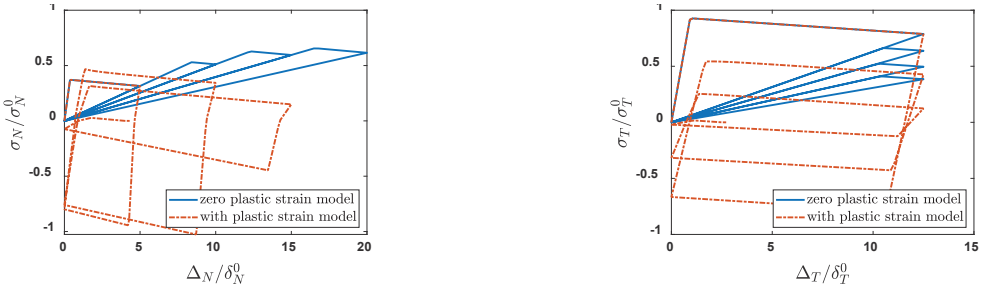

(a) (b)

Figure 3.8 Traction comparison between zero plastic strain model and with plastic strain model, (a) normal direction, (b) tangential direction

(2) With plastic strain model versus strain rate and plastic strain model

With plastic strain model is compared with the model that combines strain rate and plastic strain together, so this comparison shows the effect of strain rate. From Figure 3.9, the shape of damage factor for these two models are very similar because both have the update of bilinear cohesive law parameters, and the difference is that the cohesive element using strain rate and plastic strain model fails faster. One is at time step 474, and the other is at time step 347. From Figure 3.10, the traction response is also different. For with plastic strain model, the traction response is like a straight-line loop, and this is because for each cycle the mixed mode ratio is fixed. For strain rate and plastic strain model, because of the effect of strain rate, the bilinear cohesive law parameters are changing through the whole process, which makes the traction response much smoother. This smoother traction loop response agrees better with experiment of plastic material under cyclic loading condition.

Even though the cohesive element using strain rate and plastic strain model fails faster than the one using with plastic strain model, its consumed energy is larger. This can be seen from the traction in Figure

3.10, and under same displacement, the traction for strain rate and plastic strain model is larger. This difference is a good verification of critical energy release rate update equation and the positive critical energy release rate coefficient, m_N and m_T.

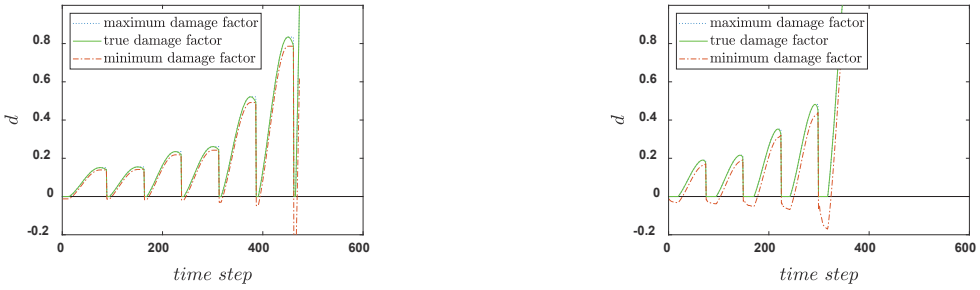

(a) (b)

Figure 3.9 Damage factor comparison, (a) with plastic strain model, (b) strain rate and plastic strain model

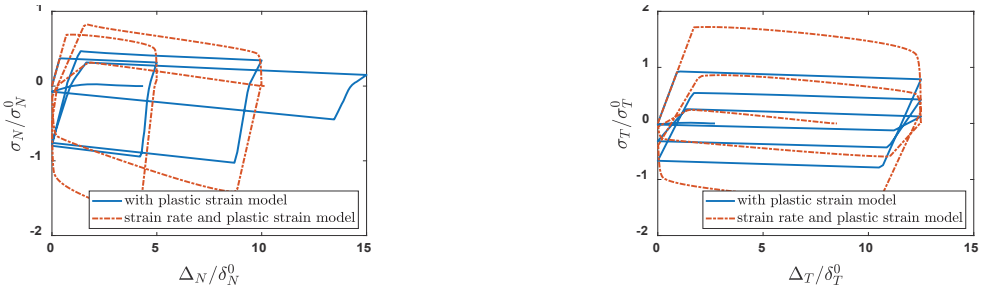

(a) (b)

Figure 3.10 Traction comparison between with plastic strain model & strain rate and plastic strain model, (a) normal direction, (b) tangential direction

(3) Comparison of three different damage factor models

To better explain this generalized damage factor model, damage factor and traction obtained from three typical damage factor models (convex, linear, and concave) are compared here. For the damage factor growth shown in Figure 3.11, convex damage factor increases fastest; linear damage factor is slower than that; the concave damage factor is the slowest. This difference agrees with the different damage factor shapes shown in Figure 3.1 (a). The time of failure is also different. The convex damage factor fails at time step 221; the linear damage factor fails at time step 437; the concave damage factor does not fail in this simulation, and its maximum damage factor is less than 0.1. This shows that different damage factor models can produce totally different evolution of damage factor and failure result.

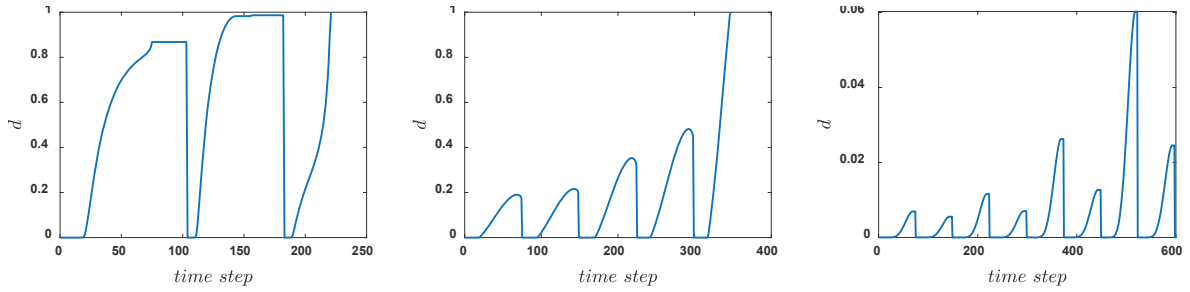

(a) (b) (c)

Figure 3.11 Damage factor comparison, (a) convex damage factor, (b) linear damage factor, (c) concave damage factor

The traction responses for different damage factor models also differ a lot, but all of them have a kind of loop traction because of the consideration of plastic strain. Look at the unloading part in the first loop (red rectangle) shown in Figures 3.12 and 3.13, the convex damage factor model has the smallest plastic strain, because it is closest to the maximum damage factor model (no plastic strain). For the three damage factor models, the plastic strain in normal direction in the first loop is $3.5\delta_N^0$, $4.9\delta_N^0$, and $5.0\delta_N^0$, respectively; the plastic strain in tangential direction in the first loop is $8.7\delta_T^0$, $12.3\delta_T^0$, and $12.3\delta_T^0$, respectively.

The plastic strain for linear damage factor model and concave damage factor model is larger and almost the same. This is because δ^0 6×10^{-4} mm is much smaller than δ^f 5×10^{-2} mm in this example, and then linear damage factor is very close to minimum damage factor. This similarity of plastic strain can be verified from Figure 3.1 (b). The conclusion here is that it should be careful to use linear damage factor model when δ^0 is much smaller than δ^f, because in this case the linear damage factor model could be almost a minimum damage factor model, which has the largest plastic strain that may overestimate the plasticity of a material.

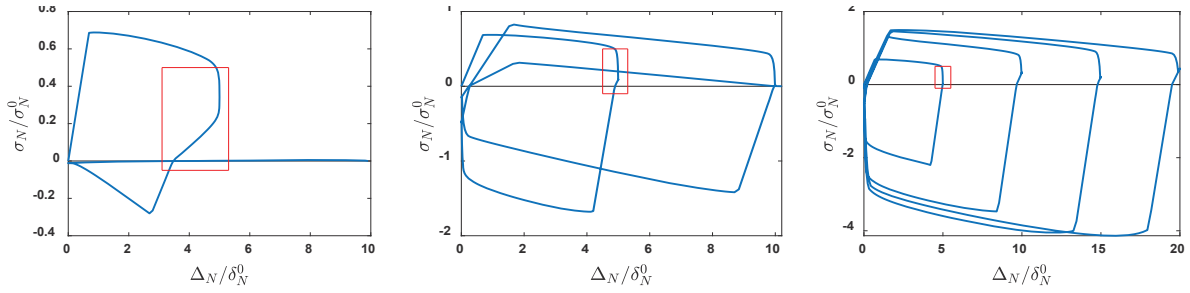

(a) (b) (c)

Figure 3.12 Normal traction comparison, (a) convex damage factor, (b) linear damage factor, (c) concave damage factor

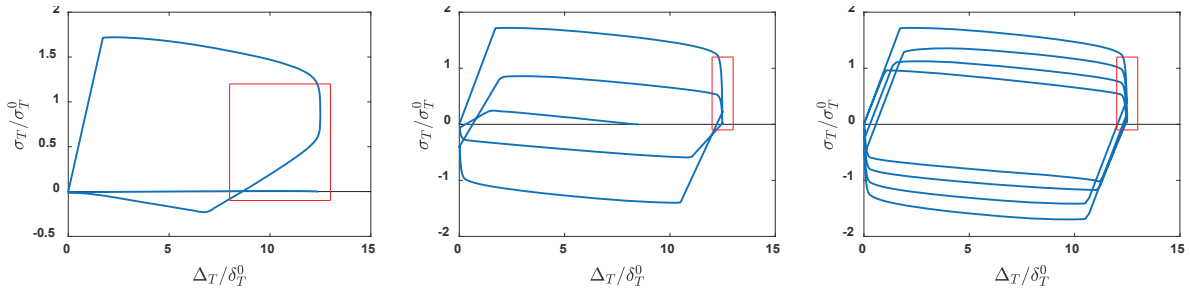

(a) (b) (c)

Figure 3.13 Tangential traction comparison, (a) convex damage factor, (b) linear damage factor, (c) concave damage factor

3.4.2 Mode I of tapered double cantilever beam

(1) Introduction of the TDCB test

This Tapered Double Cantilever Beam (TDCB) test is referred from [32,33], and it is used to verify the effects of strain rate, plastic strain, and variable damping. The dimensions and FEM model of tapered double cantilever beam are shown in Figure 3.14. Hexahedral element and triangular prism element with small element size 1 mm are used in the model, totally 58240 bulk elements and 890 cohesive elements. The adherend is steel 1.6358, which has high enough yield strength to guarantee purely elastic deformation in this experiment [33]. The adherent is crash-optimized adhesive Terokal 5077, and the relations between bilinear cohesive law parameters and strain rate are obtained from [33], see Equation (3.14) and Figure 3.15.

$$\begin{cases} E_N^0(\dot{\varepsilon}) = E_N^{ref} \\ \sigma_N^0(\dot{\varepsilon}) = \sigma_N^{ref} + \sigma_N^k(ln\dfrac{\dot{\varepsilon}}{\dot{\varepsilon_{min}}})^2 \\ G_{IC}^0(\dot{\varepsilon}) = G_{IC}^{ref} + \left(G_{IC}^{inf} - G_{IC}^{ref}\right)e^{-\frac{\dot{\varepsilon_{GIC}}}{\dot{\varepsilon}}} \end{cases} \tag{3.14}$$

where, E_N^{ref} is 5707 MPa/mm, σ_N^{ref} is 35.81 MPa, σ_N^k is 0.115 MPa, $\dot{\varepsilon_{min}}$ is 1.80 × 10^{-6} s^{-1}, G_{IC}^{ref} is 2610 J/m^2, G_{IC}^{inf} is 3630 J/m^2, and $\dot{\varepsilon_{GIC}}$ is 1.30 × 10^{-2} s^{-1}. The stiffness E_N^0 is of minor concern to crash simulations for Terokal 5077, and a constant value is used in simulations [33]. Its value is obtained from dividing the Young's modulus of Terokal 5077 by the thickness of adherent, 0.3 mm.

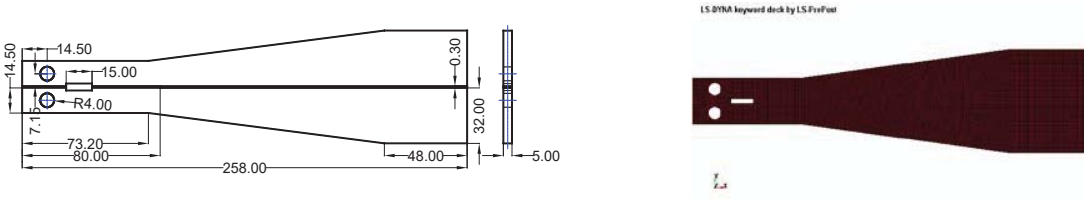

(a) (b)

Figure 3.14 (a) dimensions of TDCB, unit [mm], (b) FEM model of TDCB

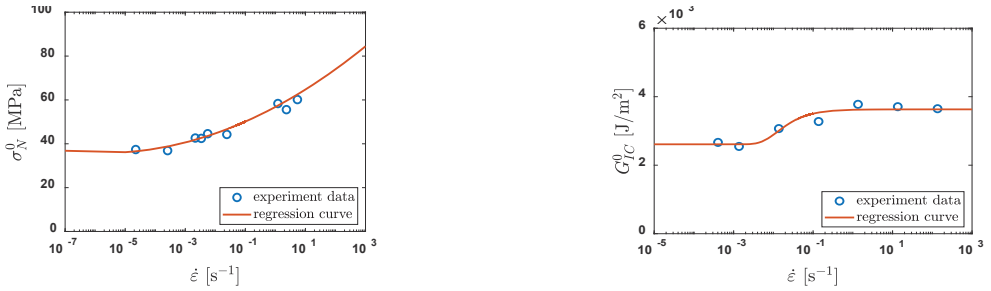

(a) (b)

Figure 3.15 (a) fracture strength versus strain rate [33], (b) critical energy release rate versus strain rate [33]

(2) Verification of strain rate and plastic strain in TDCB test

To verify the effect of strain rate, three different velocities, 6×10^{-4} mm/s, 1.7×10^{-1} mm/s, and 1.7×10^{2} mm/s, are applied in simulation [33]. For the lowest velocity 6×10^{-4} mm/s, the experiment takes about 4.6 hours, and it would take much more time in explicit simulation. To save time, a conversion from velocity to strain rate is obtained from numerical simulations in [33], see Equation (3.15), and the converted strain rate is used to get bilinear cohesive law parameters for each velocity case. This means that bilinear cohesive law parameters used in this Section 3.4.2 are constants. Table 3.2 shows the obtained parameters. To simplify the problem, double bilinear model parameters in negative Mode I are 5 times of that in Mode II.

$$\frac{v_{test}}{\dot{\varepsilon}} = 1.46 \text{ mm [33]} \tag{3.15}$$

Table 3.2 Bilinear cohesive law parameters for TDCB test

Velocity [mm/s]	Strain Rate [s^{-1}]	Stiffness [MPa/mm]	Fracture Strength [MPa]	Critical Energy Release Rate [J/mm^2]
6.0×10^{-4}	4.10×10^{-4}	5707	39.2	2610
1.7×10^{-1}	1.16×10^{-1}	5707	49.9	3580
1.7×10^{2}	1.16×10^{2}	5707	73.0	3630

Here, force-displacement curves obtained from maximum damage factor model (no plastic strain) for

the three cases are shown in Figure 3.16 (a). It can be seen that peak force is influenced by strain rate. Peak force for 6×10^{-4} mm/s case is about 920 N, but it is about 1090 N for 1.7×10^{-1} mm/s and 1.7×10^{2} mm/s cases.

Another effect is plastic strain. Experiment results and simulation results obtained from different damage factor models are shown in Figures 3.16 (b), 3.16 (c), and 3.16 (d). The big difference happens in the unloading part. For the maximum damage factor model, it does not have any residual plastic deformation after unloading; for the linear damage factor model [33], it has largest residual plastic deformation, but it does not agree well with experiment results; for the convex damage factor model, the residual plastic deformation is very close to experiment results. After residual plastic deformation is obtained, the error of this deformation with respect to experiment results can be calculated, as shown in Table 3.3. For the linear damage factor model, the residual plastic deformations for the three cases are all larger than experiment results, and the percentage error can be as high as 102.88%. however, for convex damage factor model, this percentage error can be as low as about 4%.

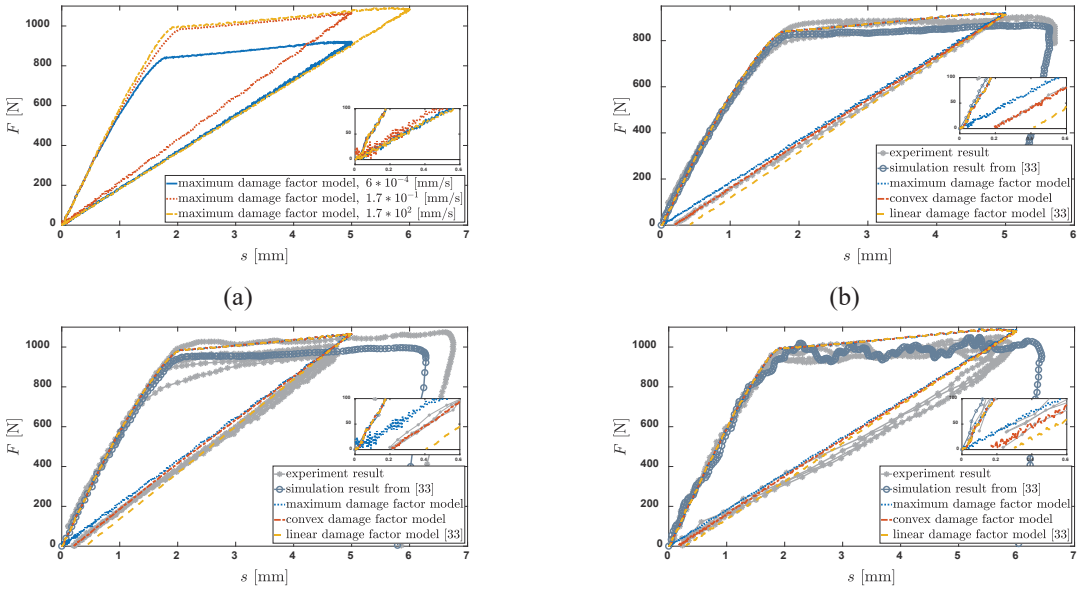

(a) (b)

(c) (d)

Figure 3.16 Force-displacement curve, (a) three velocities without plastic strain, (b) 6×10^{-4} mm/s case, (b) 1.7×10^{-1} mm/s case, (c) 1.7×10^{2} mm/s case

Table 3.3 Comparison of residual plastic deformation between experiment and simulation

Velocity [mm/s]	Exp. Plastic Deformation [mm]	Sim. Plastic Deformation (linear) [mm]	Error of Plastic Deformation (linear) [%]	Sim. Plastic Deformation (convex) [mm]	Error of Plastic Deformation (convex) [%]
6.0×10^{-4}	0.208	0.422	102.88	0.211	1.44
1.7×10^{-1}	0.217	0.413	90.32	0.209	-3.69
1.7×10^{2}	0.172	0.299	73.84	0.177	2.91

(3) Verification of variable damping in TDCB test

To truly verify strain rate effect, the update of bilinear cohesive law parameters in this section is based on the strain rate at each time step, which is different from the above where cohesive law parameters are constants. Considering the time needed in simulation is much longer than that in experiment, only the 1.7×10^{2} mm/s case is investigated here, which takes about 70 ms for the experiment. It would take 4.6 hours and 70 s to conduct the experiment for 6×10^{-4} mm/s and 1.7×10^{-1} mm/s cases, respectively.

The first method to decrease oscillation is about how to update bilinear cohesive law parameters. There are two ways to update: parameters are always updated before cohesive element fails, or parameters are only updated before the initiation of damage, and then the parameters are fixed. [33] suggests that the second one could increase numerical stability, but no numerical study is presented to verify. Here, these two ways to update parameters are investigated and results are shown in Figure 3.17 (a). As we can see, because of the high velocity 1.7×10^{2} mm/s and oscillation in cohesive elements, bilinear cohesive law parameters change dramatically before it fails, and this makes the force-displacement curve oscillate very much. However, the second way that updates only before the damage initiation can still capture the force-displacement curve well, and the oscillation decreases a lot.

Apart from the way to update cohesive law parameters, the high stiffness in cohesive element can also introduce some oscillations. As shown in Figure 3.17 (b), there are still some small oscillations in the force-displacement curve for the case without damper, but after the proposed variable damper is coupled into the bilinear cohesive law, the oscillation is further damped. Based on dozens of numerical simulations, 0.5 MPa/(mm/s) is chosen as the best damping coefficient in this example. A better way to determine this

damping coefficient could be from frequency analysis of stress oscillation.

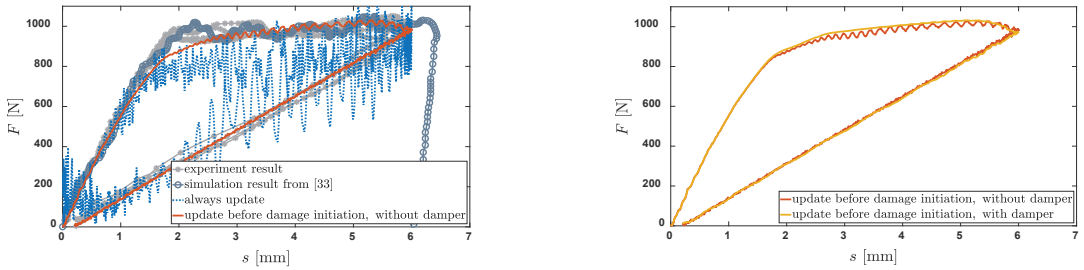

(a) (b)

Figure 3.17 (a) comparison of different ways to update bilinear cohesive law parameters, (b) comparison between without damper and with damper

Different from a constant damper, the case with damper in Figure 3.17 (b) is a variable damper, where two variables proposed in Section 3.3 are used to remove discontinuous force at the start and end of bilinear cohesive law. To show the effect of these two variables on removing discontinuous force, force-displacement curves obtained from a variable damper with start discontinuity and a damper with end discontinuity are compared in Figure 3.18. Oscillation is observed at the beginning of force-displacement curve in Figure 3.18 (a), but this oscillation is not observed in Figure 3.18 (b) where the damper only has end discontinuity. The reason could be that at the start of a bilinear cohesive law or when the separation is very small, the traction from the "original bilinear cohesive law" is very small, but the traction from a constant damper can be very large because this traction is only related to strain rate. And this huge traction from the constant damper can influence the correct response of cohesive element. Oscillation is also observed during the loading process for both cases. Totally speaking, the dampers with start and end force discontinuities both lead to incorrect simulation results, and the two variables proposed in this dissertation can remove this discontinuous force and ensures correct force response.

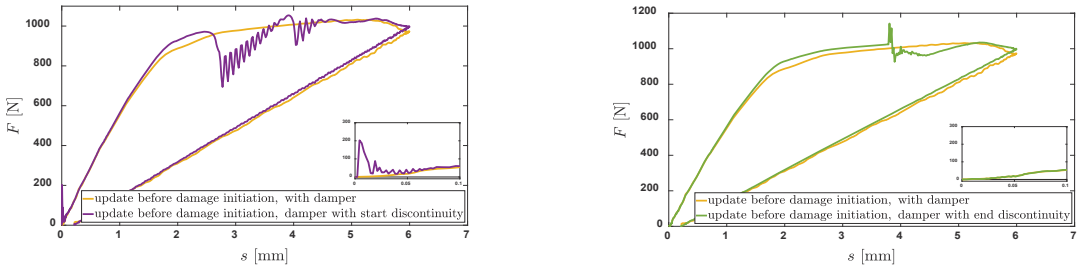

(a) (b)

Figure 3.18 Comparison of force-displacement curve, (a) damper with start discontinuity, (b) damper with end discontinuity

3.4.3 PMMA plate under tensile load

(1) Introduction of the PMMA test

PMMA test is originally reported in [91,92], and the specimen is shown in Figure 3.19. Two steps are needed for this experiment. First, a universal test machine loads the specimen in tension at a load level ΔH on top and bottom sides. The strain energy per unit area U stored in the pre-strained plate is calculated from Equation (3.16) [91]. Second, a small sharp crack is initiated at middle point of the specimen by a razor. Then the small crack propagates straight across the specimen. By changing the load level, different values of elastic strain energy can be obtained. In the simulation, L is 32 mm; H is 16 mm; W is 0.5 mm; l is 4 mm; h is 0.4 mm. ΔH is 0.08 mm, 0.10 mm, 0.12 mm, and 0.14 mm. The corresponding strain energy per unit area are 2472 N/m, 3863 N/m, 5562 N/m, and 7571 N/m, respectively. The characteristic of the dynamic fracture has been well presented in [91]: at low load level there is a main crack with some small local branching; at high load level there are main crack, sub-crack, and some local branching, see Figure 3.20.

(a) (b)

Figure 3.19 (a) dimensions of PMMA plate, (b) FEM model of PMMA plate

$$U = \frac{1}{2}\frac{E(2\Delta H)^2}{H} = \frac{2E(\Delta H)^2}{H} \tag{3.16}$$

(a)

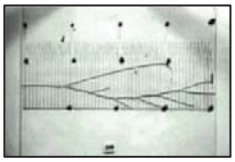

(b)

Figure 3.20 (a) main crack with some small local branching [91], (b) main crack, sub-crack and some local branching [91]

Different from paper [91,93] where implicit static and explicit dynamic analysis are used together, the simulation in this dissertation is a fully explicit dynamic analysis. To simulate the initiation of crack propagation, Single-Point-Constraint (SPC) is applied to the first cohesive element at the 4 mm long edge crack, and this SPC is released at 4 ms (1.5 ms is for stabilizing the model after loading), see Figure 3.21 (a). To make sure that this first cohesive element would fail right after the release of SPC, a small critical energy release rate is used in this individual cohesive element. Lower order triangular prism element with 0.25 mm size is used in simulation, totally 22691 bulk elements and 33829 cohesive elements.

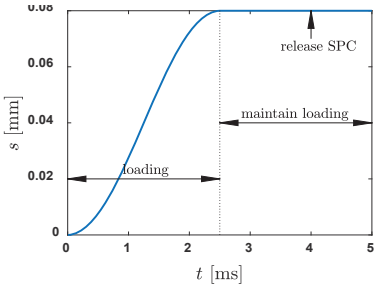

(a)

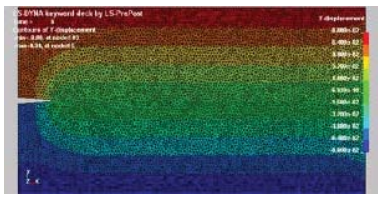

(b)

Figure 3.21 (a) prescribed boundary condition, (b) y displacement result at 4 ms in finite element model

(2) Verification of constitutive law, artificial compliance, and strain rate in PMMA test

Three different constitutive laws are compared. The first one is from [91] where an extrinsic bilinear cohesive law is used; the second one is from [93] where a trapezoidal cohesive law is used with Distinct Lattice Spring Method (DLSM); the third one is the proposed double bilinear model in this dissertation, see Figure 3.22. There are many papers where trapezoidal cohesive law is used in simulation to investigate plastic strain, and the plastic strain of PMMA is also presented in many papers [94]. Considering that plastic strain is not significant in PMMA, a convex damage factor model with small plastic strain is used here. Note that the first two constitutive laws only have positive quadrant in the publications.

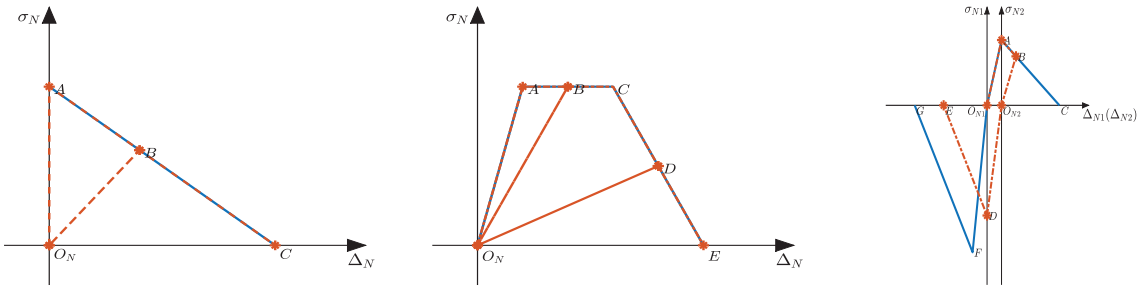

(a) (b) (c)

Figure 3.22 Comparison of constitutive law, (a) extrinsic bilinear cohesive law [91], (b) trapezoidal cohesive law [93], (c) proposed double bilinear model

The material parameters for PMMA are: Young's modulus E 3090 MPa, Poisson's ratio ν 0.35, density ρ 1180Kg/m^3, and fracture strength σ^0 75 MPa. For cohesive element, stiffness and fracture strength are constants because these two parameters do not change too much in experiment [91]. To consider the influence of strain rate, separation at the end of softening part δ^f is velocity dependent in [91], see Equation (3.17). δ^{f0} is static value of critical crack opening distance, 0.008 mm; $\dot{\delta}^0$ is scaling crack opening rate, 5 mm/s; $\dot{\delta}$ is velocity between the opposite surfaces in cohesive element.

$$\delta^f = \delta^{f0}\left[1 + \left(\frac{\dot{\delta}}{\dot{\delta}^0}\right)^2\right] \tag{3.17}$$

Even though all parameters can be obtained from [91], it is still necessary to investigate the stiffness of cohesive element for the FEM model in this dissertation. Here, three different stiffness are investigated in simulation, $1E/l_b$, $10E/l_b$, and $20E/l_b$, as shown in Figure 3.23. From the stress wave, the decrease of effective stiffness for the three cases are 47.61%, 10.95%, and 3.10% of bulk element stiffness, respectively. And $20E/l_b$ is high enough to control artificial compliance in an acceptable range. It is also found that the amplitude of stress wave is influenced by stiffness. The higher the stiffness, the closer to bulk element only case. To consider a larger fracture toughness under compressive load, the static critical energy release rate in negative Mode I is 3 times of that in Mode II, see Table 3.4.

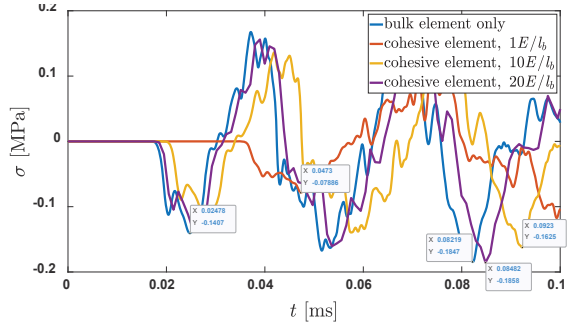

Figure 3.23 The influence of stiffness on stress wave propagation in PMMA test

Table 3.4 Bilinear cohesive law parameters for PMMA test

Parameter	Positive Mode I	Negative Mode I	Mode II
Stiffness [MPa/mm]	247200	247200	91556
Fracture strength [MPa]	75	75	75
Static critical energy release rate [N/mm]	0.3	0.9	0.3

The fracture results obtained from the proposed double bilinear model are shown in Figure 3.24. The history variable in these figures is damage factor. When strain rate is considered, the fracture paths follow the patterns found in experiment. Compared with the experiment fracture shown in Figure 3.20 (b) at highest load level, Figure 3.24 (d) with main crack and sub-crack is almost same with experiment. In [91], local branching is not clear, and small fragmentations in the simulation are not found in experiment. In [93], DLSM modal is a node-based model and almost perfect symmetric, and then the fracture result obtained is also symmetric, which does not agree with experiment result. The distribution of bulk triangle prism elements in CZM is not symmetric along the center line, and CZM is a mesh-dependent method, which make the simulation result not symmetric and can capture the main crack and sub-crack.

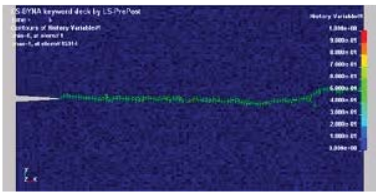

(a)

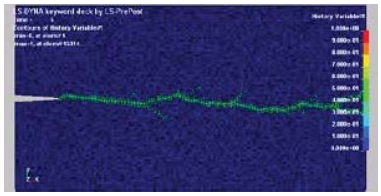

(b)

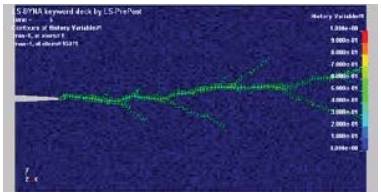

(c)

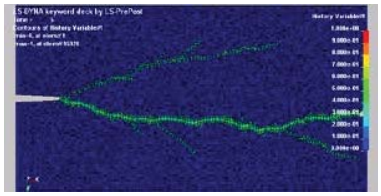

(d)

Figure 3.24 Damage factor results [0,1] considering strain rate, (a) 0.08 mm case, (b) 0.10 mm case, (c) 0.12 mm case, (d) 0.14 mm case

Another important thing is crack velocity in this experiment. The crack velocity versus strain energy per unit area from [91] is plotted in Figure 3.25. With the increase of this energy density (per unit area), the crack velocity increases fast and almost convergences at high energy density. For the simulation, because the artificial compliance cannot be removed, crack velocity is slower than experiment even with higher stiffness $20E/l_b$ case. From this comparison, it is necessary to check artificial compliance when using cohesive element in simulation.

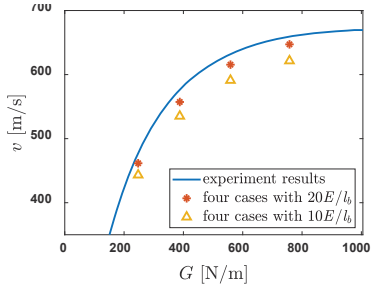

Figure 3.25 Crack velocity versus stored energy per unit area

When strain rate is not considered, a single main crack is found for all the four loading levels even with same FEM model, as shown in Figure 3.26, which is totally different from the experiment results. From this comparison, strain rate must be considered into this simulation.

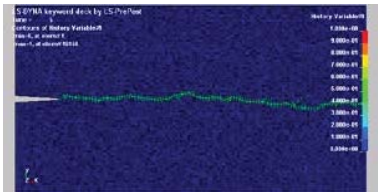

(a)

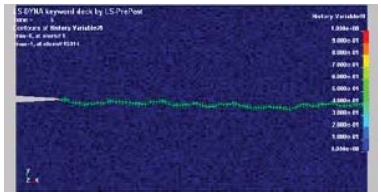

(b)

(c) (d)

Figure 3.26 Damage factor results [0,1] without considering strain rate, (a) 0.08 mm case, (b) 0.10 mm case, (c) 0.12 mm case, (d) 0.14 mm case

3.4.4 Kalthoff block under impact load

(1) Introduction of Kalthoff test

Kalthoff test is investigated by Kalthoff in 2000 [95]. High strength maraging steel X2 NiCoMo 1895 shows a failure mode transition: failure occurs by tensile cracks at low rate; failure by adiabatic shear bands is observed at higher rate above a certain limit velocity. A block with two symmetric initial cracks is impacted by a projectile with initial speed to make the block have tensile failure. This test has been used by many researchers for fracture propagation verification [96,97]. However, the models used in these papers are all simplified as 2D models, and this is different from the experiment. In this dissertation, some interesting findings are observed by using 3D model, and the stress obtained from 3D model can show the difference between different constitutive laws in bilinear cohesive law. Dimensions and FEM model of the specimen are shown in Figure 3.27. Due to the symmetry of the plate and boundary condition, only half of the block is modelled.

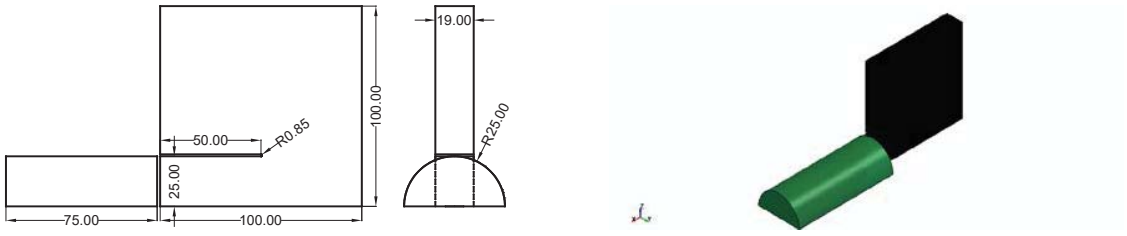

(a) (b)

Figure 3.27 (a) dimensions of Kalthoff steel block, unit [mm], (b) FEM model of Kalthoff steel block

(2) Verification of constitutive law, artificial compliance, and variable damping in Kalthoff test

The comparison here is between constant stiffness model and double bilinear model, as shown in Figure 3.28. In the proposed double bilinear model, a convex damage factor model is used to consider the

effect of plastic strain. Lower order tetrahedron meshes with 1, 2, and 3 mm size are used in simulation. For 1 mm case, it contains 1,367,727 bulk elements and 2,695,244 cohesive elements.

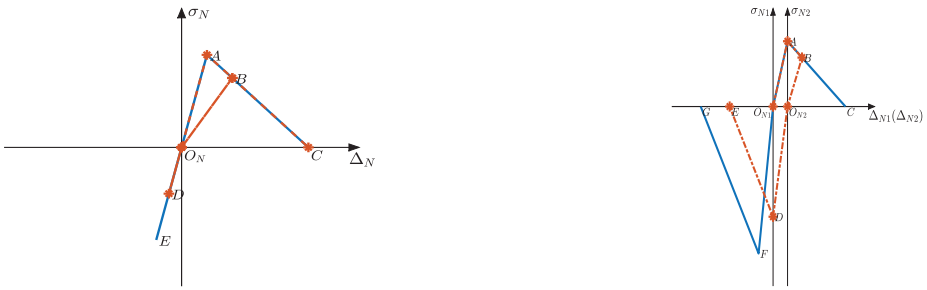

(a) (b)

Figure 3.28 Comparison of constitutive law, (a) constant stiffness model [97], (b) proposed double bilinear model

Like PMMA test, artificial compliance is also checked to select proper stiffness. Here, four different stiffness are investigated in 1 mm size model, $1E/l_b$, $10E/l_b$, $20E/l_b$, and $50E/l_b$, as shown in Figure 3.29. Different from Figure 3.23, this simulation shows that the higher the stiffness, the smaller the stress, but same thing is that the stress wave is closer to bulk elements only case when stiffness increases. From the stress wave, the decrease of effective stiffness for the four cases are 48.63%, 10.25%, 5.60%, and 2.39% of bulk element stiffness, respectively. And $50E/l_b$ is high enough to control artificial compliance in an acceptable range. Considering cohesive law parameters under different strain rates are not available, the parameters used in this simulation are constants. The main point here is to compare constitutive law. The material property of the steel block [87]: Young's modulus E 190 GPa, Poisson's ratio ν 0.3, density ρ 8000 Kg/m^3, and Mode I stress intensity factor K_I 68 MPa$\sqrt{}$m, see Table 3.5.

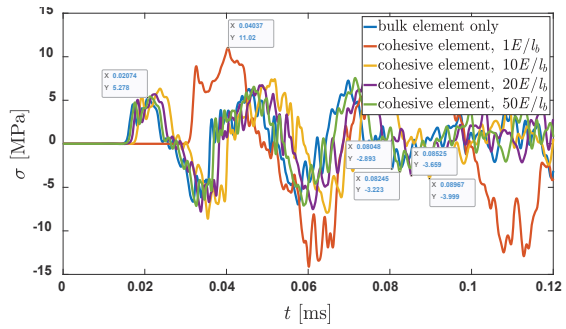

Figure 3.29 The influence of stiffness on stress wave propagation in Kalthoff test

Table 3.5 Bilinear cohesive law parameters for Kalthoff test

Parameter	Positive Mode I	Negative Mode I	Mode II
Stiffness [MPa/mm]	9500000	28500000	3653846
Fracture strength [MPa]	2100	6300	2100
Static critical energy release rate [N/mm]	24.33	121.65	72.99

In Figures 3.30 and 3.31, simulations with different element size have almost same fracture path, and the 70 degrees line found in experiment [95] is plotted as a reference. Generally speaking, three simulations capture the fracture path along the 70 degrees line correctly. The fracture path for 1 mm case is better than 2 mm and 3 mm cases. The reason is that if the bulk elements size is too large, the potential fracture path determined by bulk elements is not able to capture free fracture propagation perfectly. The fracture path obtained from Smoothed Particle Hydrodynamics method in [97] is also plotted. However, its fracture path is more like a curve, not a straight line found in experiment, and some extra fracture at the left side of the block does not shown in experiment.

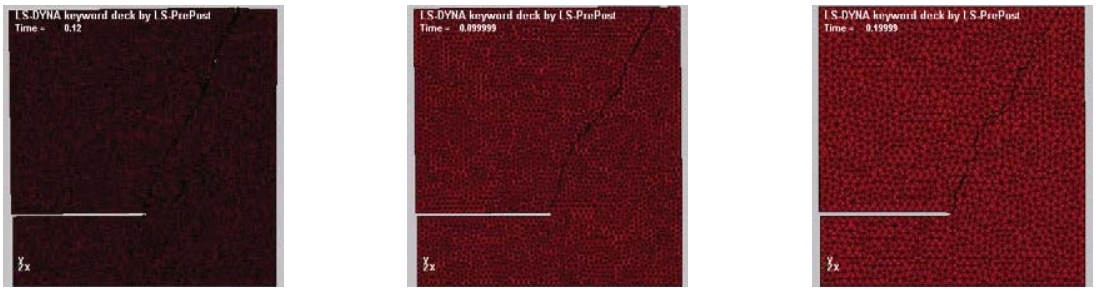

(a) (b) (c)

Figure 3.30 Simulation results using tetrahedron mesh (failed cohesive elements are deleted), (a) 1 mm case, (b) 2 mm case, (c) 3 mm case

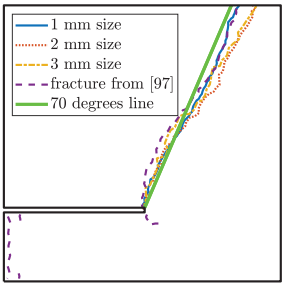

Figure 3.31 Comparison of fracture path between [97] and proposed double bilinear model

Apart from fracture path, another meaningful comparison is the stress, which is a topic few mentioned

in other papers. The stress at same cohesive element along the fracture path but from different constitutive law are compared. For constant stiffness model (an uncoupled model) result in Figure 3.32 (a), when normal traction is negative, normal stress changes independently and dramatically without the restraint of tangential stress. This kind of oscillation is not reasonable, and it is only because of the constitutive law used. However, for double bilinear model result in Figure 3.32 (b), it is more stable and reasonable. The second comparison is damping. After introducing variable damping, the stress oscillation is much alleviated, see Figure 3.33.

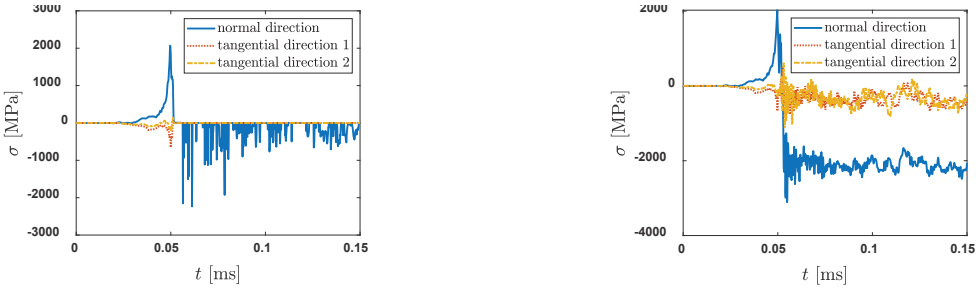

(a) (b)

Figure 3.32 Comparison of stress, (a) constant stiffness model, (b) double bilinear model

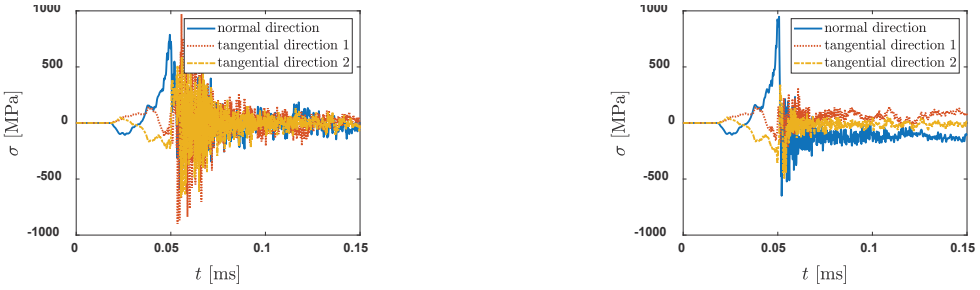

(a) (b)

Figure 3.33 Comparison of stress, (a) constant stiffness model without damping, (b) double bilinear model with variable damping

Another difference because of the variable damping is from the detached fragments along the fracture path, as shown in Figure 3.34. After introducing a variable damper, the new model has less detached fragments and can avoid excessive cohesive element deletion compared with the constant stiffness model. The proposed double bilinear model in this dissertation agrees with the experiment better.

(a) (b)

Figure 3.34 Comparison of detached fragments, (a) constant stiffness model without damper, (b) double bilinear model with variable damper

4 Phase field modeling of brittle fracture

In this section, phase field model for brittle fracture is investigated. Geometric function and degradation function are investigated separately to solve the nonlinearity and inelasticity in the stress-strain curve of classical phase field model. First, by using a generalized quadratic geometric function and applying phase zeroing, nonlinearity and inelasticity can be completely removed, and a good thing is that this still leads to a linear FEM problem. Second, instead of using a second order degradation function, some higher order degradation functions with more constrains could give more options for stress-strain curve. However, higher order degradation function leads to a nonlinear FEM problem, and Newton-Raphson method is used to solve this nonlinear problem. Both methods proposed in this dissertation work well for brittle materials.

4.1 Background of phase field model

4.1.1 Crack surface density function and fracture energy

Griffith's theory states that a crack propagates when the reduction in potential energy due to crack growth is equal to or greater than the increase in surface energy due to the creation of new free surfaces, which is applicable to elastic materials that fracture in brittle fashion. The difficult that limits the numerical application of this theory is how to calculate fracture length and area. To bypass this difficult, line integral and surface integral have been transformed into volume integral. In [43,48], fracture surface of a 1D case is investigated in sequence through an assumed phase field function $\varphi(x) \rightarrow$ homogeneous differential equation $\rightarrow$ Euler-Lagrange equation L. Since this process is clear in [43], it is ok to do this backward from Euler-Lagrange equation

$$L = \int_{\Omega} [\alpha(\varphi) + l^2(\varphi')^2]\mathrm{d}V\,, \tag{4.1}$$

where, $\alpha(\varphi)$ is called geometric function in some papers [50,54]; l is a parameter called length scale to adjust the crack band of phase field. For a 1D case, fracture surface Γ is the cross-section of a bar and a constant, and any small $\mathrm{d}V$ can be expressed as $\Gamma \mathrm{d}x$. Put $\mathrm{d}V = \Gamma \mathrm{d}x$ into Equation (4.1), the relation between L and Γ can be obtained as

$$L = \int_{\Omega} [\alpha(\varphi) + l^2(\varphi')^2]\,\Gamma \mathrm{d}x = c\Gamma. \tag{4.2}$$

Combining Equation (4.1) and Equation (4.2), fracture surface Γ can be expressed as

$$\Gamma = \frac{1}{c}L = \int_{\Omega} \frac{1}{c}[\alpha(\varphi) + l^2(\varphi')^2]\mathrm{d}V = \int_{\Omega} \gamma \mathrm{d}V\,, \tag{4.3}$$

where, c is a constant to act on Euler-Lagrange equation L to get correct fracture surface, but the c here contains length scale parameter, i.e., $c = \tilde{c}l$. The $\tilde{c}$ is equal to the constant in [54] that not containing length scale parameter

$$c = \int_{\Omega} [\alpha(\varphi) + l^2(\varphi')^2]\,\mathrm{d}x = \tilde{c}l; \tag{4.4}$$

the integrand in Equation (4.3) is called as crack surface density function γ. To get this constant c, homogeneous differential equation should be obtained from Euler-Lagrange equation L first, and phase field function should be obtained by solving the homogeneous differential equation. Next, put phase field function $\varphi(x)$ into Equation (4.4) and do the integration, then c can be obtained. For example, if $\alpha(\varphi)$ is φ^2, homogeneous differential equation is obtained as $\varphi - l^2\varphi'' = 0$; $\varphi(x)$ is solved as $e^{-|x|/l}$; c is obtained as $2l$; γ is obtained as $[\varphi^2 + l^2(\varphi')^2]/2l$; which is the one used in the classical phase field model in [43]. For the description of a fracture state at location $x = 0$, the comparison between non-smooth phase field and diffusive phase field obtained from the classical phase field model is shown in Figure 4.1.

(a) (b)

Figure 4.1 (a) non-smooth phase field, (b) diffusive phase field with length scale l

This 1D case can be extended into 2D and 3D cases as

$$\gamma = \frac{1}{c}[\alpha(\varphi) + l^2|\nabla\varphi|^2], \tag{4.5}$$

where, $\nabla\varphi$ is $\left(\frac{\partial\varphi}{\partial x}, \frac{\partial\varphi}{\partial y}\right)$ or $\left(\frac{\partial\varphi}{\partial x}, \frac{\partial\varphi}{\partial y}, \frac{\partial\varphi}{\partial z}\right)$. According to Griffith's theory, the energy needed for developing

fracture surface Γ is expressed as

$$\Psi_c = G_c\Gamma = G_c \int_{\Omega} \mathrm{d}A \approx G_c \int_{\Omega} \gamma \mathrm{d}V\,, \tag{4.6}$$

where, G_c is critical energy release rate or fracture toughness of a material with unit N/mm.

4.1.2 Derivation of the governing equations of phase field model

Since fracture energy is defined, governing equations of phase field model can be derived. Consider an arbitrary body $\Omega \subset \mathbb{R}^{dim}$ $(dim = 1, 2, 3)$ with external boundary $\partial\Omega \subset \mathbb{R}^{dim-1}$ and sharp crack set $\Gamma \subset \mathbb{R}^{dim-1}$. During the time interval $[0, T]$ of interest, displacement at position $\boldsymbol{x}$ and time t is denoted by $\boldsymbol{u}(\boldsymbol{x}, t)$. The external boundary is divided into time-dependent Dirichlet boundary $\partial\Omega_u$ and time-dependent Neumann boundary $\partial\Omega_t$ with outward normal vector $\boldsymbol{n}$. Prescribed time-dependent displacement $\boldsymbol{u}^p$ and surface traction $\boldsymbol{t}^p$ are applied on $\partial\Omega_u$ and $\partial\Omega_t$, respectively, i.e., $\boldsymbol{u}(\boldsymbol{x}, t) = \boldsymbol{u}^p(\boldsymbol{x}, t)$ on $\partial\Omega_u$ and $\boldsymbol{\sigma} \cdot \boldsymbol{n} = \boldsymbol{t}^p(\boldsymbol{x}, t)$ on $\partial\Omega_t$, where $\boldsymbol{\sigma}$ is symmetric Cauchy stress tensor. For simplicity, $\partial\Omega_u$ and $\partial\Omega_t$ satisfy $\partial\Omega_u \cup \partial\Omega_t = \partial\Omega$ and $\partial\Omega_u \cap \partial\Omega_t = \emptyset$. The sharp crack has outward normal vector $\boldsymbol{n}_c$. Body force $\boldsymbol{b}$ is distributed in the entire body Ω. For small deformation, the body is described by its displacement field $\boldsymbol{u}(\boldsymbol{x}, t)$ and strain field $\boldsymbol{\varepsilon}(\boldsymbol{x}, t) = \nabla^{sym}\boldsymbol{u}(\boldsymbol{x}, t)$, where symmetric gradient operator ∇^{sym} maps displacement field to strain field. For phase field, time-dependent Dirichlet boundary is $\varphi(\boldsymbol{x}, t) = 1$ on $\partial\Omega_\Gamma$, where $\partial\Omega_\Gamma$ is fracture surface, and the flux of phase field through the external boundary is 0, i.e., $\nabla\varphi \cdot \boldsymbol{n} = 0$. The schematic of displacement field and phase field is shown in Figure 4.2.

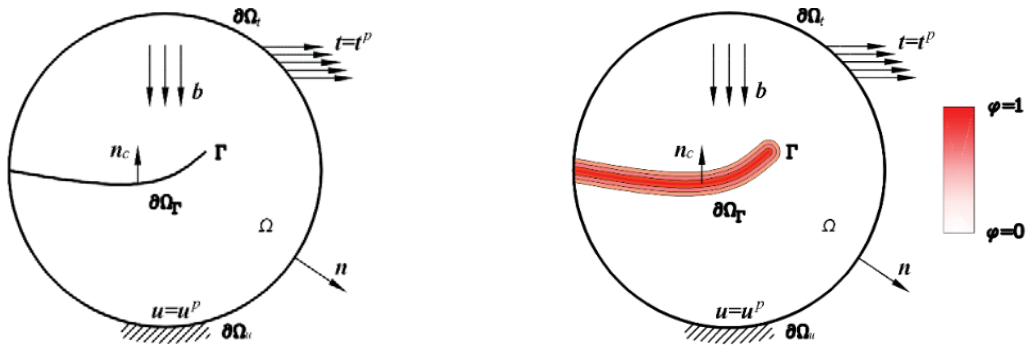

(a) (b)

Figure 4.2 (a) displacement field, (b) phase field

The variational principle used for dynamic problem is called Hamilton's principle. According to this principle, the variation of energy functional is taken with respect to time as

$$\delta \int_{t_1}^{t_2} \left(\Psi_{kin} - \Psi_{pot} + \Psi_{ext}\right) \mathrm{d}t = 0, \tag{4.7}$$

where, kinetic energy, potential energy, and external work are expressed as

$$\Psi_{kin}(\dot{\boldsymbol{u}}, \dot{\varphi}) = \int_{\Omega} \frac{1}{2} \rho \dot{\boldsymbol{u}} \cdot \dot{\boldsymbol{u}} \mathrm{d}V + \int_{\Omega} \frac{1}{2} \varrho \dot{\varphi} \dot{\varphi} \mathrm{d}V\,, \tag{4.8}$$

$$\Psi_{pot}(\boldsymbol{u}, \Gamma) \approx \int_{\Omega} \psi_s \mathrm{d}V + \int_{\Omega} G_c \gamma \mathrm{d}V\,, \tag{4.9}$$

$$\Psi_{ext}(\boldsymbol{u}) = \int_{\partial\Omega} \boldsymbol{t} \cdot \boldsymbol{u} \mathrm{d}A + \int_{\Omega} \boldsymbol{b} \cdot \boldsymbol{u} \mathrm{d}V\,, \tag{4.10}$$

respectively. Note that a generalized kinetic energy is presented here, where coefficient ϱ with unit Kg/m is used to describe the kinetic energy from phase field [50]. Generalized Euler-Lagrange equation L is expressed as

$$L = \Psi_{kin} - \Psi_{pot} + \Psi_{ext}, \tag{4.11}$$

and the minimization of this generalized Euler-Lagrange equation L gives the unknowns wanted, i.e.,

$$(\boldsymbol{u}, \varphi) = \mathrm{ArgInf}\{L\}. \tag{4.12}$$

To consider the degradation of stress with the increase of phase, strain energy ψ_s^0 is multiplied with a degradation function $g(\varphi)$,

$$\psi_s = g(\varphi)\psi_s^0, \tag{4.13}$$

where, superscript 0 in ψ_s^0 is used to differentiate undegraded and degraded strain energy. However, it is also found that a degradation function on the whole strain energy cannot avoid fracture under compressive load [57]. To solve this issue, usually, the strain energy is split into two parts, and only one of them is influenced by degradation function. In this dissertation, tensile and compressive strain energy split is used, and degradation function is only applied to tensile strain energy as

$$\psi_s = g(\varphi)\psi_s^{0+} + \psi_s^{0-}. \tag{4.14}$$

Based on the definition of positive and negative strain energy from the spectral decomposition of strain tensor, strain matrix at position $\boldsymbol{x}$ and time t is expressed as its eigen value ε_i and eigen vector $\boldsymbol{n}_i$,

$$\boldsymbol{\varepsilon}(\boldsymbol{x},t) = \nabla^{sym}\boldsymbol{u}(\boldsymbol{x},t) = \sum_{i=1}^{3} \varepsilon_i \, \boldsymbol{n}_i \otimes \boldsymbol{n}_i, \tag{4.15}$$

where, $\otimes$ is tensor product of vectors. The strain energy and its tensile and compressive parts are expressed as

$$\psi_s^0 = \frac{1}{2}\sigma_{ij}^0 \varepsilon_{ij} = \frac{\lambda}{2}(\varepsilon_1 + \varepsilon_2 + \varepsilon_3)^2 + \mu(\varepsilon_1^2 + \varepsilon_2^2 + \varepsilon_3^2), \tag{4.16}$$

$$\psi_s^{0\pm} = \frac{1}{2}\sigma_{ij}^{0\pm} \varepsilon_{ij}^{\pm} = \frac{\lambda}{2}\langle \varepsilon_1 + \varepsilon_2 + \varepsilon_3 \rangle_{\pm}^2 + \mu\left(\langle \varepsilon_1 \rangle_{\pm}^2 + \langle \varepsilon_2 \rangle_{\pm}^2 + \langle \varepsilon_3 \rangle_{\pm}^2\right), \tag{4.17}$$

where, λ and μ are elastic constants; Macaulay brackets $\langle \bullet \rangle_+$ and $\langle \bullet \rangle_-$ mean

$$\langle \varepsilon_i \rangle_+ = \begin{cases} 0, & \varepsilon_i \le 0 \\ \varepsilon_i, & \varepsilon_i > 0 \end{cases}, \tag{4.18}$$

$$\langle \varepsilon_i \rangle_- = \begin{cases} \varepsilon_i, & \varepsilon_i \le 0 \\ 0, & \varepsilon_i > 0 \end{cases}. \tag{4.19}$$

Combining Equations (4.8) - (4.10) and Equation (4.11) gives the generalized Euler-Lagrange equation

$$\begin{aligned} L = \int_\Omega \frac{1}{2}\rho \dot{\boldsymbol{u}} \cdot \dot{\boldsymbol{u}} \mathrm{d}V + \int_\Omega \frac{1}{2}\varrho \dot{\varphi}\dot{\varphi} \mathrm{d}V - \int_\Omega [g(\varphi)\psi_s^{0+} + \psi_s^{0-}] \mathrm{d}V - \\ \int_\Omega G_c \frac{1}{c}[\alpha(\varphi) + l^2 |\nabla \varphi|^2] \mathrm{d}V + \int_{\partial\Omega} \boldsymbol{t} \cdot \boldsymbol{u} \mathrm{d}A + \int_\Omega \boldsymbol{b} \cdot \boldsymbol{u} \mathrm{d}V . \end{aligned} \tag{4.20}$$

This generalized Euler-Lagrange equation L has four functions (u, v, w, φ) of four variables (x, y, z, t) with their first derivatives as

$$L = L\left(\begin{array}{c} x, y, z, t, u, v, w, \varphi, \frac{\partial u}{\partial x}, \frac{\partial u}{\partial y}, \frac{\partial u}{\partial z}, \frac{\partial u}{\partial t}, \\ \frac{\partial v}{\partial x}, \frac{\partial v}{\partial y}, \frac{\partial v}{\partial z}, \frac{\partial v}{\partial t}, \frac{\partial w}{\partial x}, \frac{\partial w}{\partial y}, \frac{\partial w}{\partial z}, \frac{\partial w}{\partial t}, \frac{\partial \varphi}{\partial x}, \frac{\partial \varphi}{\partial y}, \frac{\partial \varphi}{\partial z}, \frac{\partial \varphi}{\partial t} \end{array} \right). \tag{4.21}$$

For this kind of Euler-Lagrange equation, a stationary point exists when Equation (4.22) is satisfied [98],

$$\frac{\partial L}{\partial f_i} - \sum_{j=1}^{n} \frac{1}{\partial x_j} \frac{\partial L}{\partial f_{i,j}} = 0. \tag{4.22}$$

Based on Equation (4.22), governing equations of phase field model with a generalized geometric function

$\alpha(\varphi)$ can be obtained as

$$\begin{cases} g(\varphi)\sigma_{ij,j}^{0+} + \sigma_{ij,j}^{0-} + b_i = \rho\ddot{u}_i \\ -g'(\varphi)\psi_s^{0+} - \dfrac{G_c}{c}\alpha'(\varphi) + \dfrac{2l^2 G_c}{c}\Delta\varphi = \varrho\ddot{\psi} \end{cases}. \tag{4.23}$$

where, both geometric function $\alpha(\varphi)$ and degradation function $g(\varphi)$ will be investigated in this dissertation.

To have an idea of the degradation function, the classical one is explained. For the degradation function, it should decrease from 1 to 0 when phase increases from 0 to 1, and its first derivative should be in a small range when phase reaches to 1 to limit the driving force to be a small number [43]. The basic requirements are set as

$$\begin{cases} g(\varphi = 0) = 1 \\ g(\varphi = 1) = 0 \\ g'(\varphi = 1) = 0 \end{cases}. \tag{4.24}$$

The only second order polynomial function satisfying Equation (4.24) is

$$g(\varphi) = (1-\varphi)^2, \tag{4.25}$$

which is used in the classical phase field model. The advantage of this degradation function is that it does not influence the linearity of the FEM formulation.

After the degradation function is defined, governing equations of phase field model can be updated as

$$\begin{cases} (1-\varphi)^2\sigma_{ij,j}^{0+} + \sigma_{ij,j}^{0-} + b_i = \rho\ddot{u}_i \\ 2(1-\varphi)\psi_s^{0+} - \dfrac{G_c}{c}\alpha'(\varphi) + \dfrac{2l^2 G_c}{c}\Delta\varphi = \varrho\ddot{\psi} \end{cases}, \tag{4.26}$$

and the governing equations are subject to time-dependent Dirichlet boundary and time-dependent Neumann boundary conditions

$$\begin{cases} \boldsymbol{u} = \boldsymbol{u}^p, & \text{on } \partial\Omega_u \times [0,T] \\ \boldsymbol{\sigma}\cdot\boldsymbol{n} = \boldsymbol{t}^p, & \text{on } \partial\Omega_t \times [0,T] \\ \varphi = 1, & \text{on } \partial\Omega_\Gamma \times [0,T] \\ \nabla\varphi\cdot\boldsymbol{n} = 0, & \text{on } \partial\Omega \times [0,T] \end{cases}. \tag{4.27}$$

4.1.3 Irreversibility of phase field model

One more important thing for the update of phase is the irreversibility of fracture, i.e., $\Gamma(t) \subset \Gamma(t +$

Δt). To satisfy this requirement, the derivative of Γ with respective to time should be non-negative,

$$\dot{\Gamma} = \frac{\mathrm{d}\Gamma}{\mathrm{d}t} \geq 0, \text{or} \tag{4.28}$$

$$\dot{\Gamma} \approx \int_{\Omega} \dot{\gamma} \mathrm{d}V = \int_{\Omega} \frac{\partial \gamma}{\partial \varphi} \dot{\varphi} \mathrm{d}V \geq 0. \tag{4.29}$$

Two conditions are obtained as

$$\begin{cases} \dfrac{\partial \gamma}{\partial \varphi} = \dfrac{1}{c}[\alpha'(\varphi) - 2l^2 \Delta \varphi] \geq 0 \\ \dot{\varphi} \geq 0 \end{cases}. \tag{4.30}$$

The first condition in Equation (4.30) is ensured by a constitutive assumption that relates the functional derivative to a positive driving force [43]. The later one is a straightforward assumption that no healing effect (no stiffness increase) happens during the fracture process. To satisfy the second condition, strain energy is enforced to be monotonically increasing,

$$H = \begin{cases} H, & \psi_s^{0+} \leq H \\ \psi_s^{0+}, & \psi_s^{0+} > H \end{cases}, \tag{4.31}$$

where, H is the maximum history strain energy, and the ψ_s^{0+} in Equation (4.26~2) can be replaced as H. ψ_s^{0+} and H satisfy the Kuhn-Tucker conditions for loading and unloading [44],

$$\psi_s^{0+} - H \leq 0, \dot{H} \geq 0, \dot{H}(\psi_s^{0+} - H) = 0. \tag{4.32}$$

The irreversibility of fracture is an easy and straightforward assumption for fracture propagation, and this model has been used in many brittle materials. However, this irreversibility defined from $\dot{\varphi} \geq 0$ and $\dot{H} \geq 0$ applies to material at any amount of strain, which means the stiffness of material could decrease at the very beginning when load is applied. Clearly, this conflicts with linear elastic theory for brittle materials. A more meaningful explanation of irreversibility condition $\Gamma(t) \subset \Gamma(t + \Delta t)$ could be in the range where stress already passes fracture strength or fracture already develops, not the whole range including linear elastic part. Analytical solutions and more discussions about this will be shown in next section.

4.2 Different phase field model obtained from different geometric function

As mentioned above, the irreversibility defined from $\dot{\varphi} \geq 0$ could lead to stiffness reduction even at

small strain, and length scale as the only parameter to adjust fracture strength also has its limitation. In this section, to solve these problems, a generalized quadratic geometric function is proposed to build a length scale insensitive phase field. Before that, some different geometric functions used in publications are shown in Table 4.1, and the main idea is that a narrower crack band and different stress-strain curve can be obtained by using different geometric function. Note that here I limit my discussion within the geometric functions lower than or equal to second order to keep the linearity of FEM formulation. Also note that the degradation function $g(\varphi) = (1-\varphi)^2$ in the classical phase field model is used in this Section 4.2 to keep the linearity of FEM formulation.

Table 4.1 Geometric function $\alpha(\varphi)$ and resulting phase $\varphi(x)$

$\alpha(\varphi)$	ξ	c	$\varphi(x)$
φ^2 [43]	0	2	$e^{-\frac{\lvert x\rvert}{l}}$
φ [71]	1	8/3	$(1-\frac{\lvert x\rvert}{2l})^2$
$2\varphi-\varphi^2$ [54]	2	π	$1-\sin\left(\frac{\lvert x\rvert}{l}\right)$
$\xi\varphi+(1-\xi)\varphi^2$	$0<\xi<1$	related to ξ	$\frac{2-\xi}{2-2\xi}e^{-\frac{\sqrt{1-\xi}\lvert x\rvert}{l}}-\frac{\xi}{2-2\xi}$

The last case in Table 4.1 is the proposed generalized quadratic geometric function in this dissertation, which could cover the first three cases in Table 4.1. Because of the requirement of $\alpha(\varphi=0)=0$ for Γ convergence, the constant term is 0 [54]. To the best of author's knowledge, even though this generalized quadratic geometric function has been used in [54,99] before, a fixed $\xi=2$ is recommended in [54,99] to get narrowest crack band, and the length scale insensitive phase field model is built by using a generalized degradation function. However, in this dissertation, geometric function with an independent variable ξ is used to build a length scale insensitive phase field model, and different phase profile (ranged from exponential profile to linear profile) and fracture strength can be obtained. For this generalized quadratic geometric function, the corresponding crack surface density function is expressed as

$$\gamma=\frac{1}{c}[\xi\varphi+(1-\xi)\varphi^2+l^2(\varphi')^2], \tag{4.33}$$

and the homogeneous differential equation used to obtain phase field function $\varphi(x)$ is expressed as

$$\xi + 2(1-\xi)\varphi - 2l^2\varphi'' = 0. \tag{4.34}$$

Depending on the value of ξ, three different solutions are obtained as

(1) $\xi < 1$, $r_1 = -\frac{\sqrt{1-\xi}}{l}$, $r_2 = \frac{\sqrt{1-\xi}}{l}$, $\varphi(x) = c_1 e^{-\frac{\sqrt{1-\xi}|x|}{l}} + c_2 e^{\frac{\sqrt{1-\xi}|x|}{l}} + f^*$,

(2) $\xi = 1$, $r_1 = r_2 = 0$, $\varphi(x) = \frac{1}{4l^2}x^2 + c_1 x + c_2$,

(3) $\xi > 1$, $r_1 = 0 - \frac{\sqrt{\xi-1}}{l}i$, $r_2 = 0 + \frac{\sqrt{\xi-1}}{l}i$, $\varphi(x) = e^{0x}\left[c_1 \cos\left(\frac{\sqrt{\xi-1}|x|}{l}\right) + c_2 \sin\left(\frac{\sqrt{\xi-1}|x|}{l}\right)\right] + f^*$,

where, r_1 and r_2 are the eigen values of the differential equation; c_1 and c_2 are constants that can be determined from boundary conditions; f^* is a particular solution; i is imaginary unit (all the other i in this dissertation represents integer number). For the case $\xi = 1$, there is no independent variable other than x; for the case $\xi > 1$, phase field function $\varphi(x)$ is a periodic function, which might have problem for describing a situation that fracture is only at origin but all other positions are intact. In this dissertation, $\xi < 1$ is used. For $\xi < 1$, considering the boundary conditions $\varphi(0) = 1$ and $\varphi'(\pm\infty) = 0$, the solution is rewritten as $\varphi(x) = \frac{2-\xi}{2-2\xi}e^{-\sqrt{1-\xi}|x|/l} - \frac{\xi}{2-2\xi}$.

To make a visual comparison, the phase field functions of the first three cases in Table 4.1 are plotted in Figure 4.3 (a). Classical phase field model with $\alpha(\varphi) = \varphi^2$ is plotted as a reference, which is a global domain phase field model with limits of integration in $[-\infty, +\infty]$ for fracture surface calculation. However, $\alpha(\varphi) = \varphi$ and $\alpha(\varphi) = 2\varphi - \varphi^2$ has nonmonotonic solution, and a special technique might be needed for fracture surface calculation to make their limits of integration in $[0,2l]$ and $[0, \pi l/2]$, respectively. Compared with $\alpha(\varphi) = \varphi^2$, the advantage of $\alpha(\varphi) = \varphi$ and $\alpha(\varphi) = 2\varphi - \varphi^2$ is a narrower crack band.

For $\alpha(\varphi) = \xi\varphi + (1-\xi)\varphi^2$, phase field function with different ξ values are plotted in Figure 4.3 (b). When $\xi < 0$, the minimum phase is larger than 0, and some remapping technique is needed to map phase back to 0 to describe intact state; when $\xi = 0$, it is the classical phase field model; when $0 < \xi < 1$, phase has an intersection with x axis. So, only $0 < \xi < 1$ is used in this dissertation, which is not same as the first three cases in Table 4.1. Different from nonmonotonic solutions for case 2 and case 3 in Table 4.1, the

advantage of using $0 < \xi < 1$ is that it has monotonic solution, and negative phase can be easily set as 0 to control the limits of integration and the crack band. The deep reason to do phase zeroing here is that, the range of phase from $\varphi(x) = \frac{2-\xi}{2-2\xi} e^{-\sqrt{1-\xi}|x|/l} - \frac{\xi}{2-2\xi}$ (according to crack surface derivation) over the whole x domain $x \in [-\infty, +\infty]$ is $[-\frac{\xi}{2-2\xi}, 1]$, and the range of phase from $\varphi(\varepsilon) = \frac{E\varepsilon^2 - G_c\xi/\tilde{c}l}{E\varepsilon^2 + 2G_c(1-\xi)/\tilde{c}l}$ (according to homogenous solution, will see in Equation (4.57)) over the whole strain domain $\varepsilon \in [-\infty, +\infty]$ is also $[-\frac{\xi}{2-2\xi}, 1]$, and the limits of integration for fracture surface calculation will not be affected if fracture surface is initially defined on positive phase $\varphi(x)$, or no violation of Γ convergence when fracture surface is calculated based on positive phase $\varphi(\varepsilon)$.

However, phase zeroing is not always correct for every model. For example, if geometric function $\alpha(\varphi) = \varphi^2$ and a higher order degradation function $g(\varphi) = 1 - 3\varphi^2 + 2\varphi^3$ are used in phase field model, the range of phase from $\varphi(x) = e^{-|x|/l}$ (according to crack surface derivation) over the whole x domain $x \in [-\infty, +\infty]$ is $[0,1]$, but the range of phase from $\varphi(\varepsilon) = 1 - G_c/3El\varepsilon^2$ (according to homogenous solution, will see in Equation (4.77)) over the whole strain domain $\varepsilon \in [-\infty, +\infty]$ is $[-\infty, 1]$. In this case, phase zeroing on $\varphi(\varepsilon)$ would definitely decrease the limits of integration for fracture surface calculation on $\varphi(x)$ which should be over the whole x domain $x \in [-\infty, +\infty]$, and then problem could happen with Γ convergence.

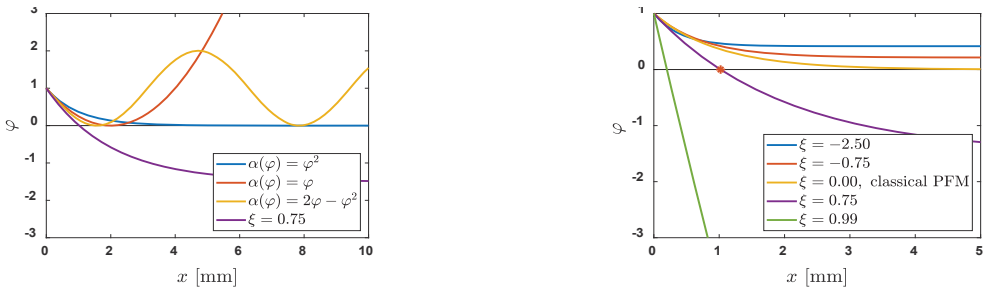

(a) (b)

Figure 4.3 (a) comparison of phase results used in publications, (b) phase results of the proposed geometric function with different ξ, $\xi < 1$

For the classical phase field model, constant c is obtained from Equation (4.4) with the limits of

integration $x \in [-\infty, +\infty]$. However, for the length scale insensitive phase field model in this dissertation, smaller limits of integration are used to get correct fracture surface and enable Γ convergence. According to the phase field function $\varphi(x)$ for the generalized quadratic geometric function, the limits of integration is obtained as $x \in \left[\frac{l}{\sqrt{1-\xi}}\ln(\frac{\xi}{2-\xi}), -\frac{l}{\sqrt{1-\xi}}\ln(\frac{\xi}{2-\xi})\right]$. Considering that the constant c for the classical phase field model will be expressed as $2l$ later in the FEM formulation, to keep this consistency, constant c for the proposed phase field model is also obtained from Equation (4.4) as

$$c = \frac{2\left[1-\xi+\xi^2\ln\left(\frac{\xi}{2-\xi}\right)/4\right]}{\sqrt{(1-\xi)^3}}l = \tilde{c}l, \tag{4.35}$$

where, $\tilde{c}$ is just a constant obtained from c/l. $\tilde{c}$ without length scale l will be used in FEM formulation later, not c.

According to degradation function, negative phase would lead to stiffness increasing, which is not true in reality. Another thing is the damaged band caused by a fracture should not be infinite. Based on these two points, phase zeroing is needed, and this could also be helpful for controlling the damaged range. To verify the Γ convergence would not be affected by phase zeroing, a 1D case is shown here. Original phase profile and phase profile after zeroing negative phase are shown in Figure 4.4. The Γ integration is shown in Equation (4.36). After phase zeroing, there is no contribution to Γ where phase is 0, so the limits of integration are reduced to the range of positive phase. Putting the phase solution in Table 4.1 and constant c in Equation (4.35) into Equation (4.36) and doing the integration, Γ equals 1, which verifies the Γ convergence for this 1D problem. Note that this Γ convergence is guaranteed by using the correct constant c in Equation (4.35). More investigations about Γ convergence in 2D and 3D cases will be my future work.

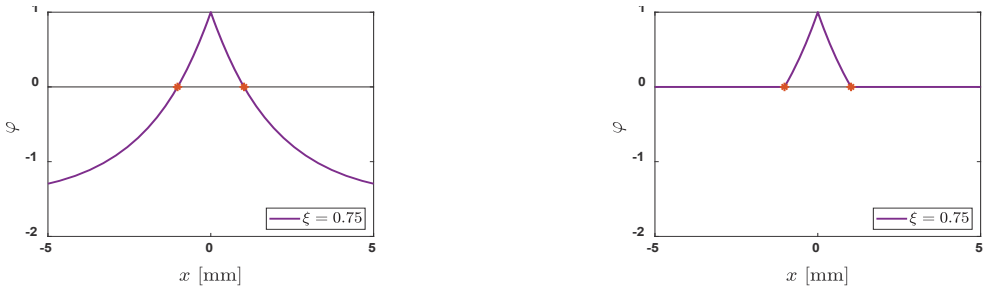

(a) (b)

Figure 4.4 (a) original phase profile, (b) phase profile after zeroing negative phase

$$\Gamma = \int_{-\infty}^{+\infty} \gamma dx = \int_{\frac{l}{\sqrt{1-\xi}}\ln\left(\frac{\xi}{2-\xi}\right)}^{-\frac{l}{\sqrt{1-\xi}}\ln\left(\frac{\xi}{2-\xi}\right)} \gamma dx = \int_{\frac{l}{\sqrt{1-\xi}}\ln\left(\frac{\xi}{2-\xi}\right)}^{-\frac{l}{\sqrt{1-\xi}}\ln\left(\frac{\xi}{2-\xi}\right)} \frac{1}{c}[\xi\varphi + (1-\xi)\varphi^2 + l^2(\varphi')^2]dx = 1 \quad (4.36)$$

To better understand the effect of phase on material's constitutive law, homogeneous and nonhomogeneous solutions of the classical phase field model and the proposed phase field model are investigated. A 1D tensile test is investigated in Section 4.2.1 and Section 4.2.2, which makes strain energy non-negative. Material parameters used include Young's modulus E 41000 MPa and critical energy release rate G_c 0.05 N/mm. A 3D tensile test is investigated in Section 4.2.3.1, and one more parameter needed is Poisson's ratio υ 0.18. In this dissertation, the special case with $\varrho = 0$ is considered, but more researches are still needed for $\varrho \neq 0$.

4.2.1 Analytical solution and FEM formulation of the classical phase field model

4.2.1.1 Homogeneous solution of the classical phase field model

First, homogeneous solution of the classical phase field model is presented. Ignore the last term at left-hand side and the term at right-hand side in Equation (4.26~2), put $\alpha(\varphi) = \varphi^2$ and $c = 2l$ into it, and express loading condition with respect to strain $H = E\varepsilon^2/2$, the relation between phase and strain for loading condition is obtained as

$$\varphi = \frac{E\varepsilon^2}{E\varepsilon^2 + G_c/l}. \quad (4.37)$$

And the relation between stress and strain can be obtained by using $\sigma = (1-\varphi)^2 E\varepsilon$,

$$\sigma = \left(\frac{G_c/l}{E\varepsilon^2 + G_c/l}\right)^2 E\varepsilon. \tag{4.38}$$

Figure 4.5 plots the relation obtained from Equations (4.37) and (4.38). With the increase of strain, phase is kept monotonically increasing from 0 to 1. A larger length scale l leads to a faster increase of phase, a smaller range of stress-strain curve, and a lower fracture strength. The stiffness reduction can be seen from Figure 4.5 (a), where at any non-zero strain there is a phase larger than 0 and then a degradation function value less than 1.

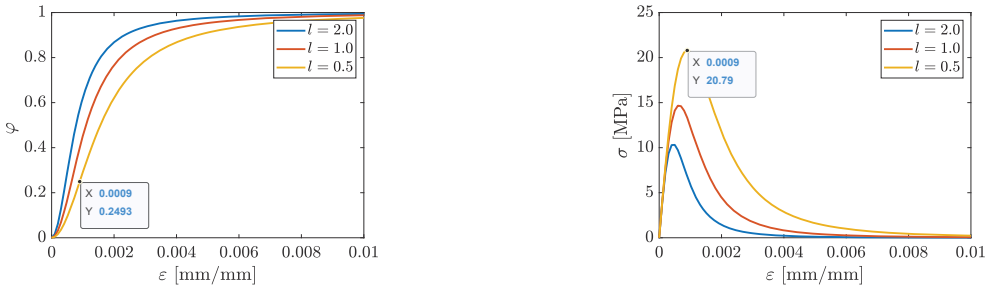

(a) (b)

Figure 4.5 Homogeneous solution of the classical phase field model, (a) phase versus strain, (b) stress versus strain

Fracture stress and strain can be easily obtained from the derivative of Equation (4.38) as

$$\begin{cases} \sigma_c = \dfrac{9}{16}\sqrt{EG_c/6l} \\ \varepsilon_c = \sqrt{G_c/6lE} \end{cases}. \tag{4.39}$$

Note that the phase at fracture stress and strain is a fixed number (0.25), nothing to do with length scale l, see the data tips in Figure 4.5. According to Equation (4.39), when length scale l approaches 0, this fracture stress goes to infinite, which agrees with linear elastic fracture mechanics theory: stress goes to infinity as it approaches infinitely close to crack tip.

4.2.1.2 Nonhomogeneous solution of the classical phase field model

Second, nonhomogeneous solution of the classical phase field model is presented. Ignore the term at right-hand side in Equation (4.26~2), put $\alpha(\varphi) = \varphi^2$ and $c = 2l$ into it, and express loading condition with respect to stress $H = \sigma^2/2E$, the governing equation of Equation (4.26~2) is rewritten as

$$\frac{\sigma^2}{E}(1-\varphi) - \frac{G_c}{l}\varphi + lG_c\varphi'' = 0. \tag{4.40}$$

Since Equation (4.40) satisfies over the whole domain, its integration with respect to φ is also equal to 0, and this integration gives the first derivative of phase

$$\varphi' = \frac{\mathrm{d}\varphi}{\mathrm{d}x} = \pm\sqrt{\frac{2}{lG_c}\left[\frac{\sigma^2}{2E}(1-\varphi)^2 + \frac{G_c}{2l}\varphi^2 - c^*\right]}, \tag{4.41}$$

$$c^* = \frac{\sigma_\infty^2}{2E}(1-\varphi_\infty)^2 + \frac{G_c}{2l}\varphi_\infty^2, \tag{4.42}$$

where, c^* is a constant determined from boundary condition $\varphi'(\infty) = 0$; σ_∞ and φ_∞ are the stress and phase at infinite position, respectively. The relation between position and phase can be obtained by integrating Equation (4.41) with respect to φ again,

$$x = \pm\int_{\varphi(x)}^{\varphi(0)} \frac{1}{\sqrt{\frac{2}{lG_c}\left[\frac{\sigma^2}{2E}(1-\varphi)^2 + \frac{G_c}{2l}\varphi^2 - c^*\right]}}\mathrm{d}\varphi\,, \tag{4.43}$$

where, $\varphi(0)$ is assumed to be the maximum phase, which could be 1 or less than 1. For any other phase not at the origin, its position can be found from Equation (4.43), which then gives the relation between phase and position, as shown in Figure 4.6.

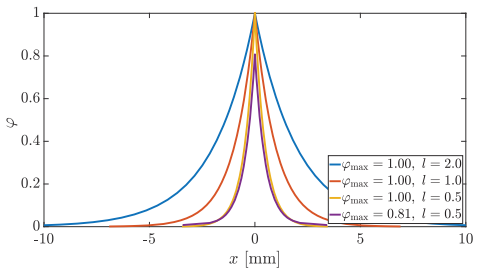

Figure 4.6 Nonhomogeneous solution of the classical phase field, phase versus position

4.2.1.3 Linear FEM formulation of the classical phase field model

For the strong form of Equation (4.26~1), without considering damping effect, the matrix form of the motion of equation is expressed as (which can also be obtained from Hamilton's principle)

$$\boldsymbol{M}\ddot{\boldsymbol{u}}_n + \boldsymbol{K}\boldsymbol{u}_n = \boldsymbol{F}_n^{ext}, \tag{4.44}$$

where, $\boldsymbol{M}$ is mass matrix; $\boldsymbol{K}$ is stiffness matrix; $\boldsymbol{F}_n^{ext}$ is external force at nth step. Explicit scheme with central difference method is used to solve displacement,

$$\boldsymbol{M}\frac{\boldsymbol{u}_{n+1}-2\boldsymbol{u}_n+\boldsymbol{u}_{n-1}}{\Delta t^2}+\boldsymbol{K}\boldsymbol{u}_n=\boldsymbol{F}_n^{ext}, \tag{4.45}$$

where, Δt is time step size. $\boldsymbol{M}$, $\boldsymbol{K}\boldsymbol{u}_n$ and $\boldsymbol{F}_n^{ext}$ are expressed as

$$\boldsymbol{M}=\int_{\Omega}\boldsymbol{N}^T\rho\boldsymbol{N}\mathrm{d}V\,, \tag{4.46}$$

$$\boldsymbol{K}\boldsymbol{u}_n=\int_{\Omega}\boldsymbol{B}^T\boldsymbol{\sigma}_n\mathrm{d}V=\int_{\Omega}\boldsymbol{B}^T[g(\varphi)\boldsymbol{\sigma}_n^{0+}+\boldsymbol{\sigma}_n^{0-}]\mathrm{d}V\,, \tag{4.47}$$

$$\boldsymbol{F}_n^{ext}=\int_{\Omega}\boldsymbol{N}^T\boldsymbol{b}_n\mathrm{d}V+\int_{\Omega}\boldsymbol{N}^T\boldsymbol{t}_n\mathrm{d}A\,, \tag{4.48}$$

respectively. Note that the stress is updated with phase. $\boldsymbol{K}\boldsymbol{u}_n$ is also called internal force $\boldsymbol{F}_n^{int}$, and the new displacement at $(n+1)$th step is obtained as

$$\boldsymbol{u}_{n+1}=\frac{\left(\boldsymbol{F}_n^{ext}-\boldsymbol{F}_n^{int}\right)\Delta t^2}{\boldsymbol{M}}+2\boldsymbol{u}_n-\boldsymbol{u}_{n-1}. \tag{4.49}$$

After displacement field is solved, phase field can be solved based on displacement, strain, and strain energy. For the strong form of Equation (4.26~2), ignore the term at right-hand side and use Galerkin's method, the weak form is expressed as

$$\int_{\Omega}\boldsymbol{N}_i^T\left[2H-2H\varphi-\frac{G_c}{l}\varphi+lG_c\Delta\varphi\right]\mathrm{d}V=0. \tag{4.50}$$

Apply integration by parts, Gauss's divergence theorem, and boundary condition of Equation (4.27~4) ($\nabla\varphi\cdot\boldsymbol{n}=0$), the order of the last term is decreased from two to one as

$$\int_{\Omega}\boldsymbol{N}_i^T lG_c\Delta\varphi\mathrm{d}V=\int_{\partial\Omega}\boldsymbol{N}_i^T lG_c\nabla\varphi\cdot\boldsymbol{n}\mathrm{d}A-\int_{\Omega}\boldsymbol{B}_i^T lG_c\nabla\varphi\mathrm{d}V=-\int_{\Omega}\boldsymbol{B}_i^T lG_c\nabla\varphi\mathrm{d}V\,. \tag{4.51}$$

For the φ and $\nabla\varphi$, they can be expressed by shape function matrix, strain-displacement matrix, and phase unknows, $\varphi=\boldsymbol{N}_j\boldsymbol{\varphi}_j$, $\nabla\varphi=\boldsymbol{B}_j\boldsymbol{\varphi}_j$, $j=1,\dots,8$ for hexahedron element,

$$\int_{\Omega}\left[\boldsymbol{N}_i^T2H-\boldsymbol{N}_i^T2H\boldsymbol{N}_j\boldsymbol{\varphi}_j-\boldsymbol{N}_i^T\frac{G_c}{l}\boldsymbol{N}_j\boldsymbol{\varphi}_j-\boldsymbol{B}_i^T lG_c\boldsymbol{B}_j\boldsymbol{\varphi}_j\right]\mathrm{d}V=0. \tag{4.52}$$

For the application of iso-parametric element, $\mathrm{d}V$ is mapped into natural coordinate system as $\mathrm{d}V=|\boldsymbol{J}|\mathrm{d}\xi\mathrm{d}\eta\mathrm{d}\varsigma$. The weak form is further updated as

$$\int_{\Omega} \left[\boldsymbol{N}_i^T 2H - \boldsymbol{N}_i^T 2H \boldsymbol{N}_j \boldsymbol{\varphi}_j - \boldsymbol{N}_i^T \frac{G_c}{l} \boldsymbol{N}_j \boldsymbol{\varphi}_j - \boldsymbol{B}_i^T l G_c \boldsymbol{B}_j \boldsymbol{\varphi}_j \right] |\boldsymbol{J}| \mathrm{d}\xi \mathrm{d}\eta \mathrm{d}\varsigma = 0. \tag{4.53}$$

Stiffness matrix and force vector can be obtained as

$$\boldsymbol{K}_{ij} = \int_{\Omega} \left(\boldsymbol{N}_i^T 2H |\boldsymbol{J}| \boldsymbol{N}_j + \boldsymbol{N}_i^T \frac{G_c}{l} |\boldsymbol{J}| \boldsymbol{N}_j + \boldsymbol{B}_i^T l G_c |\boldsymbol{J}| \boldsymbol{B}_j \right) \mathrm{d}\xi \mathrm{d}\eta \mathrm{d}\varsigma , \tag{4.54}$$

$$\boldsymbol{F}_i = \int_{\Omega} \boldsymbol{N}_i^T 2H |\boldsymbol{J}| \mathrm{d}\xi \mathrm{d}\eta \mathrm{d}\varsigma , \tag{4.55}$$

and the phase unknows can be obtained directly by solving a system of linear equations,

$$\boldsymbol{K}\boldsymbol{\varphi} = \boldsymbol{F}. \tag{4.56}$$

For the classical phase field model, one advantage is that the crack surface density function used keeps the linearity of this phase problem, so no iteration is needed in calculation. Staggered method is used in this dissertation to solve the displacement-phase coupled problem for its robustness. The basic idea of this method is that displacement field and phase field in Equation (4.26) can be solved in turn and independently (see Figure 4.7), and both explicit and implicit schemes can be used to solve it [52]. Hu et al. [100] present a detailed overview of the implementation of explicit and implicit phase field models. Note that only explicit scheme is used in this dissertation.

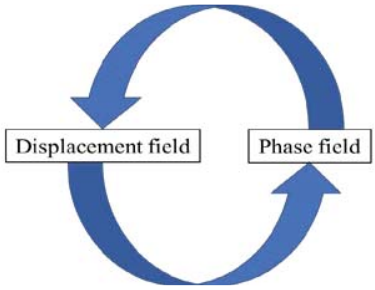

Figure 4.7 Staggered method for displacement-phase coupled problem

4.2.2 Analytical solution and FEM formulation of the proposed phase field model

4.2.2.1 Homogeneous solution of the proposed phase field model

Similarly, ignore the last term at left-hand side and the term at right-hand side in Equation (4.26~2), put $\alpha(\varphi) = \xi\varphi + (1-\xi)\varphi^2$ and $c = \tilde{c}l$ into it, and express loading condition with respect to strain $H = E\varepsilon^2/2$, the relation between phase and strain for loading condition is obtained as

$$\varphi = \frac{E\varepsilon^2 - G_c\xi/\tilde{c}l}{E\varepsilon^2 + 2G_c(1-\xi)/\tilde{c}l}. \tag{4.57}$$

And the relation between stress and strain can be obtained by using $\sigma = (1-\varphi)^2 E\varepsilon$,

$$\sigma = \left[\frac{G_c(2-\xi)/\tilde{c}l}{E\varepsilon^2 + 2G_c(1-\xi)/\tilde{c}l}\right]^2 E\varepsilon. \tag{4.58}$$

Figures 4.8 and 4.9 show homogeneous solution from Equations (4.57) and (4.58) for the length scale insensitive phase field model. Figure 4.8 shows results with same ξ but different l equal to 2.0, 1.0, and 0.5, which is similar as the results in Figure 4.5 for the classical phase field model, but negative phase is found here like its phase field function $\varphi(x)$. Figure 4.9 shows results with same l but different ξ equal to 0.25, 0.50, and 0.75. A larger ξ gives a lower negative phase and larger fracture strength. Another thing to mention is the range of negative phase, where a larger ξ gives a larger range of negative phase. From these four figures, it is clear that the range of negative phase (or linear elastic range after phase zeroing) can be adjusted by l and ξ.

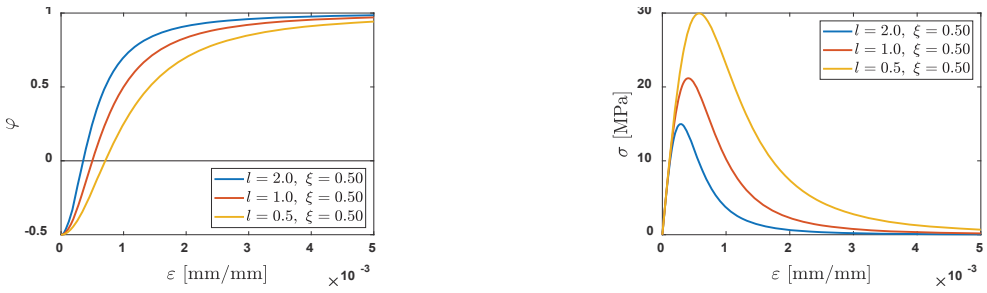

(a) (b)

Figure 4.8 Homogeneous solution of the length scale insensitive phase field model with same ξ, (a) phase versus strain, (b) stress versus strain

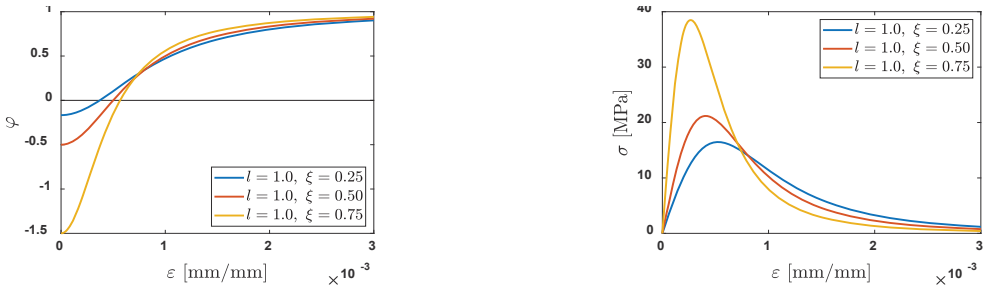

(a) (b)

Figure 4.9 Homogeneous solution of the length scale insensitive phase field model with same length scale l, (a) phase versus strain, (b) stress versus strain

For the case with $l = 1.0$ and $\xi = 0.75$ in Figures 4.8 and 4.9, after the zeroing of negative phase, new phase-strain curve and new stress-strain curve are shown in Figures 4.10 (a) and 4.10 (b), respectively. This new phase-strain curve is similar to damage-separation curve observed in bilinear cohesive law [5] where damage is 0 at initial part to get linear elastic behavior. And it is widely known that bilinear cohesive law can handle linear elastic behavior well.

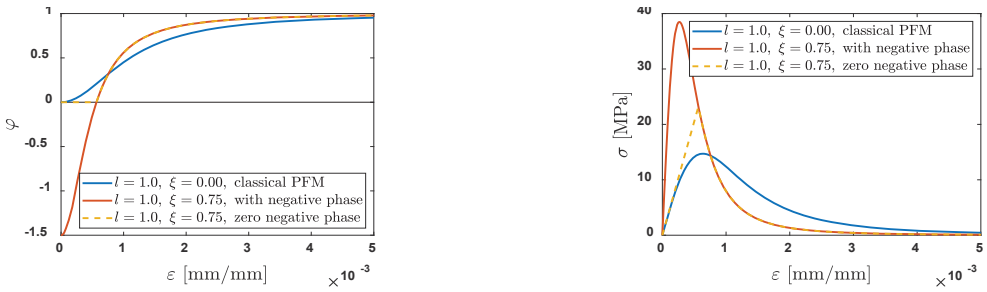

(a) (b)

Figure 4.10 (a) phase-strain curve after zeroing negative phase, (b) stress-strain curve after zeroing negative phase

4.2.2.2 Nonhomogeneous solution of the proposed phase field model

Similarly, ignore the term at right-hand side in Equation (4.26~2), put $\alpha(\varphi) = \xi\varphi + (1-\xi)\varphi^2$ and $c = \tilde{c}l$ into it, and express loading condition with respect to stress $H = \sigma^2/2E$, the governing equation of Equation (4.26~2) is rewritten as

$$\frac{\sigma^2}{E}(1-\varphi) - \frac{G_c}{\tilde{c}l}[\xi + 2(1-\xi)\varphi] + \frac{2lG_c}{\tilde{c}}\varphi'' = 0. \tag{4.59}$$

Since Equation (4.59) satisfies over the whole domain, its integration with respect to φ is also equal to 0, and this integration gives the first derivative of phase

$$\varphi' = \frac{\mathrm{d}\varphi}{\mathrm{d}x} = \pm\sqrt{\frac{\tilde{c}}{lG_c}\left[\frac{\sigma^2}{2E}(1-\varphi)^2 + \frac{G_c\xi}{\tilde{c}l}\varphi + \frac{G_c}{\tilde{c}l}(1-\xi)\varphi^2 - c^*\right]}, \tag{4.60}$$

$$c^* = \frac{\sigma_\infty^2}{2E}(1-\varphi_\infty)^2 + \frac{G_c\xi}{\tilde{c}l}\varphi_\infty + \frac{G_c}{\tilde{c}l}(1-\xi)\varphi_\infty^2. \tag{4.61}$$

The relation between position and phase can be obtained by integrating Equation (4.60) with respect to φ again,

$$x = \pm \int_{\varphi(x)}^{\varphi(0)} \frac{1}{\sqrt{\frac{\tilde{c}}{lG_c}\left[\frac{\sigma^2}{2E}(1-\varphi)^2 + \frac{G_c\xi}{\tilde{c}l}\varphi + \frac{G_c}{\tilde{c}l}(1-\xi)\varphi^2 - c^*\right]}} \mathrm{d}\varphi\,. \tag{4.62}$$

For any other phase not at the origin, its position can be found from Equation (4.62), which then gives the relation between phase and position, as shown in Figure 4.11. Figure 4.11 (b) shows phase versus position after the zeroing of negative phase. Since nonhomogeneous solution (phase versus position) has nothing to do with degradation function, the nonhomogeneous solution plotted here with maximum phase equal to 1 is totally same as phase field function $\varphi(x)$ obtained during the derivation of crack surface density function.

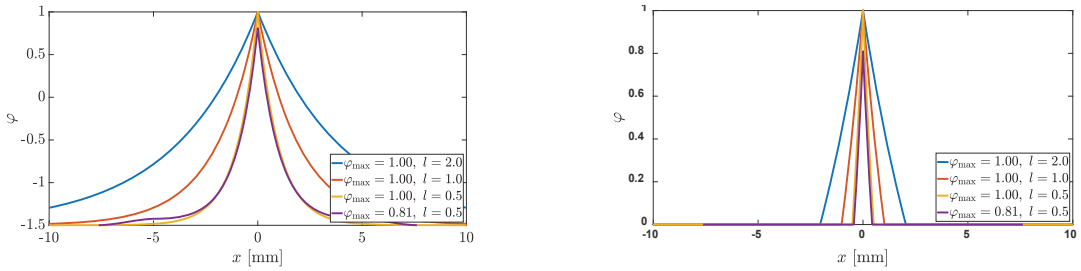

(a) (b)

Figure 4.11 Nonhomogeneous solution, (a) phase versus position, (b) phase versus position after zeroing negative phase

4.2.2.3 Linear FEM formulation of the proposed phase field model

The FEM formulation of displacement field has been presented in Section 4.2.1.3, so only phase field is derived here. For the strong form of Equation (4.26~2), ignore the term at right-hand side and use Galerkin's method, the weak form is expressed as

$$\int_{\Omega} \boldsymbol{N}_i^T \left[2(1-\varphi)H - \frac{G_c}{\tilde{c}l}[\xi + 2(1-\xi)\varphi] + \frac{2lG_c}{\tilde{c}}\Delta\varphi\right] \mathrm{d}V = 0. \tag{4.63}$$

Apply integration by parts, Gauss's divergence theorem, and boundary condition of Equation (4.27~4) ($\nabla\varphi \cdot \boldsymbol{n} = 0$), the order of the last term is decreased from two to one. Follow the same procedure shown in Section 4.2.1.3, stiffness matrix and force vector can be obtained for the proposed phase field model as

$$\boldsymbol{K}_{ij} = \int_{\Omega} \left[\boldsymbol{N}_i^T 2H|\boldsymbol{J}|\boldsymbol{N}_j + \boldsymbol{N}_i^T \frac{2G_c}{\tilde{c}l}(1-\xi)|\boldsymbol{J}|\boldsymbol{N}_j + \boldsymbol{B}_i^T \frac{2lG_c}{\tilde{c}}|\boldsymbol{J}|\boldsymbol{B}_j\right] \mathrm{d}\xi\mathrm{d}\eta\mathrm{d}\varsigma\,, \tag{4.64}$$

$$\boldsymbol{F}_i = \int_{\Omega} \left(\boldsymbol{N}_i^T 2H|\boldsymbol{J}| - \boldsymbol{N}_i^T \frac{G_c}{\tilde{c}l}\xi|\boldsymbol{J}|\right) \mathrm{d}\xi\mathrm{d}\eta\mathrm{d}\varsigma\,, \tag{4.65}$$

and Equation (4.56) is still used to solve the phase unknowns. Compared with Equations (4.54) and (4.55) for the classical phase field model, the proposed phase field model is still a linear FEM problem, and the difference with the classical phase field model is the middle term in the stiffness matrix Equation (4.64) and one extra term in the force vector Equation (4.65). Another thing is phase zeroing, which can be done similarly like monotonically increasing phase $\dot{\varphi} \geq 0$. However, the fundamental of this problem is still the same, so these changes would not heavily influence the modeling efficiency of the proposed phase field model. The comparison of modeling efficiency is compared later through a tensile test.

4.2.3 Numerical verification of the phase field model using different geometric function

4.2.3.1 Tensile test of different phase field model

The presented above are the phase field models using different geometric function, and a tensile test is presented to verify their basic features. Dimensions, boundary condition, and load for the tensile test are shown in Figure 4.12. Hexahedron element with full integration method is used in the simulation. To let fracture develops at the center of the bar, a small cross-section reduction is made at the center, which could lead to stress concentration and high strain energy at that position. Because the specimen in this example is intact at the beginning, phase is initialized as 0. Material parameters used include Young's modulus E 41000 MPa and critical energy release rate G_c 0.05 N/mm.

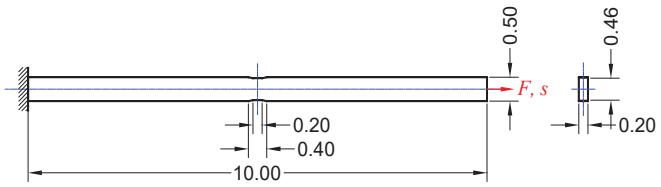

Figure 4.12 Dimensions, boundary condition, and load of the tensile test, unit [mm]

(1) Tensile test of the classical phase field model

For the classical phase field model, the influence of length scale l on tensile test is investigated. Figure 4.13 shows the phase results of three different l 2.0, 1.0, and 0.5 with element size 0.1 mm. With the decrease of l, the crack band gets smaller, which agrees with the nonhomogeneous solutions in Figure 4.6.

The detailed phase value is plotted in Figure 4.14 (a). Compared with analytical results, numerical results are still not close enough, and the possible reason could be the large element size used in simulations. The stress-strain curve is plotted in Figure 4.14 (b). It is clear to see that linear elastic behavior is not recreated in this simulation. With the decrease of l, fracture stress gets bigger, which agrees with Figure 4.5 (b). Even though stress-strain curve does not converge to analytical results, the stress-strain curve is almost the same for two different element size used for the $l = 0.5$ case, which could show that element size is not as sensitive as length scale l.

(a)

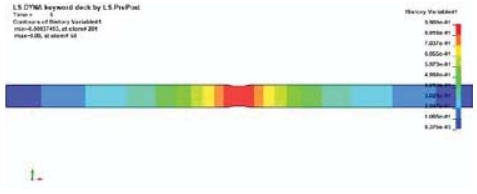

(b)

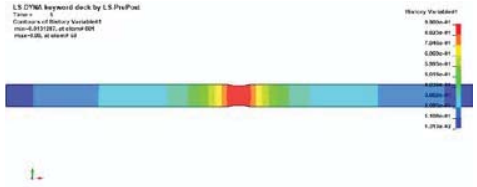

(c)

Figure 4.13 Phase result [0,1] of the classical phase field model, (a) length scale $l = 2.0$, (b) length scale $l = 1.0$, (c) length scale $l = 0.5$

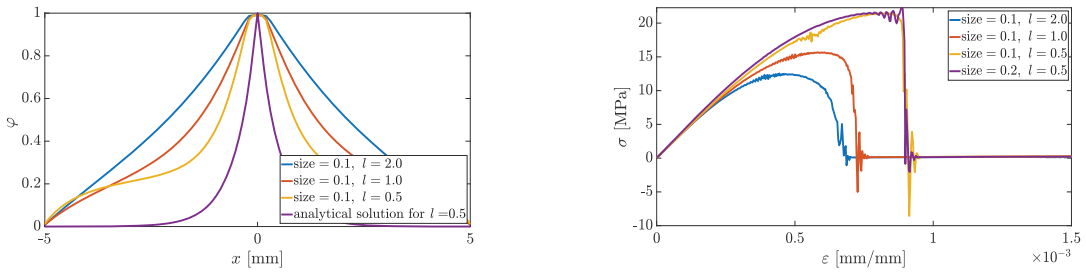

(a) (b)

Figure 4.14 Numerical results of the classical phase field model, (a) phase versus position, (b) stress versus strain

For the constitutive law of bilinear cohesive law in [5], damage factor (similar as phase for phase field model) is 0 before reaching fracture strength in constitutive law, which makes it agree with linear elastic theory. If this is applied in the classical phase field model with length scale $l = 1.0$, new phase results can be obtained, as shown in Figure 4.15 (a). Here, only a simple remapping from [0.25,1] to [0,1] is used to update the phase results, and phase result below 0.25 is set as 0. Further, if strain energy is reversible before reaching fracture strength (or reaching phase 0.25), new phase results can be obtained, as shown in Figure 4.15 (b).

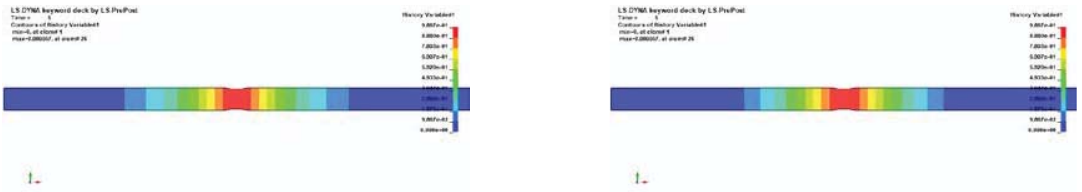

(a) (b)

Figure 4.15 Phase result [0,1] of the classical phase field model, (a) length scale $l = 1.0$ with phase remapping, (b) length scale $l = 1.0$ with phase remapping and strain energy reversible

Detailed phase results for the three cases are shown in Figure 4.16. Compared with the classical phase field model, phase remapping and strain energy reversible before reaching fracture strength makes phase more concentrated at the center of the bar. For the position where strain energy is so small that stress does not reach to fracture strength, if reversibility of strain energy is considered, the phase gets back to 0 after the strain energy is released. This is true for brittle materials before reaching linear elastic limit. Here, phase remapping and reversibility of strain energy are used to show these changes qualitatively, and more discussion about this will be on the proposed phase field model in next section.

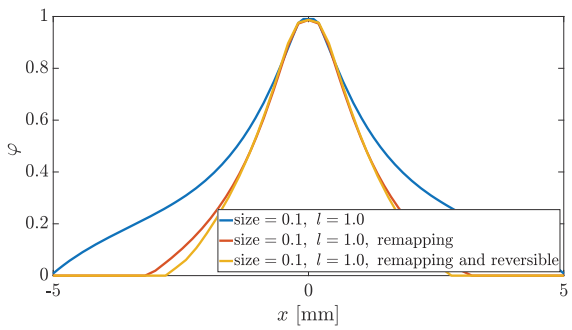

Figure 4.16 Phase versus position for different cases for the classical phase field model

(2) Tensile test of the proposed phase field model

The proposed length scale insensitive phase field model is also applied in this tensile test. The phase results obtained with length scale $l = 1.0$ and $\xi = 0.75$ is shown in Figure 4.17 (b). It is clear to see that for the same length scale l, the crack band for the length scale insensitive phase field model is smaller. The minimum phase in Figure 4.17 (a) is a small positive number, but the minimum phase in Figure 17 (b) is 0. The phase versus position is plotted in Figure 4.18. For the classical phase field model, the phase decreases slowly; however, the model proposed in this dissertation has phase that drops to 0 faster and gives a narrower crack band, which agrees with phase profile in Figures 4.3 (b) and 4.11 (b).

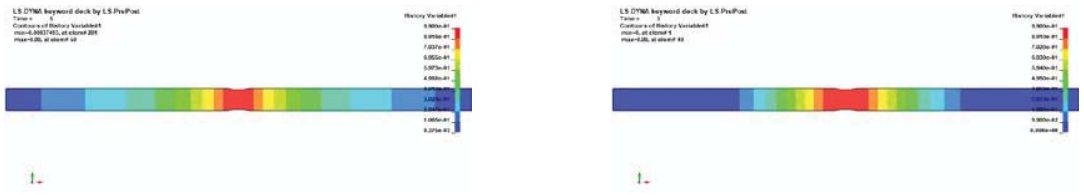

(a) (b)

Figure 4.17 Phase result [0,1], (a) length scale $l = 1.0$ for the classical phase field model, (b) length scale $l = 1.0$ and $\xi = 0.75$ for the length scale insensitive phase field model

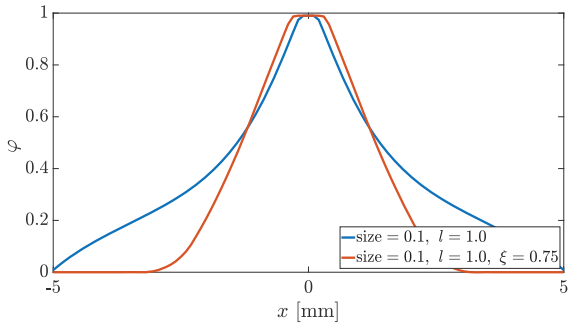

Figure 4.18 Phase versus position of the classical phase field model and the length scale insensitive phase field model

The stress-strain curve is also obtained from this simulation and compared with the classical phase field model, as shown in Figure 4.19. The biggest difference is the slope. Because linear elastic property is enabled in the length scale insensitive phase field model, the slope is almost constant before it drops. The slope is 22.9/0.00056 = 40893 MPa, which is almost equal to the Young's modulus of the material, 41000 MPa. An interesting thing is that for $l = 1.0$, stress drops at almost same strain for both classical phase field

model and length scale insensitive phase field model. The reason could be that strain at fracture strength in Figure 4.10 (b) is almost same for these two models, and stress-strain curve beyond fracture strength does not matter that much for this tensile test. The fracture strength can be adjusted by setting different length scale l and parameter ξ.

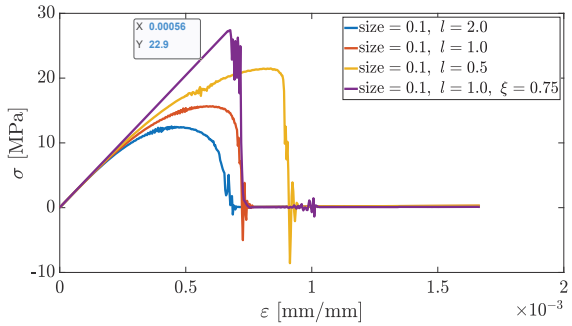

Figure 4.19 Comparison of stress-strain curves between the classical phase field model and the length scale insensitive phase field model

For the case with $l = 1.0$, the classical phase field model takes 6 hours and 52 minutes; the proposed phase field model takes 6 hours and 41 minutes. So, both phase field models have almost same modeling efficiency in this tensile test, and this agrees with the analysis in Section 4.2.1. This modeling efficiency should be also true for large scale simulation since the computation of these two models is almost same. Because linear elastic behavior is guaranteed by phase zeroing in the proposed phase field model, it can still obtain linear elastic behavior even using larger elements. However, mesh convergence should still be checked before using large elements for the proposed phase field model.

4.2.3.2 Mode I failure of wedge splitting test

First, the wedge splitting test conducted by Trunk [101] is considered, which has been used for verification in [101,102]. The specimen has a square shape with dimensions 800 mm × 800 mm × 400 mm, and simply supported at the center of each half of the bottom edge. A vertical notch is made up to about half of the height of the specimen. Two horizontal force are applied by a vertically pushed wedge. The detailed dimensions, boundary condition, and load are shown in Figure 4.20. The material parameters used include Young's modulus E 28300 MPa, Poisson's ratio υ 0.18, fracture strength σ_f 2.12 MPa, and critical energy release rate G_c 0.373 N/mm. Force and displacement data are recorded during the simulation.

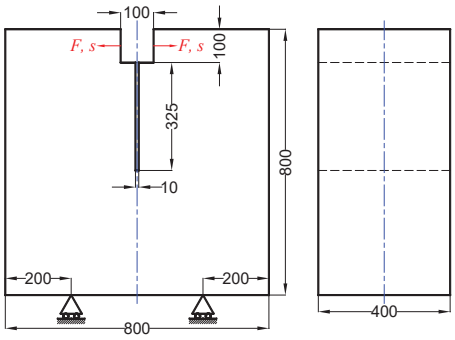

Figure 4.20. Dimensions, boundary condition, and load of the wedge splitting test, unit [mm]

Hexahedron element is used to mesh the specimen. Considering the size of the specimen, local refinement with 2 mm element along the fracture path is used, and larger element is used at other positions. The model consists of 6842 elements and 13988 nodes. The length scale l used in the two models is 5, which satisfies the requirement that the ratio between length scale and element size is larger than two in [43]. Running time for this simulation is about 13 hours. The phase results obtained from classical phase field model and length scale insensitive phase field model are shown in Figure 4.21. Even though same length scale l is used, it is clear to see that the length scale insensitive phase field model has a narrower crack band, which is true for brittle materials that have smaller crack zone near the crack tip. Relatively speaking, even though smaller length scale l can be used to have a narrower crack band, the phase profile for the length scale insensitive phase field model can still drop to 0 faster than the classical phase field model.

(a) (b)

Figure 4.21 Phase result of the wedge splitting test, (a) classical phase field model, (b) length scale insensitive phase field model

The force-displacement curve is obtained for the two models, as shown in Figure 4.22. Even though both two models agree somehow with experiment data, a clear stiffness reduction is found in the classical

phase field model. With the help of extra parameter ξ in the length scale insensitive phase field model, fracture strength can be adjusted, and a peak force very close to experiment result can be obtained. However, the fracture strength for the classical phase field model is only determined by length scale. In this simulation, considering the small fracture strength (about 2 MPa) for concrete, length scale $l = 5$ gives a higher peak force in the force-displacement curve, which is also found in the next two examples.

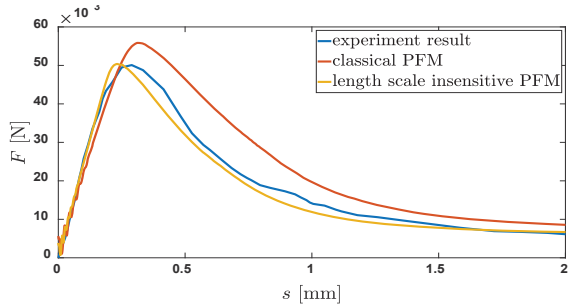

Figure 4.22 Comparison of force-displacement curve of the wedge splitting test

4.2.3.3 Mixed-mode failure of L-shaped panel test

The mixed mode failure of L-shaped panel test conducted by Winkler [104] is considered, and this example is used in [103,105] for brittle fracture. The specimen has a square shape with dimensions 500 mm × 500 mm × 100 mm, and fixed at the left bottom edge. A vertical force is applied at the position 30 mm away from the right face. The detailed dimensions, boundary condition, and load are shown in Figure 4.23. The material parameters used are Young's modulus E 20000 MPa, Poisson's ratio υ 0.18, fracture strength σ_f 2.5 MPa, and critical energy release rate G_c 0.13 N/mm. Force and displacement data at the load position are recorded during the simulation.

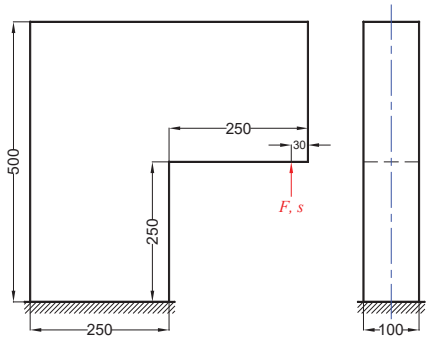

Figure 4.23 Dimensions, boundary condition, and load of the L-shaped panel test, unit [mm]

Considering the size of the specimen, local refinement with 2 mm element is also used along the fracture path, and bigger element is used at other positions. The model consists of 5896 elements and 12132 nodes. The length scale l used in the two models is 5 like in Section 4.2.3.2. Running time for this simulation is about 9 hours. The phase results are shown in Figure 4.24. Same thing found from the comparison is that a narrower crack band is observed for the length scale insensitive phase field model, and the phase in the proposed phase field model drops faster to 0 than the classical phase field model. To better see the difference of the two models, the phase field before fracture develops is also plotted, as shown in Figure 4.25. At the same time step, for the classical phase field model, non-zero phase value appears near the lower right face because of the high stress at that area, which would lead to some extra calculated fracture surface from Equation (4.3), but in experiment fracture does not develop at that area. For the length scale insensitive phase field model, because the negative phase is set as 0, no stiffness reduction happens near the lower right face.

(a) (b)

Figure 4.24 Phase result of the L-shaped panel test, (a) classical phase field model, (b) length scale insensitive phase field model

(a) (b)

Figure 4.25 Phase result of the L-shaped panel test before fracture develops, (a) classical phase field model, (b) length scale insensitive phase field model

The force-displacement curve is obtained for the two models, as shown in Figure 4.26. Some similar conclusions like in Section 4.2.3.2 are found. Because of the extra parameter used, the fracture strength can be adjusted based on the material's parameters, and a better force-displacement curve is obtained for the length scale insensitive phase field model.

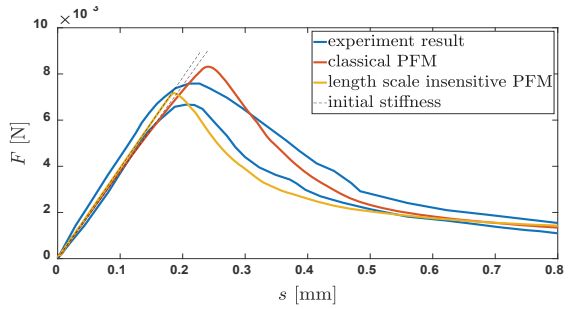

Figure 4.26 Comparison of force-displacement curve of the L-shaped panel test

4.2.3.4 Mixed-mode failure of notched beam test

The mixed mode failure of notched beam test conducted by Gálvez et al. [106] is considered, which has been used for verification in [50,107]. The specimen has a rectangular shape with dimensions 375 mm × 75 mm × 50 mm, and simply supported around the bottom center and fixed at the right bottom. A vertical downward force is applied at the position 100 mm away from the top center. The detailed dimensions, boundary condition, and load are shown in Figure 4.27. The material parameters used are Young's modulus E 38000 MPa, Poisson's ratio υ 0.2, fracture strength σ_f 3.0 MPa, and critical energy release rate G_c 0.07 N/mm. Force and displacement data at the load position are recorded during the simulation.

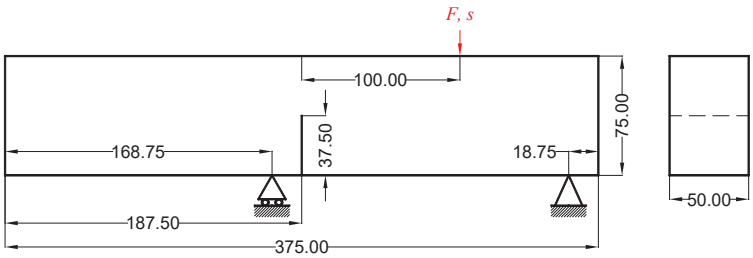

Figure 4.27 Dimensions, boundary condition, and load of the notched beam test, unit [mm]

Considering the size of the specimen, local refinement with 1.5 mm element along the fracture path is used, and bigger element size is used at other positions. The model consists of 8790 elements and 18198 nodes. The length scale l used in the two models is same as Section 4.2.3.2 and Section 4.2.3.3. Running

time for this simulation is about 15 hours. The phase results are shown in Figure 4.28. A narrower crack band is observed for the length scale insensitive phase field model. Because the high stress is spread along the fracture path, a much wider crack band is found for the classical phase field model, and the extra calculated fracture surface could lead to an error of the fracture energy and fracture surface. More investigation about the Γ convergence is still needed. Same thing as Section 4.2.3.3, the phase is 0 before fracture develops for the length scale insensitive phase field model, but some non-zero phase appears at boundary and notch for the classical phase field model, as shown in Figure 4.29.

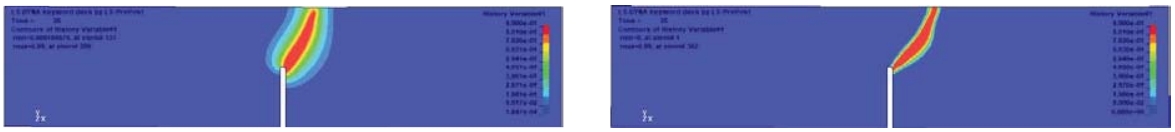

(a) (b)

Figure 4.28 Phase result of the notched beam test, (a) classical phase field model, (b) length scale insensitive phase field model

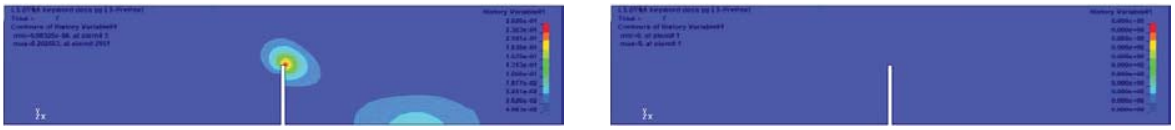

(a) (b)

Figure 4.29 Phase result of the notched beam test before fracture develops, (a) classical phase field model, (b) length scale insensitive phase field model

The reason to choose this experiment is that a perfect linear force-displacement curve is obtained in experiment [105]. Some similar conclusions like in Section 4.2.3.2 and Section 4.2.3.3 are found. Because of the extra parameter used, the fracture strength can be adjusted based on the material's parameters, and a better force-displacement curve is obtained for the length scale insensitive phase field model, as shown in Figure 4.30. For the length scale insensitive phase field model, this linear elastic behavior is recreated in the simulation, but there is a clear stiffness reduction before fracture develops for the classical phase field model.

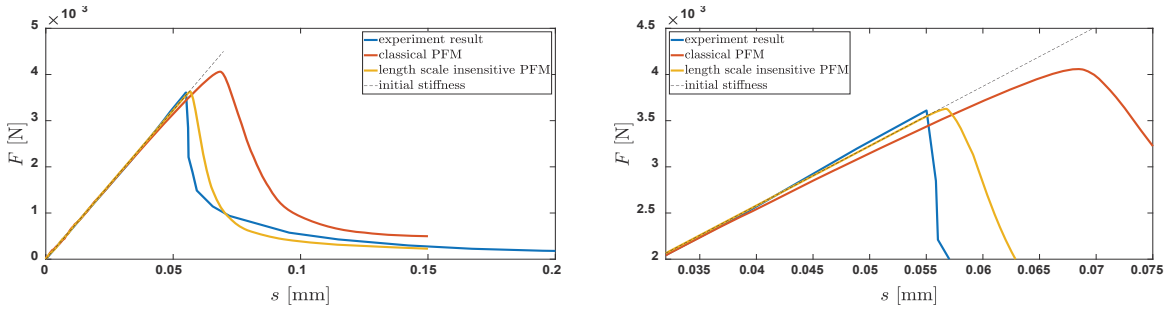

(a) (b)

Figure 4.30 Comparison of force-displacement curve of the notched beam test, (a) the whole range, (b) the range near the peak force

4.3 Different phase field model obtained from different degradation function

In the previous section, geometric function has been used to solve nonlinearity and inelasticity in the stress-strain curve of the classical phase field model. In this section, this problem is investigated from the point of view of degradation function, but the geometric function $\alpha(\varphi) = \varphi^2$ used in the classical phase field is adopted here. To better understand the influence of this degradation function on stress-strain curve, the relation between stress and phase is shown as

$$\sigma_{ij} = g(\varphi)\sigma_{ij}^{0+} + \sigma_{ij}^{0-} = g(\varphi)E\varepsilon_{ij}^{+} + E\varepsilon_{ij}^{-}. \tag{4.66}$$

From the equation above, stiffness E is only controlled by degradation function $g(\varphi)$, so this degradation function is the deep reason for stiffness reduction. Figure 4.31 shows the degradation function in the classical phase field model. From this figure, it is easy to see that degradation function decreases fast at the zero phase. However, for a good degradation function, its value should be almost 1 for a certain strain range to enable linearity of stress-strain curve, or an "ideal" degradation function like a step function. In this dissertation, the first derivative of degradation function at zero phase will be used to describe how fast the degradation function decreases.

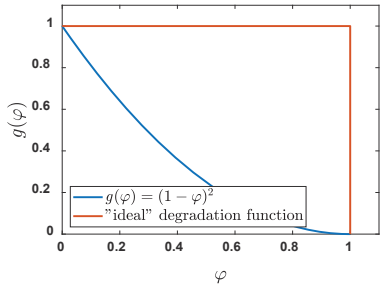

Figure 4.31 The relation between degradation function and phase

Before introducing the generalized polynomial degradation function, some degradation functions used in publications are summarized and analyzed first, as shown in Table 4.2, where the first derivative at zero phase is calculated. The first in Table 4.2 is the one in the classical phase field model. The second, third, and last in Table 4.2 are a function of only phase, which means a fixed degradation function and a fixed stress-strain curve. The analytical homogenous solution for the last is not available, which makes it difficult to further investigate properties based on homogeneous solution. To consider more possible stress-strain curves in one degradation function, it is better to have some extra variables to adjust this degradation function. The fourth in Table 4.2 is a good degradation function, but only second-order and third-order terms also limit its application. The fifth and sixth in Table 4.2 are more complicated, but this could lead to phase not in [0,1], and then difficult to get homogeneous solution. The disadvantage of the sixth is that its first derivative at zero phase can only be in $[-\infty, -1]$.

Table 4.2 Some degradation functions used in publications

Degradation function $g(\varphi)$	**Note**
$(1-\varphi)^2$ [43]	First derivative at zero phase is -2
$(1-\varphi)^2(2\varphi+1)$ [48]	First derivative at zero phase is 0
$(1-\varphi)^3(3\varphi+1)$ [48]	First derivative at zero phase is 0
$(3-s)\varphi^2+(s-2)\varphi^3$ [76]	First derivative at zero phase is $-s$
$\frac{(1-\varphi)^p}{(1-\varphi)^p+Q(\varphi)}$ [54]	$Q(\varphi)$ is a polynomial function
$\frac{\exp(\beta\varphi)-[\beta\varphi+(1-\beta)]\exp(\beta)}{(\beta-1)\exp(\beta)+1}$ [56]	First derivative at zero phase is in $[-\infty, -1]$
$1-\sin(\pi\varphi/2)$ [77]	First derivative at zero phase is $-\pi/2$

Zhang et al. [78] use the degradation function in [54] with $p=2$ and a quadratic polynomial function $Q(\varphi)=210\varphi(1-0.5\varphi)$, but an extra phase constraint function is used to get a successful simulation. The

reason could be that the algebraic fraction degradation function used makes it hard for phase in [0,1]. For this degradation function, all the five numerical homogenous solutions are shown in Figure 4.32. For a correct solution, its real part should increase from 0 to 1 with the increase of strain, but imaginary part should be 0. From this point, it can be seen that this degradation function does not make phase in [0,1].

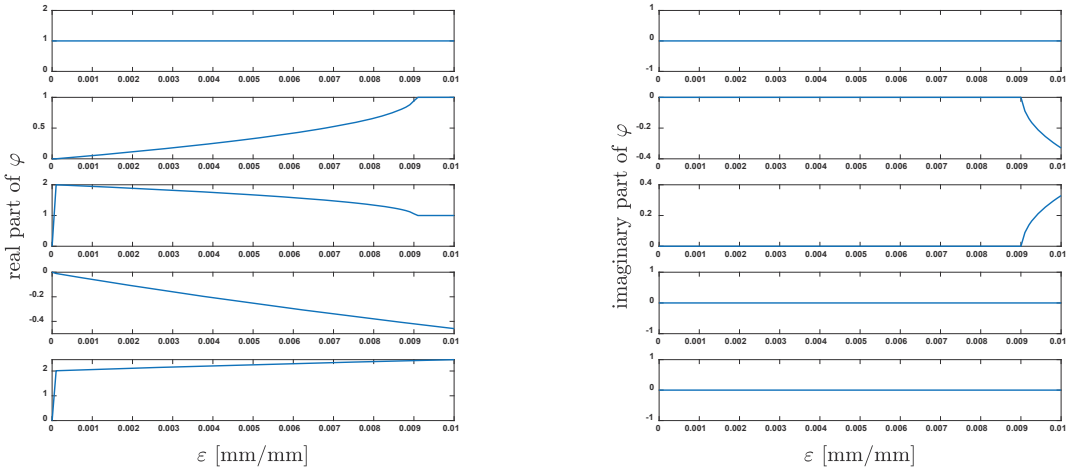

(a) (b)

Figure 4.32 Five homogenous solutions obtained from degradation function used in [78], (a) real part, (b) imaginary part

Based on the analysis above, generalized polynomial degradation functions are investigated to cover more stress-strain curves in one model, and some good properties of polynomial functions are explored. To check the influence of the first derivative of degradation function at zero phase, several different degradation functions are considered. First, follow the form of the classical phase field model, a third and a fourth order of degradation functions are considered, which have first derivative at zero phase equal to -3 and -4, respectively,

$$\begin{cases} g(\varphi) = (1-\varphi)^2, & \text{case 1} \\ g(\varphi) = (1-\varphi)^3, & \text{case 2} \\ g(\varphi) = (1-\varphi)^4, & \text{case 3} \end{cases}. \tag{4.67}$$

Case 1 is the degradation function in the classical phase field model. Next, to better control the rate of the decrease of degradation function at zero phase, one more constraint is considered as the first derivative of degradation function at zero phase, i.e.,

$$\begin{cases} g(\varphi = 0) = 1 \\ g(\varphi = 1) = 0 \\ g'(\varphi = 1) = 0 \\ g'(\varphi = 0) = c1 \end{cases}. \tag{4.68}$$

Four constraints give a third order polynomial degradation function. By setting a different $c1$ value in Equation (4.68), four more degradation functions are obtained as

$$\begin{cases} g(\varphi) = 1 - \varphi - \varphi^2 + \varphi^3, & \text{case 4} \\ g(\varphi) = 1 - 0.5\varphi - 2\varphi^2 + 1.5\varphi^3, & \text{case 5} \\ g(\varphi) = 1 - 0.1\varphi - 2.8\varphi^2 + 1.9\varphi^3, & \text{case 6} \\ g(\varphi) = 1 - 3\varphi^2 + 2\varphi^3, & \text{case 7} \end{cases}. \tag{4.69}$$

These seven cases are selected so that the constant $c1$ in Equation (4.68) for case 1 to case 7 are -2, -3, -4, -1, -0.5, -0.1, and 0, respectively. Figure 4.33 shows that degradation function decreases slower if this first derivative of degradation function at zero phase is closer to 0. Follow this pattern, more constrains can lead to even higher order degradation function, but it is necessary to check to avoid overfitting since degradation function should be monotonically decreasing. Even though the constant $c1$ in case 6 is -0.1, it is still very close to case 7 with constant $c1$ equal to 0. Higher order degradation function makes the phase field model a nonlinear problem, and Newton-Raphson method will be used to solve this nonlinear problem.

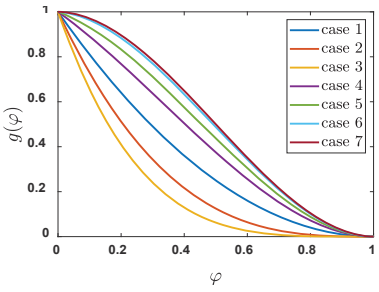

Figure 4.33 The relation between degradation function and phase for the seven cases

Similar as Section 4.2, homogeneous and nonhomogeneous solutions of these phase field models for a 1D bar under tensile load are investigated, which makes strain energy non-negative. Material parameters used include Young's modulus E 41000 MPa and critical energy release rate G_c 0.05 N/mm. For the 3D simulation in Section 4.3.2.1, one more material parameter needed is Poisson's ratio υ 0.18. For the rest of this section, case 1 will be called linear phase field model; case 2 to case 7 will be called nonlinear phase field model.

4.3.1 Analytical solution and FEM formulation of the proposed phase field model

4.3.1.1 Homogeneous solution of the proposed phase field model

For the homogeneous solutions of case 2 to case 7, if use $\alpha(\varphi) = \varphi^2$ and ignore spatial derivative of φ, the strong form of Equation (4.23~2) is reduced to

$$-g'(\varphi)\psi_s^{0+} - \frac{G_c}{l}\varphi = 0. \tag{4.70}$$

The first derivative of degradation function for the six cases are obtained as

$$g'(\varphi) = \begin{cases} -3(1-\varphi)^2, & \text{case 2} \\ -4(1-\varphi)^3, & \text{case 3} \\ -1-2\varphi+3\varphi^2, & \text{case 4} \\ -0.5-4\varphi+4.5\varphi^2, & \text{case 5} \\ -0.1-5.6\varphi+5.7\varphi^2, & \text{case 6} \\ -6\varphi+6\varphi^2, & \text{case 7} \end{cases}. \tag{4.71}$$

Put Equation (4.71) into Equation (4.70) and consider loading condition as strain, $\psi_s^{0+} = E\varepsilon^2/2$, φ can be calculated for these six cases. Depending on the order of degradation function, two or three solutions can be obtained for each case. For case 3, its analytical complex results are not shown because of its complexity, and only analytical real result is shown here. For case 2,

$$\varphi = \begin{cases} 1+\dfrac{G_c}{3El\varepsilon^2}+\sqrt{\left(1+\dfrac{G_c}{3El\varepsilon^2}\right)^2-1} \\ 1+\dfrac{G_c}{3El\varepsilon^2}-\sqrt{\left(1+\dfrac{G_c}{3El\varepsilon^2}\right)^2-1} \end{cases}; \tag{4.72}$$

for case 3,

$$\varphi = \sqrt[3]{\sqrt[2]{\frac{a^3}{27}+\frac{a^2}{4}}-\frac{a}{2}}-\frac{1}{3}\frac{a}{\sqrt[3]{\sqrt[2]{\frac{a^3}{27}+\frac{a^2}{4}}-\frac{a}{2}}}+1, \qquad a = \frac{G_c}{2El\varepsilon^2}; \tag{4.73}$$

for case 4,

$$\varphi = \begin{cases} \frac{1}{3} - \frac{G_c}{3El\varepsilon^2} + \sqrt{\left(\frac{1}{13} - \frac{G_c}{13El\varepsilon^2}\right)^2 - \frac{1}{3}} \\ \frac{1}{3} - \frac{G_c}{3El\varepsilon^2} - \sqrt{\left(\frac{1}{13} - \frac{G_c}{13El\varepsilon^2}\right)^2 - \frac{1}{3}} \end{cases}; \tag{4.74}$$

for case 5,

$$\varphi = \begin{cases} \frac{4}{9} - \frac{2G_c}{9El\varepsilon^2} + \sqrt{\left(\frac{2}{81} - \frac{G_c}{81El\varepsilon^2}\right)^2 - \frac{1}{9}} \\ \frac{4}{9} - \frac{2G_c}{9El\varepsilon^2} - \sqrt{\left(\frac{2}{81} - \frac{G_c}{81El\varepsilon^2}\right)^2 - \frac{1}{9}} \end{cases}; \tag{4.75}$$

for case 6,

$$\varphi = \begin{cases} \frac{28}{57} - \frac{10G_c}{57El\varepsilon^2} + \sqrt{\left(\frac{140}{3249} - \frac{50G_c}{3249El\varepsilon^2}\right)^2 + \frac{1}{57}} \\ \frac{28}{57} - \frac{10G_c}{57El\varepsilon^2} - \sqrt{\left(\frac{140}{3249} - \frac{50G_c}{3249El\varepsilon^2}\right)^2 + \frac{1}{57}} \end{cases}; \tag{4.76}$$

and for case 7,

$$\varphi = \begin{cases} 1 - \frac{G_c}{3El\varepsilon^2}. \\ 0 \end{cases} \tag{4.77}$$

The homogeneous solutions of these six nonlinear phase field models are plotted in Figure 4.34. Considering that a phase in [0,1] is the desired one, only the solution 1 in these figures are used to describe stress-strain curve later. For Figure 4.34 (b) of case 3, solution 2 and solution 3 are complex number that are not what we want, and absolute value is calculated and plotted here. From these figures, if the first derivative of degradation function at zero phase is closer to 0, phase result has a relative larger strain range with almost 0 value. And from Figure 4.34 (c) to Figure 4.34 (f), with the first derivative of degradation function at zero phase closer to 0, the two solutions get closer, and these two solutions intersect with each other when first derivative is 0.

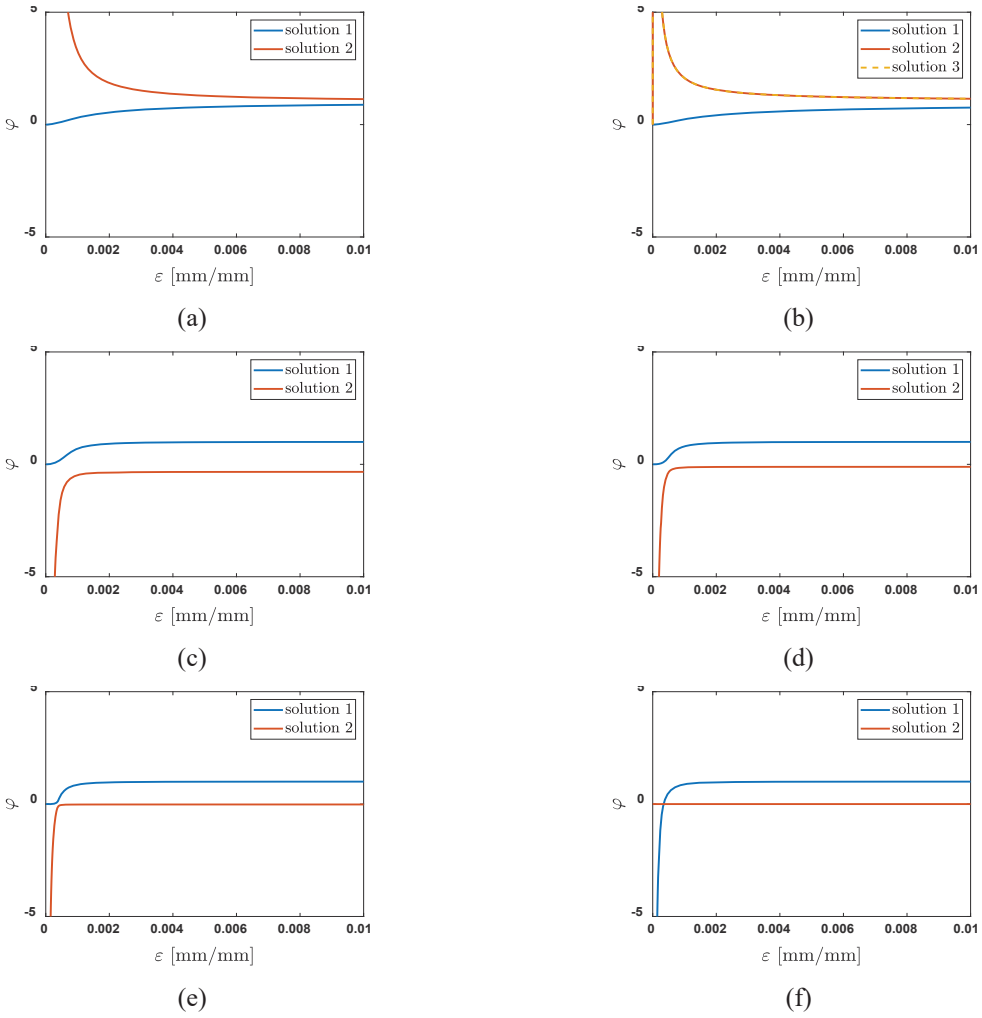

Figure 4.34 Homogenous solution, (a) case 2, (b) case 3, (c) case 4, (d) case 5, (e) case 6, (f) case 7

For Figure 4.34 (f) of case 7, if negative phase is forced to be zero, there is no stiffness reduction for a certain strain range, which could give a "perfect" linear relation between stress and strain. The phase versus strain, and degradation function versus strain for these seven cases are shown in Figure 4.35. As we can see, if the first derivative of degradation function at zero phase is closer to 0, degradation function decreases slower, which leads to slower decrease of stiffness in stress-strain curve at small strain.

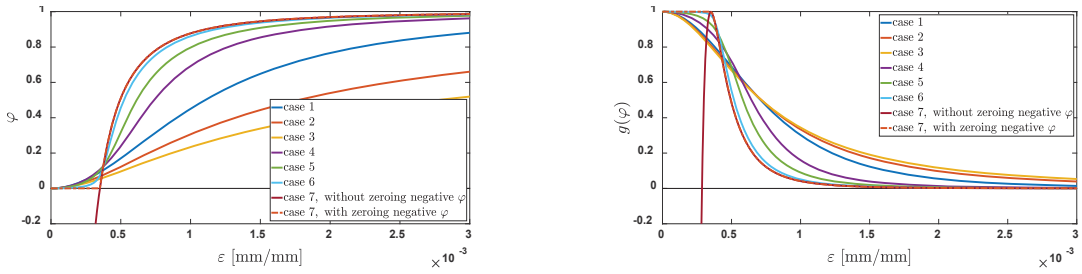

(a) (b)

Figure 4.35 (a) phase versus strain, (b) degradation function versus strain

Phase versus strain can be compared with damage factor in bilinear cohesive law. It is widely known that bilinear cohesive law can handle linear elastic behavior very well, and the damage factor used in [5] is shown in Figure 4.36 (a), where damage factor is 0 before stress reaches to fracture strength, and then damage factor increases to 1 with the increase of separation. $1 - g(\varphi)$ for phase field model case 3 and case 6 are plotted in Figure 4.36 (b). Case 6 agrees with the damage factor found in bilinear cohesive law much better than case 3. From this comparison, it is clear that by changing degradation function, a better degradation function for describing linear elastic behavior can be obtained.

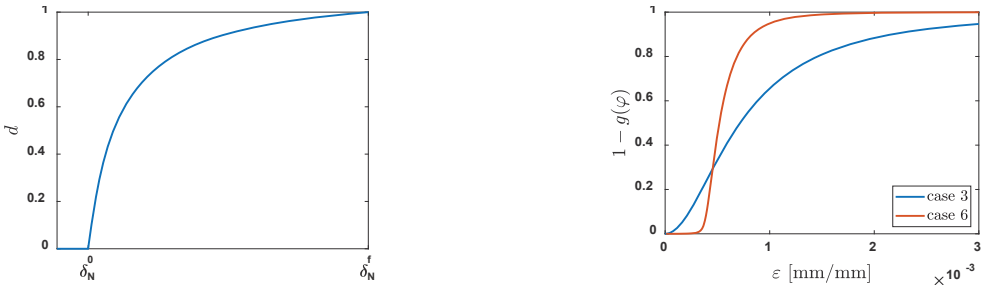

(a) (b)

Figure 4.36 (a) damage factor in bilinear cohesive law, (b) degradation function in phase field model

After the relation between phase and strain is obtained, the relation between stress and strain can be obtained by using $\sigma = g(\varphi)E\varepsilon$ since only tension is considered here. For the readability and avoid repetition, stress-strain curve is plotted, but the detailed formula of the stress is not shown here. From Figure 4.37, it is found that a larger first derivative (or closer to 0) has less stiffness reduction before stress reaches to fracture strength, which agrees with what found from the degradation function. One more thing to mention is that length scale is adjusted to get same fracture strength. With a larger first derivative, the length scale is also larger. Case 1 has length scale equal to 1, and case 6 could have a length scale as large as

3.0250 to get same fracture strength. What's more, according to the investigation in [43], it is suggested that l/h should be larger than 2 (h represents element size here). From these two points, the practical significance of this finding is that, compared with the classical phase field model, linear elastic behavior can be obtained even with larger element size for case 6.

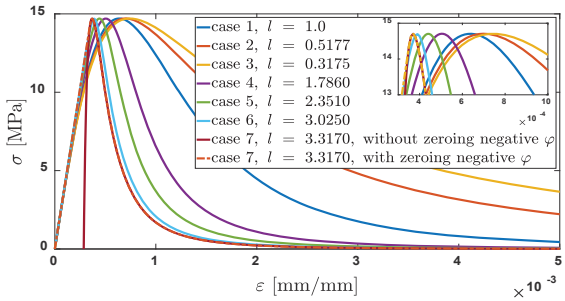

Figure 4.37 Stress-strain curve for the seven cases

Even though phase zeroing is used for case 7 to get homogeneous and nonhomogeneous solutions here, it does not mean that phase zeroing is totally correct. For case 7, the range of phase from $\varphi(x) = e^{-|x|/l}$ (according to crack surface derivation) over the whole x domain $x \in [-\infty, +\infty]$ is [0,1], but the range of phase from $\varphi(\varepsilon) = 1 - G_c/3El\varepsilon^2$ (according to homogenous solution) over the whole strain domain $\varepsilon \in [-\infty, +\infty]$ is $[-\infty, 1]$. In this situation, phase zeroing on $\varphi(\varepsilon)$ would definitely decrease the limits of integration for fracture surface calculation that should be over the whole x domain $x \in [-\infty, +\infty]$, and then problem could happen with Γ convergence. However, this kind of degradation function is used in [48,76], see Table 4.2. To avoid this Γ convergence issue, case 6 will be my choice for later simulations in Section 4.3.2, not case 7.

4.3.1.2 Nonhomogeneous solution of the proposed phase field model

Nonhomogeneous solution can be obtained following the procedure in Section 4.2.1 and Section 4.2.2, but it does not provide too much useful information compared with homogeneous solution. Because phase profile $\varphi(x)$ is derived from fracture surface density function [43], which has nothing to do with degradation function, the nonhomogeneous solution should be same for the seven cases. Here, only the fracture situation with maximum phase equal to 1 and same fracture strength is plotted, see Figure 4.38.

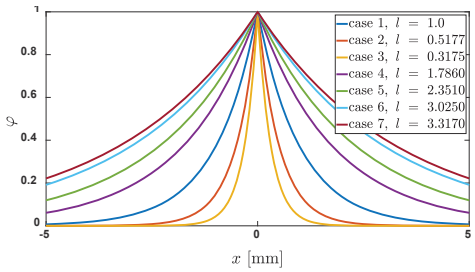

Figure 4.38 Nonhomogeneous solutions for the seven cases

4.3.1.3 Nonlinear FEM formulation (Newton-Raphson method) of the proposed phase field model

Only the FEM formulation of phase field is presented here. For the strong form in Equation (4.23~2), without considering kinetic energy from phase field, it can be rewritten as

$$\Delta\varphi - \frac{1}{lG_c}\left[g'(\varphi)H + \frac{G_c}{l}\varphi\right] = 0. \tag{4.78}$$

Since this equation is a nonlinear FEM problem now, phase cannot be directly solved like the linear phase field model, but delta phase can be solved by using Newton-Raphson method. For the convenience to show this derivation, the second term at left-hand side in Equation (4.78) is expressed as $F(\varphi)$, i.e., $F(\varphi) = -\frac{1}{lG_c}\left[g'(\varphi)H + \frac{G_c}{l}\varphi\right]$, so

$$\Delta\varphi + F(\varphi) = 0. \tag{4.79}$$

Galerkin method is still used to construct the weak form of this equation as

$$\int_{\Omega} N_i^T[\Delta\varphi + F(\varphi)]\mathrm{d}V = 0. \tag{4.80}$$

Consider the first-order Taylor series, $\Delta\varphi$ and $F(\varphi)$ can be expressed as

$$\Delta\varphi = \Delta\varphi_0 + \Delta(\varphi - \varphi_0) = \Delta\varphi_0 + \Delta\delta\varphi, \tag{4.81}$$

$$F(\varphi) = F(\varphi_0) + F'(\varphi_0)(\varphi - \varphi_0) = F(\varphi_0) + F'(\varphi_0)\delta\varphi, \tag{4.82}$$

where, φ_0 is the phase result obtained from previous time step. Put Equations (4.81) and (4.82) back to Equation (4.80), the weak form can be updated as

$$\int_{\Omega} N_i^T[\Delta\varphi_0 + \Delta\delta\varphi + F(\varphi_0) + F'(\varphi_0)\delta\varphi]\mathrm{d}V = 0. \tag{4.83}$$

Rearranging the delta phase to left-hand side and all the other terms to right-hand side gives

$$\int_{\Omega} N_i^T [\Delta\delta\varphi + F'(\varphi_0)\delta\varphi]\mathrm{d}V = -\int_{\Omega} N_i^T [\Delta\varphi_0 + F(\varphi_0)]\mathrm{d}V\,. \tag{4.84}$$

For the two terms $N_i^T \Delta\delta\varphi$ and $N_i^T \Delta\varphi_0$, using integration by parts and divergence theorem, and considering the boundary condition in Equation (4.27~4) ($\nabla\varphi \cdot \boldsymbol{n} = 0$) gives

$$\int_{\Omega} N_i^T \Delta\delta\varphi \mathrm{d}V = \int_{\partial\Omega} N_i^T \nabla\delta\varphi \cdot \boldsymbol{n}\mathrm{d}A - \int_{\Omega} B_i^T \nabla\delta\varphi \mathrm{d}V = -\int_{\Omega} B_i^T \nabla\delta\varphi \mathrm{d}V\,, \tag{4.85}$$

$$\int_{\Omega} N_i^T \Delta\varphi_0 \mathrm{d}V = \int_{\partial\Omega} N_i^T \nabla\varphi_0 \cdot \boldsymbol{n}\mathrm{d}A - \int_{\Omega} B_i^T \nabla\varphi_0 \mathrm{d}V = -\int_{\Omega} B_i^T \nabla\varphi_0 \mathrm{d}V\,. \tag{4.86}$$

Putting Equations (4.85) and (4.86) back to Equation (4.84) gives

$$\int_{\Omega} [B_i^T \nabla\delta\varphi - F'(\varphi_0) N_i^T \delta\varphi]\mathrm{d}V = \int_{\Omega} \left[N_i^T F(\varphi_0) - B_i^T \nabla\varphi_0\right]\mathrm{d}V\,. \tag{4.87}$$

By using the finite element expression of phase and phase gradient,

$$\begin{cases} \nabla\delta\varphi = B_j \delta\varphi_j \\ \delta\varphi = N_j \delta\varphi_j \\ \nabla\varphi_0 = B_j \varphi_{0j} \end{cases}, \tag{4.88}$$

Equation (4.87) is further updated as

$$\int_{\Omega} [B_i^T B_j - F'(\varphi_0) N_i^T N_j]\delta\varphi_j \mathrm{d}V = \int_{\Omega} \left[N_i^T F(\varphi_0) - B_i^T B_j \varphi_{0j}\right]\mathrm{d}V\,. \tag{4.89}$$

According to iso-parametric element and numerical integration, the tangent stiffness matrix and unbalanced force vector are obtained as

$$\boldsymbol{K}_{ij}^t = \int_{\Omega} [B_i^T B_j - F'(\varphi_0) N_i^T N_j]|\boldsymbol{J}|\mathrm{d}\xi\mathrm{d}\eta\mathrm{d}\varsigma\,, \tag{4.90}$$

$$\boldsymbol{F}_i^u = \int_{\Omega} \left[N_i^T F(\varphi_0) - B_i^T B_j \varphi_{0j}\right]|\boldsymbol{J}|\mathrm{d}\xi\mathrm{d}\eta\mathrm{d}\varsigma\,. \tag{4.91}$$

Then the unknow delta phase can be solved by

$$\boldsymbol{K}^{\boldsymbol{t}} \delta\boldsymbol{\varphi} = \boldsymbol{F}^u. \tag{4.92}$$

The new phase at next time step is obtained by adding delta phase to the phase in the last time step as

$$\boldsymbol{\varphi} = \boldsymbol{\varphi}_0 + \delta\boldsymbol{\varphi}. \tag{4.93}$$

Usually, one iteration does not make the solution convergent. To solve this, L_2 norm of delta phase is calculated as $L_2 = |\delta\boldsymbol{\varphi}|/n$, and only if the condition in Equation (4.94) is satisfied, the calculation will move to next time step. 0.01 is small enough for two adjacent iteration, and this could guarantee the convergence of the phase field.

$$L_2 = \frac{|\delta\boldsymbol{\varphi}|}{n} \leq 0.01 \tag{4.94}$$

4.3.2 Numerical verification of the phase field model using different degradation function

4.3.2.1 Tensile test of different phase field model

A tensile test is used to show the difference of these phase field models. The Dimensions, boundary condition, and load of this tensile test are totally same as that in Section 4.2.3.1, so no more description about this FEM model is made here.

Two simulations are conducted to check the properties of linear phase field model for case 1. First one is about the linearity of brittle materials. Three different length scale l 0.5, 1.0, and 2.0 are used in the simulation up to the fracture of the bar. The displacement load and stress-strain curve results for this simulation are shown in Figures 4.39 (a) and 4.40 (a), respectively. As shown in Figure 4.39 (a), the stress-strain curve obtained from tensile test is much different from the homogeneous solution. A clear stiffness reduction happens before the bar breaks, which conflicts with the linearity property of brittle materials. However, with the decrease of length scale l, fracture strength increases and linearity property gets better, which makes sense because damaged area is smaller now.

Second one is about the elasticity of brittle materials. A process with loading, unloading, and reloading is used to check this property. The displacement load and stress-strain curve results for this simulation are shown in Figures 4.39 (b) and 4.40 (b), respectively. As shown in Figure 4.40 (b), even though the linearity is found during unloading and reloading, this unloading does not follow the original stress-strain curve, which means elasticity is not followed in this model. One more thing to note is that the stiffness determined

from the strain energy threshold from the first load cycle is less than the Young's modulus of this material, which shows the possible issue of setting strain energy threshold to solve stiffness reduction problem.

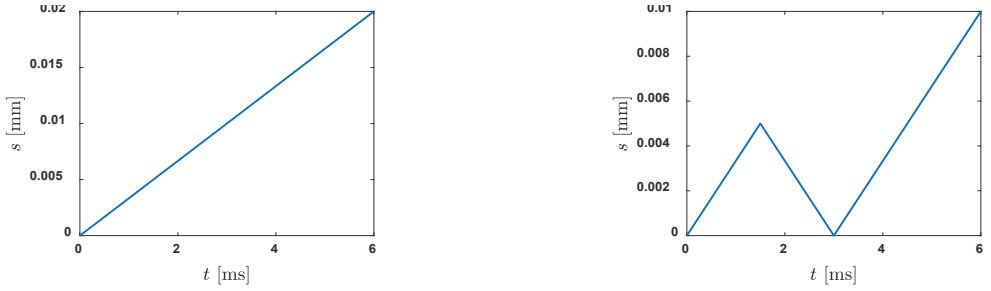

(a) (b)

Figure 4.39 Displacement load at right end, (a) no unloading to fracture, (b) with unloading to fracture

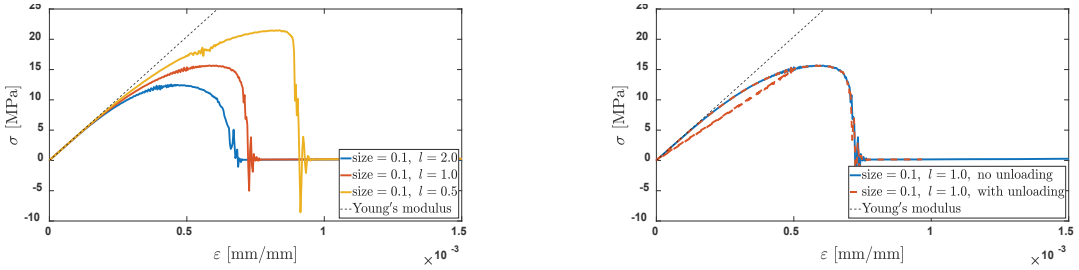

(a) (b)

Figure 4.40 Stress-strain curve for linear phase field model, (a) no unloading to fracture (nonlinear), (b) with unloading to fracture (nonelastic)

Newton-Raphson method can be used to solve nonlinear problem, but it does not limit to nonlinear problem. To verify the correctness of the nonlinear FEM formulation and the correctness of the use of Newton-Raphson method in LS-DYNA, the linear phase field model is also solved by Newton-Raphson method. The obtained stress-strain curve from no-iteration method and with-iteration method (Newton-Raphson method) are shown in Figure 4.41, and the two solutions are almost same, only a small difference after the bar breaks. From this comparison, Newton-Raphson method works well in this dissertation.

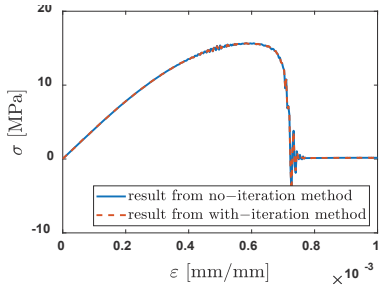

Figure 4.41 Stress-strain curve obtained from no-iteration method and with-iteration method

Linearity and elasticity properties are also investigated for the nonlinear phase field model from case 2 to case 7. For the simplicity of this tensile test, length scale equal to 1.0 is used in all the seven cases, and stress-strain curves obtained are shown in Figure 4.42. It is clear to see that a larger first derivative (or closer to 0) gives a stress-strain curve closer to brittle material and a higher fracture strength, which agrees with the finding about length scale from homogeneous solution. Compared with case 1, case 6 is more suitable for brittle materials, and a larger fracture strength for case 6 means that larger element can be used and more computationally efficient.

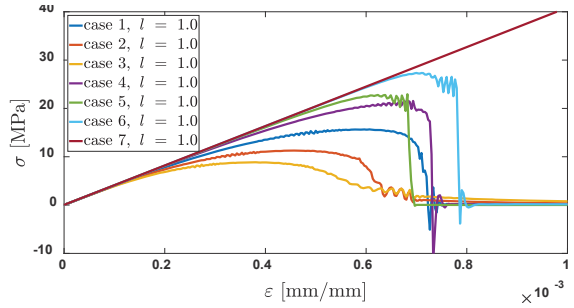

Figure 4.42 Stress-strain curves obtained from the seven cases

From the investigation in [43], it is suggested that l/h should be larger than 2. This empirical formula is also investigated here. Length scale $l = 1.0$ for both case 3 and case 6 are simulated with element size 0.1, 0.2, and 0.5 mm, which gives l/h 10, 5, and 2, respectively. From Figure 4.43, the results obtained from l/h equal to 10, 5, and 2 are almost same, which means the empirical formula is good in this simulation. It is also found that by using a larger length scale $l = 2.0$, case 6 has a smaller fracture strength. From this comparison, case 6 can still captures the linear elastic behavior even with larger length scale, which could mean larger element size and better computational efficiency in some large-scale simulations.

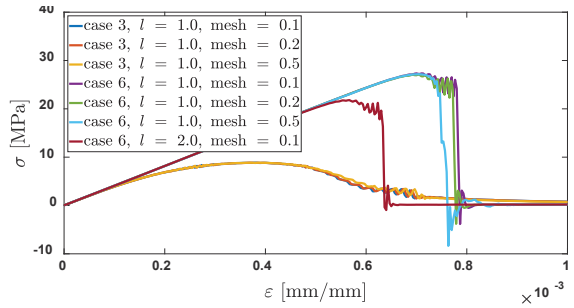

Figure 4.43 The investigation of the relation between length scale and element size

Following the same idea, if a degradation function decreases slowly at an even larger phase range, it would be more suitable for brittle materials and have a larger fracture strength under the same length scale. Apart from the constrains in Equation (4.68), three more higher order degradation functions can be obtained by considering extra constrains as follow,

$$\{g(\varphi = \varphi^*) = c2, \quad \text{fourth order}, \tag{4.95}$$

$$\begin{cases} g''(\varphi = 0) = 0 \\ g(\varphi = \varphi^*) = c2' \end{cases} \quad \text{fifth order}, \tag{4.96}$$

$$\begin{cases} g''(\varphi = 0) = 0 \\ g'''(\varphi = 0) = 0, \\ g(\varphi = \varphi^*) = c2 \end{cases} \quad \text{sixth order}, \tag{4.97}$$

where, φ^* is a number between 0 and 1. $g(\varphi = \varphi^*) = c2$ can be used in fine tuning for a wanted degradation.

The three higher order degradation function versus phase are plotted in Figure 4.44 (a). It is clear to see that these three higher order degradation functions decrease much slower compared with the previous case 3 and case 6. And these degradation functions are also applied in the same tensile test again. Fifth order and sixth order do not break in the simulation because of its high fracture strength. Fourth order breaks with a much higher fracture strength, and the linearity is perfectly kept in its stress-strain curve. By using different degradation function, this proposed nonlinear phase field model could also be a length scale insensitive phase field model.

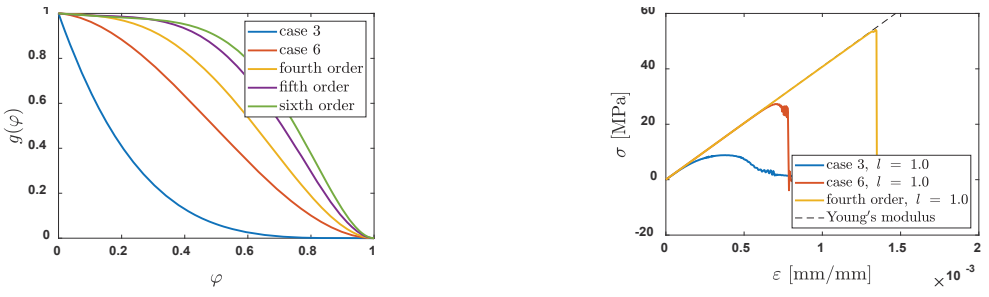

(a) (b)

Figure 4.44 (a) higher order polynomial degradation function, (b) comparison of stress-strain curves obtained from different degradation functions

4.3.2.2 Mode I failure of single-edge notched beam

The single-edge notched beam test conducted by Hoover et al. [108] is considered, which has been used for verification in many papers [109,110]. A comprehensive set of experimental data based on three point bending of single edge notched beam is presented in [108]. The specimen has a rectangular shape with dimensions of 223 mm × 93 mm × 40 mm, which is simply supported at both sides 11 mm away from the edge. A vertical notch is made up to 14 mm from the middle bottom of the specimen. Vertical force is applied at the top center of the specimen. The detailed dimensions, boundary condition, and load are shown in Figure 4.45. The material parameters used are Young's modulus E 41000 MPa, Poisson's ratio υ 0.17, fracture strength σ_f 3.5 MPa, and critical energy release rate G_c 0.07 N/mm. Force and displacement data are recorded during the simulation.

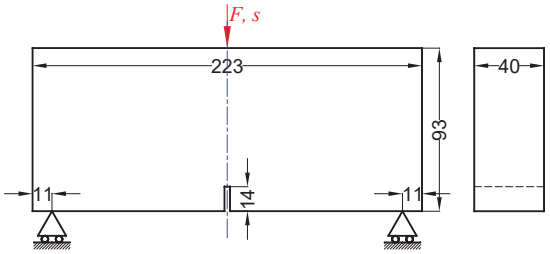

Figure 4.45 Dimensions, boundary condition, and load of the single-edge notched beam test, unit [mm]

Hexahedron element is used to mesh the specimen. Considering the size of the specimen and the time needed for simulation, local refinement with about 1 mm element along the fracture path is used, but larger element is used at other positions. To show the difference caused by degradation function, case 3 and case 6 are compared here. Because same length scale leads to different fracture strength for these two cases, length scale is adjusted separately for these two cases, case 3 with l equal to 2.0 and case 6 with l equal to 3.4. The phase field results obtained for these two cases are shown in Figure 4.46. It is clear that case 3 with higher nonlinearity in stress-strain curve has a larger crack area. However, the crack area for case 6 is more localized along the crack path, which is true for brittle materials that have smaller damage zone near the crack tip.

(a) (b)

Figure 4.46 Phase field results obtained from different cases, (a) case 3, (b) case 6

The force-displacement curves obtained for the two cases are shown in Figure 4.47. Even though both two models agree somehow with experiment data, case 6 is closer to experiment data. One clear difference happens before reaching peak force. Case 6 almost has no stiffness reduction, but clear stiffness reduction happens in case 3 before the peak force. After the peak force, the force in case 6 drops fast, but case 3 drops slowly, which could be because of the larger damage zone in case 3. Another thing is peak force, even with the smallest allowable length scale for case 3 (2.0 used in simulation), it still has a peak force lower than experiment result. To solve this issue, a smaller element and a smaller length scale should be used, which could give a higher fracture strength and higher peak force. However, case 6 can handle this problem even with a larger element and larger length scale.

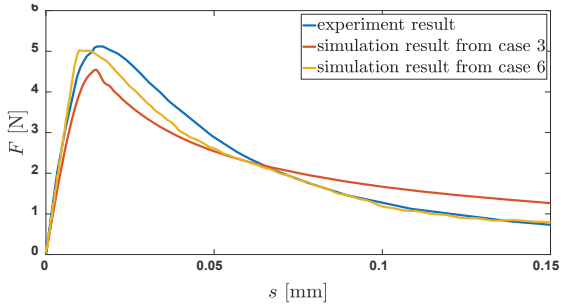

Figure 4.47 Force-displacement curves obtained from different cases, (a) case 3, (b) case 6

4.3.2.3 Mixed-mode failure of single-edge notched plate

The single-edge notched plate test conducted by Ambati et al. [111] is considered. The specimen is a notched plate, with a rectangular shape of dimensions 65 mm × 120 mm. The specimen is fixed at lower pin, and load is applied at top pin, and a hole offset from the center is used to induce mixed-mode fracture. A horizontal 10 mm notch is made 55 mm below the top surface. The detailed dimensions, boundary condition, and load are shown in Figure 4.48. The material parameters used are Young's modulus E 41000

MPa, Poisson's ratio υ 0.22, and critical energy release rate G_c 2.28 N/mm. Force and displacement data are recorded during the simulation.

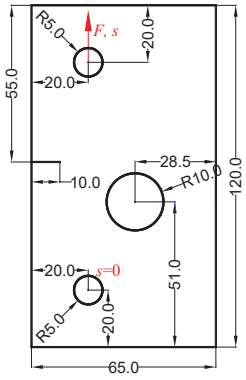

Figure 4.48 Dimensions, boundary condition, and load of the notched plate with hole test, unit [mm]

Hexahedron element is also used to mesh the specimen. Considering the smaller size of the specimen, local refinement with about 0.5 mm element along the fracture path is used, but larger element is used at other positions. By using the minimum length scale $l = 1.0$ in this simulation, phase field results obtained from case 3 and case 6 are shown in Figure 4.49. For case 3, there is no clear fracture like that in experiment, and the high phase is spread out over a large area. However, for case 6, the fracture path is almost same as experiment results.

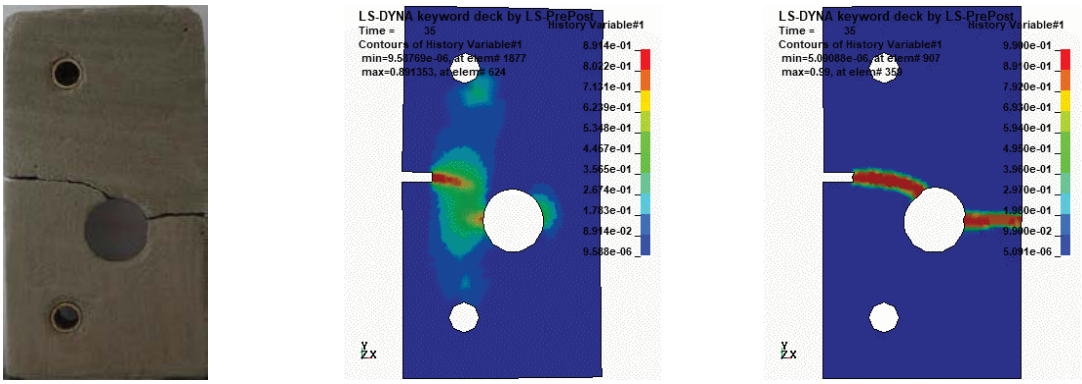

(a) (b) (c)

Figure 4.49 Phase field results obtained from different cases, (a) experiment, (b) case 3, (c) case 6

The force-displacement curve is obtained for these two cases, as shown in Figure 4.50. For this simulation, a fixed length scale $l = 1.0$ is used for both cases. Because no fracture happens in case 3, there is no force drop in its force-displacement curve, which is totally different from the experiment. The stiffness

reduction is very clear for case 3 in this simulation. Case 6 almost has no stiffness reduction before the peak force, and force drops fast after it breaks. The peak force in case 6 is a little lower than experiment, and this could also be solved by using a smaller element and a smaller length scale. Compared with $l = 0.25$ used in [112], a relatively larger length scale $l = 1.0$ for case 6 in this dissertation can still capture the force-displacement curve well.

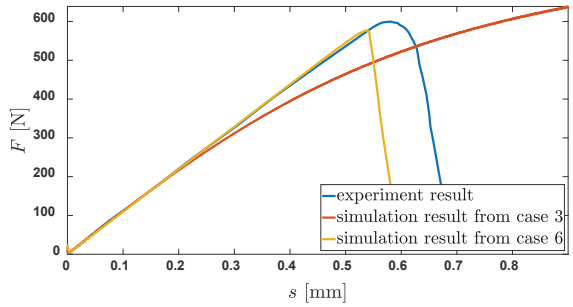

Figure 4.50 Force-displacement curves obtained from different cases, (a) case 3, (b) case 6

5 Phase field modeling of ductile fracture

In this section, phase field model for ductile fracture is investigated. Based on the ductile material with isotropic hardening, phase field model is coupled into this material. One difference from the classical phase field model for brittle fracture is the calculation of strain energy, where strain energy is not limited in the linear elastic range. To model the degradation of material, parameters for ductile material with isotropic hardening are multiplied with degradation function, i.e., Young's modulus, yield stress, and hardening modulus. Depending on the degradation function, both linear and nonlinear FEM formulation can also be used like the modeling of brittle fracture in Section 4.

5.1 Plasticity formulation of ductile material with isotropic hardening

For the ductile material with isotropic hardening, three important phenomenological properties are explained. First, there is an elastic domain, i.e., a range of stress within which the behavior of material can be considered as purely elastic, no evolution of plastic strain; second, if the material is further loaded beyond the yield stress, then plastic yielding or plastic flow takes place, i.e., the evolution of plastic strain; third, accompanying the evolution of plastic strain, an evolution of yield stress itself is also observed, which is known as hardening. These three properties correspond to the yield criterion, plastic flow, and hardening law, respectively. Here, a 1D elastoplastic constitutive model is presented to show how it works,

1. Elastoplastic split of axial strain: $\varepsilon = \varepsilon^e + \varepsilon^p$,
2. Uniaxial elastic law: $\sigma = E\varepsilon^e$,
3. Yield function: $\Phi(\sigma, \sigma_y) = |\sigma| - \sigma_y$,
4. Plastic flow: $\dot{\varepsilon}^p = \dot{\vartheta}\mathrm{sign}(\sigma)$,
5. Hardening law: $\sigma_y = \sigma_y(\bar{\varepsilon}^p)$, $\dot{\bar{\varepsilon}}^p = \dot{\vartheta}$,
6. Loading/ unloading criterion: $\Phi \leq 0$, $\dot{\vartheta} \geq 0$, $\Phi\dot{\vartheta} = 0$,

where, sign is the signum function; $\dot{\vartheta}$ can be further expressed as $\dot{\vartheta} = |\dot{\varepsilon}^p| = \dot{\bar{\varepsilon}}^p$; $\bar{\varepsilon}^p$ is accumulated plastic strain (a positive number for both tensile and compressive situations). For isotropic hardening in 1D case,

the yield stress is assumed to be update at the same time for both tensile and compressive directions, see stress-strain curve in Figure 5.1 (a), where stresses at points b and e are respectively equal and opposite to stresses at points c and d. Figure 5.1 (b) shows the isotropic hardening in 2D case, where yield surface expands in all directions, and different from kinematic hardening, the center of yield surface does not move during plastic flow.

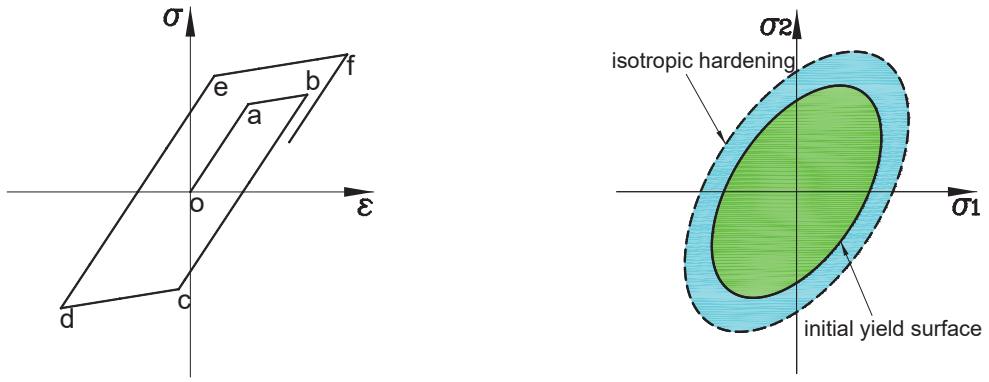

(a) (b)

Figure 5.1 Evolution of yield stress in ductile material with isotropic hardening, (a) stress-strain curve in 1D case, (b) yield surface in 2D case

5.1.1 Von Mises yield criterion

In 3D case, yield criterion is a little different, and Von Mises yield criterion is one of the most adopted criteria for the plasticity of materials. The plasticity formulation will be derived based on deviatoric component, so at first deviatoric stress and deviatoric strain are shown as

$$S_{ij} = \sigma_{ij} - \frac{1}{3}\sigma_{ij}\delta_{ij}, \tag{5.1}$$

$$Y_{ij} = \varepsilon_{ij} - \frac{1}{3}\varepsilon_{ij}\delta_{ij}, \tag{5.2}$$

where, S_{ij} is deviatoric stress; σ_{ij} is original stress; Y_{ij} is deviatoric strain; ε_{ij} is original strain; δ_{ij} is Kronecker delta function. Deviatoric stress S_{ij} is the component that acts to change the volume of the material only; hydrostatic pressure $\sigma_{ij}\delta_{ij}/3$ is the component that acts to change the shape only. The Von Mises yield criterion states that yielding occurs when the effective stress or Von Mises stress reaches the yield stress, and it is expressed in terms of the second invariant of the deviatoric stresses as

$$\sigma_V = \vec{s}^{n+1} = \sqrt{\frac{3}{2}\vec{S}_{ij}^{n+1}\vec{S}_{ij}^{n+1}}, \tag{5.3}$$

$$\Phi(\sigma, \sigma_y) = \vec{s}^{n+1}\vec{s}^{n+1} - \sigma_y^{n+1}\sigma_y^{n+1} \leq 0, \tag{5.4}$$

where, σ_V is Von Mises stress; $\vec{s}^{n+1}$ is effective trial deviatoric stress; $\vec{S}_{ij}^{n+1}$ is trial deviatoric stress based on linear elastic stress prediction; $\vec{\bullet}$ means trial terms in this dissertation; $(n+1)$ means the time step. Equation (5.4) shows the Von Mises yield criterion. If Equation (5.4) is satisfied, $\vec{S}_{ij}^{n+1}$ will be equal to S_{ij}^{n+1}, otherwise $\vec{S}_{ij}^{n+1}$ will be modified to get the correct S_{ij}^{n+1}. According to radial return method, correct deviatoric stresses S_{ij}^{n+1} is obtained as

$$S_{ij}^{n+1} = \frac{\sigma_y^{n+1}}{\vec{s}^{n+1}}\vec{S}_{ij}^{n+1} = m\vec{S}_{ij}^{n+1}. \tag{5.5}$$

If it is in this situation, plastic flow and hardening law will be considered later. Figure 5.2 shows the radial return method for ductile material with isotropic hardening in 3D case. Point A represents the stress solution at nth time step, and point B corresponds to the linear elastic stress prediction at $(n+1)$th time step, and vector BC represents the stress correction. The OC/OB value equals the scale factor $\sigma_y^{n+1}/\vec{s}^{n+1} = m$ in Equation (5.5). Radial return means that linear elastic stress prediction point B would return back to yield surface along the radial direction OB. See [113] for more detailed information about this topic.

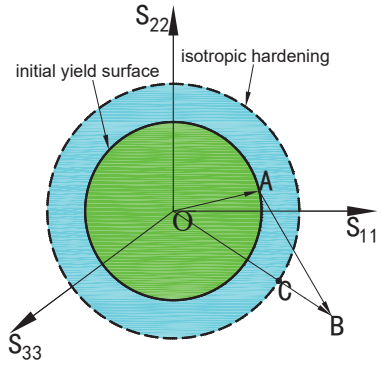

Figure 5.2 Radial return method for ductile material with isotropic hardening in 3D case

5.1.2 Plastic flow

Plastic flow, which relates the plastic strain increment to the current stress and the stress increment.

To obtain this relation, the Jaumann rate of the deviatoric stress S_{ij} is expressed first from deviatoric stress and deviatoric strain separately as

$$\dot{S}_{ij}^{J} = \dot{S}_{ij} - S_{ip}W_{pj} - S_{jp}W_{pi}, \tag{5.6}$$

$$\dot{S}_{ij}^{J} = 2G\dot{Y}_{ij}, \tag{5.7}$$

where, J means Jaumann; W is spin tensor; G is shear modulus. Combing Equations (5.6) and (5.7) gives the rate of deviatoric stress as

$$\dot{S}_{ij} = S_{ip}W_{pj} + S_{jp}W_{pi} + 2G\dot{Y}_{ij}. \tag{5.8}$$

Using Euler forward method, $\dot{S}_{ij}$ can be expressed as

$$\vec{S}_{ij}^{n+1} = S_{ij}^{n} + \dot{S}_{ij}^{n}\mathrm{d}t. \tag{5.9}$$

Put Equation (5.8) into Equation (5.9), the trial deviatoric stress at $(n+1)$th time step $\vec{S}_{ij}^{n+1}$ is expressed as

$$\vec{S}_{ij}^{n+1} = S_{ij}^{n} + \left(S_{ip}^{n}W_{pj}^{n} + S_{jp}^{n}W_{pi}^{n} + 2G\dot{Y}_{ij}^{n}\right)\mathrm{d}t = S_{ij}^{n} + \left(S_{ip}^{n}W_{pj}^{n} + S_{jp}^{n}W_{pi}^{n}\right)\mathrm{d}t + 2G\dot{Y}_{ij}^{n}\mathrm{d}t. \tag{5.10}$$

Define $\left(S_{ip}^{n}W_{pj}^{n} + S_{jp}^{n}W_{pi}^{n}\right)\mathrm{d}t$ as R_{ij}^{n} and write $S_{ij}^{n} + R_{ij}^{n}$ as SR_{ij}^{n}, Equation (5.10) can be further updated as

$$\vec{S}_{ij}^{n+1} = SR_{ij}^{n} + 2G\dot{Y}_{ij}^{n}\mathrm{d}t. \tag{5.11}$$

Note that $\dot{Y}_{ij}^{n}\mathrm{d}t$ is just the delta deviatoric strain ΔY_{ij}^{n}, and Equation (5.11) can be rewritten as

$$\vec{S}_{ij}^{n+1} = SR_{ij}^{n} + 2G\Delta Y_{ij}^{n}. \tag{5.12}$$

The next step is to determine the plastic strain increment. This can be found by subtracting the deviatoric part of the strain increment that is elastic from the total deviatoric increment, thus

$$\Delta Y_{ij}^{n,p} = \Delta Y_{ij}^{n} - \frac{S_{ij}^{n+1} - SR_{ij}^{n}}{2G} = \frac{\vec{S}_{ij}^{n+1} - S_{ij}^{n+1}}{2G} = \frac{1-m}{2G}\vec{S}_{ij}^{n+1}. \tag{5.13}$$

An increment of effective plastic strain is given by definition as

$$\Delta\gamma^{n,p} = \sqrt{\frac{2}{3}\Delta Y_{ij}^{n,p}\Delta Y_{ij}^{n,p}}, \tag{5.14}$$

and putting Equation (5.13) into Equation (5.14) gives

$$\Delta\gamma^{n,p} = \sqrt{\frac{2}{3}\left(\frac{1-m}{2G}\right)^2 \vec{S}_{ij}^{n+1}\vec{S}_{ij}^{n+1}} = \sqrt{\frac{2}{3}\left(\frac{1-m}{2G}\right)^2 \frac{2}{3}\vec{s}^{n+1}\vec{s}^{n+1}} = \frac{1-m}{3G}\vec{s}^{n+1}, \tag{5.15}$$

$$\Delta\gamma^{n,p} = \frac{\vec{s}^{n+1} - \sigma_y^{n+1}}{3G}. \tag{5.16}$$

At this point, the relation between the plastic strain increment and the current stress and the stress increment is obtained. $\Delta\gamma^{n,p}$ will be used to update yield stress for the next time step.

5.1.3 Hardening law

Hardening law, which specifies how the yield function is modified during plastic flow. For isotropic hardening, this property modifies the yield stress as follows

$$\sigma_y^{n+1} = \sigma_y^n + E^H \Delta\gamma^{n,p}, \tag{5.17}$$

$$E^H = \frac{EE^T}{E - E^T}, \tag{5.18}$$

where, E is Young's modulus; E^H is hardening modulus; E^T is tangent modulus. This relation can be derived from Figure 5.3. The strain increment $\mathrm{d}\varepsilon$ can be divided into elastic strain increment $\mathrm{d}\varepsilon^e$ and plastic strain increment $\mathrm{d}\varepsilon^p$ as

$$\mathrm{d}\varepsilon = \mathrm{d}\varepsilon^e + \mathrm{d}\varepsilon^p. \tag{5.19}$$

And the stress increment $\mathrm{d}\sigma$ can be calculated from $\mathrm{d}\varepsilon$, $\mathrm{d}\varepsilon^e$, and $\mathrm{d}\varepsilon^p$ separately as

$$\begin{cases} \mathrm{d}\sigma = E^T \mathrm{d}\varepsilon \\ \mathrm{d}\sigma = E\mathrm{d}\varepsilon^e \\ \mathrm{d}\sigma = E^H \mathrm{d}\varepsilon^p \end{cases}. \tag{5.20}$$

When these three strain increments satisfy the Equation (5.19), the relation among E, E^T, and E^H can be obtained as Equation (5.18).

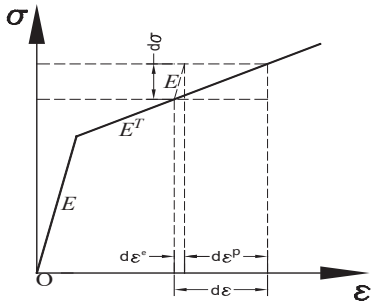

Figure 5.3 Hardening modulus obtained from tangent modulus

Above is the yield criterion, plastic flow, and hardening law in ductile material with isotropic hardening. Finally, the increment of plastic strain can be further updated if hardening law is considered. Put Equation (5.17) back into Equation (5.16) and simplify it, the plastic strain increment can be obtained from trial deviatoric stress and yield stress as Equation (5.22),

$$\Delta\gamma^{n,p} = \frac{\vec{s}^{n+1} - \sigma_y^n - E^H \Delta\gamma^{n,p}}{3G}, \tag{5.21}$$

$$\Delta\gamma^{n,p} = \frac{\vec{s}^{n+1} - \sigma_y^n}{3G + E^H}. \tag{5.22}$$

This plasticity formulation is implemented in LS-DYNA user-defined material subroutine. To make sure that the subroutine used in my code for ductile material with isotropic hardening is correct, a tensile test is investigated. Dimensions, boundary condition, and load for a tensile test are shown in Figure 5.4. Hexahedron element with full integration method and 0.1 mm size is used in the simulation. Material parameters used include Young's modulus 210000 MPa, Poisson's ratio 0.3, yield stress 120 MPa, and tangent modulus 10500 MPa. The almost same stress-strain curve as that obtained directly from LS-DYNA solver, shows the correctness of material subroutine for ductile material with isotropic hardening in this dissertation, see Figure 5.5.

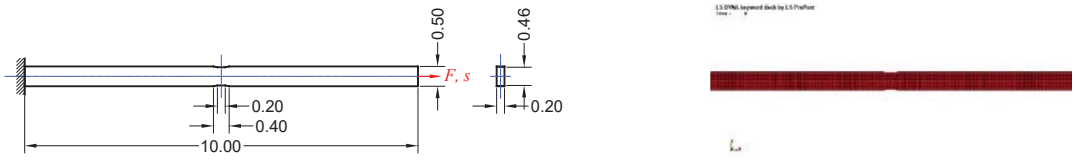

(a) (b)

Figure 5.4 (a) dimensions, boundary condition, and load of the tensile test, unit [mm], (b) finite element model

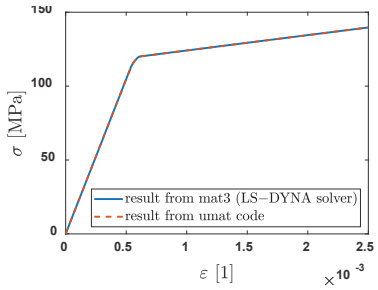

Figure 5.5 Stress-strain curve of a tensile test for ductile material with isotropic hardening

5.2 Governing equations of the phase field model for ductile fracture

Phase field modeling of ductile fracture has been investigated from different perspectives. Ambati et al. [114] propose a phase field model for ductile fracture of elastoplastic solids in the quasi-static kinematically linear regime, and it can capture the entire range of behavior of a ductile material exhibiting J2-plasticity. This model is further extended to the 3D finite strain setting in [115]. Miehe et al. [116] proposed a rigorous variational-based framework for the phase field modeling of ductile fracture in elastic-plastic solids undergoing large strains. Based on a linear perturbation analysis, Arriaga and Waisman [75] propose a stability framework to determine the onset of unstable crack growth, which leads to an analytical, energy-based criterion for the phase field model in linear elastic and visco-plastic materials. Fang et al. [117,118] present the implementation procedures of a staggered scheme for phase field fracture of elastoplastic solids in commercial finite element software Abaqus using subroutines UEL and UMAT. Based on the work of rate-independent phase-field damage model in [53], Loew et al. [119] extend the model to depend on the loading rate and time by incorporating rubber's strain-rate dependency in the constitutive description of the bulk, as well as in the damage driving force. Shi et al. [120] propose a plastic history field using the staggered algorithm scheme to perform the energy decomposition. As an efficient implementation of phase field model for ductile fracture, the method used in [117,118] will be followed in this section.

5.2.1 Derivation of governing equations

Similar to the derivation of governing equations for brittle fracture, kinetic energy, potential energy, and external work can be expressed as

$$\Psi_{kin}(\dot{\boldsymbol{u}},\dot{\varphi}) = \int_{\Omega} \frac{1}{2}\rho\dot{\boldsymbol{u}}\cdot\dot{\boldsymbol{u}}\mathrm{d}V + \int_{\Omega} \frac{1}{2}\varrho\dot{\varphi}\dot{\varphi}\mathrm{d}V\,, \tag{5.23}$$

$$\Psi_{pot}(\boldsymbol{u},\Gamma) \approx \int_{\Omega} \psi_s \mathrm{d}V + \int_{\Omega} G_c\gamma\mathrm{d}V\,, \tag{5.24}$$

$$\Psi_{ext}(\boldsymbol{u}) = \int_{\partial\Omega} \boldsymbol{t}\cdot\boldsymbol{u}\mathrm{d}A + \int_{\Omega} \boldsymbol{b}\cdot\boldsymbol{u}\mathrm{d}V\,, \tag{5.25}$$

where, γ without subscript i and j means crack surface density function, not same as that in Section 5.1 plasticity formulation. Then the Euler-Lagrange equation for the ductile material with isotropic hardening can be defined as

$$\begin{aligned} L = &\int_{\Omega} \frac{1}{2}\rho\dot{\boldsymbol{u}}\cdot\dot{\boldsymbol{u}}\mathrm{d}V + \int_{\Omega} \frac{1}{2}\varrho\dot{\varphi}\dot{\varphi}\mathrm{d}V - \int_{\Omega} g(\varphi)\psi_s^0\mathrm{d}V - \\ &\int_{\Omega} G_c\frac{1}{c}[\alpha(\varphi) + l^2|\nabla\varphi|^2]\mathrm{d}V + \int_{\partial\Omega} \boldsymbol{t}\cdot\boldsymbol{u}\mathrm{d}A + \int_{\Omega} \boldsymbol{b}\cdot\boldsymbol{u}\mathrm{d}V\,. \end{aligned} \tag{5.26}$$

Note that the strain energy in Equation (5.26) is not split into tensile part and compressive part, i.e., $\psi_s = g(\varphi)\psi_s^0$, and this is different from that for brittle fracture where $\psi_s = g(\varphi)\psi_s^{0+} + \psi_s^{0-}$, because this tensile part and compressive part split does not apply to ductile material now. In this dissertation, the split of strain energy is not considered, but more complicated split method of strain energy could be my future work.

Based on the same idea of the minimization of this Euler-Lagrange equation L, the governing equations can be derived. Basically, the governing equations of phase field model for ductile fracture in [117,118] is same as the model used in brittle fracture, but the strain energy is not limited in the linear elastic range. If geometric function $\alpha(\varphi) = \varphi^2$ is used in Equation (5.26) for ductile fracture, the governing equations can be updated as

$$\begin{cases} g(\varphi)\sigma_{ij,j}^{0+} + \sigma_{ij,j}^{0-} + b_i = \rho\ddot{u}_i \\ -g'(\varphi)\psi_s^0 - \dfrac{G_c}{l}\varphi + lG_c\Delta\varphi = \varrho\ddot{\psi} \end{cases}. \tag{5.27}$$

In [117,118], the strain energy under the stress-strain curve in Figure 5.5 is divided into three parts,

$$\psi_s^0 = \frac{1}{2}\boldsymbol{\varepsilon}^e{:}\boldsymbol{\sigma}_e + \sigma_y\varepsilon^p + \frac{1}{2}E^H\varepsilon^p\varepsilon^p = \frac{1}{2}E\boldsymbol{\varepsilon}^e{:}\boldsymbol{\varepsilon}^e + \sigma_y\varepsilon^p + \frac{1}{2}E^H\varepsilon^p\varepsilon^p, \tag{5.28}$$

where, ε^p is accumulated plastic strain. To enable the irreversibility of fracture, i.e., $\Gamma(t) \subset \Gamma(t+\Delta t)$, ψ_s^0

is equal to the maximum strain energy,

$$\psi_s^0 = \max\left(\frac{1}{2}E\boldsymbol{\varepsilon}^e:\boldsymbol{\varepsilon}^e + \sigma_y\varepsilon^p + \frac{1}{2}E^H\varepsilon^p\varepsilon^p\right). \tag{5.29}$$

After this, the Euler-Lagrange equation and the governing equations can be further updated as

$$\begin{aligned} L = \int_\Omega \frac{1}{2}\rho\dot{\boldsymbol{u}}\cdot\dot{\boldsymbol{u}}\mathrm{d}V + \int_\Omega \frac{1}{2}\varrho\dot{\varphi}\dot{\varphi}\mathrm{d}V - \int_\Omega g(\varphi)\max\left(\frac{1}{2}E\boldsymbol{\varepsilon}^e:\boldsymbol{\varepsilon}^e + \sigma_y\varepsilon^p + \frac{1}{2}E^H\varepsilon^p\varepsilon^p\right)\mathrm{d}V \\ - \int_\Omega G_c\left[\frac{1}{2l}\varphi^2 + \frac{l}{2}|\nabla\varphi|^2\right]\mathrm{d}V + \int_{\partial\Omega}\boldsymbol{t}\cdot\boldsymbol{u}\mathrm{d}A + \int_\Omega \boldsymbol{b}\cdot\boldsymbol{u}\mathrm{d}V, \end{aligned} \tag{5.30}$$

$$\begin{cases} g(\varphi)\sigma_{ij,j}^{0+} + \sigma_{ij,j}^{0-} + b_i = \rho\ddot{u}_i \\ -g'(\varphi)\max\left(\frac{1}{2}E\boldsymbol{\varepsilon}^e:\boldsymbol{\varepsilon}^e + \sigma_y\varepsilon^p + \frac{1}{2}E^H\varepsilon^p\varepsilon^p\right) - \frac{G_c}{l}\varphi + lG_c\Delta\varphi = \varrho\ddot{\psi} \end{cases}. \tag{5.31}$$

From Equations (5.30) and (5.31), the degradation function is applied to the parameters for ductile material with isotropic hardening, i.e., Young's modulus, yield stress, and hardening modulus, so the degradation of material in this dissertation is realized by decreasing these three material parameters.

This maximum strain energy will be replaced as H in the following derivations, i.e.,

$$H = \max\left(\frac{1}{2}E\boldsymbol{\varepsilon}^e:\boldsymbol{\varepsilon}^e + \sigma_y\varepsilon^p + \frac{1}{2}E^H\varepsilon^p\varepsilon^p\right). \tag{5.32}$$

In this dissertation, strain energy is obtained by integration

$$[\psi_s^0]_n = \int_0^\varepsilon \sigma\mathrm{d}\varepsilon, \tag{5.33}$$

or in a summation form as

$$[\psi_s^0]_n = [\psi_s^0]_{n-1} + \sum\sigma_{ij}\Delta\varepsilon_{ij}. \tag{5.34}$$

Same thing, the governing equations in Equation (5.31) are subject to time-dependent Dirichlet boundary and time-dependent Neumann boundary conditions as

$$\begin{cases} \boldsymbol{u} = \boldsymbol{u}^p, & \text{on } \partial\Omega_u\times[0,T] \\ \boldsymbol{\sigma}\cdot\boldsymbol{n} = \boldsymbol{t}^p, & \text{on } \partial\Omega_t\times[0,T] \\ \varphi = 1, & \text{on } \partial\Omega_\Gamma\times[0,T] \\ \nabla\varphi\cdot\boldsymbol{n} = 0, & \text{on } \partial\Omega\times[0,T] \end{cases}. \tag{5.35}$$

5.2.2 Degradation function

For the degradation function $g(\varphi)$ mentioned above, it has to satisfy some basic requirements, like

decreasing from 1 to 0 when phase increases from 0 to 1, and its first derivative should be in a small range to limit the driving force to be a small number when phase reaches to 1 [43]. Apart from these basic requirements, one more parameter investigated in this section is the first derivative of degradation function at zero phase like that in Section 4.3, see the Equation (5.36~4) below

$$\begin{cases} g(\varphi = 0) = 1 \\ g(\varphi = 1) = 0 \\ g'(\varphi = 1) = 0 \\ g'(\varphi = 0) = c1 \end{cases}. \tag{5.36}$$

Based on the different $c1$ (-2, -3, -4, -1, -0.5, -0.1, and 0), seven different degradation functions can be obtained as

$$\begin{cases} g(\varphi) = (1-\varphi)^2, & \text{case 1} \\ g(\varphi) = (1-\varphi)^3, & \text{case 2} \\ g(\varphi) = (1-\varphi)^4, & \text{case 3} \\ g(\varphi) = 1-\varphi-\varphi^2+\varphi^3, & \text{case 4} \\ g(\varphi) = 1-0.5\varphi-2\varphi^2+1.5\varphi^3, & \text{case 5} \\ g(\varphi) = 1-0.1\varphi-2.8\varphi^2+1.9\varphi^3, & \text{case 6} \\ g(\varphi) = 1-3\varphi^2+2\varphi^3, & \text{case 7} \end{cases}. \tag{5.37}$$

Note that case 1 here is the one used in the classical phase field model, and it leads to a linear FEM formulation of phase field model. Another two kinds of degradation function investigated are the one proposed by Wu [54] and sigmoid function. The sigmoid function is bounded, differentiable, monotonic, and has a first derivative which is bell shaped. To simplify the problem, only two independent parameters (a and b) are considered in this dissertation,

$$g(\varphi) = \frac{(1-\varphi)^2}{(1-\varphi)^2 + a\varphi(1+b\varphi)}, \tag{5.38}$$

$$g(\varphi) = 1 - \frac{1}{1+e^{-a(\varphi-b)}}. \tag{5.39}$$

To show the difference among these degradation functions, they are plotted in Figure 5.6. It is clear that degradation function decreases from 1 to 0 faster and faster from Figure 5.6 (a) to Figure 5.6 (b), and to Figure 5.6 (c). Sigmoid function has a small range of phase to let degradation function decrease from 1 to 0. The influence of this difference on stress-strain curve will be investigated in Section 5.4.1. Except the

case 1 in Equation (5.37), all the other degradation functions lead to a nonlinear FEM formulation of phase field model, and phase cannot be solved directly for each time step, but the delta phase can be obtained from Newton-Raphson method like that in Section 4.3.

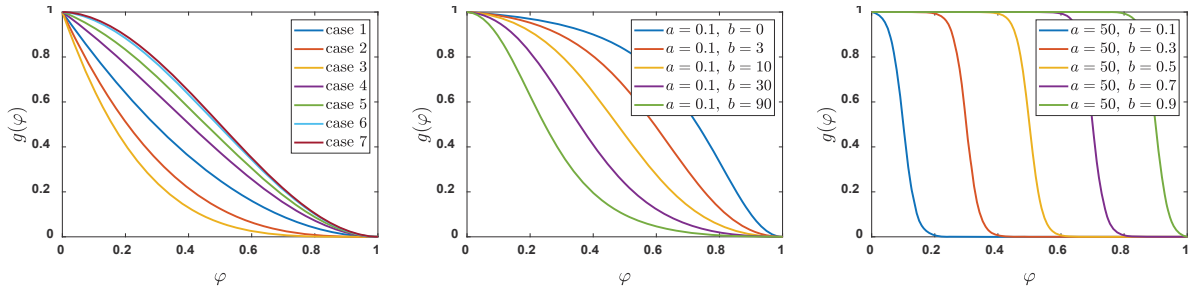

(a) (b) (c)

Figure 5.6 Degradation function, (a) polynomial function (Equation 5.37), (b) algebraic fraction function (Equation 5.38), (c) sigmoid function (Equation 5.39)

5.2.3 Analytical solution of 1D case

To better have an idea of the phase field model for plasticity behavior, a 1D case is shown here. Material parameters used include Young's modulus 210000 MPa, yield stress 120 MPa, tangent modulus 10500 MPa, length scale l 1.0, and critical energy release rate G_C 1.0 N/mm. The degradation function of case 1 in Equation (5.37) is used for simplicity. The maximum history strain energy is obtained as

$$H = \begin{cases} E\varepsilon^2/2, & \sigma < \sigma_y \\ E\varepsilon_y^2/2 + E^H\left(\varepsilon - \varepsilon_y\right)^2/2 + \sigma_y\left(\varepsilon - \varepsilon_y\right), & \sigma \geq \sigma_y \end{cases}. \tag{5.40}$$

In this dissertation, the homogenous solution of the governing equation in Equation (5.31~2) is investigated, which means the gradient of phase field is ignored. In this case, the phase can be calculated as

$$\varphi = \frac{2H}{G_c/l + 2H}. \tag{5.41}$$

And the stress can be obtained from $\sigma = (1-\varphi)^2\sigma^0$ as

$$\sigma = \begin{cases} (1-\varphi)^2 E\varepsilon, & \sigma < \sigma_y \\ (1-\varphi)^2\left[\sigma_y + E^H\left(\varepsilon - \varepsilon_y\right)\right], & \sigma \geq \sigma_y \end{cases}. \tag{5.42}$$

The stress-strain curve obtained from Equation (5.42) is plotted in Figure 5.7. Figure 5.7 (a) is comparative to the stress-strain curve of a tensile test in 3D case in Figure 5.10 (a), will see in Section 5.4.1

later. However, one thing to note is that because the 1D case here does not consider the gradient of phase field, a larger stress 57.02 MPa are frond at the maximum strain, compared with a lower stress 37.04 MPa in Figure 5.10 (a) later, where the gradient of phase field is considered. The results of three more critical energy release rate are plotted in Figure 5.7 (b), which is also comparative to the stress-strain curve in Figure 5.10 (b) later.

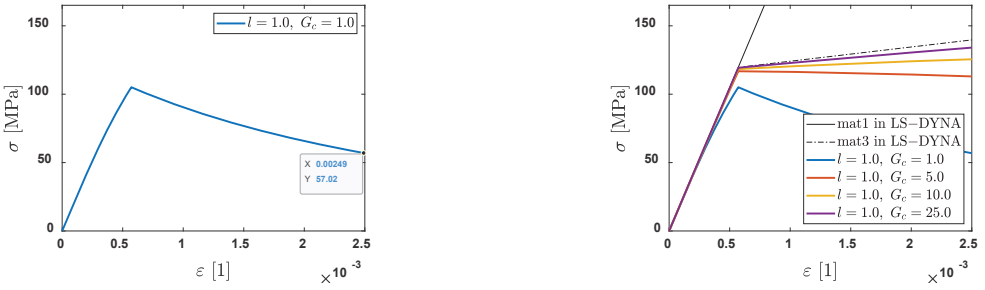

(a) (b)

Figure 5.7 Analytical solution of 1D case, (a) G_C 1.0 N/mm, (b) G_C 1.0 N/mm, 5.0 N/mm, 10.0 N/mm, and 25.0 N/mm

5.3 FEM formulation of the proposed phase field model

5.3.1 Linear and nonlinear FEM formulation of the proposed phase field model

Basically, the linear and nonlinear FEM formulation of the proposed phase field model for ductile fracture is also same as the model used in brittle fracture in Section 4.3, but the strain energy is not limited in the linear elastic range. To avoid repetition, the detailed derivation is not shown here, but stiffness matrix and force vector are presented here to show the difference. Phase can be solved directly from the linear FEM formulation, see Equation (5.45), but only delta phase can be solved from the nonlinear FEM formulation, and it is added to the phase at previous time step to get the phase at current time step, see Equation (5.49).

Linear FEM formulation of the proposed phase field model,

$$\boldsymbol{K}_{ij} = \int_{\Omega} \left(\boldsymbol{N}_i^T 2H |\boldsymbol{J}| \boldsymbol{N}_j + \boldsymbol{N}_i^T \frac{G_c}{l} |\boldsymbol{J}| \boldsymbol{N}_j + \boldsymbol{B}_i^T l G_c |\boldsymbol{J}| \boldsymbol{B}_j \right) \mathrm{d}\xi \mathrm{d}\eta \mathrm{d}\varsigma , \tag{5.43}$$

$$\boldsymbol{F}_i = \int_{\Omega} \boldsymbol{N}_i^T 2H |\boldsymbol{J}| \mathrm{d}\xi \mathrm{d}\eta \mathrm{d}\varsigma , \tag{5.44}$$

$$\boldsymbol{K\varphi} = \boldsymbol{F}. \tag{5.45}$$

Nonlinear FEM formulation of the proposed phase field model,

$$\boldsymbol{K}_{ij}^{t} = \int_{\Omega} [B_i^T B_j - F'(\varphi_0) N_i^T N_j] |\boldsymbol{J}| \mathrm{d}\xi \mathrm{d}\eta \mathrm{d}\varsigma\,, \tag{5.46}$$

$$\boldsymbol{F}_{i}^{u} = \int_{\Omega} \left[N_i^T F(\varphi_0) - B_i^T B_j \varphi_{0j}\right] |\boldsymbol{J}| \mathrm{d}\xi \mathrm{d}\eta \mathrm{d}\varsigma\,, \tag{5.47}$$

$$F(\varphi) = -\frac{1}{l G_c}\left[g'(\varphi) H + \frac{G_c}{l}\varphi\right], \tag{5.48}$$

$$\boldsymbol{K^t}\delta\boldsymbol{\varphi} = \boldsymbol{F}^{u}. \tag{5.49}$$

5.3.2 Implementation of the proposed model into LS-DYNA

The implementation of this phase filed method for ductile fracture is realized in LS-DYNA. A user-defined hexahedron solid element is used. From the simulations, I found that eight different phase values (or damage values) at eight integration points for a hexahedron solid element would cause the instability of stress equilibrium for an element. To solve this, hexahedron element with one integration point in displacement field is used, but eight integration points in phase field are used. And an average of eight phase values is used as the phase for degradation of material in displacement field. The procedure of this implementation is as follows

Step 1. Input model data, including element number, node number, and node number at boundary conditions,

Step 2. Initialize phase as 0, or use the phase calculated from last time step (Step 6),

Step 3. Calculate delta strain in subroutine usrsld,

Step 4. Move to subroutine usrmat (user-defined material) to calculate stress and strain energy,

Step 5. Based on the updated the displacement, strain, and strain energy, move to subroutine PFM (user-defined element), and then construct stiffness matrix and force vector to calculate phase,

Step 6. Go back to Step 2 to update the phase.

A detailed flowchart for the implementation of the proposed phase field model is shown in Figure 5.8.

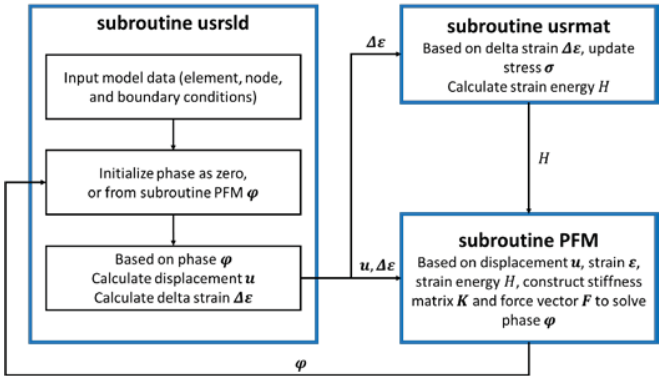

Figure 5.8 Flowchart for the implementation of the proposed phase field model

5.4 Numerical verification of the phase field model for ductile fracture

To verify the model proposed in this dissertation, several numerical simulations are investigated in this section. LS-DYNA user-defined material and user-defined element are used. First, a tensile test shows the influence of critical energy release rate and degradation function on stress-strain curve. And then three representative numerical examples show the feasibility of this model to simulate ductile fracture, including a Mode I failure of three-point bending test of edge-notched beam, a Mode II failure of single-edge notched plate, and a mixed-mode failure of asymmetrical double-notched plate.

5.4.1 Tensile test of different phase field model

Before explaining the tensile test, different type of fracture in [121] is mentioned first. With the increase of relative elongation, three kinds of fracture are brittle fracture, ductile-brittle fracture, and ductile fracture, see Figure 5.9. From the tensile test in this section, different type of fracture can be obtained by using different degradation function.

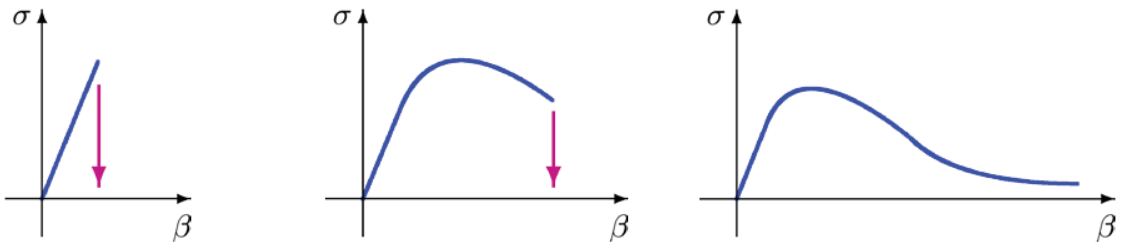

(a) (b) (c)

Figure 5.9 (a) brittle fracture, (b) ductile-brittle fracture, (c) ductile fracture

First, to verify the correctness of the use of Newton-Raphson method in LS-DYNA, the linear FEM

formulation of phase field model (case 1 in Equation (5.37)) is also solved by Newton-Raphson method. Newton-Raphson method can be used to solve nonlinear problem, but it does not limit to nonlinear problem. Dimensions, boundary condition, and load for the tensile test are totally same as that in Figure 5.4. Material parameters used include Young's modulus 210000 MPa, Poisson's ratio 0.3, yield stress 120 MPa, tangent modulus 10500 MPa, length scale l, and critical energy release rate G_C. For l 1.0 and G_C 1.0 N/mm, the obtained stress-strain curve from no iteration method and with iteration method (Newton-Raphson method) are shown in Figure 5.10 (a). The stress-strain curves obtained from no iteration method and with iteration method are almost same, which shows the correctness of the use of Newton-Raphson method in this dissertation.

For the linear FEM formulation of phase field model (case 1 in Equation (5.37)), critical energy release rate G_C is also investigated. In Figure 5.10 (a), even though it is a ductile material with isotropic hardening, no hardening is found in the stress-strain curve when critical energy release rate is too small. Stress-strain curve obtained from four different critical energy release rate (1.0 N/mm, 5.0 N/mm, 10.0 N/mm, and 25.0 N/mm) are shown in Figure 5.10 (b). When this critical energy release rate is large enough, phase is almost zero at lower strain, and hardening can be observed in the stress-strain curve. Results in Figure 5.10 are comparative to the analytical solutions in Figure 5.7.

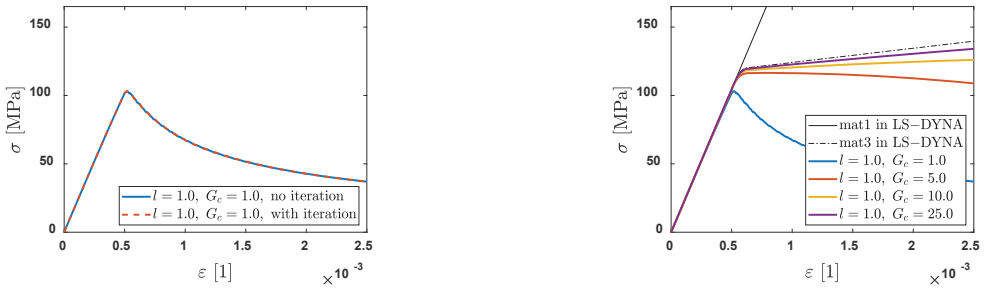

(a) (b)

Figure 5.10 (a) comparison between no iteration method and with iteration method, (b) the influence of critical energy release rate on stress-strain curve

Apart from linear FEM formulation of phase field model, to show the influence of degradation function on stress-strain curve, nonlinear FEM formulation of phase field model is investigated. The stress-strain curves obtained from polynomial degradation function, algebraic fraction degradation function, and

sigmoid degradation function are shown in Figures 5.11, 5.12, and 5.13, respectively. Note that length scale l is still 1.0 and critical energy release rate G_C is still 1.0 N/mm in these simulations. Considering that polynomial degradation functions decrease slowest among these three kinds of degradation function, see Figure 5.6, Figure 5.11 with six polynomial degradation functions is more like ductile fracture in Figure 5.9 (b), Another thing is that even though G_C is still 1.0 N/mm, hardening can be found in the stress-strain curve after using a different degradation function, which shows degradation function could help expand the scope of application.

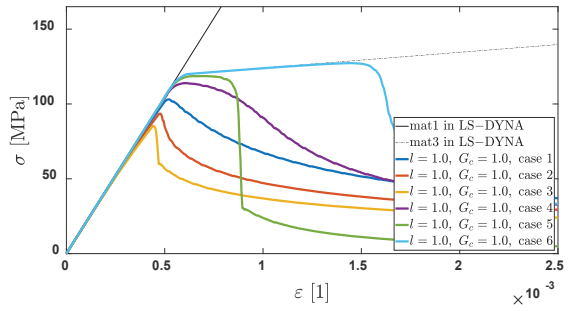

Figure 5.11 Stress-strain curve obtained from polynomial degradation function

Figures 5.12 and 5.13 show more like ductile-brittle fracture since stress drops to zero faster compared with Figure 5.11. Note that Figure 5.13 can give a perfect ductile-brittle fracture since the stress is almost zero after it breaks, and there is not a clear degradation of material before fracture happens like Figure 5.12. This is because sigmoid function can make degradation function decrease from 1 to 0 within a small range of phase. Comparison with experiment result is suggested before using this sigmoid degradation function. For the rest of numerical simulations in this section, algebraic fraction degradation function proposed by Wu [54] will be used.

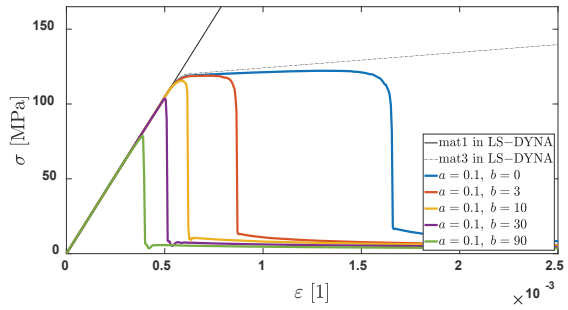

Figure 5.12 Stress-strain curve obtained from algebraic fraction degradation function

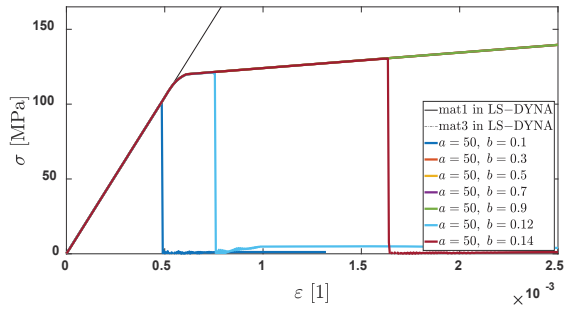

Figure 5.13 Stress-strain curve obtained from sigmoid degradation function

5.4.2 Mode I failure of three-point bending test of edge-notched beam

This example is a Mode I failure of three-point bending test of edge-notched beam, which has been investigated in [122,123]. The specimen has a rectangle shape with dimensions 250 mm × 50 mm × 25 mm, and simply supported at the positions 25 mm away from both left and right surfaces. A vertical notch is made up to 26 mm height at the center of the specimen. One vertical force is applied at the top center of the specimen. The detailed dimensions, boundary condition, and load are shown in Figure 5.14. The material parameters used include Young's modulus E 210000 MPa, Poisson's ratio υ 0.28, yield stress 394 MPa, tangent modulus 1431 MPa, and critical energy release rate G_c 94.14 N/mm. Force and displacement data are recorded during the simulation.

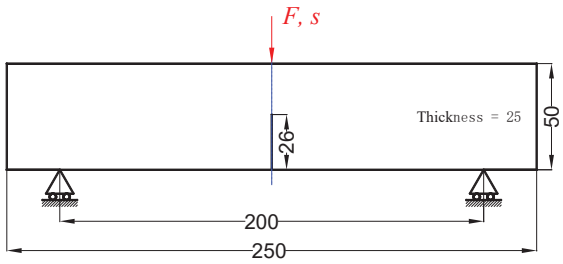

Figure 5.14 Dimensions, boundary condition, and load of the three-point bending test of edge-notched beam, unit [mm]

Hexahedron element is used to mesh the specimen. Considering the size of the specimen, local refinement with 0.4 mm element along the fracture path is used, and larger element is used at other positions. The finite element model consists of 4404 elements and 8998 nodes. The length scale l used is 0.85, which satisfies the requirement that the ratio between length scale and element size is larger than two in [43]. The degradation function result obtained from the phase field model in this dissertation is shown in Figure 5.15

(a). Since phase cannot exactly represent the level of degradation of material, degradation function is plotted in Figure 5.15 (a), not the phase. The force-displacement result is shown in Figure 5.15 (b). Even though the force obtained in this dissertation is a little larger than that in [122], totally, force-displacement curve can still capture this force-displacement relation well.

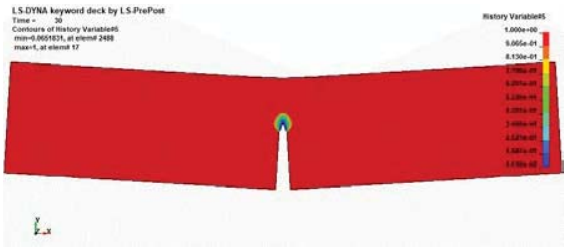

(a)

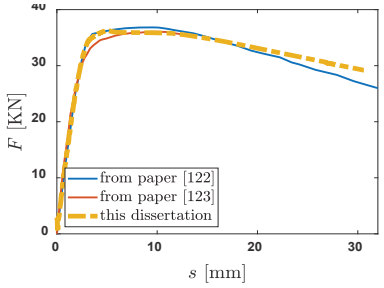

(b)

Figure 5.15 Three-point bending test of edge-notched beam, (a) degradation function result, (b) force-displacement curve result

5.4.3 Mode II failure of single-edge notched shear test

This example is a Mode II failure of single-edge notched plate, which has been investigated in [122,124]. The specimen has a square shape with dimensions 10 mm × 10 mm, and the bottom edge is fully fixed. A horizontal notch is made up to the center of the specimen from the center of left-hand side. Horizontal force is applied at the top surface of the specimen. The detailed dimensions, boundary condition, and load are shown in Figure 5.16. The material parameters used include Young's modulus E 180000 MPa, Poisson's ratio υ 0.28, yield stress 443 MPa, tangent modulus 299.5 MPa, and critical energy release rate G_c 20.9 N/mm. Force and displacement data are recorded during the simulation.

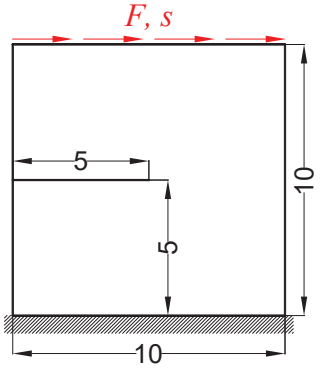

Figure 5.16 Dimensions, boundary condition, and load of the single-edge notched plate, unit [mm]

Hexahedron element is used to mesh the specimen. Considering the size of the specimen, local refinement with 0.1 mm element along the fracture path is used, and larger element is used at other positions. The model consists of 2318 elements and 4764 nodes. The length scale l used is 0.2, which satisfies the requirement that the ratio between length scale and element size is larger than two in [43]. The degradation function result obtained in this dissertation is shown in Figure 5.17 (a). Same thing, degradation function is shown in the figure. The force-displacement result is shown in Figure 5.17 (b). From the figure, it can be seen the force-displacement curve is almost same as that in the references, which shows that the model used in this dissertation handle this shear test very well.

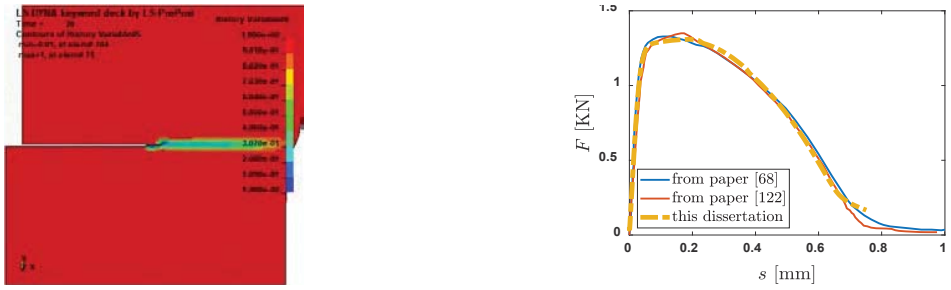

(a) (b)

Figure 5.17 Single-edge notched plate, (a) degradation function result, (b) force-displacement curve result

5.4.4 Mixed-mode failure of asymmetrical double-notched plate

This example is the mixed-mode failure of asymmetrical double-notched plate, which has been investigated in [122,125]. The specimen has a rectangle shape with dimensions 18 mm × 50 mm, and the bottom edge is fully fixed. Two horizontal notches with 2.5 mm length is made at both left-hand side and right-hand side, which would produce a mixed-mode failure. Vertical force is applied at the top surface of the specimen. The detailed dimensions, boundary condition, and load are shown in Figure 5.18. The material parameters used include Young's modulus E 72624 MPa, Poisson's ratio υ 0.33, yield stress 345 MPa, tangent modulus 249 MPa, and critical energy release rate G_c 9.3 N/mm. Force and displacement data are recorded during the simulation.

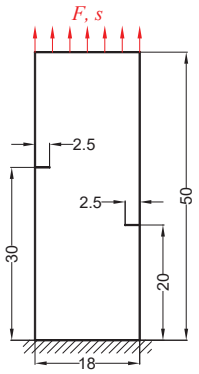

Figure 5.18 Dimensions, boundary condition, and load of the asymmetrical double-notched plate, unit [mm]

Hexahedron element is used to mesh the specimen. Considering the size of the specimen, local refinement with 0.15 mm element along the fracture path is used, and larger element is used at other positions. The model consists of 4375 elements and 8908 nodes. The length scale l used is 0.5, which satisfies the requirement that the ratio between length scale and element size is larger than two in [43]. The degradation function result obtained in this dissertation is shown in Figure 5.19 (a). The force-displacement result is shown in Figure 5.19 (b). From the figure, the force-displacement curve in this dissertation agrees well with that in reference before 0.3 mm, but the force in this dissertation is a little larger before fracture, which may show the degradation function used in this dissertation (Equation (5.38)) decreases fast from 1 to 0, and a degradation function with slower decrease from 1 to 0 is preferred. Fine tuning of degradation function is needed, but this is not the focus of this dissertation.

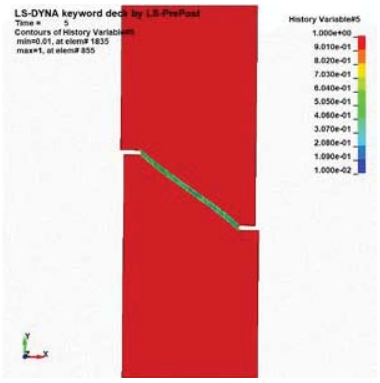

(a)

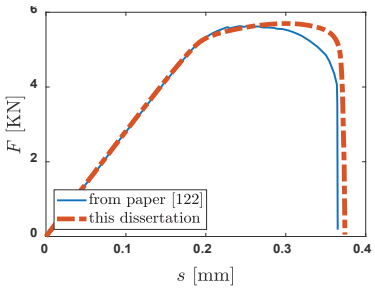

(b)

Figure 5.19 Asymmetrical double-notched plate, (a) degradation function result, (b) force-displacement curve result

6 Conclusion and future work

In this section, conclusion and future work of this dissertation are given. By using the methods proposed in this dissertation, the modeling of brittle and ductile fracture using cohesive zone model (discrete description) and phase field model (continuum description) is improved. Considering the complexity of ductile fracture, more investigations are still needed.

Conclusion

After finishing this dissertation, the conclusion is as follows:

1. For damage evolution method in bilinear cohesive law, both monotonically increasing effective separation method and monotonically increasing damage factor method have been used widely and interchangeably, but the problems in monotonically increasing effective separation method have been overlooked. The problems include discontinuous force when mixed-mode ratio changes, and unreasonable failure that makes bilinear cohesive law does not strictly follow damage criteria defined initially. Another clear problem in monotonically increasing effective separation method is that damage factor is not guaranteed to be monotonically increasing when effective separation is monotonically increasing, which means healing effect can happen in this damage evolution method.

2. For artificial compliance in cohesive zone model, it is found to be related to cohesive element modeling method and stiffness parameter selection. Zero-thickness cohesive element has small and nonzero deformation under loading, and time is needed to let stress wave passes through this deformed cohesive element, which is the deep reason why artificial compliance happens in cohesive zone model. By using finite-thickness cohesive element and proper stiffness parameter, artificial compliance can be totally removed.

3. Plastic strain is not considered in the classical bilinear cohesive law, which makes it only applicable for brittle fracture. Based on the damage factor model in the classical bilinear cohesive law, a generalized damage factor model is proposed where five typical damage factor models (maximum, convex, linear, concave, and minimum damage factor) can handle all materials from zero to maximum plastic strain in

sequence.

4. Variable damping is considered into bilinear cohesive law, which can remove discontinuous force caused by constant damping at the start and end of bilinear cohesive law. From the several numerical simulations, variable damping proposed in this dissertation can remove spurious oscillation and enables correct force response.

5. Inspired from the damage-separation relation in bilinear cohesive law, by using a generalized quadratic degradation function and zeroing negative phase, a small range of strain with zero phase in phase-strain relation is realized in phase field model, which is more suitable for brittle fracture. Stiffness reduction is not observed at a small range of strain, which gives a perfect linear elastic behavior before fracture.

6. Apart from using a second order degradation function, some higher order degradation functions with more constrains could give more options for stress-strain curve. The first derivative at zero phase closer to 0, the better for brittle fracture. Higher order degradation function leads to a nonlinear FEM problem, and Newton-Raphson method is used to solve this nonlinear problem. The stress-strain curve obtained from tensile test verifies the correctness of the use of Newton-Raphson method in this dissertation.

7. Based on the ductile material with isotropic hardening, phase field model is coupled into this material. One difference from the classical phase field model is the calculation of strain energy, where strain energy is not limited in the linear elastic range. Parameters for ductile material with isotropic hardening are multiplied with degradation function to model the degradation of material, i.e., Young's modulus, yield stress, and hardening modulus. Depending on the selection of degradation function, both linear and nonlinear FEM can also be used like the modeling of brittle fracture.

Future work

After finishing this dissertation, the future work could be as follows:

1. Cohesive zone model can handle fragment contact well, but it cannot depict the degradation of material well. However, phase field model has the opposite features that it can handle the degradation of material well but cannot simulate fragment contact well. A possible topic could be combining these two

models together.

2. Γ convergence has always been a good and meaningful topic in phase field model. For the length scale insensitive phase field model proposed in Section 4.2.2., theoretical proof of Γ convergence for a 1D case is proved, but there is no 1D, 2D, and 3D simulations to verify this point in this dissertation. If Γ convergence is satisfied, is there any requirement for the Γ convergence of this length scale insensitive phase field model?

3. For the phase field modeling of ductile fracture, even though same critical energy release rate G_C is used in the tensile test simulation, different stress-strain curve can be obtained from different degradation function, and the strain energy obtained from these stress-strain curves is also different, which could lead to different fracture energy. So, does this degradation function can influence the critical energy release rate G_C? If yes, how does it influence?

4. For the phase field modeling of ductile fracture in this dissertation, the assumption is still in small strain. To expand the application for ductile fracture and improve accuracy, large strain and geometric nonlinearity should be considered, and different kinds of ductile material can also be investigated, not limited in ductile material with isotropic hardening. This would be a more interesting but also challenging topic.

7 Appendix: Other simulations using cohesive zone model

In this section, appendix is put there. To save space and improve readability for Section 3, four more examples using cohesive zone model are presented in this section.

7.1 Drop-weight tear test of pipeline steel plate

Drop weight tear test is used to verify the artificial compliance. A 3D rectangular pipeline steel plate has a sharp V-notch with an angle of 45° and a depth of 5 mm, as shown in Figure 7.1 (a). Two rigid anvils are used to support the specimen, and a rigid hammer with a mass of 40 Kg and an initial velocity of 14 m/s is designed to impact the top middle of the specimen. Detailed information is in [126]. The pipeline steel has Young's modulus E 203 GPa, Poisson's ratio v 0.3, and density ρ 0.00785 g/mm^3. Bulk element size is 0.99 mm, and finite-thickness cohesive element size is 0.01 mm. Material parameters of the cohesive element are shown in Table 7.1. Fracture crack (failed cohesive elements are deleted during simulation) and damage factor are shown in Figure 7.1 (b).

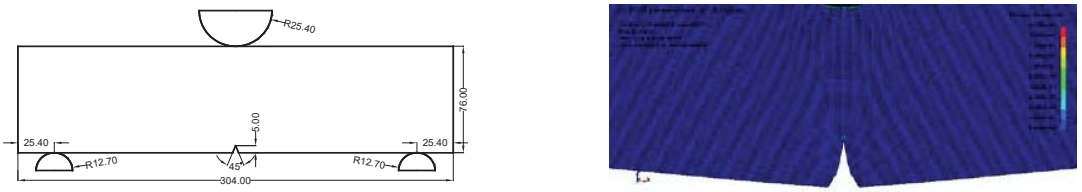

(a) (b)

Figure 7.1 (a) schematic of the plate, unit [mm], (b) fracture crack and damage factor

Table 7.1 Material parameters of the cohesive element for artificial compliance analysis [126]

Mode	Stiffness [MPa/mm]	Fracture strength [MPa]	Critical energy release rate [N/mm]
Mode I	27405000	1800	101

Reaction force from the impactor and its displacement are compared. From Figure 7.2 (a), the curve obtained in this dissertation agrees with [126] well, especially at the initial part. However, the simulation is not very close to experiment at the initial part, and the possible reason could be the difference of boundary condition between experiment and simulation. In Figure 7.2 (b), finite-thickness cohesive element is compared with zero-thickness cohesive element. Even though zero-thickness cohesive element also agrees

with [126], the delay of response can be seen clearly, and the delay gets bigger when time increases.

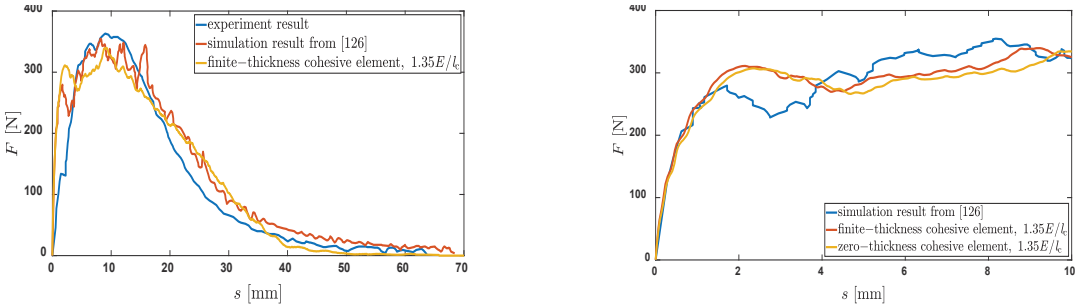

(a) (b)

Figure 7.2 (a) comparison between finite-thickness cohesive element and publications, (b) comparison between finite-thickness cohesive element and zero-thickness cohesive element

7.2 Mixed-mode bending with three mixed mode ratios

(1) Introduction to MMB test

The mixed-mode bending test is used to determine the interlaminar facture toughness of continuous fiber-reinforced composite materials at various mixed mode ratios, and this test method has been successfully used to test the toughness of both fiber composites and adhesive joints [127]. The experiment used in this dissertation is refereed from [128]. A 3D finite element analysis is conducted in this section. The dimensions of the test setup and finite element model are shown in Figure 7.3. The recommended height of lever in [127] is 0.3L (18 mm in this example); L is the half length of the beam, which is 60 mm in this example. Revolute joint is used at connections where rotation is needed in the setup, the connection between lever and upper beam, and the connection between lever and roller. The element size in lengthwise direction is 0.25 mm, which is less than the suggested size in [128], 0.3 mm.

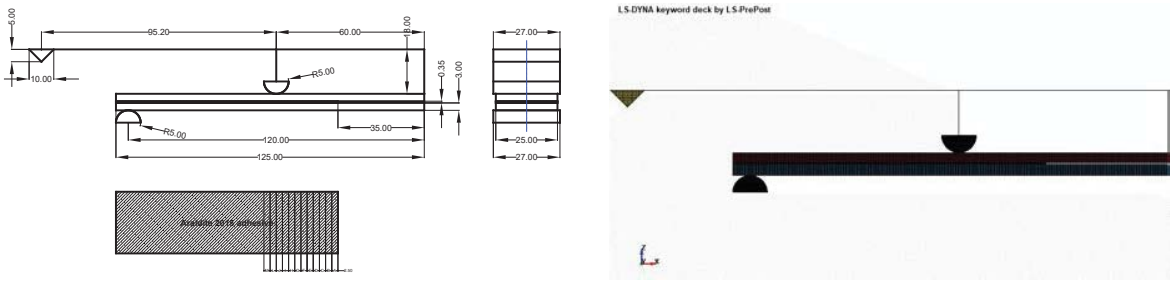

Figure 7.3 (a) dimensions of MMB specimen (25%), unit [mm], (b) finite element model of MMB specimen (25%)

According to [127] and the dimensions shown in Figure 7.3 (a), the length of lever arm for the three

different mixed mode ratios can be calculated, as shown in Table 7.2. The adherent is high strength steel that has a yield stress larger than 700 MPa, which guarantees the steel is in elastic range during the experiment. The Young's modulus is 210 GPa; the Poisson's ratio is 0.3. The adhesive is Araldite 2015 whose material parameters used in the simulation are shown in Table 7.3. The stiffness is obtained when the slope of linear range of force-displacement in simulation is close to experiment. Fracture strength are obtained by trial and error to match the experiment data. The focus of this section is energy release rate. To investigate the energy relation of the adhesive, the energy release rate of some small pieces of adhesive (from A to M shown in Figure 7.3 (a)) is extracted, and the width of each small piece is 2.5 mm.

Table 7.2 Lever arm length corresponding to the three different mixed mode ratios

Mixed mode ratio	25%	50%	75%
Length of lever arm [mm]	95.2	51.1	35.4

Table 7.3 Bilinear cohesive law parameters for MMB test

Parameters	**Positive Mode I**	**Negative Mode I**	**Mode II**
Stiffness [MPa/mm]	2643	2643	2643
Fracture strength [MPa]	8.95	53.7	17.9
Critical energy release rate [N/mm]	0.51	122	6.1

To investigate the influence of different damage factor model on residual plastic strain, the unloading part is considered, and the displacement load is shown in Figure 7.4. Convergence analysis about simulation time has been done, and 100 ms is used in simulation.

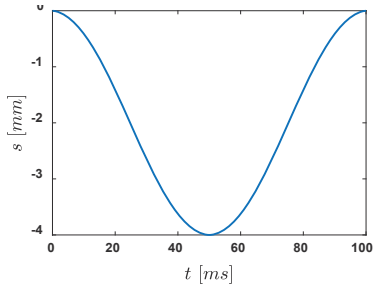

Figure 7.4 Prescribed motion at the free end of lever arm in MMB simulation

Benzeggagh-Kenane law is used with η being 2.19 according to [128], as shown in Equation (7.1). G is the summation of G_I and G_{II}.

$$G_{IC} + (G_{IIC} - G_{IC})\left(\frac{G_{II}}{G}\right)^{\eta} = G \tag{7.1}$$

(2) Validation of the proposed bilinear cohesive law

First, the force-displacement relation obtained from three mixed mode ratios is compared with experiment and simulation results in [128], as shown in Figure 7.5. The simulation results in this dissertation agree well with the experiment. Second, the energy release rate relation obtained from three mixed mode ratios is shown in Figure 7.6, where the energy release rate increases with the increase of distance between the small piece and the initial crack. The reason for this phenomenon is that the shear displacement is larger where it is closer to the middle of the beam, but for the place close to the initial crack, larger normal displacement means smaller local mixed mode ratio and smaller energy release rate. All three mixed mode ratios reach highest energy release rate at the forth small piece "D".

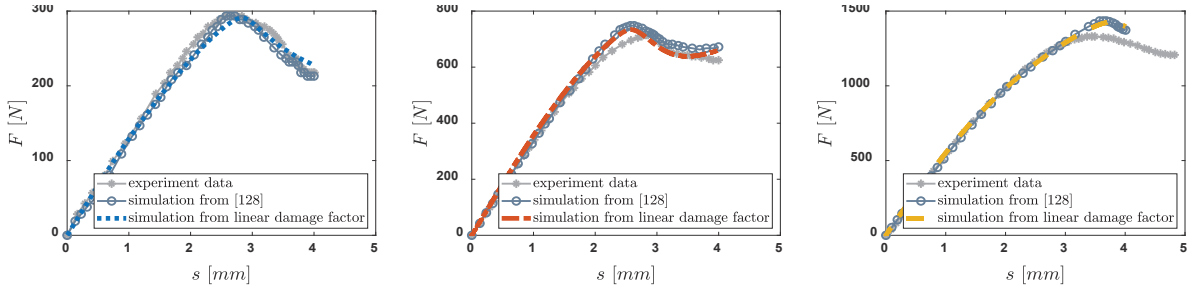

(a) (b) (c)

Figure 7.5 Comparison of force-displacement, (a) 25% case, (b) 50% case, (c) 75% case

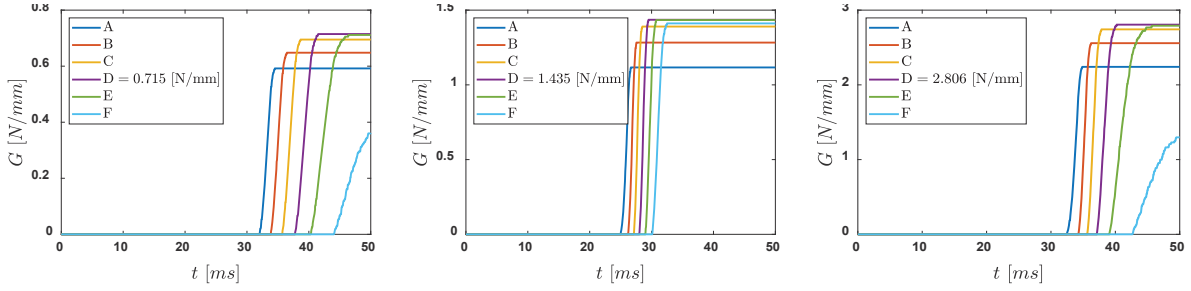

(a) (b) (c)

Figure 7.6 Comparison of energy release rate, (a) 25% case, (b) 50% case, (c) 75% case

The maximum energy release rate is obtained and then compared with experiment and simulation in [128], as shown in Table 7.4. Even though the energy release rate is smaller compared with the simulation results in [128], the energy release rate for 25% and 50% cases are still in the acceptable range of experiment.

For the 75% case, the difference is beyond the range of experiment, as shown in Figure 7.7. Such a difference can be attributed to the fact that with the increase of mixed mode ratio, the influence of Mode II becomes more pronounced which enlarges the plastic strains and the assumption of linear elastic hypothesis considered for the model is not valid any longer [128].

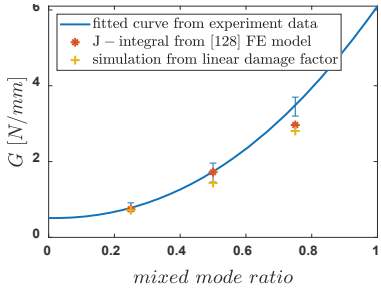

Figure 7.7 Critical energy release rate envelope developed using Benzeggagh-Kenane law

Table 7.4 Comparison of energy release rate for MMB test

Mixed mode ratio	**Experiment [N/mm]**	**Simulation in [128] [N/mm]**	**Simulation in this dissertation [N/mm]**
25%	0.782	0.745	0.715
50%	1.798	1.720	1.435
75%	3.534	2.965	2.806

The difference of energy release rate between simulation and experiment can be explained through mixed mode ratio. First, the separation at the initiation of damage and the separation at the failure of damage are needed to be calculated. δ_m^0 and δ_m^f can be obtained, as shown in Equation (7.2). To differentiate two kinds of mixed mode ratios, two characters are used. Mixed mode ratio β, $\beta = \frac{\Delta_{m,T}}{\Delta_{m,N}}$; mixed mode ratio γ, $\gamma = \frac{G_{II}}{G}$. After δ_m^0 and δ_m^f are obtained, G_I and G_{II} can be calculated. And then γ can be calculated based on G_I and G_{II}. The relation between β and γ is shown in Equation (7.3). Because the method in this dissertation is a displacement-based method, β is an important parameter in simulation since it is calculated from displacement. And the relation between energy release rate G and mixed mode ratio β is shown in Equation (7.4).

$$\begin{cases} \delta_m^0 = \delta_N^0 \delta_T^0 \sqrt{\dfrac{1+\beta^2}{(\beta\delta_N^0)^2 + (\delta_T^0)^2}} \\ \delta_m^f = \dfrac{2(1+\beta^2)}{\delta_m^0 (E_N^0 + \beta^2 E_T^0)} \left[G_{IC} + (G_{IIC} - G_{IC}) (\dfrac{\beta^2 E_T^0}{E_N^0 + \beta^2 E_T^0})^\eta \right] \end{cases} \tag{7.2}$$

$$\gamma = \frac{G_{II}}{G} = \frac{0.5 E_T^0 \delta_{m,T}^0 \delta_{m,T}^f}{0.5 E_N^0 \delta_{m,N}^0 \delta_{m,N}^f + 0.5 E_T^0 \delta_{m,T}^0 \delta_{m,T}^f} = \frac{\beta^2 E_T^0}{E_N^0 + \beta^2 E_T^0} \tag{7.3}$$

$$G = G_{IC} + (G_{IIC} - G_{IC}) \gamma^\eta = G_{IC} + (G_{IIC} - G_{IC}) \left(\frac{\beta^2 E_T^0}{E_N^0 + \beta^2 E_T^0} \right)^\eta \tag{7.4}$$

From Equation (7.4), even though E_N^0 and E_T^0 can be considered as constants, the ratio between E_N^0 and E_T^0 can still have an influence on the final energy release rate. Another important parameter is the β. For displacement-based method, stiffness and fracture strength can influence the length of cohesive zone in normal and shear directions and the displacements in normal and shear directions as well. Different normal and shear displacements mean different mixed mode ratio and energy release rate at each time step. Turon et al. [129] investigate the influence of fracture strength on energy release rate, and the conclusion is that the normal and shear fracture strength should satisfy a specific ratio to get correct energy release rate. Carvalho et al. [130] propose a piece-wise linear traction-separation law to solve this energy release rate issue. Different from the displacement-based method, De Moura et al. [19] develop a new energy-based method to get correct energy relation, and a constant global mode ratio is obtained even with important variations of local mode ratio. For the displacement-based method, stiffness and fracture strength can have a big influence on the final energy release rate, and more research is needed on this, but the detail of this influence is beyond the scope of this dissertation.

One more thing needed to mention is the residual plastic strain. Three different damage factor models are used in simulation, and the force-displacement curves are obtained for 25% case, as shown in Figure 7.8. It is clear to see that maximum damage factor model has zero residual plastic strain; linear damage factor model has larger residual plastic strain than that in convex damage factor model. Those findings agree with the conclusions in Section 3.4.2. Residual plastic strain is found in the experiment when unloading part is conducted, but the classical bilinear cohesive law is not able to handle this.

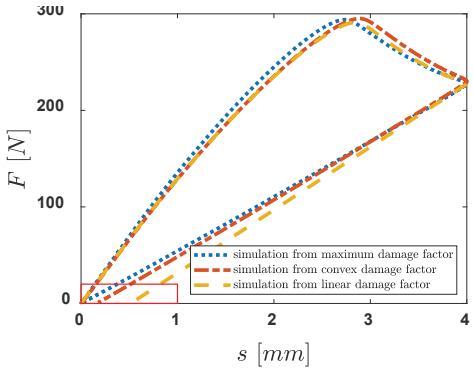

Figure 7.8 Comparison of residual plastic strain in MMB 25% case obtained from different damage factor models

7.3 Aluminum beam under impact load

(1) Introduction to the aluminum beam impact test

This aluminum beam impact test has been conducted by several authors [131,132]. In [132], an experiment study of impact of blunt nose projectile has been carried out at velocity ranging from 11 m/s to 114 m/s on clamped aluminum beams of different thickness. Three different modes of failure have been observed with the increase of the velocity of strike, Type I (fracture at the point of strike, tensile fracture), Type II (fracture at one or both supports, shear fracture), and Type III (fracture at the point of strike with bulging and turning around supports after fracture). The simulation in this dissertation is referend from [132]. The dimensions and finite element model of the setup is shown in Figure 7.9, and two different thickness are applied in the simulations, 1.55 mm and 4.95 mm.

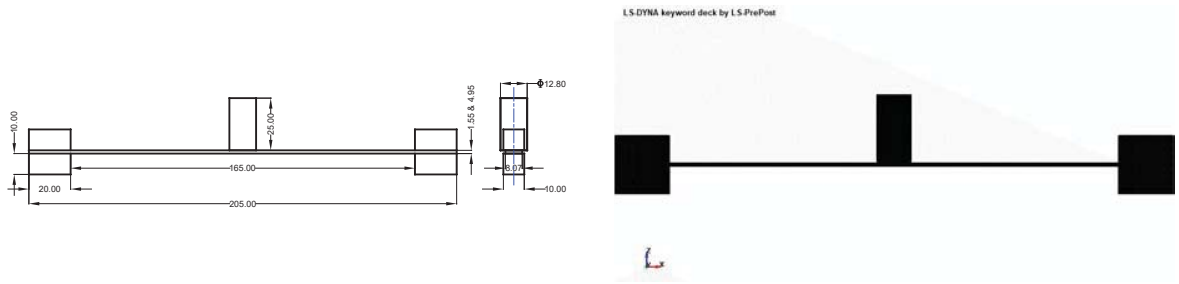

(a) (b)

Figure 7.9 (a) dimensions of aluminum beam, unit [mm], (b) finite element model of aluminum beam

Considering the effect of strain rate, the bulk element is strain rate dependent. The effect of strain rate on stress-strain for Aluminum 1100 H14 is obtained from [133], as shown in Figure 7.10. However, there are papers show that strain rate does not have a big influence on fracture energy, so the critical energy

release rate is not strain rate dependent in this dissertation. From the simulation results, the fracture strength is really important for the fracture propagation, and it should be a little larger than the tensile strength. The relation between fracture strength and tensile strength has been investigated in [134]. In this simulation, for 1.55 mm case, fracture strength is 1.25 times of static tensile strength; for 4.95 mm case, fracture strength is 1.50 times of static tensile strength. The reason for this difference could be the thickness of beam. There are researches [135] showing that the thickness of beam can also influence the tensile strength. Yield strength and tensile strength decrease when the thickness is reduced below a critical thickness [135], but this influence is beyond the scope of this dissertation. The bilinear cohesive law parameters used in this dissertation are shown in Table 7.5.

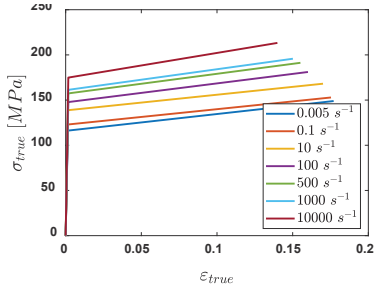

Figure 7.10 True stress–true strain behaviors at different strain rates for Aluminum 1100 H14 [133]

Table 7.5 Bilinear cohesive law parameters for aluminum beam impact test

Parameter	Positive Mode I	Negative Mode I	Mode II
Stiffness [MPa/mm]	700000	700000	7000000
Fracture strength [MPa]	186.25 (223.41)	558.75 (670.23)	186.25 (223.41)
Critical energy release rate [N/mm]	15	135	45

(2) Simulation results of the aluminum beam impact test

In [97], this aluminum beam impact test has been investigated through a SPH method. However, a different fracture type is obtained at high velocity, and the fracture happens at both sides of the strike, which leads to a small detached part at the center of the beam. But this fracture type does not appear in experiment. In this dissertation, for 1.55 mm case, four typical velocities, 20 m/s, 30 m/s, 50 m/s, and 75 m/s, are investigated; for 4.95 mm case, two typical velocities, 75 m/s and 105 m/s, are investigated. Figure 7.12 shows the simulation results for 1.55 mm case with no fracture, type I, type II, and Type III fractures,

respectively. Figure 7.13 shows the simulation results for 4.95 mm case with no fracture and type II fracture, respectively. From the comparison between experiment and simulation, it shows that the simulation results obtained from the proposed method agree well with experiment results.

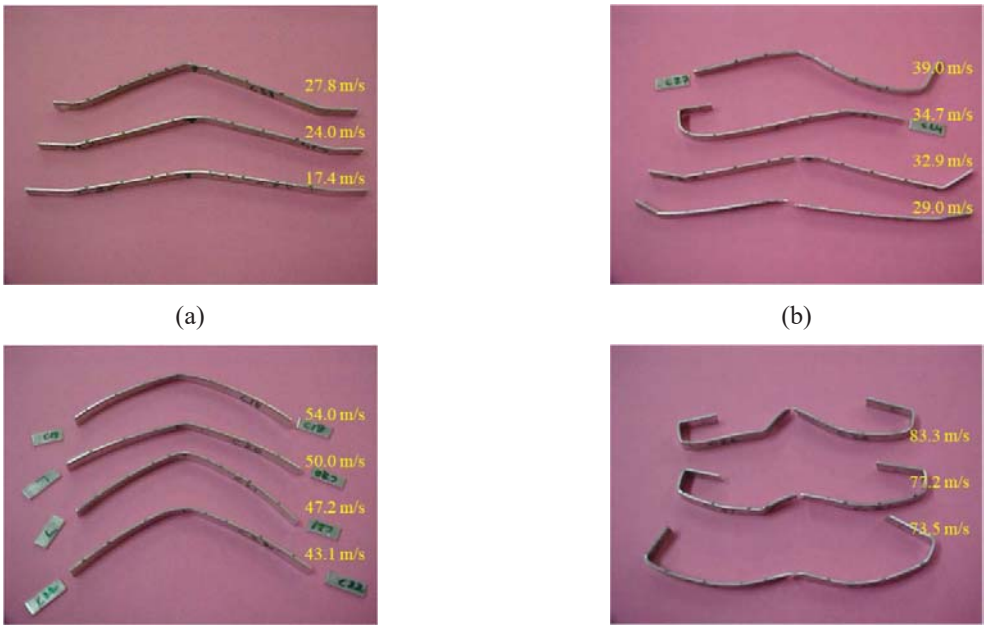

(a) (b)

(c) (d)

Figure 7.11 Experiment results for 1.55 mm thickness [132], (a) no fracture, (b) type I fracture, (c) type II fracture, (d) Type III fracture

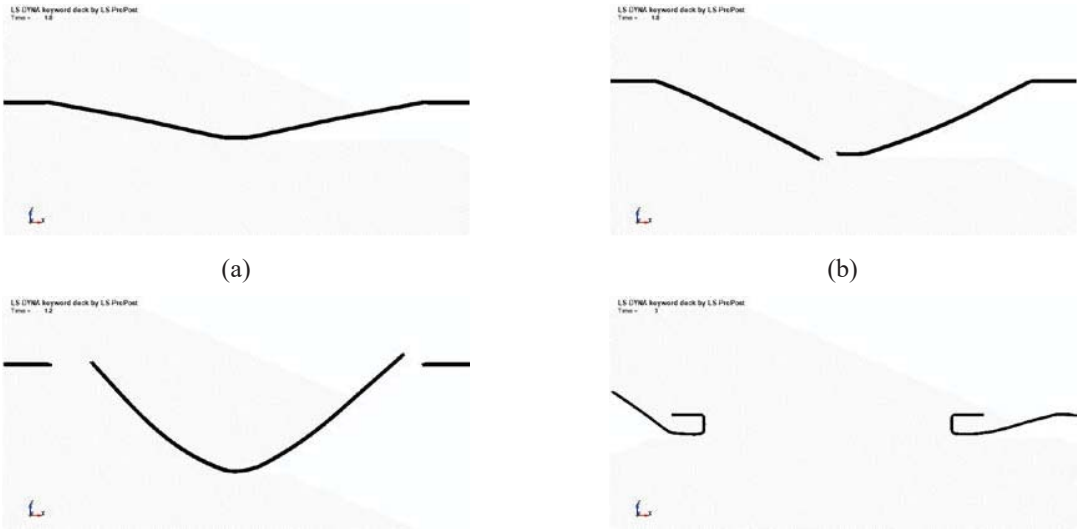

(a) (b)

(c) (d)

Figure 7.12 Simulation results for 1.55 mm thickness, (a) 20 m/s case, (b) 30 m/s case, (c) 50 m/s case, (d) 75 m/s case

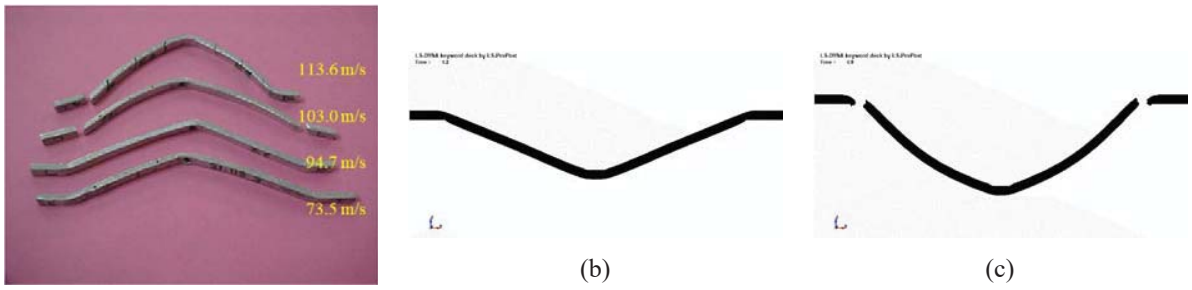

(a) (b) (c)

Figure 7.13 (a) experiment results for 4.95 mm thickness [132], (b) simulation result 75 m/s case, (c) simulation result 105 m/s case

7.4 Concrete block under impact load

(1) Introduction to the concrete block impact test

This concrete block impact test is referred from [136]. The concrete block is fixed by four strips at four edges, and a projectile with an initial velocity 114 m/s is used to impact the concrete block. The dimensions of the concrete block are shown in Figure 7.14 (a); due to the symmetry of the block and boundary condition, only half of the block is modelled, as shown in Figure 7.14 (b). The material of the concrete is a kind of Reactive Powder Concrete (RPC), which is a special mixture that is cured to have a higher compressive strength than that of common concrete.

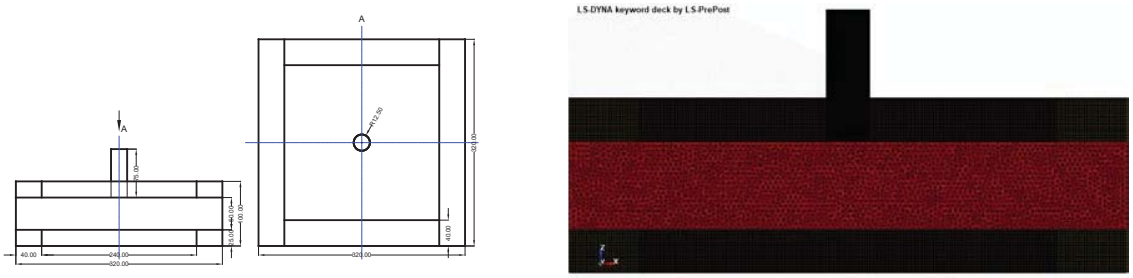

(a) (b)

Figure 7.14 (a) dimensions of concrete block, unit [mm], (b) finite element model of concrete block

Compared with the common concrete that is a typical brittle material, the RPC shows more plasticity. From the stress-strain curve and force-deflection curve shown in Figure 7.15, it is clear to see that the RPC-1 used in the paper [137] is different from the common brittle material. Here, RPC-0 means the percent of steel fiber is 0; RPC-1 means the percent of steel fiber is 1%. In [137], the effect of plasticity on damage of

reactive powder concrete columns is investigated experimentally and numerically. Since this material is not a pure brittle material, plastic strain is expected to be introduced into its constitutive model. This material is modelled with Johnson–Holmquist Concrete-JHC material type using LS-DYNA, and the detailed material parameters used are from [136]. Considering that plastic strain is needed for this material, the double bilinear model is used, and the bilinear cohesive law parameters are shown in Table 7.6.

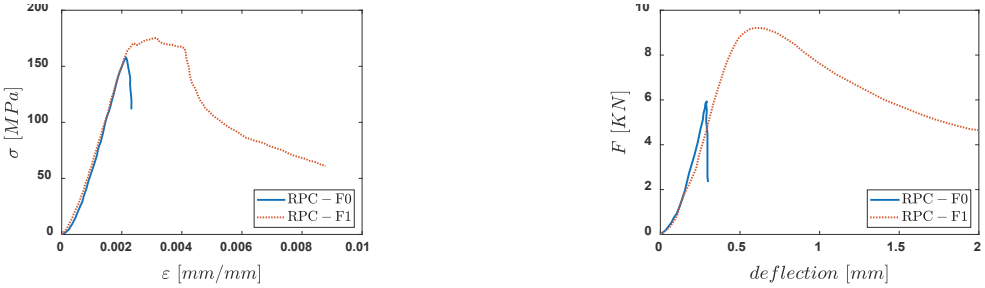

(a) (b)

Figure 7.15 (a) stress-strain curve [136], (b) force-deflection curve [136]

Table 7.6 Bilinear cohesive law parameters for concrete block impact test

Parameter	Positive Mode I	Negative Mode I	Mode II
Stiffness [MPa/mm]	750000	750000	312500
Fracture strength [MPa]	18.63	236.66	93.15
Static critical energy release rate [N/mm]	0.08	0.96	0.32

(2) Simulation results of the concrete block impact test

The experiment result is shown in Figure 7.16 (a), and the simulation results in Figure 7.16 (b) is obtained from element erosion method [136]. However, it is well known that the conservation of mass and energy is an inherent problem for element erosion method. What's more, since some elements will be deleted in simulation, the contact between detached debris with undamaged block cannot be guaranteed. Totally speaking, the simulation using element erosion method can capture the main cracks shown in experiment, but some detailed small branches and sub-branching are not obtained, which could be the verification of the limitation of element erosion method.

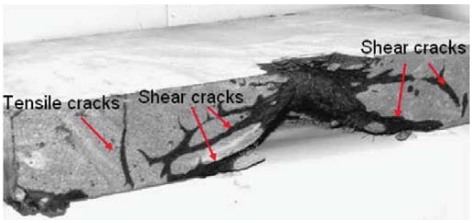

(a)

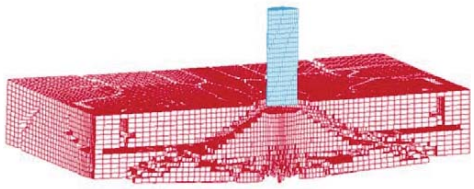

(b)

Figure 7.16 (a) experiment results [136], (b) simulation results using element erosion method [136]

The simulation results obtained from the proposed method are shown in Figure 7.17. As shown in Figure 7.17 (b), the tensile and shear cracks are captured in the simulation, and several small branches and sub-branching can also be seen from the simulation, which is an improvement compared with element erosion method. After the simulation, the detached debris is obtained, and this detached debris is close to the results obtained in experiment. From the comparison, it is easy to find that cohesive zone model is a better choice for cracking propagation problem. For this simulation, tetrahedron element is used in the model, and similar stress data showing the difference between different constitutive laws like in Section 3.4.4 is obtained. To avoid redundancy, it is not shown here.

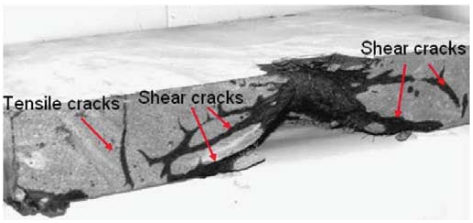

(a)

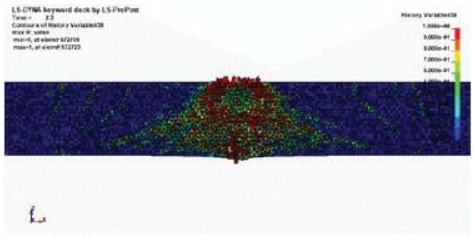

(b)

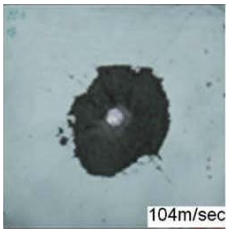

(c)

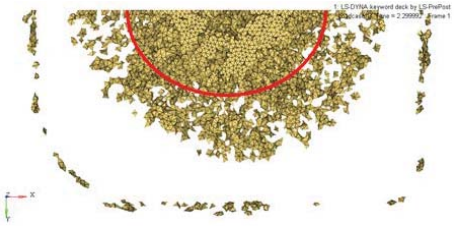

(d)

Figure 7.17 (a) experiment results from [136], (b) damage factor from simulation, (c) bottom view from [136], (d) bottom view from simulation

Reference

[1] Borden, M. J. (2012). Isogeometric analysis of phase-field models for dynamic brittle and ductile fracture (Doctoral dissertation).

[2] Song, J. H., Wang, H., & Belytschko, T. (2008). A comparative study on finite element methods for dynamic fracture. Computational Mechanics, 42(2), 239-250.

[3] Tabiei, A., & Meng, L. (2023). Improved cohesive zone model: integrating strain rate, plastic strain, variable damping, and enhanced constitutive law for fracture propagation. International Journal of Fracture, 1-24.

[4] Remmers, J. J., Borst, R. D., & Needleman, A. (2003). A cohesive segments method for the simulation of crack growth. Computational mechanics, 31, 69-77.

[5] Meng, L., & Tabiei, A. (2021). An irreversible bilinear cohesive law considering the effects of strain rate and plastic strain and enabling reciprocating load. Engineering Fracture Mechanics, 252, 107855.

[6] Deogekar, S. S. (2015). A Computational Study of Dynamic Brittle Fracture Using the Phase-Field Method (Doctoral dissertation, University of Cincinnati).

[7] Buljak, V., & Ranzi, G. (2021). Constitutive Modeling of Engineering Materials: Theory, Computer Implementation, and Parameter Identification. Academic Press.

[8] Niazi, M., Wisselink, H., Meinders, T., & ten Horn, C. (2010). Implementation of an Anisotropic Damage Material Model using a General Second Or-der Damage Tensor.

[9] Zreid, I., & Kaliske, M. (2014). On the gradient enhancement of microplane damage models. PAMM, 14(1), 155-156.

[10] Tabiei, A., & Meng, L. (2023). A length scale insensitive phase field model based on geometric function for brittle materials. Theoretical and Applied Fracture Mechanics, 125, 103902.

[11] Barenblatt, G. I. (1959). The formation of equilibrium cracks during brittle fracture. General ideas and hypotheses. Axially-symmetric cracks. Journal of applied mathematics and mechanics, 23(3), 622-636.

[12] Dugdale, D. S. (1960). Yielding of steel sheets containing slits. Journal of the Mechanics and Physics

of Solids, 8(2), 100-104.

[13] De Morais, A. B., Pereira, A. B., De Moura, M. F. S. F., Silva, F. G. A., & Dourado, N. (2015). Bilinear approximations to the mixed-mode I–II delamination cohesive law using an inverse method. Composite Structures, 122, 361-366.

[14] May, M., Hesebeck, O., Marzi, S., Böhme, W., Lienhard, J., Kilchert, S., ... & Hiermaier, S. (2015). Rate dependent behavior of crash-optimized adhesives–Experimental characterization, model development, and simulation. Engineering Fracture Mechanics, 133, 112-137.

[15] Freed, Y., & Banks-Sills, L. (2008). A new cohesive zone model for mixed mode interface fracture in bimaterials. Engineering Fracture Mechanics, 75(15), 4583-4593.

[16] Liu, P. F., & Islam, M. M. (2013). A nonlinear cohesive model for mixed-mode delamination of composite laminates. Composite Structures, 106, 47-56.

[17] Fernández-Cañadas, L. M., Iváñez, I., & Sanchez-Saez, S. (2016). Influence of the cohesive law shape on the composite adhesively-bonded patch repair behaviour. Composites Part B: Engineering, 91, 414-421.

[18] Abrate, S., Ferrero, J. F., & Navarro, P. (2015). Cohesive zone models and impact damage predictions for composite structures. Meccanica, 50(10), 2587-2620.

[19] De Moura, M. F. S. F., J. P. M. Gonçalves, and F. G. A. Silva. "A new energy based mixed-mode cohesive zone model." International Journal of Solids and Structures 102 (2016): 112-119.

[20] LS-DYNA Keysword User's Manual. "Vol. II Material Models." Livermore Software Technology Corporation (LSTC), Livermore, CA, USA; 2019.

[21] Hou, J. P, N. Petrinic, C. Ruiz, and S. R. Hallett. "Prediction of impact damage in composite plates." Composites Science and Technology 60, no. 2 (2000): 273-281.

[22] Hou, J. P., N. Petrinic, and C. Ruiz. "A delamination criterion for laminated composites under low-velocity impact." Composites science and technology 61, no. 14 (2001): 2069-2074.

[23] Naik, N. K., Y. Chandra Sekher, and Sailendra Meduri. "Polymer matrix woven fabric composites subjected to low velocity impact: Part I-damage initiation studies." Journal of Reinforced Plastics and Composites 19, no. 12 (2000): 912-954.

[24] Naik, Niranjan K., Y. Chandra Sekher, and Sailendra Meduri. "Damage in woven-fabric composites subjected to low-velocity impact." Composites Science and Technology 60, no. 5 (2000): 731-744.

[25] Naik, N. K., Sailendra Meduri, and Y. Chandrasekher. "Polymer matrix woven fabric composites subjected to low velocity impact: part III—Effect of incident impact velocity and impactor mass." Journal of reinforced plastics and composites 20, no. 9 (2001): 720-743.

[26] Kregting, Rene. "Cohesive zone models: towards a robust implementation of irreversible behavior." Philips Applied Technologies (2005).

[27] Gao, Wei, Jibang Xiang, Shunhua Chen, Shuohui Yin, Mengyan Zang, and Xuejun Zheng. "Intrinsic cohesive modeling of impact fracture behavior of laminated glass." Materials & Design 127 (2017): 321-335.

[28] Zhang, Wenlong, and Ala Tabiei. "Improvement of an exponential cohesive zone model for fatigue analysis." Journal of Failure Analysis and Prevention 18, no. 3 (2018): 607-618.

[29] Peng, X., Yong, H., & Zhou, Y. (2020). Finite element modeling of single-lap joint between GdBa2Cu3O7-x-coated conductors using cohesive elements. Physica C: Superconductivity and its Applications, 570, 1353600.

[30] Song, S. H., Paulino, G. H., & Buttlar, W. G. (2006). A bilinear cohesive zone model tailored for fracture of asphalt concrete considering viscoelastic bulk material. Engineering Fracture Mechanics, 73(18), 2829-2848.

[31] Fan, J., & Tadmor, E. B. (2019). Rescaling cohesive element properties for mesh independent fracture simulations. Engineering Fracture Mechanics, 213, 89-99.

[32] Marzi, S., O. Hesebeck, M. Brede, and F. Kleiner. "A rate-dependent cohesive zone model for adhesively bonded joints loaded in Mode I." Journal of adhesion science and technology 23, no. 6 (2009): 881-898.

[33] Marzi, Stephan, Olaf Hesebeck, Markus Brede, and Felix Kleiner. "A rate-dependent, elasto-plastic cohesive zone mixed-mode model for crash analysis of adhesively bonded joints." In 7th European LS-DYNA conference. 2009.

[34] Carlberger, Thomas, Anders Biel, and Ulf Stigh. "Influence of temperature and strain rate on cohesive properties of a structural epoxy adhesive." International Journal of Fracture 155, no. 2 (2009): 155-166.

[35] Cui, Hao. "Simulation of ductile adhesive failure with experimentally determined cohesive law." Composites Part B: Engineering 92 (2016): 193-201.

[36] Cazes, F., Simatos, A., Coret, M., & Combescure, A. (2010). A cohesive zone model which is energetically equivalent to a gradient-enhanced coupled damage-plasticity model. European Journal of Mechanics-A/Solids, 29(6), 976-989.

[37] LS-DYNA Keyword User's Manual. "Vol. I." Livermore Software Technology Corporation (LSTC), CA, USA (2019).

[38] Xu, C., Siegmund, T., & Ramani, K. (2003). Rate-dependent crack growth in adhesives: I. Modeling approach. International journal of adhesion and adhesives, 23(1), 9-13.

[39] Xu, C., Siegmund, T., & Ramani, K. (2003). Rate-dependent crack growth in adhesives II. Experiments and analysis. International journal of adhesion and adhesives, 23(1), 15-22.

[40] Wang, J., Qin, Q. H., Kang, Y. L., Li, X. Q., & Rong, Q. Q. (2010). Viscoelastic adhesive interfacial model and experimental characterization for interfacial parameters. Mechanics of Materials, 42(5), 537-547.

[41] Giambanco, G., & Fileccia Scimemi, G. (2006). Mixed mode failure analysis of bonded joints with rate-dependent interface models. International journal for numerical methods in engineering, 67(8), 1160-1192.

[42] Miehe, C., Hofacker, M., & Welschinger, F. (2010). A phase field model for rate-independent crack propagation: Robust algorithmic implementation based on operator splits. Computer Methods in Applied Mechanics and Engineering, 199(45-48), 2765-2778.

[43] Miehe, C., Welschinger, F., & Hofacker, M. (2010). Thermodynamically consistent phase-field models of fracture: Variational principles and multi-field FE implementations. International journal for numerical methods in engineering, 83(10), 1273-1311.

[44] Borden, M. J., Verhoosel, C. V., Scott, M. A., Hughes, T. J., & Landis, C. M. (2012). A phase-field

description of dynamic brittle fracture. Computer Methods in Applied Mechanics and Engineering, 217, 77-95.

[45] Borden, M. J., Hughes, T. J., Landis, C. M., & Verhoosel, C. V. (2014). A higher-order phase-field model for brittle fracture: Formulation and analysis within the isogeometric analysis framework. Computer Methods in Applied Mechanics and Engineering, 273, 100-118.

[46] Wu, J. Y., & Huang, Y. (2020). Comprehensive implementations of phase-field damage models in Abaqus. Theoretical and Applied Fracture Mechanics, 106, 102440.

[47] Francfort, G. A., & Marigo, J. J. (1998). Revisiting brittle fracture as an energy minimization problem. Journal of the Mechanics and Physics of Solids, 46(8), 1319-1342.

[48] Bourdin, B., Francfort, G. A., & Marigo, J. J. (2000). Numerical experiments in revisited brittle fracture. Journal of the Mechanics and Physics of Solids, 48(4), 797-826.

[49] Feng, Y., & Li, J. (2022). Phase-field cohesive fracture theory: A unified framework for dissipative systems based on variational inequality of virtual works. Journal of the Mechanics and Physics of Solids, 159, 104737.

[50] Wu, J. Y., Nguyen, V. P., Nguyen, C. T., Sutula, D., Sinaie, S., & Bordas, S. P. (2020). Phase-field modeling of fracture. Advances in applied mechanics, 53, 1-183.

[51] Schlüter, A., Willenbücher, A., Kuhn, C., & Müller, R. (2014). Phase field approximation of dynamic brittle fracture. Computational Mechanics, 54(5), 1141-1161.

[52] Liu, G., Li, Q., Msekh, M. A., & Zuo, Z. (2016). Abaqus implementation of monolithic and staggered schemes for quasi-static and dynamic fracture phase-field model. Computational Materials Science, 121, 35-47.

[53] Miehe, C., & Schänzel, L. M. (2014). Phase field modeling of fracture in rubbery polymers. Part I: Finite elasticity coupled with brittle failure. Journal of the Mechanics and Physics of Solids, 65, 93-113.

[54] Wu, J. Y. (2017). A unified phase-field theory for the mechanics of damage and quasi-brittle failure. Journal of the Mechanics and Physics of Sol-ids, 103, 72-99.

[55] Braun, S. G., Ewins, D. J., Rao, S. S., & Leissa, A. W. (2002). Encyclopedia of vibration: Volumes 1,

2, and 3. Appl. Mech. Rev., 55(3), B45-B45.

[56] Steinke, C., & Kaliske, M. (2019). A phase-field crack model based on directional stress decomposition. Computational Mechanics, 63(5), 1019-1046.

[57] Nguyen, T. T., Yvonnet, J., Waldmann, D., & He, Q. C. (2020). Implementation of a new strain split to model unilateral contact within the phase field method. International Journal for Numerical Methods in Engineering, 121(21), 4717-4733.

[58] Swamynathan, S., Jobst, S., & Keip, M. A. (2021). An energetically consistent tension–compression split for phase-field models of fracture at large deformations. Mechanics of Materials, 157, 103802.

[59] Li, T., Marigo, J. J., Guilbaud, D., & Potapov, S. (2016). Gradient damage modeling of brittle fracture in an explicit dynamics context. International Journal for Numerical Methods in Engineering, 108(11), 1381-1405.

[60] Seleš, K., Lesičar, T., Tonković, Z., & Sorić, J. (2019). A residual control staggered solution scheme for the phase-field modeling of brittle fracture. Engineering Fracture Mechanics, 205, 370-386.

[61] Lu, Y., Helfer, T., Bary, B., & Fandeur, O. (2020). An efficient and robust staggered algorithm applied to the quasi-static description of brittle fracture by a phase-field approach. Computer Methods in Applied Mechanics and Engineering, 370, 113218.

[62] Zhang, P., Hu, X., Wang, X., & Yao, W. (2018). An iteration scheme for phase field model for cohesive fracture and its implementation in Abaqus. Engineering Fracture Mechanics, 204, 268-287.

[63] Wu, J. Y., Huang, Y., & Nguyen, V. P. (2020). On the BFGS monolithic algorithm for the unified phase field damage theory. Computer Methods in Applied Mechanics and Engineering, 360, 112704.

[64] Braides, A. (1998). Approximation of free-discontinuity problems (No. 1694). Springer Science & Business Media.

[65] Braides, A. (2002). Gamma-convergence for Beginners (Vol. 22). Clarendon Press.

[66] Linse, T., Hennig, P., Kästner, M., & de Borst, R. (2017). A convergence study of phase-field models for brittle fracture. Engineering Fracture Mechanics, 184, 307-318.

[67] Freddi, F. (2019). Fracture energy in phase field models. Mechanics Research Communications, 96,

29-36.

[68] Miehe, C., Schaenzel, L. M., & Ulmer, H. (2015). Phase field modeling of fracture in multi-physics problems. Part I. Balance of crack surface and failure criteria for brittle crack propagation in thermo-elastic solids. Computer Methods in Applied Mechanics and Engineering, 294, 449-485.

[69] Wang, T., Ye, X., Liu, Z., Chu, D., & Zhuang, Z. (2019). Modeling the dynamic and quasi-static compression-shear failure of brittle materials by explicit phase field method. Computational Mechanics, 64(6), 1537-1556.

[70] Wang, T., Ye, X., Liu, Z., Liu, X., Chu, D., & Zhuang, Z. (2020). A phase-field model of thermo-elastic coupled brittle fracture with explicit time integration. Computational Mechanics, 65(5), 1305-1321.

[71] Pham, K., Amor, H., Marigo, J. J., & Maurini, C. (2011). Gradient damage models and their use to approximate brittle fracture. International Journal of Damage Mechanics, 20(4), 618-652.

[72] Alessi, R., Marigo, J. J., & Vidoli, S. (2015). Gradient damage models coupled with plasticity: variational formulation and main properties. Mechanics of Materials, 80, 351-367.

[73] Karma, A., Kessler, D. A., & Levine, H. (2001). Phase-field model of mode III dynamic fracture. Physical Review Letters, 87(4), 045501.

[74] Lancioni, G., & Corinaldesi, V. (2018). Variational modelling of diffused and localized damage with applications to fiber-reinforced concretes. Meccanica, 53(3), 531-551.

[75] Arriaga, M., & Waisman, H. (2018). Stability analysis of the phase-field method for fracture with a general degradation function and plasticity induced crack generation. Mechanics of Materials, 116, 33-48.

[76] Arriaga, M., & Waisman, H. (2018). Multidimensional stability analysis of the phase-field method for fracture with a general degradation function and energy split. Computational Mechanics, 61, 181-205.

[77] Yin, B., Steinke, C., & Kaliske, M. (2020). Formulation and implementation of strain rate-dependent fracture toughness in context of the phase-field method. International Journal for Numerical Methods in Engineering, 121(2), 233-255.

[78] Zhang, W., Tabiei, A., & French, D. (2021). A numerical implementation of the length-scale independent phase field method. Acta Mechanica Sinica, 37, 92-104.

[79] Kim, N. H. (2014). Introduction to nonlinear finite element analysis. Springer Science & Business Media.

[80] Bak, B. L., Lindgaard, E., & Lund, E. (2014). Analysis of the integration of cohesive elements in regard to utilization of coarse mesh in laminated composite materials. International Journal for Numerical Methods in Engineering, 99(8), 566-586.

[81] Rahulkumar, P., Jagota, A., Bennison, S. J., & Saigal, S. (2000). Cohesive element modeling of viscoelastic fracture: application to peel testing of polymers. International Journal of Solids and Structures, 37(13), 1873-1897.

[82] Spring, D. W., & Paulino, G. H. (2014). A growing library of three-dimensional cohesive elements for use in ABAQUS. Engineering Fracture Mechanics, 126, 190-216.

[83] Davila, Carlos, Pedro Camanho, and Marcelo de Moura. "Mixed-mode decohesion elements for analyses of progressive delamination." In 19th AIAA applied aerodynamics conference, p. 1486. 2001.

[84] Camanho, Pedro P., and Carlos G. Dávila. "Mixed-mode decohesion finite elements for the simulation of delamination in composite materials." (2002).

[85] Bui, Q. V. "A modified Benzeggagh-Kenane fracture criterion for mixed-mode delamination." Journal of Composite Materials 45, no. 4 (2011): 389-413.

[86] Blal, N., Daridon, L., Monerie, Y., & Pagano, S. (2013). Micromechanical-based criteria for the calibration of cohesive zone parameters. Journal of computational and applied mathematics, 246, 206-214.

[87] Tabiei, A., & Zhang, W. (2017). Cohesive element approach for dynamic crack propagation: Artificial compliance and mesh dependency. Engineering Fracture Mechanics, 180, 23-42.

[88] Klein, P. A., Foulk, J. W., Chen, E. P., Wimmer, S. A., & Gao, H. J. (2001). Physics-based modeling of brittle fracture: cohesive formulations and the application of meshfree methods. Theoretical and Applied Fracture Mechanics, 37(1-3), 99-166.

[89] Liu, Y., F. P. van der Meer, and L. J. Sluys. "Cohesive zone and interfacial thick level set modeling of the dynamic double cantilever beam test of composite laminate." Theoretical and Applied Fracture Mechanics 96 (2018): 617-630.

[90] Kolluri, M., J. P. M. Hoefnagels, J. A. W. van Dommelen, and M. G. D. Geers. "Irreversible mixed mode Interface delamination using a combined damage-plasticity cohesive zone enabling unloading." International Journal of Fracture 185, no. 1-2 (2014): 77-95.

[91] Zhou, F., Molinari, J. F., & Shioya, T. (2005). A rate-dependent cohesive model for simulating dynamic crack propagation in brittle materials. Engineering fracture mechanics, 72(9), 1383-1410.

[92] Shioya, T., & Zhou, F. (1996). Dynamic fracture toughness and crack propagation in brittle material. In Constitutive relation in high/very high strain rates (pp. 105-112). Springer, Tokyo.

[93] Kazerani, T., Zhao, G., & Zhao, J. (2010). Dynamic fracturing simulation of brittle material using the distinct lattice spring method with a full rate-dependent cohesive law. Rock mechanics and rock engineering, 43(6), 717-726.

[94] Davenport, J. C., & Smith, D. J. (1995). The influence of plasticity and geometry on the mixed mode fracture of PMMA. In Constraint Effects in Fracture Theory and Applicatons: Second Volume. ASTM International.

[95] Kalthoff, J. F. (2000). Modes of dynamic shear failure in solids. International Journal of Fracture, 101(1), 1-31.

[96] Menouillard, T., Rethore, J., Combescure, A., & Bung, H. (2006). Efficient explicit time stepping for the eXtended Finite Element Method (X-FEM). International Journal for Numerical Methods in Engineering, 68(9), 911-939.

[97] Chakraborty, S., & Shaw, A. (2013). A pseudo-spring based fracture model for SPH simulation of impact dynamics. International Journal of Impact Engineering, 58, 84-95.

[98] Pascale, P., & Vemaganti, K. (2021). A Variational Model of Elasto-Plastic Behavior of Materials. Journal of Elasticity, 147(1), 257-289.

[99] Wu, J. Y., & Nguyen, V. P. (2018). A length scale insensitive phase-field damage model for brittle fracture. Journal of the Mechanics and Physics of Solids, 119, 20-42.

[100] Hu, X., Tan, S., Xia, D., Min, L., Xu, H., Yao, W., ... & Rabczuk, T. (2023). An overview of implicit and explicit phase field models for quasi-static failure processes, implementation and computational

efficiency. Theoretical and Applied Fracture Mechanics, 103779.

[101] Trunk, B. G. (1999). Einfluss der Bauteilgrösse auf die Bruchenergie von Beton (Doctoral dissertation, ETH Zurich).

[102] Feng, Y., Fan, J., & Li, J. (2021). Endowing explicit cohesive laws to the phase-field fracture theory. Journal of the Mechanics and Physics of Solids, 152, 104464.

[103] Zhang, X., Vignes, C., Sloan, S. W., & Sheng, D. (2017). Numerical evaluation of the phase-field model for brittle fracture with emphasis on the length scale. Computational Mechanics, 59(5), 737-752.

[104] Winkler, B. J. (2001). Traglastuntersuchungen von unbewehrten und bewehrten Betonstrukturen auf der Grundlage eines objektiven Werkstoffgesetzes für Beton. Innsbruck University Press.

[105] Gerasimov, T., & De Lorenzis, L. (2019). On penalization in variational phase-field models of brittle fracture. Computer Methods in Applied Mechanics and Engineering, 354, 990-1026.

[106] Gálvez, J. C., Elices, M., Guinea, G. V., & Planas, J. (1998). Mixed mode fracture of concrete under proportional and nonproportional loading. International Journal of Fracture, 94(3), 267-284.

[107] Wu, J. Y. (2018). A geometrically regularized gradient-damage model with energetic equivalence. Computer Methods in Applied Mechanics and Engineering, 328, 612-637.

[108] Hoover, C. G., Bažant, Z. P., Vorel, J., Wendner, R., & Hubler, M. H. (2013). Comprehensive concrete fracture tests: Description and results. Engineering fracture mechanics, 114, 92-103.

[109] Hoover, C. G., & Bažant, Z. P. (2014). Cohesive crack, size effect, crack band and work-of-fracture models compared to comprehensive concrete fracture tests. International Journal of Fracture, 187(1), 133-143.

[110] Lorentz, E. (2017). A nonlocal damage model for plain concrete consistent with cohesive fracture. International Journal of Fracture, 207(2), 123-159.

[111] Ambati, M., Gerasimov, T., & De Lorenzis, L. (2015). A review on phase-field models of brittle fracture and a new fast hybrid formulation. Computational Mechanics, 55, 383-405.

[112] Navidtehrani, Y., Betegón, C., & Martínez-Pañeda, E. (2021). A unified Abaqus implementation of the phase field fracture method using only a user material subroutine. Materials, 14(8), 1913.

[113] de Souza Neto, E. A., Peric, D., & Owen, D. R. (2011). Computational methods for plasticity: theory and applications. John Wiley & Sons.

[114] Ambati, M., Gerasimov, T., & De Lorenzis, L. (2015). Phase-field modeling of ductile fracture. Computational Mechanics, 55, 1017-1040.

[115] Ambati, M., Kruse, R., & De Lorenzis, L. (2016). A phase-field model for ductile fracture at finite strains and its experimental verification. Computational Mechanics, 57, 149-167.

[116] Miehe, C., Aldakheel, F., & Raina, A. (2016). Phase field modeling of ductile fracture at finite strains: A variational gradient-extended plasticity-damage theory. International Journal of Plasticity, 84, 1-32.

[117] Fang, J., Wu, C., Li, J., Liu, Q., Wu, C., Sun, G., & Li, Q. (2019). Phase field fracture in elasto-plastic solids: Variational formulation for multi-surface plasticity and effects of plastic yield surfaces and hardening. International Journal of Mechanical Sciences, 156, 382-396.

[118] Fang, J., Wu, C., Rabczuk, T., Wu, C., Ma, C., Sun, G., & Li, Q. (2019). Phase field fracture in elasto-plastic solids: Abaqus implementation and case studies. Theoretical and Applied Fracture Mechanics, 103, 102252.

[119] Loew, P. J., Peters, B., & Beex, L. A. (2019). Rate-dependent phase-field damage modeling of rubber and its experimental parameter identification. Journal of the Mechanics and Physics of Solids, 127, 266-294.

[120] Shi, Q., Yu, H., Guo, L., Hao, L., & Huang, K. (2022). A phase field model with plastic history field for fracture of elasto-plastic materials. Engineering Fracture Mechanics, 268, 108447.

[121] Del Piero, G. (2013). A variational approach to fracture and other inelastic phenomena. Journal of Elasticity, 112, 3-77.

[122] Li, W., Ambati, M., Nguyen-Thanh, N., Du, H., & Zhou, K. (2023). Adaptive fourth-order phase-field modeling of ductile fracture using an isogeometric-meshfree approach. Computer Methods in Applied Mechanics and Engineering, 406, 115861.

[123] Kumar, S., Singh, I. V., & Mishra, B. K. (2014). A coupled finite element and element-free Galerkin approach for the simulation of stable crack growth in ductile materials. Theoretical and Applied Fracture

Mechanics, 70, 49-58.

[124] Aldakheel, F., Noii, N., Wick, T., Allix, O., & Wriggers, P. (2021). Multilevel global–local techniques for adaptive ductile phase-field fracture. Computer Methods in Applied Mechanics and Engineering, 387, 114175.

[125] Yin, B., & Kaliske, M. (2020). A ductile phase-field model based on degrading the fracture toughness: Theory and implementation at small strain. Computer Methods in Applied Mechanics and Engineering, 366, 113068.

[126] Ren, Z. J., & Ru, C. Q. (2013). Numerical investigation of speed dependent dynamic fracture toughness of line pipe steels. Engineering Fracture Mechanics, 99, 214-222.

[127] Standard test method for mixed mode I – mode II interlaminar fracture toughness of unidirectional fiber-reinforced polymer-matrix composites. ASTM D6671/D6671M - 2019.

[128] Sadeghi, M. Z., J. Zimmermann, A. Gabener, and K. U. Schroeder. "The applicability of J-integral approach in the determination of mixed-mode fracture energy in a ductile adhesive." International Journal of Adhesion and Adhesives 83 (2018): 2-8.

[129] Turon, A., P. P. Camanho, J. Costa, and J. Renart. "Accurate simulation of delamination growth under mixed-mode loading using cohesive elements: definition of interlaminar strengths and elastic stiffness." Composite structures 92, no. 8 (2010): 1857-1864.

[130] De Carvalho, N. V., M. W. Czabaj, and J. G. Ratcliffe. "Piecewise-linear generalizable cohesive element approach for simulating mixed-mode de-lamination." Engineering Fracture Mechanics 242 (2021): 107484.

[131] Liu, J., & Jones, N. (1987). Experimental investigation of clamped beams struck transversely by a mass. International Journal of Impact Engineering, 6(4), 303-335.

[132] Mannan, M. N., Ansari, R., & Abbas, H. (2008). Failure of aluminium beams under low velocity impact. International Journal of Impact Engineering, 35(11), 1201-1212.

[133] Raguraman, M., Deb, A., & Jagadeesh, G. (2009). A numerical study of projectile impact on thin aluminium plates. Proceedings of the Institution of Mechanical Engineers, Part C: Journal of Mechanical

Engineering Science, 223(11), 2519-2530.

[134] Wang, Y. J., & Ru, C. Q. (2016). Determination of two key parameters of a cohesive zone model for pipeline steels based on uniaxial stress-strain curve. Engineering Fracture Mechanics, 163, 55-65.

[135] Suh, C. H., Jung, Y. C., & Kim, Y. S. (2010). Effects of thickness and surface roughness on mechanical properties of aluminum sheets. Journal of mechanical science and technology, 24(10), 2091-2098.

[136] Tai, Y. S. (2009). Flat ended projectile penetrating ultra-high strength concrete plate target. Theoretical and Applied Fracture Mechanics, 51(2), 117-128.

[137] Abdulraheem, M. S., & Kadhum, M. M. (2018). Experimental and numerical study on post-fire behaviour of concentrically loaded reinforced reactive powder concrete columns. Construction and Building Materials, 168, 877-892.